

**THE INTERPLAY OF ARCHITECTURE AND CORRELATED
VARIABILITY IN NEURONAL NETWORKS**

A Dissertation

Presented to

the Faculty of the Department of Mathematics

University of Houston

In Partial Fulfillment

of the Requirements for the Degree

Doctor of Philosophy

By

James Trousdale

August, 2013

THE INTERPLAY OF ARCHITECTURE AND CORRELATED VARIABILITY IN NEURONAL NETWORKS

James Trousdale

APPROVED:

Dr. Krešimir Josić,
Chairman
Department of Mathematics, University of Houston

Dr. William Ott
Department of Mathematics, University of Houston

Dr. Andrew Török
Department of Mathematics, University of Houston

Dr. Yuri Dabaghian
Department of Computational & Applied Mathematics,
Rice University
Jan and Dan Duncan Neurological Research Institute,
Baylor College of Medicine

Dean, College of Natural Sciences and Mathematics

Acknowledgements

Coming soon

**THE INTERPLAY OF ARCHITECTURE AND CORRELATED
VARIABILITY IN NEURONAL NETWORKS**

An Abstract of a Dissertation
Presented to
the Faculty of the Department of Mathematics
University of Houston

In Partial Fulfillment
of the Requirements for the Degree
Doctor of Philosophy

By
James Trousdale
August, 2013

Abstract

This much is certain: neurons are coupled, and they exhibit covariations in their output. The extent of each does not have a single answer. Moreover, the strength of neuronal correlations, in particular, has been a subject of hot debate within the neuroscience community over the past decade, as advancing recording techniques have made available a lot of new, sometimes seemingly conflicting, datasets. The impact of connectivity and the resulting correlations on the ability of animals to perform necessary tasks is even less well understood. In order to answer relevant questions in these categories, novel approaches must be developed. This work focuses on three somewhat distinct, but inseparably coupled, crucial avenues of research within the broader field of computational neuroscience. First, there is a need for tools which can be applied, both by experimentalists and theorists, to understand how networks transform their inputs. In turn, these tools will allow neuroscientists to tease apart the structure which underlies network activity. The Generalized Thinning and Shift framework, presented in Chapter 4, addresses this need. Next, taking for granted a general understanding of network architecture as well as some grasp of the behavior of its individual units, we must be able to reverse the activity to structure relationship, and understand instead how network structure determines dynamics. We achieve this in Chapters 5 through 7 where we present an application of linear response theory yielding an explicit approximation of correlations in integrate-and-fire neuronal networks. This approximation reveals the explicit relationship between correlations, structure, and marginal dynamics. Finally, we must strive to understand the functional impact of network dynamics and architecture on the tasks that a neural network performs. This need motivates our analysis of a biophysically detailed model of the blow fly visual system in Chapter 8. Our hope is that the work presented here represents significant advances in multiple directions within the field of computational neuroscience.

Contents

1	Introduction	1
2	Correlations and stochastic processes	13
2.1	Statistical measures of stochastic processes	14
2.1.1	General measures of correlation	14
2.1.2	Point processes	20
2.2	Copulas	27
2.2.1	Archimedean copulas	29
2.2.2	The Gaussian copula	29
3	Modeling of neurons and their interactions	32
3.1	Integrate-and-fire neuron models	33
3.1.1	The leaky integrate-and-fire neuron	34
3.1.2	The exponential integrate-and-fire neuron	35
3.1.3	The general integrate-and-fire neuron	36
3.2	Models of synaptic interaction	36
3.2.1	Current-based synapses	37
3.2.2	Conductance-based synapses	38
3.2.3	Electrical synapses	40

3.3	The diffusion approximation	43
3.3.1	The effective time constant form	44
3.3.2	The diffusion approximation for multiplicative Poisson noise	45
3.3.3	Consideration of additive noise sources	46
4	A generative spike train model with time-structured higher order correlations	48
4.1	Defining the Generalized Thinning and Shift Model	49
4.1.1	GTaS model simulation	50
4.2	Examples of applications of the GTaS framework	51
4.2.1	Relation to SIP/MIP processes	51
4.2.2	Generation of synfire-like cascade activity	53
4.2.3	Timing-selective network	60
4.3	Cumulant structure of a GTaS process	65
4.3.1	Second order cumulants (covariance)	67
4.3.2	Third order cumulants	70
4.3.3	General cumulants	71
5	Introduction to Linear Response Theory	80
5.1	Firing rate linear response theory	82
5.2	Linear response approximation of correlations	83
5.2.1	Independent noise	86
5.2.2	Correlated noise	93
5.2.3	Conductance-based synaptic interactions	95
5.3	Calculation of firing statistics for IF neurons	97
5.3.1	Review of existing results	99
5.3.2	Derivation of firing statistics for conductance synapses	105
6	Analysis of Neuronal Networks Using Linear Response	109
6.1	Path expansion of correlations	110

6.2	Linear response application to coupled microcircuits	112
6.2.1	Feed-forward inhibitory microcircuit	112
6.2.2	Bi-directional excitatory microcircuit	116
6.3	Linear response applications to large networks	121
6.3.1	All-to-all networks	122
6.3.2	Random networks	127
6.3.3	Distance-dependent networks	142
6.4	Validity of the linear response approximation	146
6.4.1	Accuracy of linear response in the all-to-all network of Figure 6.5 . .	147
6.4.2	Accuracy of the linear response theory in different firing regimes . .	150
6.4.3	Failure of the linear response theory of correlations at third order . .	151
7	Motif Cumulants and Average Correlations	156
7.1	Graphical structure of neuronal networks	158
7.1.1	Preliminaries	158
7.1.2	Second order motif cumulants	160
7.1.3	Motif moments and higher order cumulants	162
7.2	Motif cumulants determine average second order correlation	173
7.2.1	Single population networks	174
7.2.2	Multi-population networks	177
8	Efficient encoding of the ego-rotational axis in the fly brain	183
8.1	Modeling the vertical system response to optic flow	184
8.1.1	Model of the VS network	184
8.1.2	Generation of images and optic flow patterns	190
8.2	Implementation of estimators for the rotational axis	192
8.2.1	Optimal linear estimator	193
8.2.2	Modeling the joint distribution of VS axonal responses using copulas	195
8.2.3	Computation of the MMSE	198

CONTENTS

8.3	Steady-state encoding of the axis of rotation	200
8.4	Dynamical effects of coupling on VS network responses	200
8.5	Steady-state encoding of the axis of rotation	201
8.5.1	MSE of the OLE is independent of coupling in steady-state	203
8.6	Transient encoding of the axis of rotation	207
8.6.1	MMSE is independent of coupling in the transient state	208
8.7	The role of coupling	211
8.7.1	Coupling improves partial decoding in simplified model	213
8.7.2	Comparison of the MMSE with a zero-crossing estimator	216
8.8	Factors determining partial decoding improvement	219
8.8.1	Trial-to-trial variations vs. tuning curve smoothing	220
8.8.2	Axonal filtering	220
8.8.3	Partial readout subset size and VS cell identity	223
9	Discussion	225
A	Notation tables	240
	Bibliography	244

List of Figures

- 1.1 **Example of a GTaS process exhibiting “synfire-like” firing patterns (A)** Raster plot of event times for an example multivariate Poisson process $\mathbf{X} = (X_1, \dots, X_6)$ generated using the methods presented in Chapter 4. This model exhibits independent marginal events (blue) and population-level, chain-like events (red). **(B)** Some second order population cumulant densities (i.e., second order correlation between individual unit activities and population activity) for this model [173]. Greater mass to the right (resp. left) of $\tau = 0$ indicates that the cell tends to lead (resp. follow) in pairwise-correlated events. **(C)** Third-order cross-cumulant density for processes X_1, X_2, X_3 . The quantity $\kappa_{123}^X(\tau_1, \tau_2)$ yields the probability of observing spikes in cells 2 and 3 at an offset τ_1, τ_2 from a spike in cell 1, respectively, in excess of what would be predicted from the first and second order cumulant structure. All statistical quantities are precisely defined in Chapter 2. 4
- 1.2 **Linear response theory admits an expansion of correlations in terms of motifs within the network the network (A)** Linear response theory can serve as an important tool for understanding how architecture in dynamics shape the statistics of responses in large, complex networks. This is enacted via an expansion of correlations by contributions due to different motifs embedded within the network architecture. We highlight some second order motifs — motifs which involve a pair of connections and up to three cells. **(B)** Some second order motifs involving cells of two distinct populations, with edge color indicating whether the motifs connect cells of a single population (red, blue) or both populations (purple). 6

- 1.3 **Local features of network architecture can strongly influence global behavior** The black line indicates the relation between the density of connections and average output correlation in truly random (i.e., Erdős-Rényi), excitatory-only integrate-and-fire neuronal networks, as predicted by the cumulant resummation theory of Chapter 7. The dark gray dots indicate simulations of integrate-and-fire networks. Fluctuations about the line are due essentially to finite-size effects — in particular, finite networks are generally not perfectly regular, and thereby exhibit residual higher order structure within their architecture. The light gray dots indicate output correlation in networks designed to be non-Erdős-Rényi. The adjacency graphs associated with these networks featured dependent edges — i.e., pairs of connections were not present or absent independently. This yielded, in turn, significant deviations in the dynamics of the corresponding networks from what is expected in the case of underlying Erdős-Rényi graphs. 9
- 1.4 **The VS network extracts motion parameters from optic flow-related information.** (A) (Left) The ten VS cells in one lobula plate (LP) as reconstructed from two-photon image stacks. Each neuron is T-shaped, with an elongated dendrite sampling a thin vertical stripe in the retinotopically organized LP (VS 1 to 10 arranged from distal to proximal in the LP, [117]). Inset indicates approximate orientation (a: anterior, p: posterior, l: lateral, m: medial, d: dorsal, v: ventral). Adapted from [56]. (Right) Connectivity scheme of the VS network. VS cell axons are electrically coupled to nearest neighbors. There is a functionally mutually inhibitory (or “repulsive”) interaction between VS1 and VS10. Receptive field (RF) centers indicate azimuthal position in the horizontal equatorial plane of right side VS neurons, taking 0° to represent the anteroposterior axis of the fly. Left side VS neuron receptive field centers are given by reflection across 0° [30]. (B) Examples of images used to generate the optic flow stimuli presented to the VS network model. Details of image generation are given in the Methods, along with parameters and procedure for generation of rotational optic flow stimuli. (C) The marginalization problem: Parameters of ego-motion (such as the axis of rotation, θ_{stim}) are first probabilistically embedded in the external world (Image), and additional layers of variability (noise) are imposed by the processing in VS cells at the dendritic (De) and axonal (Ax) stages (\bar{V} denotes time-averaged membrane potential; see Methods). Reading-out the azimuthal rotation axis from the VS population response amounts to marginalize — extract a notion of the posterior distribution of the stimulus from the axonal responses. 12

3.1	Illustrating the membrane potential and spiking dynamics of integrate-and-fire model neurons.	(A) The time evolution of the membrane potential of an LIF neuron receiving excitatory Poisson current inputs. The corresponding output spike train is displayed at the top of the panel. (B) Same as panel A, but for the EIF neuron model. Unlike the LIF, the EIF neuron features a spike initiation phase in its subthreshold dynamics in which the membrane potential exhibits a smooth but rapid escape.	34
3.2	Implementing coupling amongst integrate-and-fire model neurons.	(A) Time evolution of the membrane potential of a LIF neuron (with spiking dynamics — i.e., the threshold and reset — neglected) receiving current-based excitatory Poisson input. (B) Same as panel A for conductance-based input. The input spike train was precisely that used for panel A. Note that the jump size now depends on the membrane potential at the time of arrival for the input pulse. (C) Time evolution of the membrane potentials (bottom) and resulting spike trains (top) for a pair of electrically coupled LIF neurons. (D) Same as panel C, except for EIF neurons. The nature of the spiking dynamics strongly modulates the effect of gap junction coupling on output spiking correlations. The strength of the gap-junction synapses was set to $g_{gap} = 10g_L$	39
3.3	The diffusion approximation.	Left to right: input parameters of an LIF neuron receiving excitatory and inhibitory Poisson noise are moved towards the region of validity for the diffusion approximation (i.e., input weights are decreased and input rates are increased).	47
4.1	The GTaS simulation protocol.	(A) Step 1: Simulate the mother process - a time-homogeneous Poisson process with event times $\{t^j\}$. (B) Step 2: For each t^j in step 1, select a set $D^j \subset \mathbb{D}$ according to the distribution p_D , and project the event at time t^j to the subsets with indices in D^j . The legend indicates the colors assigned to three possible markings in this example. (C) Step 3: For each pair (t^j, D^j) generated in the previous two steps, draw random vectors \mathbf{Y}^j from Q_{D^j} , and shift the event times in the daughter processes by the corresponding values Y_i^j	51

4.2 **An example of a six dimensional GTaS model exhibiting synfire-like cascading firing patterns.** (A) A raster-plot of spiking activity over a 100ms window. Blue spikes indicate either marginal or pairwise events (i.e., events corresponding to markings for sets $D \subset \mathbb{D}$ with $|D| \leq 2$). Red spikes indicate population-wide events which have shift-times given by cumulative sums of independent exponentials, as described in the text. Arrows indicate the location of the first spike in the cascade. (B) A second-order cross-cumulant κ_{13}^X (black line) of this model is composed of contributions from two sources: correlations due to second-order markings, which have Gaussian shifts (c_{13}^2 – dashed red line), and correlations due to the occurrence of population wide events (c_{13}^N – dashed blue line). (C) Density plots of the third-order cross-cumulant density for triplets **i**) (1, 2, 3) and **ii**) (1, 2, 4) — the latter is given explicitly in Eq. (4.6). 55

4.3 **Population cumulants for the synfire-like cascading GTaS process of Figure 4.2.** (A) Second order population cumulant densities for processes 1,3 and 6. Greater mass to the right (resp. left) of $\tau = 0$ indicates that a cell tends to lead (resp. follow) in pairwise-correlated events. (B) Third order population cumulant for processes X_1, X_2 in the cascading GTaS process. Concentration of the mass in different regions of the plane indicates temporal structure of events correlated between X_1, X_2 relative to the remainder of the population (see the text). (C) Same as (B), but for processes X_3, X_4 . (D) Same as (B), but for processes X_1, X_6 . Population cumulants are defined in Eq. (2.15). 59

4.4 **Using the GTaS model to probe a timing-selective network.** (A) Example input (left) and output (right) for the nearest neighbor LIF network receiving input with synchronous input. (B) Same as (A), but for cascading input. (C) Scatter plot of the output spike count of the network receiving synchronous (horizontal axis) and cascading input (vertical axis) with $\mu_{\text{shift}} = 2, \sigma_{\text{shift}} = 0.3$. The red line is the diagonal. (D) Average gain (rate in response to cascading input divided by rate in response to synchronous input) as a function of the standard deviation of the gamma variates which compose the shift vectors for population-level events (μ_{shift} was fixed at 2). The red dot indicates the value of σ_{shift} used in panel C. Inset shows the same gain as panel D, but for varying the mean of the shift distribution ($\sigma_{\text{shift}} = 0.3$). Spike counts in panels C and D were obtained for trials of length $T = 100$ 63

4.5 **Illustrating the representation given by Eq. (4.10).** (A) Performing the decomposition at second order ($\bar{D} = \{1, 2\}$, see Eq. (4.11) and the surrounding discussion) with $N = 4$. (B) Same as panel A, but for three processes with $\bar{D} = \{1, 2, 3\}$ (see Eq. (4.16) and the surrounding discussion). 67

5.1 **Depicting the firing rate linear response approximation Eq. (5.2).** (A) A spike train is generated and supplies an input current to an exponential integrate-and-fire neuron. (B) The membrane potential of the neuron is driven by intrinsic white noise fluctuations and the spike train in panel A. Each realization of the intrinsic noise corresponds to a realization of the output spike train (red ticks). (C) Fixing the input spike train, repeat the simulation in panel B many times for independent realizations of the intrinsic noise process, generating a raster plot. A dot in the raster indicates a spike in that time bin (horizontal axis) for a specific trial (vertical axis). (D) Averaging the output spike train across trials yields the time-dependent firing rate, or PSTH (grey indicates the Monte Carlo estimation of the PSTH, and black is the theoretical prediction). Spikes in the fixed input spike train shown in panel A (repeated at the bottom of panel D for ease of comparison) drive deviations in the (constant) background firing rate, a quantity determined by the mean and variance of the intrinsic noise. 84

5.2 **Equations (5.8) and (5.9) give rise to an iterative approximation of network activity.** (A) We approximate the activity y_1 of cell 1, embedded in the depicted recurrent microcircuit. (B) The first approximation y_1^1 of the activity of neuron 1 reflects only the effect of input from the uncoupled approximations y_j^0 of activity for its afferent partners. (C) The second approximation y_1^2 of the activity of neuron 1 now reflects the effects of length two chains through the circuit. In particular, the output of neuron 1 now reflects the impact of its own activity ($y_1^0 \rightarrow y_2^1 \rightarrow y_1^2$), and the approximation of neuron 1's activity now also reflects the indirect input from neuron 4 through neuron 3. (D) The difference between higher order approximations and the second order approximation will be improved resolution of the recurrent loop between cells 1 and 2. At each step, effects due to a longer chain through this loop will be included, and owing to this recurrence, the approximation does not converge in finitely many iterations. 89

5.3 **Illustrating the the accuracy of the linear response approximation of correlations in a random network.** Comparison of Monte Carlo estimation of second order cross-cumulant densities (black lines) with their linear response approximations (blue lines, Eq. (5.12)) for nine neuron pairs from a size $N = 100$ random network consisting of 80 excitatory and 20 inhibitory cells. The connection probability was 0.2. A cross-cumulant density is exhibited for one example neuron pair from each of nine possible pairings of neuron classes (EE, EI, II) and first order connectivity (bidirectional, unidirectional or none). 92

5.4 **Linear response of correlations for common input.** (A) Comparison of second order cross-cumulant density from simulations and theory (see Eq. (5.15)) for a pair of neurons receiving common white noise input. The input correlation was $c = 0.25$ and the infinite window correlation between the spiking output of the neurons was ≈ 0.21 . (B) Comparison of the steady-state auto-covariance density (δ -peak removed) for the one of the neurons without (Eq. (5.15)) and with (Eq. (5.16)) the adjustment to the power spectrum acquired via a naive linear response application. 95

5.5 **Exhibiting the linear response approximation of correlations for conductance-based synapses.** Comparison of the theoretical prediction (blue) with the Monte Carlo estimation (black) of the second-order cross cumulant density of a pair of excitatory neurons reciprocally coupled via conductance-based synapses. 98

6.1 **Motifs appearing in the linear response diagrammatic expansion of correlations given in Eq. (6.2).** (A) An n^{th} order chain motif in a recurrent network connecting the pair of cells (i, j) . Within the linear response path expansion of correlations (Eq. (6.2), the contributions to correlations of such motifs are captured by the term in Eq. (6.3). (B) An $(n + m)^{th}$ order diverging motif which contributes to the correlation (i, j) in a recurrent network. Within the linear response path expansion of correlations (Eq. (6.2), the contributions to correlations of such motifs are captured by the term in Eq. (6.4). 112

6.2 **Linear response path expansion of correlations in a feed-forward inhibitory (FFI) microcircuit.** (A) Linear response path expansion of the second order correlations for cells (E_2, I) in the FFI microcircuit. Each of the three terms appearing in the finite expansion correspond to the contribution of a different motif, and their values are denoted in Eq. (6.6). (B) Comparison of the linear response approximation of correlations with Monte Carlo estimation of the second-order cross-cumulant density for the pair (E_2, I) in the FFI microcircuit. Results are plotted for two values of the inhibitory time constant τ_I . The solid line corresponds to $\tau_I = 5$ ms, and the dashed line to $\tau_I = 10$ ms. (C) Plot of the three contributions to the cross-cumulant density for the pair (E_2, I) as determined from the linear response expansion of their correlation structure (Eq. (6.6)). Solid and dashed lines again correspond to values for the two different inhibitory synaptic time constants. The inset shows the two inhibitory synaptic kernels. 114

6.3 **Linear response path expansion of correlations in a bidirectional excitatory microcircuit.** (A) The cross-cumulant density of the two cells can be represented in terms of contributions from an infinite sequence of submotifs (See Eq. (6.8)). Though we show only a few “chain” motifs in one direction, one should note that there will also be contributions to the cross-cumulant from chain motifs in the reverse direction in addition to indirect common input motifs (See Figure 6.1). (B), (E) Linear response kernels in the excitable (B) and oscillatory (E) regimes. (C), (F) Comparison of the cross-cumulant density computed from Monte Carlo simulation and linear response theory (from Eq. (6.7)) with first and third order contributions (from Eq. (6.8)) in the excitable (C) and oscillatory (F) regimes. (D), (G) Comparison of the auto-cumulant density computed from Monte Carlo simulation and linear response theory (from Eq. (6.7)) with zeroth and second order contributions (from Eq. (6.8)) in the excitable (D) and oscillatory (G) regimes. 117

6.4 **Inclusion of autaptic connections in the all-to-all network has a negligible impact on correlations.** (A) Comparison of the linear response theory prediction of a second order cross-cumulant density in an all-to-all network of size $N = 100$ with (solid line) and without (dashed line) autaptic connections. Relative L^2 difference was approximately 0.0043 (the two lines are almost exactly on top of one another). (B) Same as panel A, for a second order auto-cumulant density. Relative L^2 difference was approximately 0.0016. 123

6.5 **Linear response theory of correlations in all-to-all networks, and the importance of higher order motifs.** (A) Some of the submotifs contributing to correlations in the all-to-all network. (B) Comparison of Monte Carlo estimation cross-cumulant density between two excitatory cells in an all-to-all network with the linear response theoretical prediction obtained using Eq. (6.11) (Solid lines – precisely tuned network with $\tilde{\varphi} \equiv 0$ [$G_E = -G_I = 140 \text{ mV} \cdot \text{ms}$, $\tau_E = \tau_I = 10 \text{ ms}$], dashed – non-precisely tuned network with $\tilde{\varphi} \neq 0$ [$G_E = 168 \text{ mV} \cdot \text{ms}$, $G_I = -210 \text{ mV} \cdot \text{ms}$, $\tau_E = 10 \text{ ms}$, $\tau_I = 5 \text{ ms}$]). The population sizes were $N_E = 80, N_I = 20$. (C) Comparison of first and second order contributions to the cross-correlation function in panel A in the precisely tuned (left) and non-precisely tuned (right) network. In both cases, the long window correlation coefficient $\rho_{ij}^y(\infty)$ was 0.05. The blue line indicates the contribution due to the direct connection between the two cells, while the dotted green line captures contributions due to second order chain motifs, and the dashed green line second order diverging motifs (common input). 124

- 6.6 **Application of the linear response to a random network reveals the average second order temporal correlation structure.** (A) A comparison of numerically obtained excitatory-inhibitory cross-correlations to the approximation given by Eq. (6.31). (B) Mean and standard deviation for the distribution of correlation functions for excitatory-inhibitory pairs of cells. (Solid line – mean cross-correlation, shaded area – one standard deviation from the mean, calculated using bootstrapping in a single network realization). (C) Mean and standard deviation for the distribution of cross-correlation functions conditioned on cell type *and* first order connectivity for a reciprocally coupled excitatory-inhibitory pair of cells. (Solid line – mean cross-correlation function, shaded area – one standard deviation from the mean found by bootstrapping). (D) Average reduction in L^2 error between cross-correlation functions and their respective first-order conditioned averages, relative to the error between the cross-correlations and their cell-type averages. Blue circles give results for a precisely tuned network, and red squares for a network with stronger, faster inhibition. Error bars indicate two standard errors above and below the mean. G_E, G_I, τ_E, τ_I for panels A-C are as in the precisely tuned network of Figure 6.5, and the two networks of panel D are as in the networks of the same figure. 129
- 6.7 **Spiking correlation structure within distance-dependent neuronal networks.** (A) Exhibiting the relationship between pairwise asymptotic spike count correlation coefficients (Eq. (2.12)). The blue line indicates the linear response prediction (Eq. (6.1)) while black indicates the estimation of the distance-correlation relationship acquired from Monte Carlo simulation. The “circular boxcar” network was of size $N = 100$ with $N_E = 80$, and the synaptic footprints were $\sigma_E = 20^\circ, \sigma_I = 60^\circ$. (B) Decomposition of the linear response prediction of the distance-correlation relationship in panel A into contributions up to specified orders (acquired using Eq. (6.2)). (C) Correlation between the pooled (summed) spiking outputs of the circular boxcar network. Pools were formed as collections of neurons with preferred orientations falling within an interval of length twice the pool radius. The network was approximately radially symmetric, and thus, only the relative positions of the pools (compare blue and red lines), as opposed to the absolute positions, mattered in determining pooled correlation. Black lines indicate values obtained by pooling randomly from the circular boxcar network (solid black line) and pooling randomly from a random network (i.e., one without distance-dependent architecture – broken black line). (D) Same as panel A, but for a “planar boxcar” network. The planar network was of size $N = 1000$ with $N_E = 800$. The distance metric was Euclidean, and we set $\sigma_E = 0.15, \sigma_I = 0.4$ 144

- 6.8 **Error analysis of the linear response theory.** (A) The Pearson correlation coefficient between the time-dependent firing activity (PSTH) calculated from Monte Carlo simulations and linear response theory for an array of σ (noise intensity) and G_E (total excitatory/inhibitory connection weight) values for a single EIF neuron receiving 80 excitatory and 20 inhibitory Poisson inputs at 17 Hz, convolved with alpha synaptic kernels (see Eq. (5.6)). These inputs emulated the total drive received by a neuron in the precisely balanced, all-to-all network considered in Figure 6.5. A higher correlation indicates a closer match between simulations and theory. The red dot indicates the parameters used for Figure 6.5. (B) The cross-correlation function between two excitatory cells in the precisely balanced, all-to-all network from Monte Carlo simulations and linear response theory at four points in (σ, G_E) space, indicated by the black dots in panel A. 149
- 6.9 **The performance of linear response theory in various firing regimes.** For the feed-forward inhibitory microcircuit considered in the manuscript (see Figure 6.2), we varied the effective rest potential $E_L + E_{\xi,i}$ (see Eq. (5.4) and Figure 6.2) to the cell E_2 between three values — (A) $E_L + E_{\xi,i} = -59$ mV, (B) $E_L + E_{\xi,i} = -54$ mV (this is the value used in Figure 6.2), (C) $E_L + E_{\xi,i} = -49$ mV. Insets give the firing rate and the coefficient of variation of the interspike interval distribution of cell E_2 150
- 6.10 **Linear response fails to capture third order correlations even qualitatively.** (A) Monte Carlo-estimated third order cross-cumulant density for the triplet (1,2,3) in the 3-cell excitatory microcircuit described in Section 6.4.3.2. Colors indicate function values at the corresponding lags τ_1 (horizontal axis) and τ_2 (vertical axis) — see color bar (far right). (B) Same as panel A, but displays the linear response approximation to the third-order cross-cumulant density derived by an two-dimensional inverse Fourier transform of Eq. (6.39). 154
- 6.11 **Linear response theory captures “half” of the third-order correlations in a bidirectional inhibitory microcircuit.** (A) Comparing the singular contribution calculated from Monte Carlo simulation (black line) with the linear response prediction (blue line). Note that for $\tau_1 > 0$, the blue and black lines lie almost exactly on top of each other. (B) Monte Carlo-estimated third order cross-cumulant density for the triplet (1,2,1) in the 2-cell inhibitory microcircuit described in Section 6.4.3.3. Colors indicate function values at the corresponding lags τ_1 (horizontal axis) and τ_2 (vertical axis) — see color bar (far right). (C) Same as panel A, but displays the linear response approximation to the third-order cross-cumulant density obtained from a two-dimensional inverse Fourier transform of Eq. (6.39). 155

7.1 **Second order motifs within a recurrent network.** (Left) Second order sub-motifs — motifs involving two connections and at most three cells — are embedded within the graph of a network. (Right) The three types of second order motifs: chain, diverging and converging. 157

7.2 **Diagrammatic expansion of the probability of occurrence for motifs.** (A) The probability of observing a third order chain motif, μ_3 , can be expanded in terms of empirical motif cumulants of lesser or equal order. (B) Same as panel A, but for a third order diverging motif, $\mu_{2,1}$ 164

7.3 **Second order motifs in a two population network.** In a two population network, twenty different second order motifs can be defined depending on the motif type (converging, diverging or chain) as well as the subpopulation identity of each neuron in the motif. In this case, the two populations, represented by different colored shapes, are excitatory and inhibitory neurons. 169

7.4 **The relationship between second order motif frequencies and average correlation in excitatory-only EIF networks.** (A) Three dimensional scatter plot of average correlations obtained from Monte Carlo simulation of excitatory-only networks of exponential integrate-and-fire neurons, given as a function of second order motif frequencies. The x , y and z coordinates indicate the quantities q_{div} , q_{ch} and q_{con} , respectively. The color of a point indicates the average second order covariance calculated for that network (see color bar). Each of the 265 points displayed corresponds to an adjacency matrix of size $N = 100$ sampled randomly according to the methods prescribed in Section 7.1.1.1. Second order motif frequencies were calculated from the adjacency matrices as in Eqs. (7.3–7.5), and the effective interaction strength was $\Psi_{ER}(\tilde{A}w) = 0.2$ (see Eq. (7.1)). The average spiking correlation coefficient ranged from 0.0036 to 0.0078 in the networks considered. (B) Linear regression coefficients which relate average second order covariance obtained from Monte Carlo simulation of the integrate-and-fire network to the frequencies of second order motifs in this dataset. 175

- 7.5 **Accuracy of the “cumulant resumming” approximation of average covariance in excitatory-only EIF networks.** (A) Scatter plot of average correlation obtained from the motif cumulant resumming approximation (horizontal axis, see Eq. (7.27)) against that obtained from Monte Carlo simulation of the integrate-and-fire network (vertical axis). The dashed line represents the diagonal, and each of the 265 points corresponds to one of the networks considered in Figure 7.4. (B) Coefficients of the least squares linear regression of average covariance against the frequency of second order motif frequencies for the 265 networks considered in panel A. Bars represent the values obtained by performing the regression on the prediction of average covariance obtained from the motif cumulant resumming approximation Eq. (7.27), and dots indicate the values obtained by considering the average covariances obtained from simulations (same data as Figure 7.4B). 178
- 7.6 **The relationship between second order motif frequencies and average correlation in EIF networks with excitatory and inhibitory neurons.** (A) Three dimensional scatter plot of average correlations obtained from Monte Carlo simulation of an excitatory-only network of EIF neurons, given as a function of weighted linear combinations of second order motif frequencies. The x, y and z coordinates indicate weighted linear combinations of diverging, chain and converging motifs, respectively. The weightings are explained in a technical note within Section 7.2.2. The color of a point indicates the average second order covariance calculated for that network (see color bar). Each of the 265 points displayed corresponds to an adjacency matrix of size $N = 100$ ($N_E = 80$) sampled randomly according to the methods prescribed in Section 7.1.1.1. The effective interaction strength was $\Psi_{ER}(\bar{A}w) \approx 0.234$ (see Eq. (7.1)). The average spiking correlation coefficient ranged from 0.015 to 0.055 in the networks considered. (B) Linear regression coefficients which relate average second order covariance obtained from Monte Carlo simulation of the EIF network to the weighted linear combinations of second order motif frequencies on the axes in panel A for the 265 networks considered in panel A. 179

7.7 Accuracy of the “cumulant resummung” approximation of average covariance in EIF networks with excitatory and inhibitory neurons. (A) Scatter plot of average correlation obtained from the motif cumulant resummung approximation (horizontal axis, see Eq. (7.27)) against that obtained from Monte Carlo simulation of the EIF networks (vertical axis). The dashed line represents the diagonal, and each of the 265 points corresponds to one of the networks considered in Figure 7.6. (B) The eight largest coefficients of the least squares linear regression of average covariance against the frequency of second order motif frequencies for the 265 networks considered in panel A. Bars represent the values obtained by performing the regression on the prediction of average covariance obtained from the motif cumulant resummung approximation Eq. (7.27), and dots indicate the values obtained by considering the average covariances obtained from simulations. The motifs corresponding to each regression coefficient are indicated by the graphics along the horizontal axis — for example, the first motif listed is the $E \rightarrow E \rightarrow E$ chain motif, and the last is the $E \leftarrow I \rightarrow I$ diverging motif. No converging motif regression coefficients are shown, as they were generally much smaller in magnitude for the presented motifs. 181

- 8.1 **Schematic of the VS network model.** **(A)** Spherical image rotation sequences (red curved arrow) were presented to the model of the fly vertical system (VS). The rotation axis in the equatorial plane is characterized by its azimuth, θ_{stim} . Lower right inset shows how the Reichardt detectors were arrayed on the surface of the sphere. **(B)** Schematics of the Reichardt detector. LP and HP indicate first order low- and high- pass linear filters, respectively, while \times and $-$ represent elementary signal multiplication and subtraction steps. Each detector was assembled from two subunits separated by an elevation of 2° . **(C)** Horizontal cross sections of the dendritic receptive fields for the VS neurons. The frontmost curve is for the left-side VS10 neuron (see panel E, upper inset). **(D)** The model is an assembly of a number of components: The optic flow stimulus is generated by rotations of spherical images, and is filtered by the local motion detectors (LMDs). The LMD output is separated into upward and downward components which are mapped to inhibitory ($-$), and excitatory ($+$) conductances, respectively, onto the dendrites of the VS neurons. Conductances are weighted by the position of the LMD with respect to the VS cell receptive fields (see C). Resistor symbols indicate electrical coupling of compartments, and ξ_{Ax} , resp. ξ_{De} , are independent, intrinsic noise sources to the axons, resp. dendrites, of VS cells. **(E)** Steady-state membrane potential of the twenty coupled VS neurons ($g_{gap} = 1 \mu S$) in response to stimulation by a horizontal grating with constant downward velocity. The input was a narrow, 10° wide strip centered at angle θ . The responses were obtained by sweeping the strip 360° around the visual field. Upper inset details color scheme and cell ordering for panels C and E. 186
- 8.2 **A typical response of the VS network** **(A)** Plot of the temporal response of the left-side VS1, VS5 and VS10 neurons in the uncoupled system ($g_{gap} = 0 \mu S$) to the rotation of a natural scene stimulus (see Figure 1.4B). Shaded boxes labeled **T** and **SS** indicate time intervals 10 ms in duration over which we average the VS axonal responses to obtain the transient average, $\bar{V}_{Ax}^{tr}(T)$, and the steady-state average $\bar{V}_{Ax}^{ss}(T)$, respectively. **(B)** Same as panel A, but for the coupled system ($g_{gap} = 1 \mu S$). 189

- 8.3 **Assessing the copula fit for the transient response distribution** **(A)** Blue points give a P-P plot of the fit copula (horizontal axis) against the true, empirical copula for a randomly-selected subset of three left-side VS neurons, at a random stimulus angle. We computed the copula probabilities at 1,000 points which divided the unit cube into 1,000 equal sized sub-cubes as described in the text. The black dashed line indicates the diagonal, with agreement between the true and fit models being indicated by the points lying on or near the diagonal. Optic flow presented to the system was generated by the rotation of random bar images, and the copula was fit to the transient response distribution. **(B)** Histogram of relative errors for copula probabilities. Vertical axis represents fractions of points which lie in the corresponding error range on the horizontal axis. We repeated the simulation of panel A, for a total of twenty random pairings of three left-side VS neurons and stimulus angles. We then computed the relative error (see Eq. (8.8)) between the true and fit copula probabilities at the 1,000 equally spaced points within the unit cube for all twenty copula fits, and plotted the errors as a histogram. 198
- 8.4 **The effect of coupling on VS neuronal dynamics.** **(A)** (Left) Typical axonal response of the left-side VS10 cell in the uncoupled network ($g_{\text{gap}} = 0 \mu\text{S}$) to rotations of bar images about $\theta_{\text{stim}} = 90^\circ$. Different line types indicate different, randomly generated images. (Right) Same as the left panel, but for the coupled system ($g_{\text{gap}} = 1 \mu\text{S}$). Images rotated to generate optic flow stimuli were the same ones used in the uncoupled system, with matching line types indicating matching image presentations. **(B)** Correlations for the integrated membrane potential in steady-state for the left-side VS neurons. Values above (resp. below) the diagonal are for the uncoupled (resp. coupled) system. Nearby cells were correlated at levels of approximately 0.7 and 0.97 for the uncoupled and coupled systems, respectively. **(C)** Steady-state tuning curve (mean response) and variability as a function of rotation angle for (i) VS1 and (ii) VS10 in the uncoupled system. Shaded areas indicate ± 1 s.d. of the response distribution. **(D)** Same as C, but for the coupled system. All responses and statistics for this figure were generated in the absence of intrinsic fluctuations ($\sigma_{\text{Ax}}, \sigma_{\text{De}} = 0$), and the optic flow stimuli were created by rotations of random bar images (see Section 8.1.2). . 202

8.5 **Mean-square error of the OLE for steady-state responses (A)** (Left) Lines indicate the square root of the mean-square error of the OLE for steady-state responses to filtered optic flow stimuli generated by the rotation of random bar images with a $T = 10$ ms window of integration. Line colors correspond to different coupling strengths as indicated by the legend. (Right) Bars represent the square root of the stimulus averaged mean-square error for the data plotted to the left, with bar colors corresponding to line colors. **(B)** Same as A, but for a window of integration of $T = 20$ ms. **(C)** Same as A, but for random checkerboard images. Note the different scaling of the vertical axis. **(D)** Same as A, but for natural scenes. Details regarding image generation and the technique for generating the optic flow presented to the model can be found in Section 8.1.2. 205

8.6 **Mean-square error of the MMSE for transient responses (A)** (Left) Lines indicate the square root of the mean-square error of the MMSE for transient responses to filtered optic flow stimuli generated by the rotation of random bar images with a $T = 10$ ms window of integration. Line colors correspond to different coupling strengths as indicated by the legend. (Right) Bars represent the square root of the stimulus averaged mean-square error from the data plotted to the left, with bar colors corresponding to line colors. **(B)** Same as A, but for a window of integration of $T = 20$ ms. **(C)** Same as A, but for random checkerboard images. Note the different scaling of the vertical axis. **(D)** Same as A, but for natural scenes. 209

8.7 **Mean-square error of the MMSE for a partial readout of transient responses (A)** (Left) Lines indicate the square root of the mean-square error of the MMSE for transient responses to filtered optic flow stimuli generated by the rotation of random bar images with a $T = 10$ ms window of integration. Line colors correspond to different coupling strengths as indicated by the legend. The partial readout was formed from the responses of the VS 5–7 cells on each side. (Right) Bars represent the square root of the stimulus averaged mean-square error from the data plotted to the left, with bar colors corresponding to line colors. **(B)** Same as A, but for a window of integration of $T = 20$ ms. **(C)** Same as A, but for random checkerboard images. Note the different scaling of the vertical axis. **(D)** Same as A, but for natural scenes. 212

- 8.8 **Mean-square error of the MMSE for full and partial readout from an approximating Ornstein-Uhlenbeck system (A)** (Left) Lines indicate the square root of the mean-square error of the OLE for transient responses to filtered optic flow stimuli generated by the rotation of random bar images. Line colors correspond to different coupling strengths between “axon” compartments, as indicated by the legend. (Right) Bars represent the square root of the stimulus averaged mean-square error from the data plotted to the left, with bar colors corresponding to line colors. **(B)** Same as A, but for a partial readout formed from the responses of the cells index 5, 6 and 7 on each side, imitating the partial readout considered in the full system (see Figure 8.7). 214
- 8.9 **Visualizing the zero-crossing estimator. (A)** Circles indicate the mean axonal response of the left-side VS neurons to a rotation of a random bar image about $\theta_{\text{stim}} = -85^\circ$. Error bars indicate 1 standard deviation of the response distribution. The horizontal coordinate of each dot indicates that cell’s zero angle θ^0 . **(B)** On an example realization for the response to rotation about $\theta_{\text{stim}} = -85^\circ$, the zero crossing occurred between the VS5 and VS6 cells. These cells had had zero angles of $\theta_{L,5}^0 = -73^\circ$ and $\theta_{L,6}^0 = -87^\circ$, respectively. The zero crossing estimator predicts the angle of rotation to be the zero angle of a hypothetical cell which would exhibit zero response, under the assumption that the response varies linearly with zero angle (red dashed line). 217
- 8.10 **Mean-square error of the MMSE for a full and partial readout, for the zero-crossing estimator. (A)** (Left) Lines indicate the square root of mean-square error of the zero-crossing estimator for transient responses to filtered optic flow generated by the rotation of random bar images with a $T = 10\text{ms}$ window of integration. The readout provided to the estimator consisted of the full VS population response. Line colors correspond to different coupling strengths as indicated by the legend. (Right) Bars represent the square root of the stimulus averaged mean-square error from the data plotted to the left, with bar colors corresponding to line colors. **(B)** Same as A, but for a partial readout formed from the responses of the VS5–7 cells on each side. 219

- 8.11 **Correlations encode stimulus information in a partial readout** (Left) Solid lines indicate the square root of the mean-square error of the MMSE for trial-shuffled transient responses to filtered optic flow stimuli generated by the rotation of random bar images with a $T = 10$ ms window of integration. Line colors correspond to different coupling strengths as indicated by the legend. Dashed lines indicate the error of the partial readout without shuffling for the same strengths of coupling (same data as Figure 8.7A). The partial readout was formed from the responses of the VS 5–7 cells on each side. (Right) Solid border bars represent the square root of the stimulus averaged mean-square error for the cross-trial shuffled data plotted to the left, with bar colors corresponding to line colors. Dashed border bars indicate the same, but for the non-shuffled data (as in Figure 8.7). 221
- 8.12 **A single cell with large dendritic extent cannot accurately encode the axis of rotation** (Left) Solid orange line indicates the square root of the mean-square error of the MMSE for transient responses to filtered optic flow stimuli generated by the rotation of random bar images with a $T = 10$ ms window of integration, for the full system with a partial readout consisting of the VS5–7 cells in each hemisphere (same data as Figure 8.7A). The dashed orange line is the same as the solid line, except the readout consisted of only the VS5 cell. The dashed blue line indicates the MSE for a system consisting of a single axonal compartment in each hemisphere which couples to all ten of the corresponding dendritic compartments, as described in the text. (Right) Bars represent the square root of the stimulus averaged mean-square error for the systems and readouts of the corresponding lines to the left. 222
- 8.13 **Encoding accuracy depends on cell identities for a partial readout (A)** The solid line indicates the average square root of the mean-square error of the MMSE calculated from transient responses in the uncoupled system. Input to the system consisted of filtered optic flow stimuli generated by the rotation of random bar images with a $T = 10$ ms window of integration. The MSE was averaged across 20 randomly chosen subsets for each readout subset size, except for a size one readout, where we could only consider ten readouts, corresponding to the ten VS cells. Dashed lines indicate the maximum and minimum values of the MSE observed across the randomly chosen subsets. For size three readouts, we ensured that we included the subset consisting of VS5–7 (the same subset used in Figures 8.7), and the filled circle indicates the MSE for this subset. Note the logarithmic scale of the vertical axes. **(B)** Same as panel A, but for the coupled system. 224

List of Tables

6.1	Mean and standard deviation of the distribution of excitatory-excitatory pairwise correlations in structured and random networks. The values in circular and planar boxcar networks are from the same data as Figure 6.7.	145
A.1	Notation for neuron models. Notation used in defining and discussing neuron models.	240
A.2	Mathematical notation. Mathematical notation used in the text.	241
A.3	Notation for the Generalized Thinning and Shift model. Notation used in the definition and discussion of the Generalized Thinning and Shift model in Chapter 4.	242
A.4	Notation for linear response theory applications. Notation used in the applications of linear response theory contained in Chapters 5 through 7.	243

Introduction

Recordings across the brain suggest that neural populations spike collectively – the statistics of their activity as a group are distinct from that expected in assembling the spikes from one cell at a time [11, 14, 17, 87, 106, 108, 173, 207, 239, 241, 252]. Advances in electrode and imaging technology allow us to explore the dynamics of neural populations by simultaneously recording the activity of hundreds of cells. This is revealing patterns of collective spiking that extend across multiple cells. The underlying structure is intriguing: For example, higher-order interactions among cell groups have been observed widely [7, 87, 173, 194, 241, 251, 252, 287]. A number of recent studies point to mechanisms that generate such higher-order correlations from common input processes, including unobserved neurons. This suggests that, in a given recording or given set of neurons projecting downstream, higher-order correlations may be quite ubiquitous [16, 151, 177, 308]. Moreover, these *higher-order correlations* may impact the firing statistics of downstream neurons [156], the information capacity of their output [43, 87, 187], and could be essential in learning through spike-time dependent synaptic plasticity [91, 206].

What exactly is the impact of such collective spiking on the encoding and transmission of information in the brain? This question has been studied extensively, but much remains unknown. Results to date show that the answers will be varied and rich. Patterned spiking can impact responses at the level of single cells [156, 239, 304] and neural populations [8, 232, 233, 271]. Neurons with even the simplest of nonlinearities can be highly sensitive to correlations in their inputs. Moreover, such nonlinearities are sufficient to accurately decode signals from the input to correlated neural populations [246].

An essential tool in understanding the impact of collective spiking is the ability to generate artificial spike trains with a predetermined structure across cells and across time [35, 96, 155, 176]. Such synthetic spike trains are the grist for testing hypotheses about spatiotemporal patterns in coding and dynamics. In experimental studies, such spike trains can be used to provide structured stimulation of single cells across their dendritic trees via glutamate uncaging [32, 33, 89, 214]. In addition, entire populations of neurons can be activated via optical stimulation of microbial opsins [47, 103]. Computationally, they are used to examine the response of nonlinear models of downstream cells [44, 156, 239].

Therefore, much effort has been devoted to developing statistical models of population activity. A number of flexible, yet tractable probabilistic models of joint neuronal activity have been proposed. Pairwise correlations are the most common type of interactions obtained from multi-unit recordings. Accordingly, many earlier models were designed to generate samples of neural activity patterns with predetermined first and second order statistics [35, 96, 155, 176]. In these models, higher-order correlations are not explicitly and separately controlled.

A number of different models have been used to analyze higher-order interactions.

However, most of these models assume that interactions between different cells are instantaneous (or near-instantaneous) [137, 156, 263]. A notable exception is the work of Bauerle and Grubel [19], in which methods for generating spike trains with temporal structure were developed for use in financial applications. In these previous efforts, correlations at all orders were characterized by the increase, or decrease, in the probability that groups of cells spike together at the same time, or have a common temporal correlation structure regardless of the group.

In Chapter 4, we introduce a statistical method for generating spike trains with more general correlation structures across cells and time. Specifically, we allow distinct temporal structure for correlations at second, third, and all higher orders, and do so separately for different groups of cells in the neural population. Our aim is to describe a model that can be applied in neuroscience, and can potentially be fit to emerging datasets.

A sample realization of a multivariate generalized thinning and shift (GTaS) process is shown in Fig. 1.1. The multivariate spike train consists of six marginally Poisson processes. Each event was either uncorrelated with all other events across the population, or correlated in time with an event in all other spike trains. This model was configured to exhibit activity that cascades through a sequence of neurons. Specifically, neurons with larger index tend to fire later in a population wide event (this is similar to a synfire chain [2], but with variable timing of spikes within the cascade). In Figure 1.1B, we plot the “population cross-cumulant density” for three chosen neurons – the summed activity of the population triggered by a spike in a chosen cell. The center of mass of this function measures the average latency by which spikes of the neuron in question precede those of the rest of the population [173]. Finally, Figure 1.1C shows the third-order cross-cumulant density for the three neurons. The triangular support of this function is a reflection of

a synfire-like cascade structure of the spiking shown in the raster plot of panel A: when firing events are correlated between trains, they tend to proceed in order of increasing index.

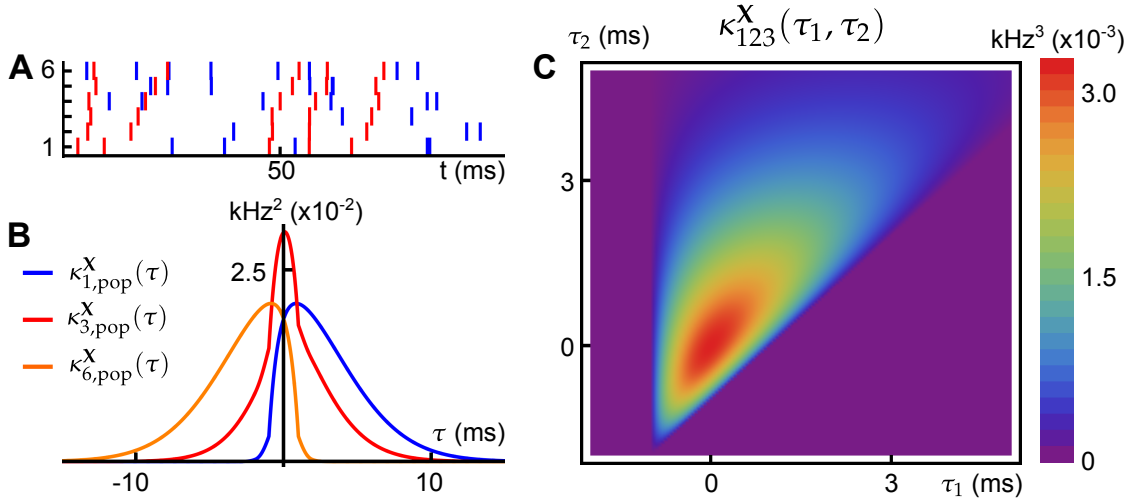


Figure 1.1: **Example of a GTaS process exhibiting “synfire-like” firing patterns (A)** Raster plot of event times for an example multivariate Poisson process $\mathbf{X} = (X_1, \dots, X_6)$ generated using the methods presented in Chapter 4. This model exhibits independent marginal events (blue) and population-level, chain-like events (red). **(B)** Some second order population cumulant densities (i.e., second order correlation between individual unit activities and population activity) for this model [173]. Greater mass to the right (resp. left) of $\tau = 0$ indicates that the cell tends to lead (resp. follow) in pairwise-correlated events. **(C)** Third-order cross-cumulant density for processes X_1, X_2, X_3 . The quantity $\kappa_{123}^{\mathbf{X}}(\tau_1, \tau_2)$ yields the probability of observing spikes in cells 2 and 3 at an offset τ_1, τ_2 from a spike in cell 1, respectively, in excess of what would be predicted from the first and second order cumulant structure. All statistical quantities are precisely defined in Chapter 2.

Beyond important and rich challenges for statistical modeling [37], the emerging data promise new perspectives on the neural encoding of information [11]. The structure of correlations in the activity of neuronal populations is of central importance in understanding the neural code [1, 20, 202, 203, 245, 259, 310]. However, theoretical [1, 139, 160, 242, 259, 310], and empirical studies [50, 191, 230] do not provide a consistent set of general principles about the impact of correlated activity. This is largely because the presence

of correlations can either strongly increase or decrease the fidelity of encoded information depending on both the structure of correlations across a population and how their impact is assessed.

A basic mechanistic question underlies the investigation of the role of collective activity in coding and signal transmission: How do single-cell dynamics, connection architecture, and synaptic dynamics combine to determine patterns of network activity? Systematic answers to this question would allow us to predict how empirical data from one class of stimuli will generalize to other stimulus classes and recording sites. Moreover, a mechanistic understanding of the origin of correlations, and knowledge of the patterns we can expect to see under different assumptions about the underlying networks, will help resolve recent controversies about the strength and pattern of correlations in mammalian cortex [51, 64, 217]. Finally, understanding the origin of correlations will inform the more ambitious aim of inferring properties of network architecture from observed patterns of activity [193, 198, 201].

In Chapters 5 through 7, we examine the link between network properties and correlated activity. First, in Chapter 5, we develop a theoretical framework that accurately predicts the structure of correlated spiking that emerges in a widely used model — recurrent networks of general integrate and fire cells. The theory naturally captures the role of single cell and synaptic dynamics in shaping the magnitude and timescale of spiking correlations. We focus on the exponential integrate and fire model, which has been shown to capture membrane and spike responses of cortical neurons [81]; however, the general approach we take can be applied to a much broader class of neurons.

Our approach is based on an extension of linear response theory to networks [167, 198].

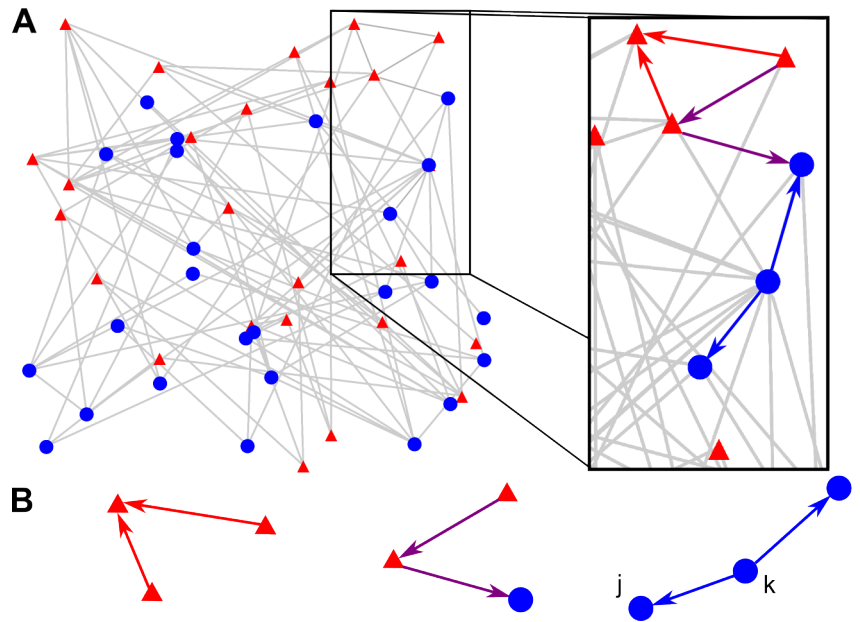


Figure 1.2: **Linear response theory admits an expansion of correlations in terms of motifs within the network** (A) Linear response theory can serve as an important tool for understanding how architecture in dynamics shape the statistics of responses in large, complex networks. This is enacted via an expansion of correlations by contributions due to different motifs embedded within the network architecture. We highlight some second order motifs — motifs which involve a pair of connections and up to three cells. (B) Some second order motifs involving cells of two distinct populations, with edge color indicating whether the motifs connect cells of a single population (red, blue) or both populations (purple).

We start with a linear approximation of a neuron’s response to an input. This approximation can be obtained explicitly for many neuron models [38, 168, 221], and is directly related to the spike triggered average [85]. The correlation structure of the network is then estimated using an iterative approach.

In Chapter 6, we first demonstrate how the linear response approximation of correlations admits an expansion of the correlation in terms of submotifs embedded within the network architecture [205, 211, 212]. In order to gain intuition for the nature of the decomposition, we first apply the theory to the analysis of correlations for a pair of simple

microcircuits.

Next, we consider applications to large networks, beginning with those featuring precisely balanced inhibition and excitation in the inputs to individual cells. In this state individual cells receive a combination of excitatory and inhibitory inputs with mean values that largely cancel. We show that, when timescales and strengths of excitatory and inhibitory connections are matched, only local interactions between cells contribute to correlations. Moreover, our theory allows us to explain how correlations are altered when precise balance is broken. In particular, we show how strengthening inhibition can synchronize the spiking activity in the network. Using the linear response theory allows us to derive results which lend an intuitive understanding of the factors shaping average correlation structure in randomly connected networks of neurons. Finally, we conduct a brief exploration of the structure of correlations within a pair of distance-dependent networks. These examples also demonstrates that linear response theory can be used as a tool for computationally efficient analysis of correlations within large networks.

At the end of Chapter 6, we carry out a thorough error analysis of the linear response theory, examining the correlation approximation across a variety of network conditions. We also briefly exhibit the failure of the linear response theory of correlations for integrate-and-fire networks when applied to the estimation of third order dependencies. Whether there exists a consistent correction to the linear response theory in this case is an open question of great import.

The *global* statistics of networks can depend sensitively on the *local* features of their architecture, as shown in Figure 1.3. In Chapter 7, we introduce a novel statistical measure of network connectivity, *motif cumulants*, in order to better understand this relationship.

Whereas *motif moments* define the true probability of observing one of the motifs appearing in the correlation decomposition of Chapter 6, a motif cumulant is a measure which, analogous to the relationship between moments and cumulants of random variables, captures the probability of seeing these same motifs *in excess of* the “best” guess given only knowledge of lower order motif cumulants. By an algebraic resumming argument, we rewrite the expansion of correlations in terms of motif cumulants. Doing so reveals an explicit link between micro-scale features of the synaptic structure — motif cumulants — and a universal feature of the dynamics this structure supports — average output correlations for the integrate-and-fire networks.

In Chapter 8, we present an analysis of part of the blow fly visual system. To motivate this study, flying organisms require fast, reliable feedback regarding ego-motion to make rapid course corrections. This information is primarily extracted from the optic flow – the motion of the external world as perceived by the organism [26, 148, 163]. In the visual system of the fly, neurons of the lobula plate receive as input a two-dimensional retinotopic representation of the optic flow, allowing them to encode the parameters of ego-motion (i.e., rotational and translational velocities) [27, 30, 142, 298]. The lobula plate serves as a primary relay between early vision and downstream motor centers [100, 268, 296, 297].

Approximately sixty large tangential cells responsive to wide-field motion have been identified within the lobula plate of each hemisphere of the blow fly [110, 115]. Ten of these neurons comprise part of the *vertical system* (VS) and are thought to encode the azimuthal direction of rotations in the horizontal plane [152, 153]. These cells were the focus of our study.

The visual information available to the fly is very rich, but only part of it is essential to control flight. Irrelevant information can be regarded as external noise, and neural

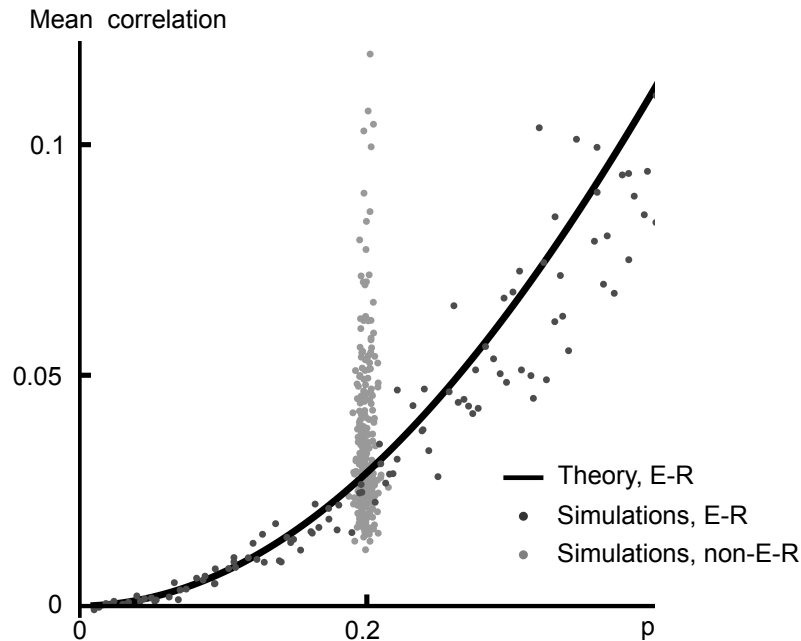


Figure 1.3: **Local features of network architecture can strongly influence global behavior** The black line indicates the relation between the density of connections and average output correlation in truly random (i.e., Erdős-Rényi), excitatory-only integrate-and-fire neuronal networks, as predicted by the cumulant resumming theory of Chapter 7. The dark gray dots indicate simulations of integrate-and-fire networks. Fluctuations about the line are due essentially to finite-size effects — in particular, finite networks are generally not perfectly regular, and thereby exhibit residual higher order structure within their architecture. The light gray dots indicate output correlation in networks designed to be non-Erdős-Rényi. The adjacency graphs associated with these networks featured dependent edges — i.e., pairs of connections were not present or absent independently. This yielded, in turn, significant deviations in the dynamics of the corresponding networks from what is expected in the case of underlying Erdős-Rényi graphs.

processing within the fly visual system produces additional, internal variability. Relevant information about the world is probabilistically represented in the resulting neural signals. The VS cells encode an essential parameter from this complex input – the horizontal axis of ego-rotation. Estimating this parameter is a problem of marginalization (see Figure 1.4C and [175]), as the quantity of interest must be disentangled from irrelevant components of the response.

Electrical coupling between adjacent VS cells significantly shapes their responses (See Figure 1.4A) [75,97]. Our goal was to examine the role of this coupling in achieving an efficient representation of the azimuthal angle of rotation in the VS population response. We extended previous studies which made generally qualitative observations about the role of coupling [56,68,292].

In contrast to most previous studies, we considered transient responses. Random rotating images (Figure 1.4B) were presented as input to a biophysically-plausible model of the VS cell network [30]. Instead of using heuristic or suboptimal estimators, we applied probabilistic modeling methods to compute optimal Bayesian estimators from the responses. Surprisingly, we found that the quality of optimal estimates of the azimuthal angle from the collective response of VS cells is independent of coupling in both transient and steady-state situations.

On the other hand, anatomical and electrophysiological characterizations of lobula plate neurons have identified a pair of pre-motor neurons at the next stage of processing of the fly's nervous system. The strongest projections of the VS population onto these descending neurons originate from a subset of the VS population [297]. We found that under a partial readout, coupling induced changes in tuning and reliability were crucial for an efficient representation of the angle of rotation. We provide an intuitive explanation of these observations. These ideas are quite general, and can offer insights into the role of coupling between neurons in other species and modalities.

Over the course of this work, we hope to address three important needs within the field of computational neuroscience: First, the Generalized Thinning and Shift framework presented in Chapter 4 addresses the need for tools which can be applied, by both experimentalists and theorists, to understand how networks transform their inputs. Next, the

linear response theory of correlations for integrate-and-fire networks presented in Chapters 5 through 7 can serve as an invaluable tool for understanding explicitly the relationship between structure and dynamics. Finally, our analysis of the fly visual system in Chapter 8 exhibits a general methodology for assessing task performance of neural networks; our hope is that our analysis will serve as a blueprint for future research, both in the fly visual system and elsewhere.

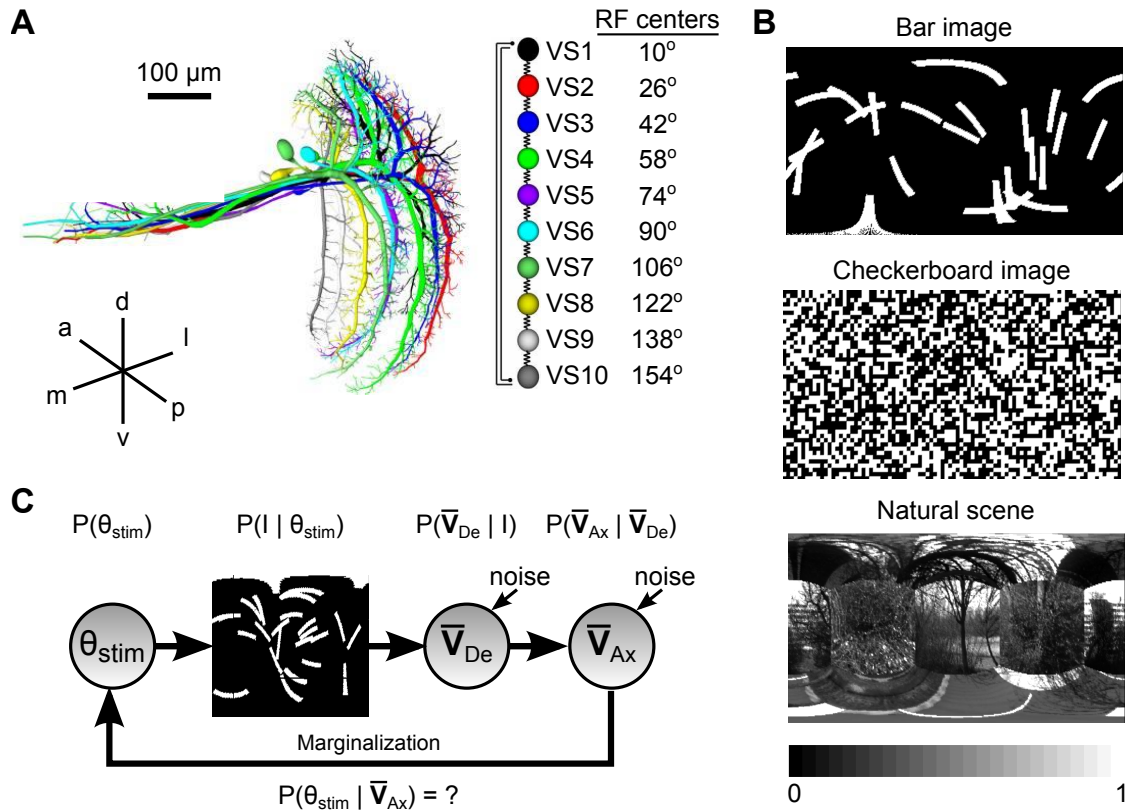


Figure 1.4: The VS network extracts motion parameters from optic flow-related information. (A) (Left) The ten VS cells in one lobula plate (LP) as reconstructed from two-photon image stacks. Each neuron is T-shaped, with an elongated dendrite sampling a thin vertical stripe in the retinotopically organized LP (VS 1 to 10 arranged from distal to proximal in the LP, [117]). Inset indicates approximate orientation (a: anterior, p: posterior, l: lateral, m: medial, d: dorsal, v: ventral). Adapted from [56]. (Right) Connectivity scheme of the VS network. VS cell axons are electrically coupled to nearest neighbors. There is a functionally mutually inhibitory (or “repulsive”) interaction between VS1 and VS10. Receptive field (RF) centers indicate azimuthal position in the horizontal equatorial plane of right side VS neurons, taking 0° to represent the anteroposterior axis of the fly. Left side VS neuron receptive field centers are given by reflection across 0° [30]. (B) Examples of images used to generate the optic flow stimuli presented to the VS network model. Details of image generation are given in the Methods, along with parameters and procedure for generation of rotational optic flow stimuli. (C) The marginalization problem: Parameters of ego-motion (such as the axis of rotation, θ_{stim}) are first probabilistically embedded in the external world (Image), and additional layers of variability (noise) are imposed by the processing in VS cells at the dendritic (De) and axonal (Ax) stages (\bar{V} denotes time-averaged membrane potential; see Methods). Reading-out the azimuthal rotation axis from the VS population response amounts to marginalize — extract a notion of the posterior distribution of the stimulus from the axonal responses.

Chapter 2

Correlations and stochastic processes

We will consider models of neuronal activity given by stochastic processes. The neuronal networks we model explicitly will have membrane potentials governed by Langevin equations, and we will model their inputs and outputs as spike trains. In this chapter, we will first cover fundamental measures of covariability amongst general numerically-valued stochastic processes, and then amongst spike trains, which we interpret as generalized functions. To conclude the chapter, we discuss copulas, a useful way of imposing a certain correlation structure onto a set of independent random variables.

Throughout most of this work (with analysis of transient responses in Chapter 8 as the lone exception), we assume the stochastic processes we consider are *jointly stationary*. In particular, if $\mathbf{X}(t) = (X_1(t), \dots, X_N(t))$ is a vector stochastic process, then the joint distribution of $\mathbf{Y}(t) = (X_{i_1}(t+t_1), X_{i_2}(t+t_2), \dots, X_{i_M}(t+t_M))$ is independent of t for any finite sequence of times $\{t_j\}_{j=1}^M$ and indices $\{i_j\}_{j=1}^M \subset \{1, 2, \dots, N\}$. We further assume these stationary processes to be ergodic; that is, for any Borel measurable $f : \mathbb{R}^M \rightarrow \mathbb{R}$, we

have

$$\lim_{T \rightarrow \infty} \frac{1}{T} \int_0^T f(\mathbf{Y}(t)) dt = \mathbf{E}[f(\mathbf{Y})],$$

whenever the expectation on the right-hand side exists. Finally, we assume that the stochastic processes we consider have finite cumulants (equivalently, finite moments) up to the order we consider.

2.1 Statistical measures of stochastic processes

Much of this work is concerned with the quantification and study of dependencies between stochastic processes representing the activity of neurons. In this section, we first review *cross-cumulants*, a useful measure of correlation amongst collections of random variables. We then briefly discuss the Wiener-Khinchin theorem and its higher order generalizations. Following this, we provide an overview of application of these statistical measures to point process, and define some additional measures which are useful in this context.

2.1.1 General measures of correlation

Cross-cumulants Consider a random vector $\mathbf{X} = (X_1, \dots, X_N) \in \mathbb{R}^N$. The cumulant generating function [88, 102, 144, 267] of \mathbf{X} is given by

$$g(t_1, \dots, t_N) = \log \left(\mathbf{E} \left[\exp \left(\sum_{j=1}^N t_j X_j \right) \right] \right).$$

The \mathbf{r} -cross-cumulant (or \mathbf{r} -joint cumulant) is then given by

$$\kappa_{\mathbf{r}}(\mathbf{X}) = \left. \frac{\partial^{|\mathbf{r}|}}{\partial t_1^{r_1} \dots \partial t_N^{r_N}} g(t_1, \dots, t_N) \right|_{t_1 = \dots = t_N = 0},$$

where $\mathbf{r} = (r_1, \dots, r_N)$ is an N -vector of positive integers, and $|\mathbf{r}| = \sum_{i=1}^N r_i$. We will often refer to the cumulant $\kappa(\mathbf{X})$ of the collection of random variables without reference to an index vector \mathbf{r} ; in this case, it is to be assumed that every variable is considered at first order:

$$\kappa(\mathbf{X}) := \kappa_{\mathbf{1}}(\mathbf{X}) = \left. \frac{\partial^N}{\partial t_1 \dots \partial t_N} g(t_1, \dots, t_N) \right|_{t_1 = \dots = t_N = 0}, \quad \text{where } \mathbf{1} = (1, \dots, 1).$$

The cross-cumulant of \mathbf{X} can be expressed combinatorially in terms of moments as

$$\kappa(\mathbf{X}) = \sum_{\pi} (|\pi| - 1)! (-1)^{|\pi|-1} \prod_{S \in \pi} \mathbf{E} \left[\prod_{i \in S} X_i \right], \quad (2.1)$$

where π runs through all partitions of $\mathbb{D} = \{1, \dots, N\}$, and S through all blocks of the partitions of π . We note that the cumulant of a set of random variables is invariant to permutations of their ordering. Equation 2.1 is derived by first noting that an \mathbf{r} -cross-cumulant can be expressed in terms of moments by expanding the cumulant generating function as a Taylor series,

$$g(t_1, \dots, t_N) = \sum_{\mathbf{r}} \frac{\kappa_{\mathbf{r}}(X_1, \dots, X_N)}{\mathbf{r}!} t_1^{r_1} \dots t_N^{r_N} \quad \text{with } \mathbf{r}! = \prod_{i=1}^N (r_i!).$$

Next, the moment generating function $M(t)$ is similarly expanded,

$$M(t) = \sum_{\mathbf{r}} \frac{\mathbf{E} [X_1^{r_1} \dots X_N^{r_N}]}{\mathbf{r}!} t_1^{r_1} \dots t_N^{r_N}.$$

Finally, by expanding $g(t) = \log M(t)$ in terms of the moment coefficients, we arrive at Eq. (2.1) by matching the polynomial coefficients for the term $\mathbf{r} = \mathbf{1}$. We also define the n^{th} cumulant of a single random variable X by

$$\kappa_n(X) = \kappa(\underbrace{X, \dots, X}_{n \text{ copies}}).$$

In Chapter 4, we will make extensive use of the following two principal characteristics of cross-cumulants [36, 185, 263, 267]:

(C1) Multilinearity - for any random variables $X, Y, \{Z_i\}_{i=2}^N$ and constants α, β , we have

$$\kappa(\alpha X + \beta Y, Z_2, \dots, Z_N) = \alpha \kappa(X, Z_2, \dots, Z_N) + \beta \kappa(Y, Z_2, \dots, Z_N).$$

This is a general form of the bilinearity which holds for covariances at second order. Property (C1) holds regardless of dependencies amongst the random variables.

(C2) If any subset of the random variables in the cumulant argument is independent from the remaining variables, the cross-cumulant is zero - i.e., if $\mathbf{X} = (X_1, \dots, X_{N_1})$ and $\mathbf{Y} = (Y_1, \dots, Y_{N_2})$ are two sets of random variables such that each X_i is independent from every Y_j , then

$$\kappa_{(\mathbf{r}_X, \mathbf{r}_Y)}(X_1, \dots, X_{N_1}, Y_1, \dots, Y_{N_2}) = 0 \quad \text{for all } \mathbf{r}_X \in \mathbb{N}_+^{N_1}, \mathbf{r}_Y \in \mathbb{N}_+^{N_2},$$

where $(\mathbf{r}_X, \mathbf{r}_Y)$ is the length $N_1 + N_2$ concatenation of the vectors $\mathbf{r}_X, \mathbf{r}_Y$.

To exhibit another central property of cumulants, we consider a 4-vector

$$\mathbf{X} = (X_1, X_2, X_3, X_4)$$

with non-zero fourth cumulant and a random variable Z independent of each X_i . Define $\mathbf{Y} = (X_1 + Z, X_2 + Z, X_3 + Z, X_4)$. Using properties (C1), (C2) above, it is elementary to show that, for example,

$$\kappa(Y_1, Y_2, Y_3) = \kappa(X_1, X_2, X_3) + \kappa_3(Z).$$

On the other hand, it is also true that

$$\kappa(\mathbf{Y}) = \kappa(Y_1, Y_2, Y_3, Y_4) = \kappa(X_1, X_2, X_3, X_4) = \kappa(\mathbf{X}).$$

That is, adding the variable Z to only a subset of the variables in \mathbf{X} results in changes to cumulants involving only the variables within that subset and no others. Cross-cumulants

for supersets of the modified variables (such as for the entire vector \mathbf{X} in the present example) are unchanged. In this sense, cross-cumulants are “pure”: an r^{th} order cross-cumulant of a collection of random variables captures exclusively dependencies amongst the collection which cannot be described by cumulants of lower order [263]. In the example above, we affected only the joint statistical properties of a subset of \mathbf{X} , and as a result, the total cumulant $\kappa(\mathbf{X})$ remained fixed.

From Eq. (2.1), it can be seen that $\kappa(X_i) = \mathbf{E}[X_i]$, $\kappa(X_i, X_j) = \mathbf{cov}[X_i, X_j]$, and

$$\kappa(X_i, X_j, X_k) = \mathbf{E}[(X_i - \mathbf{E}[X_i])(X_j - \mathbf{E}[X_j])(X_k - \mathbf{E}[X_k])].$$

That is, up to third order, cumulants and central moments agree, and thus, central moments share the properties (C1) and (C2) at these orders. However, at fourth order, we have

$$\begin{aligned} \kappa(X_i, X_j, X_k, X_l) &= \mathbf{E}[(X_i - \mathbf{E}[X_i])(X_j - \mathbf{E}[X_j])(X_k - \mathbf{E}[X_k])(X_l - \mathbf{E}[X_l])] \\ &\quad - \mathbf{cov}[X_i, X_j] \mathbf{cov}[X_k, X_l] - \mathbf{cov}[X_i, X_k] \mathbf{cov}[X_j, X_l] - \mathbf{cov}[X_i, X_l] \mathbf{cov}[X_j, X_k], \end{aligned} \tag{2.2}$$

with similar (but more complex) expressions holding at orders higher than four. As a result, central moments of fourth and higher order do not exhibit the attractive property of characterizing exclusively higher order dependencies.

Temporal statistics In this work, we will utilize *cross-cumulant densities* as a standard measure of the temporal dependence structure of a stochastic process. Given a vector stochastic process $\mathbf{X}(t) = (X_1(t), \dots, X_N(t)) \in \mathbb{R}^N$, the cross-cumulant density of $\mathbf{X}(t)$ is [36, 267]

$$\kappa^{\mathbf{X}}(\tau_1, \dots, \tau_{N-1}) = \kappa(X_1(t), X_2(t + \tau_1), \dots, X_N(t + \tau_{N-1})), \tag{2.3}$$

where we remind the reader that these definitions are for strongly stationary stochastic processes as described in the opening of this chapter. Thus, the value of t used in the definition Eq (2.3) is not relevant. When we are interested in the cumulant function of a subset of the processes \mathbf{X} , we will indicate this by a subscript — i.e., the second order cross-cumulant density of the i^{th} and j^{th} processes of \mathbf{X} is denoted

$$\kappa_{ij}^{\mathbf{X}}(\tau) = \kappa^{(X_i, X_j)}(\tau). \quad (2.4)$$

We also define the *central moment density* of the processes \mathbf{X} by

$$c^{\mathbf{X}}(\tau_1, \dots, \tau_{N-1}) = \mathbf{E}[(X_1(t) - \mathbf{E}[X_1])(X_2(t + \tau_1) - \mathbf{E}[X_2]) \cdots (X_N(t + \tau_{N-1}) - \mathbf{E}[X_N])].$$

For a pair of processes (i.e., $N = 2$), the cross-cumulant density is often referred to as the *cross-correlation function* or *cross-covariance density*. In addition, up to third order, the central moment density is equivalent to the cross-cumulant density.

A general cross-cumulant density can be expressed as

$$\kappa^{\mathbf{X}}(\tau_1, \dots, \tau_{N-1}) = \mathbf{E}[f(X_1(t), X_2(t + \tau_1), \dots, X_N(t + \tau_{N-1}))]$$

for some polynomial function f which can be derived from the combinatorial form of cross-cumulants given in Eq. (2.1). Estimation of the cross-cumulant density from data typically relies on the joint ergodicity of the processes [267],

$$\kappa^{\mathbf{X}}(\tau_1, \dots, \tau_{N-1}) = \lim_{T \rightarrow \infty} \frac{1}{T} \int_0^T f(X_{1,T}(t), X_{2,T}(t + \tau_1), \dots, X_{N,T}(t + \tau_{N-1})) dt.$$

Here, $X_{i,T}(t) = X_i(t)\mathbf{1}_{[0,T]}(t)$ is the mean-subtracted process X_i restricted to the time window $[0, T]$, and we remind the reader that all considered processes are assumed to be stationary, unless otherwise noted. All convergence results regarding stochastic processes contained in this chapter are in mean-square [306].

In many applications (such as those of Chapters 5 through 7), it is convenient to calculate spectral rather than temporal statistics of the stochastic processes under consideration. A common measure of spectral correlation is the *polyspectrum* [36], defined as

$$S^{\mathbf{X}}(\omega_1, \dots, \omega_{N-1}) = \lim_{T \rightarrow \infty} \frac{1}{T} \mathbf{E} [\tilde{X}_{1,T}^*(\omega_1 + \dots + \omega_{N-1}) \tilde{X}_{2,T}(\omega_1) \cdots \tilde{X}_{N,T}(\omega_{N-1})], \quad (2.5)$$

where X^* indicates the scalar complex conjugate of X . The Fourier transform convention throughout this work is

$$\tilde{\mathbf{X}}_T(\omega) = \mathcal{F}[\mathbf{X}_T(t)] \equiv \int_{-\infty}^{\infty} e^{-2\pi i \omega t} \mathbf{X}_T(t) dt.$$

The process $\tilde{\mathbf{X}}_T$ is known as the *spectrum* of \mathbf{X} [267]. When $N = 2$ in Eq. (2.5), the polyspectrum is often referred to as the *cross spectrum* or *cross spectral density* of \mathbf{X} when \mathbf{X} consists of two distinct processes. If \mathbf{X} consists of two identical processes, the second order quantity is referred to instead as the *power spectrum*. Likewise, the $N = 3$ case is referred to as the *bispectrum*, and the $N = 4$ case the *trispectrum* [36]. As for the cross-cumulant density, we will denote power spectra of subsets of the vector process \mathbf{X} with subscripts. For example, the cross-spectrum of X_i and X_j is

$$S_{ij}^{\mathbf{X}}(\omega) = S^{(X_i, X_j)}(\omega).$$

The classical Wiener-Khinchin theorem relates the cross-cumulant density and the power spectrum at second order [46, 267]. Generalized directly to higher orders, the theorem states that the spectral decomposition of the central moment density is given by the polyspectrum of corresponding order, i.e.,

$$S^{\mathbf{X}}(\omega_1, \dots, \omega_{N-1}) = \int \cdots \int e^{-2\pi i(\omega_1 \tau_1 + \cdots + \omega_{N-1} \tau_{N-1})} c^{\mathbf{X}}(\tau_1, \dots, \tau_{N-1}) d\tau_{N-1} \cdots \tau_1. \quad (2.6)$$

A spectral decomposition of the cross-cumulant density can be established likewise.

2.1.2 Point processes

2.1.2.1 Spike trains as point processes

Neurons communicate primarily through *spikes* (or *action potentials*) — rapid hyperpolarizations of the membrane potential followed by rapid depolarizations which create traveling waves in the membrane potential gradient which move through the body of the neuron. These spikes typically travel down the axon of the neuron. Upon reaching the site of a synapse with another neuron, the synapses is activated, initiating a sequence of molecular events. This process is described in somewhat more detail in the next chapter.

Mathematical modeling of neuronal activity involves an important choice of how to model spike trains (i.e., sequences of action potentials). One approach is to discretize time into bins, and represent the spike train by a binary word, where a 1 in a bin indicates a spike in the corresponding time interval. As the discretization of time is accommodating to computations, this is often done in practice. However, analysis of the output of a spiking neuronal system can be sensitive to this bin size [62], which should be neither too large nor too small (in which case the timescale of an action potential will not be correctly characterized by the binary sequence). Furthermore, discretization often is inconvenient for mathematical analysis of a spiking neuronal system.

A more tractable (and convenient) approach is to represent spike trains by sequences of time points $\{t_i^y\}$, each of which represents the time of an action potential. As a stochastic process, a spike train $y(t)$ takes the form

$$y(t) = \sum_{i=1}^{\infty} \delta(t - t_i^y), \quad (2.7)$$

where $\delta(t)$ is the Dirac delta function, and $0 < t_i^y \in \mathbb{R}$ is the time of the i^{th} spike of the neuron (a random variable). For theoretical considerations, this is essentially equivalent

to the representation of the spike train by a random measure N_y on the Borel sets $\mathcal{B}(\mathbb{R})$ of \mathbb{R} [57]. In particular,

$$N_y(A) = \#\{t_i^y \in A\}, \quad A \in \mathcal{B}(\mathbb{R}).$$

In addition, the random measure N_y can be expressed in terms of the spike train y via

$$N_y(A) = \int_A y(t) dt, \quad A \in \mathcal{B}(\mathbb{R}).$$

In some of what follows, it will be convenient to slightly abuse notation and write $N_y(t)$ as a random function on \mathbb{R} :

$$N_y(t) \equiv N_y([0, t]) = \#\{t_i^y \in [0, t]\}, \quad t \in \mathbb{R}.$$

The random measure N_y can itself be viewed as a stochastic process. In this context, we would call N_y the *counting process* associated with the point process y . Throughout this work, we generally choose to perform our analysis in terms of spike trains, though in Chapter 4, it will be convenient to deal primarily with the counting processes.

We will say that a vector point process $\mathbf{y}(t) = (y_1(t), \dots, y_N(t))$ with the representation in Eq. (2.7) is jointly stationary if the associated counting process $N_{\mathbf{y}} = (N_{y_1}, \dots, N_{y_N})$ satisfies the stationarity condition given in the introduction to this chapter; that is, \mathbf{y} is said to be jointly stationary if the distributions of the random vectors

$$(N_{y_{i_1}}(A_1), \dots, N_{y_{i_M}}(A_M)) \quad \text{and} \quad (N_{y_{i_1}}(A_1 + s), \dots, N_{y_{i_M}}(A_M + s))$$

agree for all finite sets of indices $\{i_j\}_{j=1}^M \subset \{1, \dots, N\}$, collections of subsets $\{A_i\}_{i=1}^M \subset \mathcal{B}(\mathbb{R})$ and $s \in \mathbb{R}$, where we define a set translation as

$$A + s = \{a + s : a \in A\}.$$

Some popular, general references on the properties of point processes are [54, 57].

2.1.2.2 Statistical measures for point processes

Spike count cumulants Statistics of spike trains, like the stationarity condition above, are properly stated in terms of their counting processes. We define general r -spike count cumulants of a vector \mathbf{y} of spike trains over windows of length T by

$$\gamma_{\mathbf{r}}^{\mathbf{y}}(T) = \frac{1}{T} \kappa_{\mathbf{r}}(N_{y_1}(T), \dots, N_{y_N}(T)). \quad (2.8)$$

Asymptotic spike count cumulants are defined by taking the limit of large T :

$$\gamma_{\mathbf{r}}^{\mathbf{y}}(\infty) \equiv \lim_{T \rightarrow \infty} \gamma_{\mathbf{r}}^{\mathbf{y}}(T). \quad (2.9)$$

At first order, the spike count cumulant equals the firing rate $r_i(T)$ of the process,

$$r_i(T) \equiv \frac{1}{T} \gamma_i^{\mathbf{y}}(T) = \frac{1}{T} \mathbf{E} [N_{y_i}(T)]. \quad (2.10)$$

Adopting the subscript notation defined in Eq. (2.4) for the cross-cumulant density, we write the spike count variances and covariances over windows of length T as

$$\gamma_{ii}^{\mathbf{y}}(T) = \frac{1}{T} \mathbf{var} [N_{y_i}(T)], \quad \gamma_{ij}^{\mathbf{y}}(T) = \frac{1}{T} \mathbf{cov} [N_{y_i}(T), N_{y_j}(T)].$$

General spike count cross-cumulants are denoted

$$\gamma_{i_1 i_2 \dots i_k}^{\mathbf{y}}(T) = \frac{1}{T} \kappa(N_{y_{i_1}}(T), N_{y_{i_2}}(T), \dots, N_{y_{i_k}}(T)). \quad (2.11)$$

Lastly, we will make use of the second order spike count correlation coefficient $\rho_{ij}^{\mathbf{y}}(T)$.

This is given by the Pearson correlation of the spike counts:

$$\rho_{ij}^{\mathbf{y}}(T) = \frac{\gamma_{ij}^{\mathbf{y}}(T)}{\sqrt{\gamma_{ii}^{\mathbf{y}}(T) \gamma_{jj}^{\mathbf{y}}(T)}}. \quad (2.12)$$

The asymptotic quantity $\rho_{ij}^{\mathbf{y}}(\infty)$ is defined by

$$\rho_{ij}^{\mathbf{y}}(\infty) = \frac{\gamma_{ij}^{\mathbf{y}}(\infty)}{\sqrt{\gamma_{ii}^{\mathbf{y}}(\infty) \gamma_{jj}^{\mathbf{y}}(\infty)}}.$$

Cross-cumulant densities The cross-cumulant density of a vector of spiking processes \mathbf{y} can be expressed as a limit of cumulants of the associated counting processes,

$$\kappa^{\mathbf{y}}(\tau_1, \dots, \tau_{N-1}) = \lim_{\Delta t \rightarrow 0} \frac{\kappa(N_{y_1}[0, \Delta t], N_{y_2}[\tau_1, \tau_1 + \Delta t], \dots, N_{y_N}[\tau_{N-1}, \tau_{N-1} + \Delta t])}{\Delta t^N}. \quad (2.13)$$

When dealing with point processes, the cross-cumulant density can be interpreted as the probability of observing spikes from the processes \mathbf{y} in the arrangement indicated by the intervals in the definition Eq. (2.13) (i.e., a spike at time t in y_1 , at time $t + \tau_1$ in y_2 , and so on) *beyond* what can be inferred from lower order cumulants. For instance, consider the conditional intensity $h_{12}(\tau)$ of a pair of spiking processes (y_1, y_2) , a second order quantity given by [54, 55]

$$h_{ij}^{\mathbf{y}}(\tau) = \lim_{\Delta t \rightarrow 0} \frac{P(N_{y_j}[\tau, \tau + \Delta t] > 0 | N_{y_i}[0, \Delta t] > 0)}{\Delta t}.$$

It is not difficult to show using the law of total expectation that

$$\kappa_{ij}^{\mathbf{y}}(\tau) = r_i h_{ij}(\tau) - r_i r_j. \quad (2.14)$$

Thus, the second-order cross-cumulant density gives the probability that a spike in y_i is followed by one in y_j at a lag τ (namely, $r_i h_{ij}(\tau)$) above what would be expected to occur by random chance ($r_i r_j$).

We note that there is nothing particular about the order of conditioning considered in the argument above. For instance, we could have defined instead the intensity function $h_{ji}^{\mathbf{y}}(\tau)$, then expressed the cross-cumulant density as

$$\kappa_{ij}^{\mathbf{y}}(\tau) = r_j h_{ji}^{\mathbf{y}}(-\tau) - r_i r_j.$$

In addition, this method of expressing the cross-cumulant density in terms of conditional firing intensities can be extended directly to third and higher orders. In all cases, the order

of conditioning is not important — only the relative arrangement of the time lags for the collection of processes under consideration matter.

Another statistic useful in the study of a correlated vector point process \mathbf{y} is the *population cumulant density*. At second-order, the population cumulant density for the i^{th} process takes the form [173]

$$\kappa_{i,\text{pop}}^{\mathbf{y}}(\tau) = \sum_{j \neq i} \kappa_{ij}^{\mathbf{y}}(\tau).$$

More generally, the k^{th} order population cumulant density corresponding to the processes $y_{i_1}, \dots, y_{i_{k-1}}$ is given by

$$\kappa_{i_1 \dots i_{k-1}, \text{pop}}^{\mathbf{y}}(\tau_1, \dots, \tau_{k-1}) = \sum_{j \neq i_1, \dots, i_k} \kappa_{i_1 \dots i_{k-1} j}^{\mathbf{y}}(\tau_1, \dots, \tau_{k-1}). \quad (2.15)$$

The population cumulant density measures the propensity of the set of neurons under consideration to spike in a certain arrangement relative to other neurons in the population.

Cross-cumulant densities with repeated spiking processes Consider the auto-cumulant density $\kappa_{ii}^{\mathbf{y}}(\tau)$. It is known that, for a general stationary point process, this function takes the form

$$\kappa_{ii}^{\mathbf{y}}(\tau) = r_i \delta(\tau) + \text{“non-singular contributions”},$$

where r_i is the constant intensity (rate) of y_i [54].

Similar singular contributions can appear in higher order cross-cumulant densities when processes are repeated. As an example, consider the third order cross-cumulant density of the triplet (i, i, j) . From Eq. (2.13), using that the third order cross-cumulant is

equal to the central moment, we can write

$$\begin{aligned}
 \kappa_{ij}^y(0, \tau_2) &= \lim_{\Delta t \rightarrow 0} \frac{\mathbf{E} \left[(N_{y_i}[0, \Delta t] - r_i \Delta t)^2 (N_{y_j}[\tau_2, \tau_2 + \Delta t] - r_j \Delta t) \right]}{\Delta t^3} \\
 &= \lim_{\Delta t \rightarrow 0} \frac{\mathbf{E} \left[N_{y_i}[0, \Delta t]^2 (N_{y_j}[\tau_2, \tau_2 + \Delta t] - r_j \Delta t) \right]}{\Delta t^3} \\
 &\quad - 2r_i \frac{\mathbf{E} \left[N_{y_i}[0, \Delta t] (N_{y_j}[\tau_2, \tau_2 + \Delta t] - r_j \Delta t) \right]}{\Delta t^2} + r_i^2 \frac{\mathbf{E} \left[N_{y_i}[0, \Delta t] - r_i \Delta t \right]}{\Delta t} \\
 &= \lim_{\Delta t \rightarrow 0} \frac{\mathbf{E} \left[N_{y_j}[\tau_2, \tau_2 + \Delta t] - r_j \Delta t \mid N_{y_i}[0, \Delta t] > 0 \right] P(N_{y_i}[0, \Delta t] > 0)}{\Delta t^3} - 2r_i \kappa_{ij}^y(\tau_2) \\
 &= \lim_{\Delta t \rightarrow 0} \frac{\kappa_{ij}^y(\tau_2)}{\Delta t} - 2r_i \kappa_{ij}^y(\tau_2),
 \end{aligned}$$

where the final equality follows from Eq. (2.14). Since the joint firing probabilities will generally remain bounded at all pairs of lags for which $\tau_1 \neq 0$, we have established that

$$\kappa_{ij}^y(\tau_1, \tau_2) = \delta(\tau_1) \kappa_{ij}^y(\tau_2) + \text{“non-singular contributions”}. \quad (2.16)$$

A similar argument establishes that, for example,

$$\kappa_{ij}^y(\tau_1, \tau_2) = \delta(\tau_2 - \tau_1) \kappa_{ij}^y(\tau_1) + \text{“non-singular contributions”}.$$

Comparable expressions hold in the general case of arbitrary order cross-cumulant densities. In short, cross-cumulant densities involving multiple copies of a spiking process will necessarily contain singular contributions proportional to lower order cross-cumulant densities of the same set of processes. These singular contributions are analogous to the delta contribution proportional to the firing rate (i.e., the first order cumulant) which appears in the second order auto-cumulant density of a spiking process. In the third order case, for example, these singular contributions can appear along “ridges” centered on the τ_1, τ_2 axes, as well as the diagonal $\tau_1 = \tau_2$.

Relating spike count cumulants and cross-cumulant densities The spike count covariance can be related directly to the second order cross-cumulant density by [54, 55, 232, 271]

$$\gamma_{ij}^y(T) = \int_{-T}^T p(\tau; T) \kappa_{ij}^y(\tau) d\tau \quad \text{with} \quad p(\tau; T) = 1 - \frac{|\tau|}{T}, \quad (2.17)$$

where the prefactor accounts for edge effects of the finite window. A similar relation holds which relates the spike count variance $\gamma_{ii}^y(T)$. to the second order auto-cumulant density $\kappa_{ii}^y(\tau)$. The integral in Eq. (2.17) can also be evaluated in the frequency domain, relating spike count covariance to the cross-spectral density by

$$\gamma_{ij}^y(T) = \int_{-\infty}^{\infty} \tilde{p}(\omega; T) S_{ij}^y(\omega) d\omega,$$

where $\tilde{p}(\omega; T) \equiv \mathcal{F}[p(\tau; T)] = \frac{4}{T\omega^2} \sin^2(\omega T/2)$.

Eq. (2.17) can be generalized to relate higher order spike count cumulants to the corresponding densities. For example, if we define

$$p(\tau_1, \tau_2; T) = \begin{cases} 1 - \frac{\max\{|\tau_1|, |\tau_2|\}}{T}, & \tau_1 \cdot \tau_2 \geq 0, \\ 1 - \frac{|\tau_1| + |\tau_2|}{T}, & \tau_1 \cdot \tau_2 < 0, \end{cases}$$

we then have that

$$\gamma_{ijk}^y(T) = \int_{-T}^0 \int_{-T}^{T-\tau_1} p(\tau_1, \tau_2) \kappa_{ijk}^y(\tau_1, \tau_2) d\tau_2 d\tau_1 + \int_0^T \int_{\tau_1-T}^T p(\tau_1, \tau_2) \kappa_{ijk}^y(\tau_1, \tau_2) d\tau_2 d\tau_1.$$

Similar expressions can be derived at higher orders. In general, the asymptotic spike count cumulants (defined in Eq. (2.9)) equal the total integral under the corresponding cross-cumulant density:

$$\gamma^y(\infty) = \int_{-\infty}^{\infty} \cdots \int_{-\infty}^{\infty} \kappa^y(\tau_1, \dots, \tau_{N-1}) d\tau_{N-1} \cdots d\tau_1. \quad (2.18)$$

Using Eqs. (2.1, 2.6), the asymptotic spike count cumulant can also be evaluated in terms

of the cross-spectral density. For instance, owing to the equivalence of second- and third-order cross-cumulants and central moments, we have at these orders

$$\gamma_{ij}^y(\infty) = S_{ij}^y(0) \quad \text{and} \quad \gamma_{ijk}^y(\infty) = S_{ijk}^y(0).$$

Our ergodicity assumptions guarantee the existence of all cumulant quantities considered, and the integrability of the cross-cumulant densities.

2.2 Copulas

Consider a random vector $\mathbf{X} = (X_1, \dots, X_N)$ with joint distribution function

$$F(x_1, \dots, x_N) = P[X_1 \leq x_1, \dots, X_N \leq x_N], \quad (x_1, \dots, x_N) \in \mathbb{R}^N,$$

and marginal distribution functions

$$F_i(x_i) = \int \cdots \int F(x_1, \dots, x_N) dx_n \cdots dx_{i+1} dx_{i-1} \cdots dx_1.$$

The *copula* C of \mathbf{X} — which can also be identified with the distribution F and marginals $\{F_i\}_{i=1}^N$ — is a function which satisfies the equality [189, 256]

$$F(x_1, \dots, x_N) = C(F_1(x_1), \dots, F_N(x_N)) \quad \forall (x_1, \dots, x_N) \in \mathbb{R}^N. \quad (2.19)$$

By the probability integral transform, each of $F_i(X_i)$ is a uniformly distributed random variable. The function C can also be defined as the joint distribution of the random vector $(F_1(X_1), \dots, F_N(X_N))$. Sklar's Theorem [256] provides uniqueness of the copula associated with a random vector on $\prod_{i=1}^N \text{Ran}(F_i)$, the Cartesian product of the ranges of the marginal distribution function, also implying that the copula is unique under the assumption of absolutely continuous distributions. A copula can be equivalently viewed as a distribution function on the N -dimensional unit hypercube with $U[0, 1]$ marginals.

The *copula density* c is defined as the density corresponding to the copula distribution C and is given by

$$c(\mathbf{u}) = \frac{\partial}{\partial u_1} \cdots \frac{\partial}{\partial u_N} C(\mathbf{u}), \quad \mathbf{u} \in [0, 1]^N. \quad (2.20)$$

Using the copula density, we can express the joint *density* f for the distribution F as

$$f(x_1, \dots, x_N) = c(F_1(x_1), \dots, F_N(x_N)) \prod_{i=1}^N f_i(x_i), \quad (2.21)$$

where

$$f_i(x_i) = \frac{\partial}{\partial x_i} F(x_i)$$

is the marginal density for the i^{th} component of \mathbf{X} .

As is clear from Eq. (2.19), the copula encapsulates completely the dependence structure of the random vector \mathbf{X} , and knowledge of the joint distribution F is equivalent to knowledge of the marginal distributions $\{F_i\}_{i=1}^N$ and the copula function C . Thus, methods which approximate the copula associated with a distribution provide an avenue for approximation of the joint distribution itself, when coupled with estimations of the marginal distributions. To this end, many parametric copula models exist which can be fit to data by the usual maximum likelihood methods. Before introducing some of these parametric models, we quickly note that if the components of the vector \mathbf{X} are independent, then

$$F(x_1, \dots, x_N) = \prod_{i=1}^N F_i(x_i),$$

leading to the definition of the *independence copula*,

$$C_{ind}(\mathbf{u}) = \prod_{i=1}^N u_i, \quad \mathbf{u} \in [0, 1]^N.$$

Clearly, if $C = C_{ind}$ in Eq. (2.19), then the components of the vector \mathbf{X} are independent.

2.2.1 Archimedean copulas

One common parametric class of copulas is the *Archimedean copulas* which are defined in terms of parametric generator functions ψ . The copula C_ψ associated with a generator ψ is defined by

$$C_\psi(\mathbf{u}) = \psi\left(\psi^{-1}(u_1) + \dots + \psi^{-1}(u_N)\right), \quad \mathbf{u} \in [0, 1]^N,$$

where it is additionally required that the function ψ be N -monotone for C_ψ to be a proper copula [183]. In other words, ψ must satisfy the conditions

- $(-1)^k \psi^{(k)}(x) \geq 0 \forall x \geq 0, k = 1, \dots, N - 2,$
- $(-1)^{N-2} \psi^{(N-2)}(x)$ is non-increasing and convex.

For example, the *Gumbel copula*, which exhibits strong correlation in the positive tails of the distribution — i.e., events in the positive tails of the joint distribution tend to occur together at a level well above chance — is an Archimedean copula with generator

$$\psi(t; \theta) = \exp\left[-t^{1/\theta}\right], \quad \theta \in [1, \infty).$$

More generally, the Archimedean copula generators can be parameterized by a vector θ . Given sample data, maximum likelihood methods can be applied to determine the most likely value of the parameter vector θ .

2.2.2 The Gaussian copula

Another commonly used copula model is the *Gaussian copula* [305], parameterized by a correlation matrix Σ , assumed to be a positive definite matrix with $\Sigma_{ii} = 1$ and $\Sigma_{ij} \in$

$[-1, 1]$. The Gaussian copula distribution function is given by

$$C_{\Sigma}^{\text{Gauss}}(\mathbf{u}) = \Phi_{\Sigma} \left(\Phi^{-1}(u_1), \dots, \Phi^{-1}(u_N) \right), \quad (2.22)$$

where Φ is the standard, univariate normal CDF, and Φ_{Σ} is the N -dimensional CDF for the Gaussian distribution with zero mean and correlation matrix Σ . In the applications of Chapter 8, it will be useful to note that the Gaussian copula density can be written in closed form as

$$c_{\Sigma}^{\text{Gauss}}(u_1, \dots, u_N) = \frac{1}{\det(\Sigma)} \exp \left[\mathbf{w}^T (\Sigma^{-1} - \mathbf{I}) \mathbf{w} \right], \quad \mathbf{w} = \left[\Phi^{-1}(u_1), \dots, \Phi^{-1}(u_N) \right]^T. \quad (2.23)$$

The Gaussian copula is advantageous to apply in that, given a collection of observations $\{\mathbf{X}^j\}_{j=1}^D$ of the random vector X , the maximum likelihood value of $\hat{\Sigma}_{ij}$ of Σ_{ij} can be determined without the need to apply a gradient descent method or other optimization techniques. In particular, the maximum likelihood value for the correlation parameter in the Gaussian copula is given by [305]

$$\hat{\Sigma}_{ij} = \text{corr} \left(\Phi^{-1}(F_i(X_i)), \Phi^{-1}(F_j(X_j)) \right).$$

The correlation computed in the previous expression is the empirically observed correlation from the samples $\{\mathbf{X}^j\}_{j=1}^D$. In Chapter 8, we apply Gaussian copulas in order to obtain an estimate of a joint distribution which is both continuous and has twenty dimensions. It is not feasible to tackle this problem directly, even with modern computational power and storage capabilities.

We conclude by noting that, in certain applications the Gaussian distribution is found to be unsuitable for fitting to the true copula as it predicts very low probabilities for joint events involving multiple marginally rare events. In many cases, however, so-called “extreme” events tend to occur in a correlated fashion (such as during a period of elevated

activity within a neuronal network, or the collective behavior of securities during financial booms or crises). In this case, one can achieve a better fit by applying the t -copula. The t -copula is a direct generalization of the Gaussian copula, and includes an additional degree of freedom with which to better capture the dependence structure [60]. The t -copula is defined similarly to the Gaussian copula in Eq. (2.22), replacing the joint distribution with the joint t distribution with correlation matrix Σ and ν degrees of freedom, and the marginal distributions with standard t distributions with ν degrees of freedom. The t -copula converges in distribution to the Gaussian copula as $\nu \rightarrow \infty$.

Modeling of neurons and their interactions

Neuronal models can vary greatly in their complexity [58, 79, 81, 84, 105, 120, 147, 159, 188, 291]. At one end, highly detailed models can consist of hundreds of coupled differential equations modeling “electrical compartments” of the neuron, and attempt to capture changes in membrane potential induced by molecular-level kinetics of ions traversing membrane channels [84, 243, 279]. These neuron models provide near-complete descriptions of responses to biophysically realistic stimulation.

On the other end of this spectrum, reduced models aim to capture salient features of neuronal activity, favoring tractability over completeness [39, 131, 182]. The models which we will primarily employ herein, the so-called *integrate-and-fire* (IF) model neurons [40, 41, 81], are of the latter type. When a neuron spikes, its membrane potential undergoes a rapid depolarization followed by a comparably rapid hyper-polarization back towards a resting potential [79, 120]. Integrate-and-fire neuron models exhibit a firing threshold on

the membrane potential which is meant to approximate realistic spiking dynamics.

In this chapter, we introduce and briefly explore the properties of integrate-and-fire neuron models. Following this, define and discuss the manner in which these neuron models are typically coupled to each other. We conclude the chapter by introducing the *diffusion approximation* in Section 3.3, motivating the consideration of white noise-driven neurons throughout most of the rest of this work. Before doing so, however, we introduce a useful change of coordinates for the parametrization of the subthreshold dynamics of conductance-driven neurons. This *effective time constant form* helps to elucidate the functional significance of differences between current- and conductance-based input modes.

3.1 Integrate-and-fire neuron models

A general integrate-and-fire model neuron receiving current input $I(t)$ neuron has a membrane potential which evolves according to the differential equation [41]

$$C_m \dot{V}(t) = F(V(t)) + I(t), \quad V_0 = v_0.$$

Upon crossing the threshold V_{th} , the membrane potential of the neuron is reset to V_r , where it is held fixed for an absolute refractory period of length τ_{ref} , after which normal voltage dynamics resume. We denote by $y(t)$, the spiking output of the neuron given by

$$y(t) = \sum_j y(t - t^j),$$

with t^j equal to the time of the j^{th} crossing of the membrane potential across the threshold V_{th} . The nature of the function $F(V)$ determines the subthreshold dynamics of the neuron model. We next discuss a few canonical integrate-and-fire neuron models.

3.1.1 The leaky integrate-and-fire neuron

One of the simplest variants of the integrate-and-fire family is the *leaky integrate-and-fire* (LIF) model [39, 41, 147, 159, 264]. In this model, the voltage-dependent dynamics are given by

$$F_{\text{LIF}}(V) = g_L(V_L - V),$$

where g_L is the membrane conductance, and $V_L < V_{\text{th}}$ is the rest potential in the absence of input ($I(t) \equiv 0$). In this case, the membrane potential will relax to the leak (or resting) potential V_L exponentially, with a time constant given by $\tau_m = C_m/g_L$ - this is the *membrane time constant* of the neuron. In Figure 3.1A, we exhibit the evolution of the membrane potential of an LIF neuron receiving Poisson input $I(t)$, where we write

$$I(t) = w \sum_{k=1}^{\infty} \delta(t - t_{in}^k) \quad \text{for } t_{in}^1 < t_{in}^2 < \dots,$$

and depict the resulting output spike train $y(t)$ at the top of the panel.

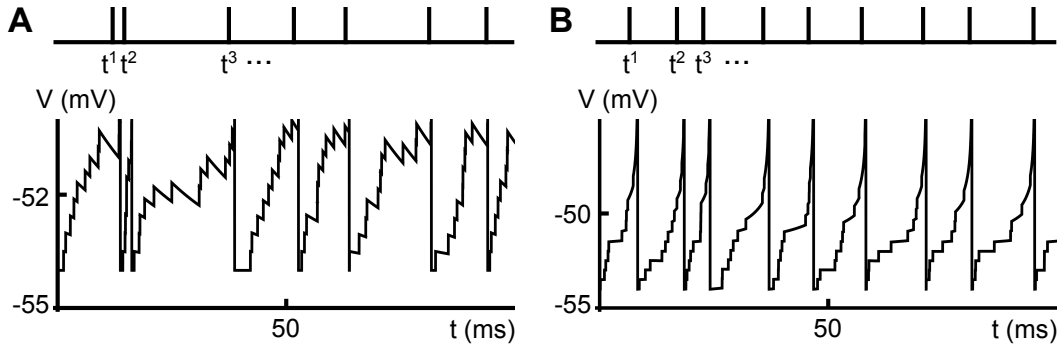


Figure 3.1: **Illustrating the membrane potential and spiking dynamics of integrate-and-fire model neurons.** (A) The time evolution of the membrane potential of an LIF neuron receiving excitatory Poisson current inputs. The corresponding output spike train is displayed at the top of the panel. (B) Same as panel A, but for the EIF neuron model. Unlike the LIF, the EIF neuron features a spike initiation phase in its subthreshold dynamics in which the membrane potential exhibits a smooth but rapid escape.

3.1.2 The exponential integrate-and-fire neuron

An important generalization of the LIF neuron presented above is the *exponential integrate-and-fire* (EIF) model neuron [41, 81]. The voltage-dependent dynamics of the EIF contain the same leak term as the LIF, but also an exponential term which models membrane potential spike dynamics induced by fast sodium currents [81]. In particular,

$$F_{\text{EIF}}(V) = g_L(V_L - V + \psi(V)), \quad \text{where} \quad \psi(V) = \Delta_T \exp\left[\frac{V - V_T}{\Delta_T}\right].$$

Typically, the parameters of the model are such that the exponential non-linearity ψ has only a minor effect on the voltage dynamics around the rest potential E_L . The parameter V_T is referred to as the “soft threshold” of the EIF model, as it solves the equation

$$F'_{\text{EIF}}(V_T) \equiv 0.$$

If set initially above this value, the membrane potential can be shown to diverge to $+\infty$ in finite time, assuming the absence of input ($I(t) \equiv 0$). Such a divergence indicates a “spike” of the EIF model. The exponential integrate-and-fire neuron has been shown to match well both subthreshold and spiking neuronal dynamics in certain cortical areas [13, 81].

In practice, one still sets a hard threshold V_{th} , but as long as the hard threshold is sufficiently high relative to the soft threshold, the spiking dynamics of the EIF are not sensitive to this value owing to the exponential escape of the potential [81], in sharp contrast to the LIF model. The parameter Δ_T shapes the spiking dynamics of the membrane potential — higher Δ_T induces a more rapid onset of spiking (i.e., depolarizations of higher slope, implying narrower spikes). In the limit that $\Delta_T \rightarrow 0$, the EIF converges to the LIF with threshold V_T . In Figure 3.1B, we exhibit the evolution of the membrane potential of an EIF neuron receiving Poisson input and depict the resulting output spike train $y(t)$ above

the trace. Note the smooth initiation of the action potentials in contrast to the LIF in panel A.

3.1.3 The general integrate-and-fire neuron

Other canonical models of the integrate-and-fire family have been considered extensively in the literature [41, 132]. Although we will not cover them in detail, much of what follows can be applied to these models as well. One particularly important example is the quadratic integrate-and-fire (QIF) model [69, 72, 161]. For this model, the subthreshold dynamics are given by

$$F(V) \propto (V - V_L)(V - V_{\text{th}}).$$

For initial values $V_0 < V_{\text{th}}$, the membrane potential will relax to the leak potential V_L , and for $V_0 > V_{\text{th}}$, the membrane potential again diverges to $+\infty$ in finite time. This model can be fit so that its dynamics mimic well those of the Morris-Lecar model (a two-dimensional neuron model exhibiting realistic spike-reset dynamics) in certain cases [69], and is equivalent to the canonical theta model after a change of variable.

Another important set of examples is the class of adaptive integrate-and-fire neurons [34, 131], which seem to achieve a nexus of simplicity (low dimensionality) and flexibility. Whether the methods herein can be applied (particularly those of Chapters 5, 6) to such models in a useful manner is an interesting topic for future research.

3.2 Models of synaptic interaction

In this section, we will review some common approximations to neuronal interactions. Briefly, chemical interactions between neurons take place when the membrane potential

3.2. MODELS OF SYNAPTIC INTERACTION

of one neuron (the *pre-synaptic* neuron) is rapidly depolarized. This rapid depolarization creates a travelling wave (also called an *action potential* or *spike*) which moves rapidly along the length of the axon of the neuron.

When this action potential reaches a synaptic terminal, it causes a small quantity of a *neurotransmitter* to be released into the synaptic cleft, a small gap between the pre-synaptic and post-synaptic terminals at the site of the interaction. These neurotransmitter molecules bind with receptors in the membrane of the post-synaptic cell, opening ion channels and eliciting a transient change in the membrane potential of the post-synaptic neuron. Typically, chemical synapses link the axon of the pre-synaptic cell to the dendrite of the post-synaptic cell, though this needn't always be the case. The change in membrane potential in the post-synaptic neuron elicited by synaptic input can be either hyperpolarizing (inhibitory) or depolarizing (excitatory) depending on the type of synapse, itself characterized by the identity of the neurotransmitter released.

3.2.1 Current-based synapses

Throughout this work, we employ reduced integrate-and-fire models of neuronal activity. In adopting these models, we choose to neglect detailed modeling of membrane potential modulations through the operation of ion channels, and other such details, and accordingly, much of the detail of chemical synaptic interactions briefly described in the opening to this section. One simple way to approximate chemical synaptic kinetics is through so-called “current-based synapses”.

One of the simplest reductions of these chemical synaptic kinetics is the approximation of such exchanges is through current-based interactions.

Considering an example leaky integrate-and-fire neuron model receiving the spiking output $x(t)$ of another neuron, the membrane potential evolves according to

$$C_m \dot{V}(t) = g_L(V_L - V(t)) + (\alpha * x)(t).$$

The filter $\alpha(t)$ is known as the *synaptic filter* or *post-synaptic current* (PSC). Upon the reception of a spike in the process $x(t)$, the current across the membrane of the postsynaptic neuron exhibits a transient change with a time-course matching that of the filter $\alpha(t)$. Synapses vary not only in polarity, but also strength and timescale, depending on many factors, such as the particular neurotransmitter involved and the number of post-synaptic binding sites available for neurotransmitter binding. The filter $\alpha(t)$ sets both the strength as well as the time-scale of the interaction. In Figure 3.2A, we show the time-evolution of the membrane potential of an LIF neuron receiving excitatory, current-based Poisson input. The synaptic filter was instantaneous (i.e., $\alpha(t) = w\delta(t)$), resulting in a fixed-size jump followed by an exponential decay in the membrane potential upon the arrival of an input pulse.

3.2.2 Conductance-based synapses

Chemical synaptic kinetics at the molecular level involve the opening and closing of ion channels in the membrane of neurons, and these channels are often themselves controlled or affected by the membrane potential of the neuron involved. In short, this imposes a membrane potential dependence on synaptic interactions which can, in many cases, be more accurately captured by considering synaptic interactions through membrane *conductances* [61], as opposed to the current-based synapses covered in Section 3.2.1.

Thus, consider again a leaky integrate-and-fire neuron receiving a spike train input $x(t)$ representing the output of a distinct neuron. The membrane potential of this neuron

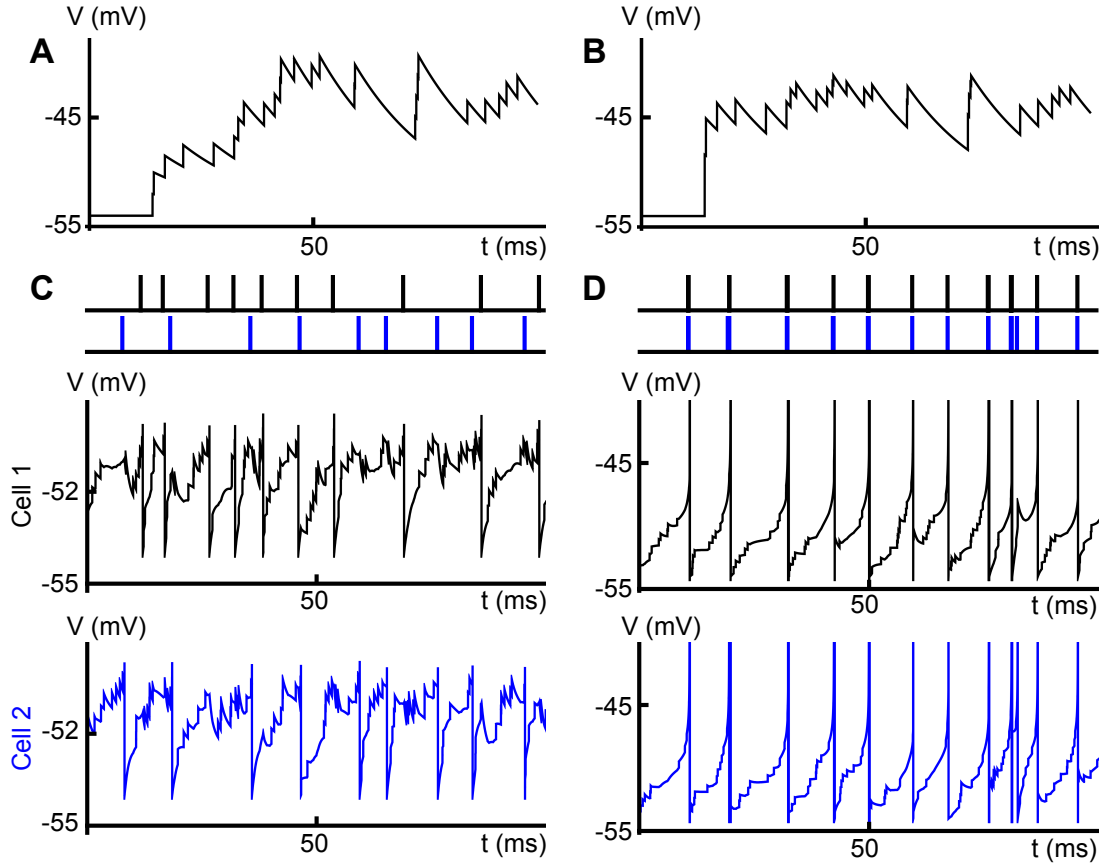


Figure 3.2: **Implementing coupling amongst integrate-and-fire model neurons.** (A) Time evolution of the membrane potential of a LIF neuron (with spiking dynamics — i.e., the threshold and reset — neglected) receiving current-based excitatory Poisson input. (B) Same as panel A for conductance-based input. The input spike train was precisely that used for panel A. Note that the jump size now depends on the membrane potential at the time of arrival for the input pulse. (C) Time evolution of the membrane potentials (bottom) and resulting spike trains (top) for a pair of electrically coupled LIF neurons. (D) Same as panel C, except for EIF neurons. The nature of the spiking dynamics strongly modulates the effect of gap junction coupling on output spiking correlations. The strength of the gap-junction synapses was set to $g_{gap} = 10g_L$.

evolves according to

$$C_m \dot{V}(t) = g_L(V_L - V(t)) + (\alpha * x)(t)(V_{syn} - V(t)).$$

Here V_{syn} sets the synaptic reversal potential (as well as the polarity of the synapse), and

the synaptic filter $\alpha(t)$ now gives the transient increase in the *post-synaptic conductance* induced by an input spike from $x(t)$.

The net effect of considering conductance-based synapses rather than current-based ones is that the closer the membrane potential of a neuron is to the synaptic reversal potential for a given synapse at the time of reception of an input, the weaker the corresponding induced post-synaptic current will be. Synapses with $V_{\text{syn}} > V_L$ are called excitatory, and others inhibitory. In Figure 3.2B, we exhibit the membrane potential evolution of an LIF neuron (with spiking dynamics removed) receiving excitatory, conductance-based Poisson input. The synaptic filter again was instantaneous, however, due to the inputs being through *conductances* as opposed to *currents* (see Figure 3.2A), there is a strong state-dependence of the jump size upon arrival of an input pulse. The input spike train in Figure 3.2B precisely matched that used in Figure 3.2A.

An important difference between the current- and conductance-based models of synaptic interaction is that a neuron receiving conductance-based inputs does not have a single membrane filter in the classical sense - rather, the timescale at which the neuron responds to inputs changes (decreases) with increasing synaptic conductance, as greater synaptic conductance has the side-effect of inducing an increase in the effective membrane conductance. This in turn leads to interesting effects such as shunting inhibition, in which a neuron can become effectively silent despite the reception of large amounts of both excitatory and inhibitory synaptic input.

3.2.3 Electrical synapses

In the early 20th century, there was a great debate within the budding neuroscientific community regarding the predominant nature of neuronal interactions. Camillo Golgi

3.2. MODELS OF SYNAPTIC INTERACTION

and others supported the *reticular hypothesis* [92], in which it was believed that neurons (and elements of the nervous system in general) formed a continuum through which information passed smoothly. Based on the work of Golgi himself, Santiago Ramón y Cajal presented an alternative theory known as the *neuron doctrine* [210], in which it was hypothesized that neurons were distinct anatomical units which communicated exclusively through “discrete” (chemical) events. An extended debate over which was the valid hypothesis ensued [281]. Ramón y Cajal’s neuron doctrine was dominant until the presence of electrical synapses was first concretely exhibited in crayfish in 1959 [83], thereby indicating there were two distinct modes for neuronal communication (chemical and electrical), and that there were elements of truth to each theory. It should be noted that chemical interactions are still believed to be the primary mode of communication for cortical neurons.

In more recent studies, electrical synapses between neurons which lie very close to each other have been shown to be much more common than was previously believed in the mammalian brain [53]. In Chapter 8, we will study a system of neurons in the brain of the blowfly *Calliphora vicina* which utilize these so-called *gap junction* synapses for robust encoding of behaviorally relevant stimuli values.

A gap junction synapse between two neurons results in the direct coupling between their membrane potentials of neurons, allowing for coupling and communication at a much shorter timescale than generally possible through chemical synapses. We will consider only bi-directional gap junction synapses, though examples of unidirectional gap junction coupling do exist [229]. We consider a pair of gap junction-coupled LIF neurons

with membrane potentials $V_1(t), V_2(t)$ evolving according to

$$C_m \dot{V}_1(t) = g_L(V_L - V_1(t)) + g_{gap}(V_2(t) - V_1(t)) + I_{in,1}(t),$$

$$C_m \dot{V}_2(t) = g_L(V_L - V_2(t)) + g_{gap}(V_1(t) - V_2(t)) + I_{in,2}(t).$$

Here, $I_{in,j}(t)$ consists of exponentially-filtered, current-based Poisson input in Sections 3.2.1 and 3.2.2. Considering the evolution of V_1 , the terms of the form $g_{gap}(V_2(t) - V_1(t))$ has the effect of continuously pulling the membrane potential of the first cell towards that of the second, and the corresponding term in the equation for the evolution of V_2 has the same effect.

The effect gap junction coupling can have on neuronal activity is exhibited in Figs. 3.2C, D. In Figure 3.2C, we show the membrane potentials and output spike trains of a pair of electrically-coupled LIF neurons receiving independent, excitatory Poisson input. Due to the sharp threshold involved in the LIF spiking dynamics, electrical coupling (though attractive in nature) can actually lead to *anti*-correlation in the output spiking of the two neurons. Compare this to Figure 3.2D, where we exhibit the activity of two electrically-coupled EIF neurons. The more realistic spiking dynamics (which involve a rapid escape towards a very high threshold) lead to the two neurons tending to pull each other along upon initiation of a spike, resulting in nearly-synchronous output spiking [166]. This is an example of a situation in which it is crucial to include more realistic spiking dynamics in the subthreshold description of neuronal activity. The role of gap junction coupling in regulating spiking dynamics has been studied extensively in the literature [48, 104, 150, 165, 166, 277, 290].

3.3 The diffusion approximation

When considering the behavior of a model neuron, or a network of such neurons, it is common to include in the input to the neuron a noisy component which represents this signal extraneous to the explicitly modeled circuit or network. Cortical neurons have been shown to exhibit highly irregular firing patterns characterized by interspike intervals with elevated coefficients of variation under a variety of conditions [237, 257, 265]. This induces a common simplifying assumption in neuronal modeling, namely, that this noisy signal consists of Poisson spike trains of both polarities (excitatory and inhibitory). The Poisson variability of the noisy inputs reflects the variability commonly exhibited by cortical neurons.

Modern estimates put the number of neurons and synapses in the human brain at about 100 billion (10^{11}) and 100 trillion (10^{14}), respectively [301]. Many neurons *in vivo* receive synaptic input from thousands of afferents, many of which can be relatively weak. In this section, we begin with an integrate-and-fire neuron receiving Poisson, conductance-based (i.e., multiplicative) input, and present the so-called *diffusion approximation* [41, 88, 107, 216, 218, 227] to the input, which allows us to treat the subthreshold dynamics of the neuron as a simple drift-diffusion process [88].

Preceding our presentation of the diffusion approximation, we introduce the *effective time constant form* and a related approximation [41, 136, 225] of subthreshold neuronal dynamics which motivates the consideration of additive noise. The effective time constant form elucidates the true nature of subthreshold neuronal dynamics in the presence of multiplicative, conductance-based inputs. The diffusion approximation, in turn, significantly increases tractability of the neuron models we consider, allowing for the analysis we will present in the sequel. These approximations have been shown to be valid in biologically

significant parameter regimes. [220, 221]

3.3.1 The effective time constant form

We will again consider the leaky integrate-and-fire neuron for concreteness. Letting $g_E(t), g_I(t)$ be the time-varying excitatory and inhibitory synaptic conductances, respectively, the membrane potential evolves according to

$$C_m \dot{V}(t) = g_L(V_L - V(t)) + g_E(t)(V_E - V(t)) + g_I(t)(V_I - V(t)). \quad (3.1)$$

After some simple algebraic manipulation, we can write the previous equation

$$C_m \dot{V}(t) = g_{\text{eff}}(V_{L,\text{eff}} - V(t)) + \delta g_E(t)(V_E - V(t)) + \delta g_I(t)(V_I - V(t)), \quad (3.2)$$

where the variation $\delta f(t)$ of a stochastic process $f(t)$ is defined as

$$\delta f(t) = f(t) - \mathbf{E}_t[f(t)],$$

and the effective membrane conductance and rest potential are

$$g_{\text{eff}} = \mathbf{E}_t[g_L + g_E(t) + g_I(t)], \quad V_{L,\text{eff}} = \frac{g_L V_L + \mathbf{E}_t[g_E(t)] E_E + \mathbf{E}_t[g_I(t)] E_I}{g_{\text{eff}}}.$$

In this *effective time constant form* [41, 225], the membrane potential is seen to have an *effective* filter with time constant

$$\tau_{\text{eff}} = \frac{C_m}{g_{\text{eff}}}.$$

Often, the synaptic conductances $g_E(t), g_I(t)$ include noise terms, and the consideration of multiplicative noise systems is generally more complicated than consideration of additive noise systems. In situations where it benefits tractability, it is common to replace the $V(t)$ in these multiplicative noise terms with its temporal average, giving membrane potential dynamics

$$C_m \dot{V}(t) = g_{\text{eff}}(V_{L,\text{eff}} - V(t)) + \delta g_E(t)(V_E - \mathbf{E}_t[V(t)]) + \delta g_I(t)(V_I - \mathbf{E}_t[V(t)]). \quad (3.3)$$

This approximation is known as the *effective time constant approximation* [41, 136, 225], and has been shown to match well the neuronal dynamics of the full model in Eq. (3.1) in biologically relevant parameter regimes [220, 221], a point we return to below.

3.3.2 The diffusion approximation for multiplicative Poisson noise

Now, consider a neuron receiving Poisson synaptic conductance drive. Assuming instantaneous synapses, we have that

$$g_E(t) = C_m w_E x_E(t), \quad g_I(t) = C_m w_I x_I(t),$$

where $x_E(t), x_I(t)$ are Poisson processes of intensity R_E, R_I , respectively. The constants w_E, w_I set the input weights, though there is a choice to be made in how to handle terms of the form $\delta(t)V(t)$ when integrating Eq. (3.2). In neuroscience applications, “instantaneous” synapses are a convenient interpretation of the physical limit of “very fast” synapses, and so the Stratonovich interpretation is appropriate [227, 267]. In this case, arrival of an excitatory spike at time t , for example, yields an instantaneous increase in the membrane potential of amplitude $u_E(E_E - V(t))$, where $u_E = 1 - e^{-w_E}$.

An integrate-and-fire neuron receiving Poisson input (either current- or conductance-based) is generally intractable when it comes to solving for essentially any firing statistic (including the firing rate) [41, 226]. Often, in order to gain some tractability, the *diffusion approximation* [41, 88, 216, 218, 227] is utilized. Under the diffusion approximation, the Poisson drive is replaced by an appropriately scaled white noise signal. In the present case, we set

$$g_E(t) = C_m(\mu_E + \sigma_E \xi_E(t)),$$

where $\xi(t)$ is a standard white noise process, and the mean μ_E and intensity σ_E are given

by

$$\mu_E = u_E R_E, \quad \sigma_E = u_E \sqrt{R_E}.$$

The inhibitory input is approximated similarly.

Thus, under the diffusion approximation, the effective time constant form of the membrane potential dynamics is

$$\tau_{\text{eff}} \dot{V}(t) = V_{L,\text{eff}} - V(t) + \sqrt{2\tau_{\text{eff}}\sigma_{\text{eff}}^2(V(t))}\xi(t), \quad (3.4)$$

where the effective time constant, rest potential and noise intensity are given (in terms of diffusion approximation parameters) as

$$g_{\text{eff}} = g_L + C_m(\mu_E + \mu_I), \quad \tau_{\text{eff}} = \frac{C_m}{g_{\text{eff}}}, \quad V_{L,\text{eff}} = \frac{g_L E_L + C_m(\mu_E E_E + \mu_I E_I)}{g_{\text{eff}}},$$

and the voltage-dependent effective noise intensity is

$$\sigma_{\text{eff}}^2(V) = \tau_{\text{eff}} \left[\sigma_E^2(E_E - V)^2 + \sigma_I^2(E_I - V)^2 \right]. \quad (3.5)$$

In Figure 3.3, we depict the time-evolution of the membrane potential of an LIF neuron receiving excitatory and inhibitory Poisson noise as parameters are moved towards the region of validity for the diffusion approximation. This approximation is valid in the limit where $w_E, w_I \ll 1$ and $r_E, r_I \gg 1$ (becoming exact as the weights tend to zero and the rates to infinity), i.e., in the case where we have many inputs which are individually weak. For the remainder of this work, we will consider exclusively neurons with noisy driving signals which are white, as opposed to Poisson.

3.3.3 Consideration of additive noise sources

Throughout this work, we will generally consider model neurons receiving *additive* white noise. As mentioned in the preceding section, the additive noise approximation has been

3.3. THE DIFFUSION APPROXIMATION

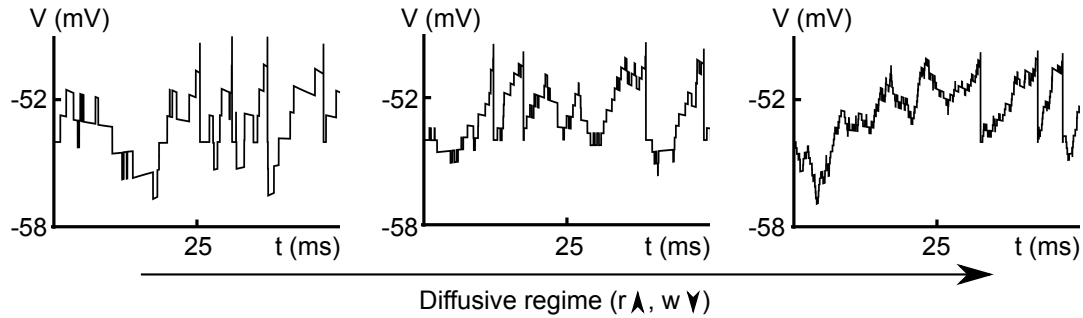


Figure 3.3: **The diffusion approximation.** Left to right: input parameters of an LIF neuron receiving excitatory and inhibitory Poisson noise are moved towards the region of validity for the diffusion approximation (i.e., input weights are decreased and input rates are increased).

shown as valid in biologically significant parameter regimes [220,221], and a neuron driven by additive fluctuations is generally simpler to analyze. If one wishes to make a consistent additive noise approximation to a Poisson-driven neuron, then the average membrane potential must be determined beforehand — for integrate-and-fire neurons, this problem is not generally analytically tractable. An alternative approach is to assume a fixed noise intensity (implicitly fixing an average membrane potential), taking the model as determined by a diffusion approximation to a Poisson-driven neuron for *some* ratio of input rates and weights. In the latter case, the rates and weights which yielded the approximating system are typically not of particular interest, so long as they can be assumed to be biophysically plausible. We elect the latter approach.

Chapter 4

A generative spike train model with time-structured higher order correlations

Emerging technologies are revealing the spiking activity in ever larger neural ensembles. Frequently, this spiking is far from independent, with correlations in the spike times of different cells. Understanding how such correlations impact the dynamics and function of neural ensembles remains an important open problem. Here we describe a new, generative model for correlated spike trains that can exhibit many of the features observed in data. Extending prior work in mathematical finance [19], this *generalized thinning and shift* (GTaS) model creates marginally Poisson spike trains with diverse temporal correlation structures. We give several examples which highlight the model's flexibility and utility.

We begin by describing the algorithm for sampling from the GTaS model. This constructive approach provides an intuitive understanding of the model's properties. We

then present a pair of examples, the first of which highlights the utility of the GTaS framework. The second example demonstrates how sample point processes from the GTaS model can be used to study population dynamics. Next, we present the analysis which yields the explicit forms for the cross-cumulant densities derived in the context of the examples. We do so by first establishing a useful distributional representation for the GTaS process, paralleling [19]. Using this representation, we derive cross-cumulants of a GTaS counting process, as well as explicit expressions for the cross-cumulant densities. After explaining the derivation at lower orders, we present a theorem which describes cross-cumulant densities at all orders.

4.1 Defining the Generalized Thinning and Shift Model

We will describe a flexible multivariate point process capable of generating a range of high order correlation structures. To do so we extend the *TaS* (thinning and shift) model of temporally- and spatially-correlated, marginally Poisson counting processes [19]. The *TaS* model itself generalizes the SIP and MIP models [156] which have been used in theoretical neuroscience [43, 232, 272]. However the *TaS* model has not been used as widely. The original *TaS* model is too rigid to generate a number of interesting activity patterns observed in multi-unit recordings [130, 173, 174]. We therefore developed the *generalized thinning and shift model* (GTaS) which allows for a more diverse temporal correlation structure.

4.1.1 GTaS model simulation

The GTaS model is parameterized first by a rate λ which determines the intensity of a “mother process” - a Poisson process on \mathbb{R} . The events of the mother process are marked, and the markings determine how each event is distributed among a collection of N daughter processes. The daughter processes are indexed by the set $\mathbb{D} = \{1, \dots, N\}$, and the set of possible markings is the power set $2^{\mathbb{D}}$, the set of all subsets \mathbb{D} . We define a probability distribution $p = (p_D)_{D \subset \mathbb{D}}$, assigning a probability to each possible marking, D . As we will see, p_D determines the probability of a joint event in all daughter processes with indices in the set D . Finally, to each marking, D , we assign a probability distribution Q_D , giving a family of shift (jitter) distributions $(Q_D)_{D \subset \mathbb{D}}$. Each (Q_D) is a distribution over \mathbb{R}^N .

The rate λ , the distribution p over the markings, and the family of jitter distributions $(Q_D)_{D \subset \mathbb{D}}$, define a vector $\mathbf{X} = (X_1, \dots, X_N)$ of dependent daughter Poisson processes described by the following algorithm, which yields a single realization (see Figure 4.1):

1. Simulate the mother Poisson process of rate λ on \mathbb{R} , generating a sequence of event times $\{t^j\}$. (Figure 4.1A).
2. With probability p_{D^j} assign the subset $D^j \subset \mathbb{D}$ to the event of the mother process at time t^j . This event will be assigned only to processes with indices in D^j . (Figure 4.1B).
3. Sample a vector $(Y_1^j, \dots, Y_N^j) = \mathbf{Y}^j$ from the distribution Q_{D^j} . For each $i \in D^j$, the time $t^j + Y_i^j$ is set as an event time for the marginal counting process X_i . (Figure 4.1C).

Hence, copies of each point of the mother process are placed into daughter processes

after a shift in time. A primary difference between the GTaS model and the TaS model presented in [19] is the dependence of the shift distributions Q_D on the chosen marking. This allows for greater flexibility in setting the temporal cumulant structure.

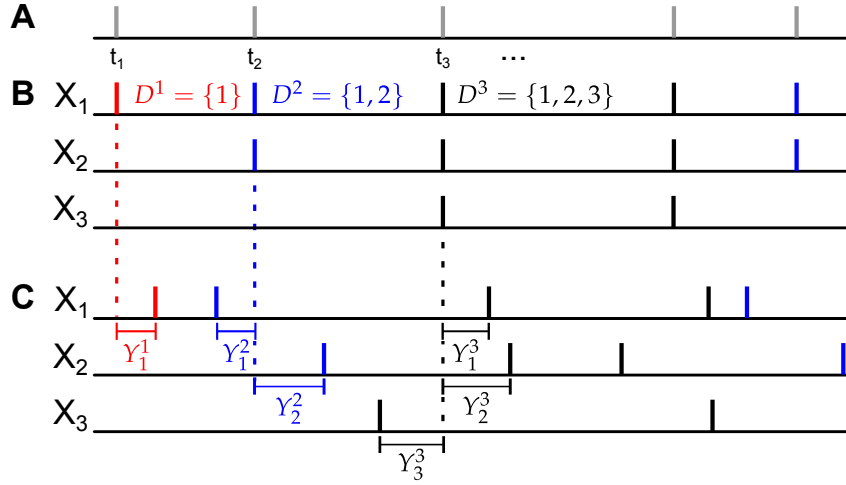


Figure 4.1: **The GTaS simulation protocol.** (A) Step 1: Simulate the mother process - a time-homogeneous Poisson process with event times $\{t^j\}$. (B) Step 2: For each t^j in step 1, select a set $D^j \subset \mathbb{D}$ according to the distribution p_D , and project the event at time t^j to the subsets with indices in D^j . The legend indicates the colors assigned to three possible markings in this example. (C) Step 3: For each pair (t^j, D^j) generated in the previous two steps, draw random vectors Y^j from Q_{D^j} , and shift the event times in the daughter processes by the corresponding values Y_i^j .

4.2 Examples of applications of the GTaS framework

4.2.1 Relation to SIP/MIP processes

Two simple models of correlated, jointly Poisson processes were defined in [156]. The resulting spike trains exhibit spatial correlations, but only instantaneous temporal dependencies. Each model was constructed by starting with independent Poisson processes,

and applying one of two elementary point process operations: superposition and thinning [54]. We show that both models are special cases of the GTaS model.

In the *single interaction process* (SIP), each marginal process X_i is obtained by merging an independent Poisson process with a common, global Poisson process. That is,

$$X_i(\cdot) = Z_i(\cdot) + Z_c(\cdot), \quad i = 1, \dots, N,$$

where Z_c and each Z_i are independent Poisson counting processes on \mathbb{R} with rates λ_c, λ_i , respectively. An SIP model is equivalent to a GTaS model with mother process rate $\lambda = \lambda_c + \sum_{i=1}^N \lambda_i$, and marking probabilities

$$p_D = \begin{cases} \frac{\lambda_i}{\lambda}, & D = \{i\}, \\ \frac{\lambda_c}{\lambda}, & D = \mathbb{D}, \\ 0, & \text{otherwise.} \end{cases}$$

Note that if $\lambda_c = 0$, each spike will be assigned to a different process X_i , resulting in N independent Poisson processes. Lastly, each shift distribution is equal to a delta distribution at zero in every coordinate (i.e., $q_D(y_1, \dots, y_N) \equiv \prod_{i=1}^N \delta(y_i)$ for every $D \subset \mathbb{D}$). Thus, all joint cumulants (among distinct marginal processes) of orders 2 through d are delta functions of equal magnitude, $\lambda p_{\mathbb{D}}$.

The *multiple interaction process* (MIP) consists of N Poisson processes obtained from a common mother process with rate λ_m by *thinning* [54]. The i^{th} daughter process is formed by independent (across coordinates and events) deletion of events from the mother process with probability $p = (1 - \epsilon)$. Hence, an event is common to k daughter processes with probability ϵ^k . Therefore, if we take the perspective of retaining, rather than deleting events, the MIP model is equivalent to a GTaS process with $\lambda = \lambda_m$, and $p_D = \epsilon^{|D|}(1 - \epsilon)^{d-|D|}$. As in the SIP case, the shift distributions are singular in every coordinate.

In Theorem 4.3.3, we present a general result which immediately yields as a corollary that the MIP model has cross-cumulant functions which are δ functions in all dimensions, scaled by ϵ^k , where k is the order of the cross-cumulant.

4.2.2 Generation of synfire-like cascade activity

The GTaS framework provides a simple, tractable way of generating cascading activity where cells fire in a preferred order across the population – as in a synfire chain, but (in general) with variable timing of spikes [2–4, 12, 130]. More generally, it can be used to simulate the activity of *cell assemblies* [17, 42, 108, 113], in which the firing of groups of neurons is likely to follow a particular order.

In the Introduction, we briefly presented one example in which the GTaS framework was used to generate synfire-like cascade activity (see Figure 1.1), and we present another in Figure 4.2. In what follows, we will present the explicit definition of this second model, and then derive explicit expressions for its cumulant structure. Our aim is to illustrate the diverse range of possible correlation structures that can be generated using the GTaS model.

Consider an N -dimensional counting process $\mathbf{X} = (X_1, \dots, X_N)$ of GTaS type, where $N \geq 4$. We restrict the marking distribution so that $p_D \equiv 0$ unless $|D| \leq 2$ or $D = \mathbb{D}$. That is, events are either assigned to a single, a pair, or all daughter processes. For sets D with $|D| = 2$, we set $Q_D \sim \mathcal{N}(0, \Sigma)$ - a Gaussian distributions of zero mean and some specified covariance. The choice of the precise pairwise shift distributions is not important. Shifts of events attributed to a single process have no effect on the statistics of the multivariate process — this will become clear in Section 4.3, where we exhibit that a GTaS process is equivalent in distribution to a sum of independent Poisson processes. In that context,

the shifts of marginal events are applied to the event times of only one of these Poisson processes, which does not impact its statistics.

It remains to define the jitter distribution for events common to the entire population of daughter processes, i.e., events marked by \mathbb{D} . We will show that we can generate cascading activity, and analytically describe the resulting correlation structure. We generate random vectors $\mathbf{Y} \sim Q_{\mathbb{D}}$ according to the following rule, for each $i = 1, \dots, N$:

1. Generate independent random variables $\varphi_i \sim \text{Exp}(\alpha_i)$ where $\alpha_i > 0$.
2. Set $Y_i = \sum_{j=1}^i \varphi_j$.

In particular, note that these shift times satisfy $Y_N \geq \dots \geq Y_2 \geq Y_1 \geq 0$, indicating the chain-like structure of these joint events.

From the definition of the model and our general result given below (see Theorem 4.3.3), we immediately have that $\kappa_{ij}^X(\tau)$, the second order cross-cumulant density for the pair of processes (i, j) , is given by¹

$$\kappa_{ij}^X(\tau) = c_{ij}^2(\tau) + c_{ij}^N(\tau), \quad (4.1)$$

where

$$c_{ij}^2(\tau) = \lambda p_{\{i,j\}} \int q_{\{i,j\}}^{\{i,j\}}(t, t + \tau) dt, \quad c_{ij}^N(\tau) = \lambda p_{\mathbb{D}} \int q_{\mathbb{D}}^{\{i,j\}}(t, t + \tau) dt \quad (4.2)$$

define the contributions to the second order cross-cumulant density by the second-order, Gaussian-jittered events and the population-level events, respectively. Therefore, correlations between spike trains in this case reflect distinct contributions from second order and

¹In the present chapter, we slightly abuse notation — when we reference the cross-cumulant densities κ^X , we are actually referring to the cross-cumulant densities of the point processes associated with the counting processes of \mathbf{X} .

higher order events. The functions $q_D^{D'}$ indicate the densities associated with the distribution Q_D , projected to the dimensions of D' . All statistical quantities are precisely defined in Chapter 2.

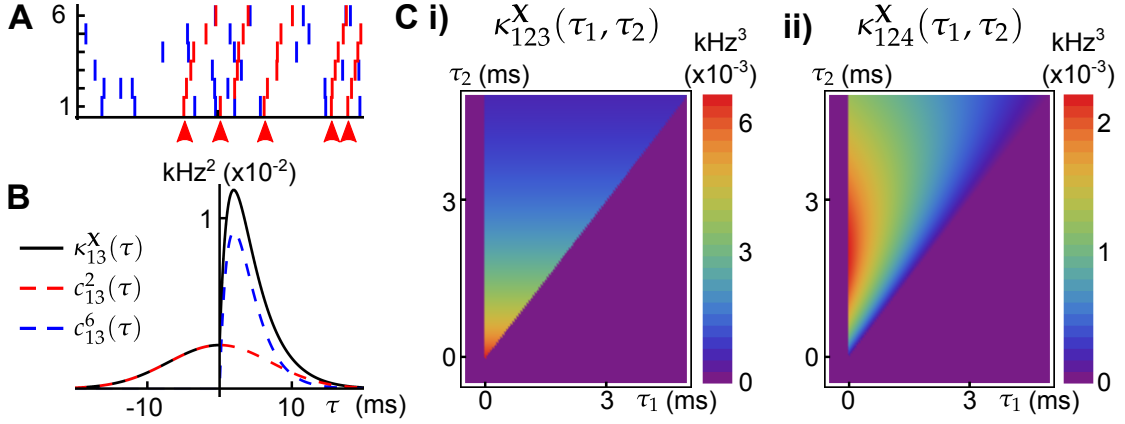


Figure 4.2: **An example of a six dimensional GTaS model exhibiting synfire-like cascading firing patterns.** (A) A raster-plot of spiking activity over a 100ms window. Blue spikes indicate either marginal or pairwise events (i.e., events corresponding to markings for sets $D \subset \mathbb{D}$ with $|D| \leq 2$). Red spikes indicate population-wide events which have shift-times given by cumulative sums of independent exponentials, as described in the text. Arrows indicate the location of the first spike in the cascade. (B) A second-order cross-cumulant κ_{13}^X (black line) of this model is composed of contributions from two sources: correlations due to second-order markings, which have Gaussian shifts (c_{13}^2 – dashed red line), and correlations due to the occurrence of population wide events (c_{13}^6 – dashed blue line). (C) Density plots of the third-order cross-cumulant density for triplets **i)** (1, 2, 3) and **ii)** (1, 2, 4) — the latter is given explicitly in Eq. (4.6).

By exploiting the hierarchical construction of the shift times, we can find an expression for the joint density $q_{\mathbb{D}}$, necessary to explicitly evaluate Eq. (4.1). For a general N -dimensional distribution,

$$f(y_1, \dots, y_N) = f(y_N | y_1, \dots, y_{N-1}) f(y_{N-1} | y_1, \dots, y_{N-2}) \cdots f(y_2 | y_1) f(y_1). \quad (4.3)$$

Since $Y_1 \sim \text{Exp}(\alpha_1)$, we have $f(y_1) = e^{-\alpha_1 y_1} \Theta(y_1)$, where $\Theta(y)$ is the Heaviside step function. Further, as $Y_i | (Y_1, \dots, Y_{i-1}) \sim Y_{i-1} + \text{Exp}(\alpha_i)$ for $i \geq 2$, the conditional densities

of the y_i 's take the form

$$f(y_i|y_1, \dots, y_{i-1}) = f(y_i|y_{i-1}) = \alpha_i e^{-\alpha_i(y_i - y_{i-1})} \Theta(y_i - y_{i-1}), \quad i \geq 2.$$

Substituting this into the identity Eq. (4.3), we have

$$q_{\mathbb{D}}(y_1, \dots, y_N) = \begin{cases} \alpha_1 e^{-\alpha_1 y_1} \prod_{i=2}^N \alpha_i e^{-\alpha_i(y_i - y_{i-1})}, & y_N \geq \dots \geq y_1 \geq 0, \\ 0, & \text{otherwise.} \end{cases} \quad (4.4)$$

Applying Theorem 4.3.3, we obtain the N^{th} order cross-cumulant density,

$$\begin{aligned} \kappa_{1\dots N}^{\mathbf{X}}(\tau_1, \dots, \tau_{N-1}) &= \lambda p_{\mathbb{D}} \int q_{\mathbb{D}}(t, t + \tau_1, \dots, t + \tau_{N-1}) \\ &= \lambda p_{\mathbb{D}} \cdot \begin{cases} \prod_{i=1}^{N-1} \alpha_{i+1} e^{-\alpha_{i+1}(\tau_i - \tau_{i-1})}, & \tau_i \geq \tau_{i-1} \forall i, \\ 0, & \text{otherwise,} \end{cases} \end{aligned} \quad (4.5)$$

where, for notational convenience, we define $\tau_0 = 0$. A raster plot of a realization of this model is shown in Figure 4.2A. We note that the cross-cumulant densities of arbitrary subcollections of the counting processes \mathbf{X} can be obtained by finding the appropriate marginalization of $q_{\mathbb{D}}$ via integration of Eq. (4.4).

As a particular example, we consider the cross-cumulant density of the marginal processes X_1, X_3 . Using Eqs. (4.2, 4.4), we find

$$c_{13}^N(\tau) = \lambda p_{\mathbb{D}} \Theta(\tau) \cdot \begin{cases} \frac{\alpha_2 \alpha_3}{\alpha_3 - \alpha_2} [e^{-\alpha_2 \tau} - e^{-\alpha_3 \tau}], & \alpha_2 \neq \alpha_3, \\ \alpha_2 \alpha_3 \tau e^{-\alpha_2 \tau} & \alpha_2 = \alpha_3. \end{cases}$$

An expression for $c_{13}^2(\tau)$ can be obtained similarly using Eq. (4.2) and recalling that $Q_{\{i,j\}} \equiv \mathcal{N}(0, \Sigma)$ for all i, j . In Figure 4.2B, we plot these contributions, as well as the full covariance density.

Similar calculations at third order yield, as an example,

$$\kappa_{124}^X(\tau_1, \tau_2) = \lambda p_{\mathbb{D}} \cdot \begin{cases} \frac{\alpha_2 \alpha_3 \alpha_4}{\alpha_4 - \alpha_3} e^{-\alpha_2 \tau_1} \left[e^{-\alpha_3(\tau_2 - \tau_1)} - e^{-\alpha_4(\tau_2 - \tau_1)} \right], & \alpha_3 \neq \alpha_4, \\ \alpha_2 \alpha_3 \alpha_4 (\tau_2 - \tau_1) e^{-\alpha_2 \tau_1 - \alpha_3(\tau_2 - \tau_1)}, & \alpha_3 = \alpha_4, \end{cases} \quad (4.6)$$

where the cross-cumulant density $\kappa_{124}^X(\tau_1, \tau_2)$ is supported only on $\tau_2 \geq \tau_1 \geq 0$. Plots of the third-order cross-cumulants for triplets (1, 2, 3) and (1, 2, 4) in this model are shown in Figure 4.2C. Note that, for the specified parameters, the conditional distribution of Y_4 — the shift applied to the events of X_4 in a joint population event — given Y_2 follows a gamma distribution, whereas $Y_3|Y_2$ follows an exponential distribution, explaining the differences in the shapes of these two cross-cumulant densities.

General cross-cumulant densities of at least third order for the cascading model will have a form similar to that given in Eq. (4.6), and will contain no signature of the correlation of strictly second order events. This highlights a key benefit of cumulants as a measure of dependence: although they agree with central moments up to third order, we know from Eq. (2.2) (or Eq. (2.1) in the general case) that central moments necessarily exhibit a dependence on lower order statistics. On the other hand, cumulants are “pure” and quantify only dependencies at the given order which cannot be inferred from lower order statistics [94].

One useful statistic for analyzing population activity through correlations is the *population cumulant density* [173]. The second order population cumulant density for cell i is defined by (see Eq. (2.15))

$$\kappa_{i,\text{pop}}^X(\tau) = \sum_{j \neq i} \kappa_{ij}^X(\tau).$$

This function is linearly related to the spike-triggered average of the population activity conditioned on that of cell i . In Figure 4.3 we show three different second-order population-cumulant functions for the cascading GTaS model of Figure 4.2A. When the

second order population cumulant for a neuron is skewed to the right of $\tau = 0$ (as is $\kappa_{1,\text{pop}}^X$ — blue line), a neuron tends to precede other cells in the population in pairwise spiking events. Similarly, skewness to the left of $\tau = 0$ ($\kappa_{6,\text{pop}}^X$ — orange line) indicates a neuron which tends to trail other cells in the population in such events. A symmetric population cumulant density indicates a neuron is a follower *and* a leader. Taken together, these three second order population cumulants hint at the chain structure of the process.

Greater understanding of the joint temporal statistics in a multivariate counting process can be obtained by considering higher-order population cumulant densities. From Eq. (2.15), we define the third-order population cumulant density for the pair (i, j) to be

$$\kappa_{ij,\text{pop}}^X(\tau_1, \tau_2) = \sum_{k \neq i,j} \kappa_{ijk}^X(\tau_1, \tau_2).$$

The third-order population cumulant density is linearly related to the spike-triggered population activity, conditioned on spikes in cells i and j separated by a delay τ_1 . In Figure 4.3B,C,D, we present three distinct third-order population cumulant densities. Examining $\kappa_{12,\text{pop}}^X(\tau_1, \tau_2)$ (panel B), we see only contributions in the region $\tau_2 > \tau_1 > 0$, indicating that the pairwise event $1 \rightarrow 2$ often precedes a third spike elsewhere in the population. The population cumulant $\kappa_{34,\text{pop}}^X(\tau_1, \tau_2)$ has contributions in two sections of the plane (panel C). Contributions in the region $\tau_2 > \tau_1 > 0$ can be understood following the preceding example, while contributions in the region $\tau_2 < 0 < \tau_1$ imply that the firing of other neurons tends to precede the joint firing event $3 \rightarrow 4$. Lastly, contributions to $\kappa_{16,\text{pop}}^X(\tau_1, \tau_2)$ (panel D) are limited to $0 < \tau_2 < \tau_1$, indicating an above chance probability of joint firing events of the form $1 \rightarrow i \rightarrow 6$, where i indicates a distinct neuron within the population.

A distinct advantage of the study of population cumulant densities as opposed to individual cross-cumulant functions in practical applications is related to data (i.e., sample

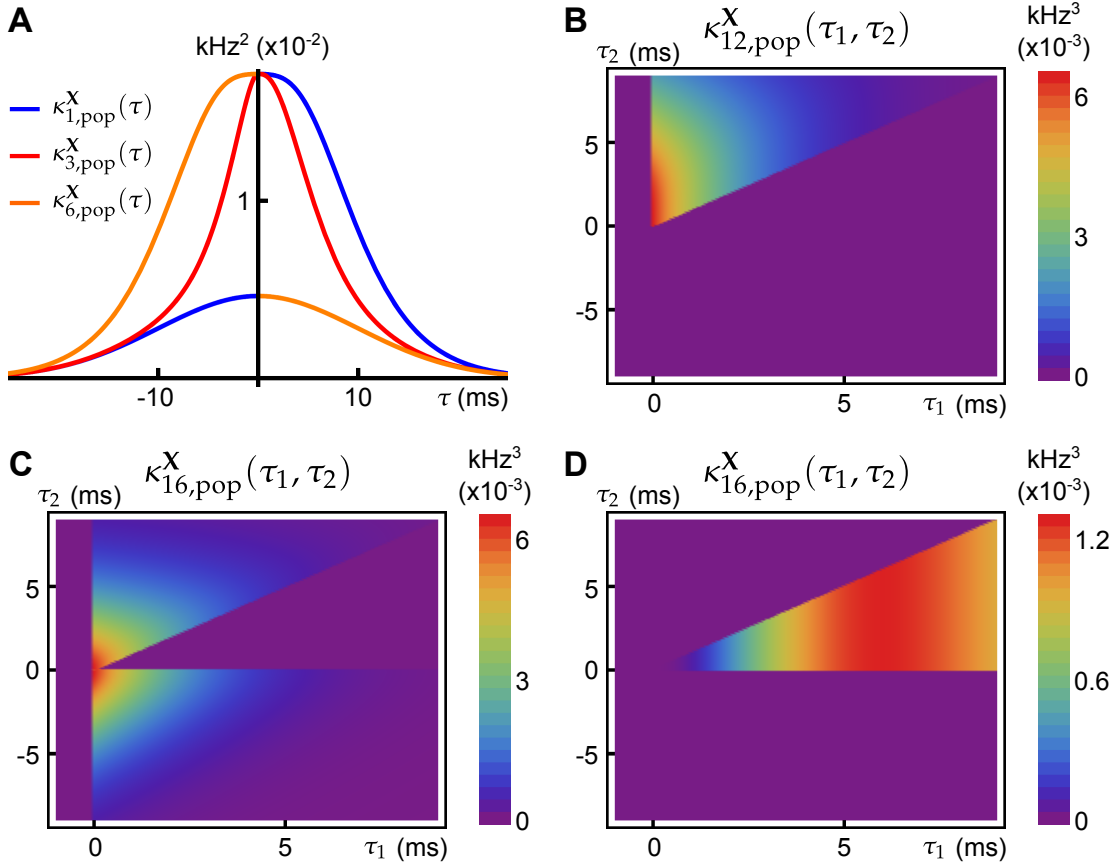


Figure 4.3: **Population cumulants for the synfire-like cascading GTaS process of Figure 4.2.** (A) Second order population cumulant densities for processes 1,3 and 6. Greater mass to the right (resp. left) of $\tau = 0$ indicates that a cell tends to lead (resp. follow) in pairwise-correlated events. (B) Third order population cumulant for processes X_1, X_2 in the cascading GTaS process. Concentration of the mass in different regions of the plane indicates temporal structure of events correlated between X_1, X_2 relative to the remainder of the population (see the text). (C) Same as (B), but for processes X_3, X_4 . (D) Same as (B), but for processes X_1, X_6 . Population cumulants are defined in Eq. (2.15).

size) limitations. In many practical applications, where the temporal structure of a collection of observed point processes is of interest, we often deal with a small, noisy samples. As a result, it can be difficult to estimate third- or higher-order cumulants. Population cumulants partially circumvent this issue by *pooling* [232, 233, 271] (or summing) responses, to amplify existing correlations and average out the noise in measurements.

We conclude this section by noting that even cascading GTaS examples can be much more general. For instance, we can include more complex shift patterns, overlapping subassemblies within the population, different temporal processions of the cascade, and more.

4.2.3 Timing-selective network

The responses of single neurons and neuronal networks in experimental [17, 184, 254] and theoretical studies [95, 125, 135, 138, 274] can reflect the temporal structure of their inputs. Here, we present a simple example that shows how a network can be selective to fine temporal features of its input, and how the GTaS model can be used to explore such examples.

4.2.3.1 Model definition

As a general network model, we consider N leaky integrate-and-fire (LIF) neurons with membrane potentials V_i obeying (see Section 3.1)

$$\frac{dV_i}{dt} = -V_i + \sum_{j=1}^N w_{ij}(\alpha * z_j)(t) + w^{\text{in}}x_i(t), \quad i = 1, \dots, N. \quad (4.7)$$

When the membrane potential of cell i reaches a threshold V_{th} , an output spike is recorded and the membrane potential is reset to zero, after which evolution of V_i resumes the dynamics in Eq. (4.7). Here w_{ij} is the synaptic weight of the connection from cell j to i , w^{in} is the input weight, and we assume time to be measured in units of membrane time constants. The function $\alpha(t) = \tau_{\text{syn}}^{-1}e^{-(t-\tau_d)/\tau_{\text{syn}}}\Theta(t - \tau_d)$ is a delayed, unit-area exponential synaptic kernel with time-constant τ_{syn} and delay τ_d . The output of the i^{th} neuron is

$$z_i(t) = \sum_j \delta(t - t_i^j),$$

where t_i^j is the time of the j^{th} spike of neuron i . In addition, the input $\{x_i\}_{i=1}^N$ is

$$x_i(t) = \sum_j \delta(t - s_i^j),$$

where the event times $\{s_i^j\}$ correspond to those of a GTaS counting process \mathbf{X} . Thus, each input spike results in a jump in the membrane potential of the corresponding LIF neuron of amplitude w^{in} . The particular network we consider will have a ring topology (nearest neighbor-only connectivity) — specifically, for $i, j = 1, \dots, N$, we let

$$w_{ij} = \begin{cases} w^{\text{syn}}, & i - j \pmod N \equiv 1 \text{ or } N - 1, \\ 0, & \text{otherwise.} \end{cases}$$

We further assume that all neurons are *excitatory*, so that $w^{\text{syn}} > 0$.

A network of LIF neurons with synaptic delay is a minimal model which can exhibit fine-scale discrimination of temporal patterns of inputs without precise tuning [133] (that is, without being carefully designed to do so, with great sensitivity to modification of network parameters). To exhibit this dependence we generate inputs from two GTaS processes. The first (the *cascading model*) was described in the preceding example. To independently control the mean and variance of relative shifts we replace the sum of exponential shifts with sums of gamma variates. We also consider a model featuring population-level events without shifts (the *synchronous model*), where the distribution $Q_{\mathbb{D}}$ is a δ distribution at zero in all coordinates.

The only difference between the two input models is in the temporal structure of joint events. In particular, the rates, and all long timescale spike count cross-cumulants (equivalent to the total “area” under the cross-cumulant density, see Eq. (2.18)) of order two and higher are identical for the two processes. We focus on the sensitivity of the network to the temporal cumulant structure of its inputs.

In Figure 4.4A,B, we present two example rasters of the nearest-neighbor LIF network receiving synchronous (left) and cascading (right) input. In the second case, there is an obvious pattern in the outputs, but the firing rate is also increased. This is quantified in Figure 4.4C, where we compare the number of output spikes fired by a network receiving synchronous input (horizontal axis) with the same for a network receiving cascading input (vertical axis), over a large number of trials. On average, the cascading input increases the output rate by a factor of 1.5 over the synchronous inputs — we refer to this quantity as the *cascade amplification factor* (CAF).

Finally, in Figure 4.4D, we illustrate how the the cascade amplification factor depends on the parameters that define the timing of spikes for the cascading inputs. First, we study the dependence on the standard deviation σ_{shift} of the gamma variates determining the shift distribution. We note that amplification factors above 1.5 hold robustly (i.e., for a range of shift σ_{shift} values). The amplification factors decrease with shift variance. In the inset to panel D, we show how the gain depends on the mean of the shift distribution μ_{shift} . On an individual trial, the response intensity will depend strongly on the total number of input spikes. Thus, in order to enforce a fair comparison, the mother process and markings used were identical in each trial of every panel of Figure 4.4. We note that network properties, such as the membrane properties of individual cells or synaptic timescales, can have an equally large impact on the cascade amplification factor — indeed, as we explain below, the observed behavior of the CAF is a result of synergy between the timescales of input and interactions within the network.

These observations have simple explanations in terms of the network dynamics and input statistics. Neglecting, for a moment, population-level events, the network is configured so that correlations in activity decrease with topographic distance. Accordingly, the

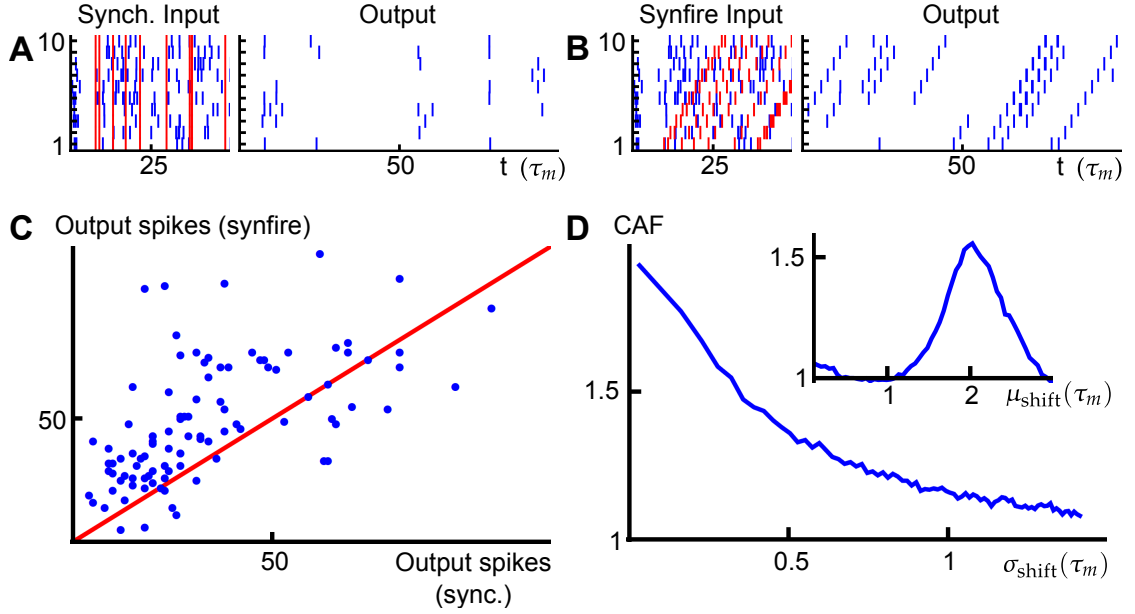


Figure 4.4: Using the GTaS model to probe a timing-selective network. (A) Example input (left) and output (right) for the nearest neighbor LIF network receiving input with synchronous input. (B) Same as (A), but for cascading input. (C) Scatter plot of the output spike count of the network receiving synchronous (horizontal axis) and cascading input (vertical axis) with $\mu_{\text{shift}} = 2$, $\sigma_{\text{shift}} = 0.3$. The red line is the diagonal. (D) Average gain (rate in response to cascading input divided by rate in response to synchronous input) as a function of the standard deviation of the gamma variates which compose the shift vectors for population-level events (μ_{shift} was fixed at 2). The red dot indicates the value of σ_{shift} used in panel C. Inset shows the same gain as panel D, but for varying the mean of the shift distribution ($\sigma_{\text{shift}} = 0.3$). Spike counts in panels C and D were obtained for trials of length $T = 100$.

probability of finding neurons that are simultaneously close to threshold also decreases with distance. Under the synchronous input model, a population-level event results in a simultaneous increase of the membrane potentials of all neurons by an amount w^{in} , but unless the input is very strong (in which case every, or almost every, neuron will fire regardless of fine-scale input structure), the set of neurons sufficiently close to threshold to “capitalize” on the input and fire will typically be restricted to a topographically adjacent subset. Neurons which do not fire almost immediately will soon have forgotten about this

population-level input. As a result, the output does not significantly reflect the chain-like structure of the inputs (Figure 4.4A, right).

On the other hand, in the case of the cascading input, the temporal structure of the input and the timescale of synapses can operate synergistically. Consider a pair of adjacent neurons in the ring network, called cells 1 and 2, arranged so that cell 2 is downstream from cell 1 in the direction of the population-level chain events. When cell 1 spikes, it is likely that cell 2 will also have an elevated membrane potential. The potential is further elevated by the delayed synaptic input from cell 1. If cell 1 spikes in response to a population-level chain event, then cell 2 imminently receives an input spike as well. If the synaptic filter and time-shift of the input spikes to each cell align, then the firing probability of cell 2 will be large relative to chance. This reasoning can be carried on across the network. Hence, synergy between the temporal structure of inputs and network architecture allows the network to selectively respond to the temporal structure of the inputs (Figure 4.4B, right).

In [156], the effect of higher order correlations on the firing rate gain of an integrate-and-fire neuron was studied by driving single cells using sums of SIP or MIP processes with equivalent firing rates (first order cumulants) and pairwise correlations (second order cumulants). In contrast, in the preceding example, the two inputs have equal long time spike count cumulants, and differ only in temporal correlation structure. An increase in firing rate was due to network interactions, and is, therefore, a population level effect. We return to this comparison in the Discussion.

These examples demonstrate how the GTaS model can be used to explore the impact of spatio-temporal structure in population activity on network dynamics. We next proceed with a formal derivation of the cumulant structure for a general GTaS process.

4.3 Cumulant structure of a GTaS process

The GTaS model defines an N -dimensional counting process. Following the standard description for a counting process, $\mathbf{X} = (X_1, \dots, X_N)$ on \mathbb{R}^N , given a collection of Borel subsets $A_i \in \mathcal{B}(\mathbb{R}), i = 1, \dots, N$, then $\mathbf{X}(A_1 \times \dots \times A_N) = (X_1(A_1), \dots, X_N(A_N)) \in \mathbb{N}^N$ is a random vector where the value of each coordinate i indicates the (random) number of points which fall inside the set A_i .

Note that the GTaS model defines processes that are marginally Poisson: For each $D \subset \mathbb{D} = \{1, \dots, N\}$, define the tail probability \bar{p}_D by

$$\bar{p}_D = \sum_{D \subset D' \subset \mathbb{D}} p_{D'}. \quad (4.8)$$

Since p_D is the probability that exactly the processes in D are marked, \bar{p}_D is the probability that all processes in D , as well as possibly other processes, are marked. An event from the mother process is assigned to daughter process X_i with probability $\bar{p}_{\{i\}}$. As noted in the presentation of the simulation protocol for the GTaS process (see Section 4.1.1), an event attributed to process i following a marking $D \ni i$ will be marginally shifted by a random amount determined by the distribution $Q_D^{\{i\}}$ which represents the projection of Q_D onto dimension i . Thus, the events in the marginal process X_i are shifted in an independent and identically distributed (IID) manner according to the mixture distribution Q_i given by

$$Q_i = \frac{\sum_{D \ni i} p_D Q_D^{\{i\}}}{\sum_{D \ni i} p_D}.$$

Note that IID shifting of the event times of a Poisson process generates another Poisson process of identical rate [234]. As a result, the process X_i is marginally Poisson with rate $\lambda \bar{p}_{\{i\}}$.

In deriving the statistics of the GTaS counting process \mathbf{X} , it will be useful to express

the distribution of \mathbf{X} as

$$\begin{pmatrix} X_1(A_1) \\ \vdots \\ X_N(A_N) \end{pmatrix} =_{\text{distr}} \begin{pmatrix} \sum_{D \ni 1} \xi(D; A_1, \dots, A_N) \\ \vdots \\ \sum_{D \ni N} \xi(D; A_1, \dots, A_N) \end{pmatrix}. \quad (4.9)$$

Here, each $\xi(D; A_1, \dots, A_N)$ is an independent Poisson process. This process counts the number of points which are marked by a set $D' \supset D$, but (after shifting) only the points with indices $i \in D$ lie in the corresponding set A_i . Precise definitions of the processes ξ and a proof of Eq. (4.9) are the subject of Theorem 4.3.1. We emphasize that the Poisson processes $\xi(D)$ do not directly count points marked for the set D , but instead points which are marked for a set containing D that, after shifting, only have their D -components lying in the corresponding sets A_i .

Suppose we are interested in calculating dependencies among a subset of daughter processes, $\{X_{i_j}\}_{i_j \in \bar{D}}$ for some set $\bar{D} \subset \mathbb{D}$, consisting of $|\bar{D}| = k$ distinct members of the collection of counting processes \mathbf{X} . The random vector consisting of the processes in this subset can be decomposed via an equality in distribution as

$$\begin{pmatrix} X_{i_1}(A_{i_1}) \\ \vdots \\ X_{i_k}(A_{i_k}) \end{pmatrix} =_{\text{distr}} \begin{pmatrix} \sum_{i_1 \in D \subset \bar{D}} \zeta_D(A_1, \dots, A_N) \\ \vdots \\ \sum_{i_k \in D \subset \bar{D}} \zeta_D(A_1, \dots, A_N) \end{pmatrix}, \quad (4.10)$$

where

$$\zeta_D(A_1, \dots, A_N) = \sum_{\substack{D' \supset D \\ (\bar{D} \setminus D) \cap D' = \emptyset}} \xi(D'; A_1, \dots, A_N).$$

We illustrate this decomposition in the cases $k = 2, 3$ in Figure 4.5. The sums in Eq. (4.10) run over all sets $D \subset \mathbb{D}$ containing the indicated indices i_j and contained within \bar{D} . The processes ζ_D are comprised of a sum of all of the processes $\xi(D')$ (described below Eq. (4.9) and precisely defined in Theorem 4.3.1) such that D' contains all of the indices D ,

but no other indices which are part of the subset \bar{D} under consideration. These sums are non-overlapping, implying that the ζ_D are also independent and Poisson.

The following examples elucidate the meaning and significance of Eq. (4.10). We emphasize that the GTaS process is a completely characterized, joint Poisson process, and we use Eq. (4.10) to calculate cumulants of a GTaS process. In principle, any other statistics can be obtained similarly.

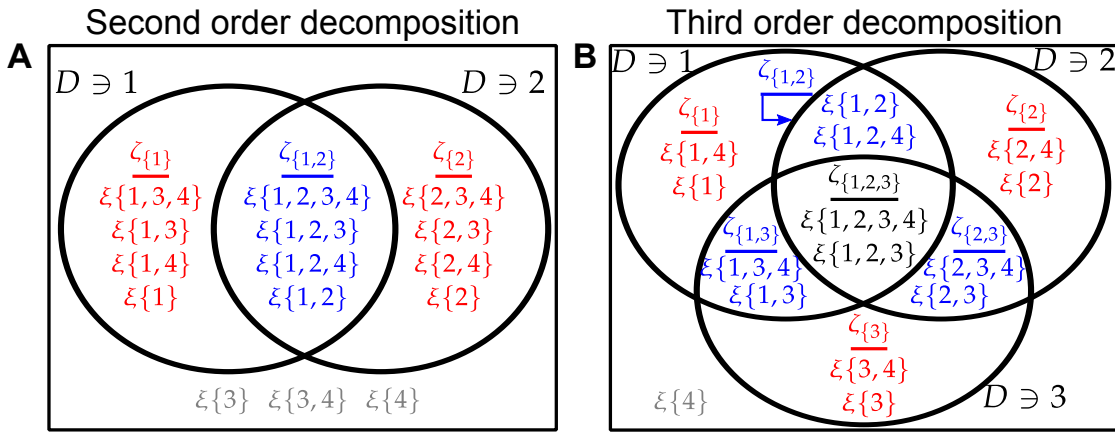


Figure 4.5: **Illustrating the representation given by Eq. (4.10)** . **(A)** Performing the decomposition at second order ($\bar{D} = \{1, 2\}$, see Eq. (4.11) and the surrounding discussion) with $N = 4$. **(B)** Same as panel A, but for three processes with $\bar{D} = \{1, 2, 3\}$ (see Eq. (4.16) and the surrounding discussion).

4.3.1 Second order cumulants (covariance)

We first generalize a well-known result about the dependence structure of temporally jittered pairs of Poisson processes, X_1, X_2 . Assume that events from a mother process with rate λ , are assigned to two daughter processes with probability p . Each event time

is subsequently shifted independently according to a univariate distribution f . The cross-cumulant density then has the form [35]

$$\kappa_{12}^X(\tau) = \lambda p \int f(t)f(t + \tau)dt = \lambda p(f \star f)(\tau).$$

We generalize this result within the GTaS framework. At second order, Eq. (4.10) has a particularly nice form. Following [19] we write for $i \neq j$ (see Figure 4.5A)

$$\begin{pmatrix} X_i(A_i) \\ X_j(A_j) \end{pmatrix} =_{\text{distr}} \begin{pmatrix} \zeta_{\{i,j\}}(A_i, A_j) + \zeta_{\{i\}}(A_i) \\ \zeta_{\{i,j\}}(A_i, A_j) + \zeta_{\{j\}}(A_j) \end{pmatrix}. \quad (4.11)$$

The process $\zeta_{\{i,j\}}$ sums all $\xi(D')$ for which $\{1, 2\} \subset D'$, while the process $\zeta_{\{i\}}$ sums all $\xi(D')$ such that $i \in D', j \notin D'$, and $\zeta_{\{j\}}$ is defined likewise.

Using the representation in Eq. (4.11), we can derive the second order cumulant (covariance) structure of a GTaS process. First, we have

$$\begin{aligned} \mathbf{cov} [X_i(A_i), X_j(A_j)] &= \kappa[X_i(A_i), X_j(A_j)] \\ &= \kappa[\zeta_{\{i,j\}}(A_i, A_j), \zeta_{\{i,j\}}(A_i, A_j)] + \kappa[\zeta_{\{i\}}(A_i), \zeta_{\{i,j\}}(A_i, A_j)] \\ &\quad + \kappa[\zeta_{\{i,j\}}(A_i, A_j), \zeta_{\{j\}}(A_j)] + \kappa[\zeta_{\{i\}}(A_i), \zeta_{\{j\}}(A_j)] \\ &= \kappa_2[\zeta_{\{i,j\}}(A_i, A_j)] + 0 \\ &= \mathbf{E} [\zeta_{\{i,j\}}(A_i, A_j)]. \end{aligned}$$

The third equality follows from the construction of the processes ζ_D : if $D \neq D'$, then the processes $\zeta_D, \zeta_{D'}$ are independent. The final equality follows from the observation that every cumulant of a Poisson random variable equals its mean.

The covariance can be further expressed in terms of model parameters (see Theorem 4.3.3 for a generalization of this result to arbitrary cumulant orders):

$$\mathbf{cov} [X_i(A_i), X_j(A_j)] = \lambda \sum_{D' \supset \{i,j\}} p_{D'} \int P(t + Y_i \in A_i, t + Y_j \in A_j \mid \mathbf{Y} \sim Q_{D'}) dt. \quad (4.12)$$

In other words, the covariance of the counting processes is given by the weighted sum of the probabilities that the (i, j) marginal of the shift distributions yield values in the appropriate sets. The weights are the intensities of each corresponding component processes $\xi(D)$ which contribute events to both of the processes i and j .

In the case that $Q_D \equiv Q$, Eq. (4.12) reduces to the solution given in [19]. Using the tail probabilities defined in Eq. (4.8), if $Q_D \equiv Q$ for all D , the integral in Eq. (4.12) no longer depends on the subset D' , and the equation can be written as

$$\mathbf{cov} [X_i(A_i), X_j(A_j)] = \lambda \bar{p}_{\{i,j\}} \int P(t + Y_i \in A_i, t + Y_j \in A_j \mid \mathbf{Y} \sim Q) dt.$$

Using Eq. (4.12), we can also compute the second order cross-cumulant density of the processes. From the definition of the cross-cumulant density (see Eq. (2.13)), this is given by

$$\begin{aligned} \kappa_{ij}^X(\tau) &= \lim_{\Delta t \rightarrow 0} \frac{\mathbf{cov} [X_i([0, \Delta t]), X_j([\tau, \tau + \Delta t])] }{\Delta t^2} \\ &= \lambda \sum_{D' \supset \{i,j\}} p_{D'} \int \lim_{\Delta t \rightarrow 0} \frac{P(t + Y_i \in [0, \Delta t], t + Y_j \in [\tau, \tau + \Delta t] \mid \mathbf{Y} \sim Q_{D'})}{\Delta t^2} dt. \end{aligned} \quad (4.13)$$

Before continuing, we note that given a random vector $\mathbf{Y} = (Y_1, \dots, Y_N) \sim Q$, where Q has density $q(y_1, \dots, y_N)$, the vector $\mathbf{Z} = (Y_2 - Y_1, \dots, Y_N - Y_1)$ has density q_Z given by

$$q_Z(\tau_1, \dots, \tau_{N-1}) = \int q(t, t + \tau_1, \dots, t + \tau_{N-1}) dt. \quad (4.14)$$

Assuming that the distributions $Q_{D'}$ have densities $q_{D'}$, and denoting by $q_{D'}^{\{i,j\}}$ the bivariate marginal density of the variables Y_i, Y_j under $Q_{D'}$, we have that

$$\kappa_{ij}^X(\tau) = \lambda \sum_{D' \supset \{i,j\}} p_{D'} \int q_{D'}^{\{i,j\}}(t, t + \tau) dt. \quad (4.15)$$

According to Eq. (4.14), the integrals present in Eq. (4.15) are simply the densities of the variables $Y_j - Y_i$, where $\mathbf{Y} \sim Q_{D'}$.

Thus, the cross-cumulant density $\kappa_{ij}^X(\tau)$, which captures the additional probability for events in the marginal processes X_i and X_j separated by τ units of time beyond what can be predicted from lower order statistics is given by a weighted sum (in this case, the lower order statistics are marginal intensities — see Eq. (2.14) and the surrounding discussion). The weights are the “marking rates” $\lambda p_{D'}$ for markings contributing events to both component processes, while the summands are the probabilities that the corresponding shift distributions yield a pair of shifts in the proper arrangement - specifically, the shift applied to the event as attributed to X_i precedes that applied to the event mapped to X_j by τ units of time. This interpretation of the cross-cumulant density is quite natural, and will carry over to higher order cross-cumulants of a GTaS process. However, as we show next, this extension is not trivial at higher cumulant orders.

4.3.2 Third order cumulants

To determine the higher order cumulants for a GTaS process, one can again use the representation given in Eq. (4.10). The distribution of a subset of three processes can be expressed in the form (see Figure 4.5B)

$$\begin{pmatrix} X_i(A_i) \\ X_j(A_j) \\ X_k(A_k) \end{pmatrix} =_{\text{distr}} \begin{pmatrix} \zeta_{\{i,j,k\}} + \zeta_{\{i,j\}} + \zeta_{\{i,k\}} + \zeta_{\{i\}} \\ \zeta_{\{i,j,k\}} + \zeta_{\{i,j\}} + \zeta_{\{j,k\}} + \zeta_{\{j\}} \\ \zeta_{\{i,j,k\}} + \zeta_{\{i,k\}} + \zeta_{\{j,k\}} + \zeta_{\{k\}} \end{pmatrix}, \quad (4.16)$$

where, for simplicity, we suppressed the arguments of the different ζ_D on the right hand side. Again, the processes in the representation are independent and Poisson distributed. The variable $\zeta_{\{i,j,k\}}$ is the sum of all random variables $\xi(D)$ (see Eq. (4.9)) with $D \supset \{i, j, k\}$, while the variable $\zeta_{\{i,j\}}$ is now the sum of all $\xi(D)$ with $D \supset \{i, j\}$, but $k \notin D$. The rest of the variables are defined likewise. Using properties (C1) and (C2) of cumulants

given in Chapter 2, and assuming that i, j, k are distinct indices, we have

$$\kappa(X_i(A_i), X_j(A_j), X_k(A_k)) = \kappa_3(\zeta_{\{i,j,k\}}) = \mathbf{E} \left[\zeta_{\{i,j,k\}} \right].$$

The second equality follows from the fact that all cumulants of a Poisson distributed random variable equal its mean. Similar to Eq. (4.12), we can write

$$\begin{aligned} \kappa(X_i(A_i), X_j(A_j), X_k(A_k)) = \\ \lambda \sum_{D' \supset \{i,j,k\}} p_{D'} \int P(t + Y_i \in A_i, t + Y_j \in A_j, t + Y_k \in A_k \mid \mathbf{Y} \sim Q_{D'}) dt. \end{aligned}$$

The third cross-cumulant density is then given similarly to the second order function by

$$\kappa_{ijk}^{\mathbf{X}}(\tau_1, \tau_2) = \lambda \sum_{D' \supset \{i,j,k\}} p_{D'} \int q_{D'}^{\{i,j,k\}}(t, t + \tau_1, t + \tau_2) dt.$$

Here, we have again assumed the existence of densities $q_{D'}$, and denoted by $q_{D'}^{\{i,j,k\}}$ the joint marginal density of the variables Y_i, Y_j, Y_k under $q_{D'}$. The integrals appearing in the expression for the third order cross-cumulant density are the probability densities of the vectors $(Y_j - Y_i, Y_k - Y_i)$, where $\mathbf{Y} \sim Q_{D'}$.

4.3.3 General cumulants

In Theorem 4.3.3 below, we will establish the general form of a cross-cumulant for a GTaS process in terms of model parameters. Before this, however, we need to establish an extension of the distributional representation result given by [19]. This is the subject of Theorem 4.3.1.

Some definitions are required: first, for subsets $A_1, \dots, A_N \in \mathcal{B}(\mathbb{R})$ and $D, D' \subset \mathbb{D}$

with $D \subset D'$, let

$$M(D, D'; A_1, \dots, A_N) := B_1 \times \dots \times B_N \text{ with } B_i := \begin{cases} A_i, & \text{for } i \in D, \\ A_i^c, & \text{for } i \in D' \setminus D, \\ \mathbb{R}, & \text{otherwise.} \end{cases}$$

In addition, setting $\mathbf{1} = (1, \dots, 1)$ to be the N -dimensional vector with all components equal to unity, and if Q_D is a measure on \mathbb{R}^N , then we define the measure $\nu(Q_D)$ by

$$\begin{aligned} \nu(Q_D)(A) &:= \int Q_D(A - t\mathbf{1}) dt \quad \text{for } A \in \mathcal{B}(\mathbb{R}^N) \\ &= \int P(\mathbf{Y} + t\mathbf{1} \in A | \mathbf{Y} \sim Q_D) dt. \end{aligned} \tag{4.17}$$

The measure $\nu(Q_D)$ can be interpreted as giving the *expected* Lebesgue measure of the subset L of \mathbb{R} for which uniform shifts by the elements of L translate a random vector $\mathbf{Y} \sim Q_D$ into A . Heuristically, one can imagine sliding the vector \mathbf{Y} over the whole real line, and counting the number of times every coordinate ends up in the “right” set — the projection of A onto that dimension. In equation form, this means that the measure $\nu(Q_D)$ can be written

$$\nu(Q_D)(A) = \mathbf{E}_{\mathbf{Y}}[\ell(\{t \in \mathbb{R} : \mathbf{Y} + t\mathbf{1} \in A\}) | \mathbf{Y} \sim Q_D],$$

where the subscript \mathbf{Y} indicates that we take the average over the distribution of $\mathbf{Y} \sim Q_D$.

Theorem 4.3.1. *Let \mathbf{X} be an N -dimensional counting process of GTaS type with base rate λ , thinning mechanism $p = (p_D)_{D \subset \mathbb{D}}$, and family of shift distributions $(Q_D)_{D \subset \mathbb{D}}$. Then, for any Borel subsets A_1, \dots, A_N of the real line, we have the following distributional representation:*

$$\begin{pmatrix} X_1(A_1) \\ \vdots \\ X_N(A_N) \end{pmatrix} \stackrel{=}{\text{distr}} \begin{pmatrix} \sum_{D \ni 1} \xi(D; A_1, \dots, A_N) \\ \vdots \\ \sum_{D \ni d} \xi(D; A_1, \dots, A_N) \end{pmatrix}, \tag{4.18}$$

4.3. CUMULANT STRUCTURE OF A GTAS PROCESS

where the random variables $\xi(D; A_1, \dots, A_N), \emptyset \neq D \subset \mathbb{D}$, are independent and Poisson distributed with

$$\mathbf{E} [\xi(D; A_1, \dots, A_N)] = \lambda \sum_{D' \supset D} p_{D'} \nu(Q_{D'}) (M(D, D'; A_1, \dots, A_N)).$$

Before providing the proof of Theorem 4.3.1, we give Theorem 1 of [19], necessary for what follows, as Lemma 4.3.2.

Lemma 4.3.2. *Let \mathbf{X} be an N -dimensional counting process of TaS type with base rate λ , thinning mechanism $p = (p_D)_{D \subset \mathbb{D}}$, and shift distribution Q . Then, for any borel subsets A_1, \dots, A_N of the real line, we have the following distributional representation:*

$$\begin{pmatrix} X_1(A_1) \\ \vdots \\ X_N(A_N) \end{pmatrix} =_{\text{distr}} \begin{pmatrix} \sum_{D \ni 1} \xi(D; A_1, \dots, A_N) \\ \vdots \\ \sum_{D \ni N} \xi(D; A_1, \dots, A_N) \end{pmatrix},$$

where the random variables $\xi(D; A_1, \dots, A_N), \emptyset \neq D \subset \mathbb{D}$, are independent and Poisson distributed with

$$\mathbf{E} [\xi(D; A_1, \dots, A_N)] = \lambda \sum_{D' \supset D} p_{D'} \nu(Q) (M(D, D'; A_1, \dots, A_N)).$$

Proof. For each marking $D' \subset \mathbb{D}$, define $\mathbf{X}^{D'}$ to be an independent TaS [19] counting process with mother process rate $\lambda p_{D'}$, shift distribution $Q_{D'}$, and markings $(p_D^{D'})_{D \subset \mathbb{D}}$ where $p_D^{D'} = 1$ if $D = D'$ and is zero otherwise (i.e., the only possible marking for $\mathbf{X}^{D'}$ is D'). We first claim that

$$\mathbf{X} =_{\text{distr}} \sum_{D'} \mathbf{X}^{D'}. \quad (4.19)$$

To see this, note that spikes in the mother process of the GTaS process of \mathbf{X} marked for a set D' occur at a rate $\lambda p_{D'}$, which is the rate of the process $\mathbf{X}^{D'}$. In addition, these event

times are then shifted by $Q_{D'}$, exactly as they are for $\mathbf{X}^{D'}$. Thus, the distribution of event times (and hence, the counting process distributions) are equivalent.

Let A_1, \dots, A_N be any Borel subsets of the real line. Applying Lemma 4.3.2 to each $\mathbf{X}^{D'}$ gives the following distributional representation:

$$\begin{pmatrix} X_1^{D'}(A_1) \\ \vdots \\ X_N^{D'}(A_N) \end{pmatrix} =_{\text{distr}} \begin{pmatrix} \sum_{D \ni 1} \xi^{D'}(D; A_1, \dots, A_N) \\ \vdots \\ \sum_{D \ni N} \xi^{D'}(D; A_1, \dots, A_N) \end{pmatrix}, \quad (4.20)$$

where the random variables $\xi^{D'}(D; A_1, \dots, A_N)$ are taken to be identically zero unless $D \subset D'$. In the latter case, they are independent and Poisson distributed with

$$\begin{aligned} \mathbf{E} \left[\xi^{D'}(D; A_1, \dots, A_N) \right] &= \lambda p_{D'} \sum_{D'' \supset D} p_{D''}^{D'} \nu(Q_{D'}) (M(D, D''; A_1, \dots, A_N)) \\ &= \lambda p_{D'} \nu(Q_{D'}) (M(D, D'; A_1, \dots, A_N)). \end{aligned}$$

The second equality above follows from the fact that $p_{D''}^{D'} = 1$ if $D'' = D'$ and is zero otherwise. Next, define

$$\xi(D; A_1, \dots, A_N) = \sum_{D'} \xi^{D'}(D; A_1, \dots, A_N) = \sum_{D' \supset D} \xi^{D'}(D; A_1, \dots, A_N).$$

As the sum of independent Poisson variables is again Poisson with rate equal to the sum of the rates, we have that $\xi(D; A_1, \dots, A_N)$ is Poisson with mean

$$\mathbf{E} [\xi(D; A_1, \dots, A_N)] = \lambda \sum_{D' \supset D} p_{D'} \nu(Q_{D'}) (M(D, D'; A_1, \dots, A_N)). \quad (4.21)$$

Finally, combining Eqs. (4.19, 4.20), we can write

$$\begin{aligned}
 \begin{pmatrix} X_1(A_1) \\ \vdots \\ X_N(A_N) \end{pmatrix} &=_{\text{distr}} \begin{pmatrix} \sum_{D'} \sum_{D \ni 1} \xi^{D'}(D; A_1, \dots, A_N) \\ \vdots \\ \sum_{D'} \sum_{D \ni N} \xi^{D'}(D; A_1, \dots, A_N) \end{pmatrix} \\
 &= \begin{pmatrix} \sum_{D \ni 1} \sum_{D'} \xi^{D'}(D; A_1, \dots, A_N) \\ \vdots \\ \sum_{D \ni N} \sum_{D'} \xi^{D'}(D; A_1, \dots, A_N) \end{pmatrix} \\
 &= \begin{pmatrix} \sum_{D \ni 1} \xi(D; A_1, \dots, A_N) \\ \vdots \\ \sum_{D \ni N} \xi(D; A_1, \dots, A_N) \end{pmatrix},
 \end{aligned}$$

which, along with Eq. (4.21), establishes the theorem. □

Finally, consider a general subset of k distinct members of the vector counting process \mathbf{X} as in Eq. (4.10). The following theorem provides expressions for the cross-cumulants of these counting processes, as well as their cross-cumulant densities, in terms of model parameters. It is worth noting that the result Theorem 4.3.3 is quite natural in its final form. Further, the simplicity of the final expression hinges crucially on our utilization of cumulants, and not moments, as a measure of codependence. The equivalent expression, given in terms of central moment functions, would be of enormous complexity at higher orders.

Theorem 4.3.3. *Let \mathbf{X} be a joint counting process of GTaS type with total intensity λ , marking distribution $(p_D)_{D \subset \mathbb{D}}$, and family of shift distributions $(Q_D)_{D \subset \mathbb{D}}$. Let A_1, \dots, A_k be arbitrary sets in $\mathcal{B}(\mathbb{R})$, and $\bar{D} = \{i_1, \dots, i_k\} \subset \mathbb{D}$ with $|\bar{D}| = k$. The cross-cumulant of the counting*

4.3. CUMULANT STRUCTURE OF A GTAS PROCESS

processes can be written

$$\kappa(X_{i_1}(A_1), \dots, X_{i_k}(A_k)) = \lambda \sum_{D' \supset \bar{D}} p_{D'} \int P(t\mathbf{1} + \mathbf{Y}^{\bar{D}} \in A_1 \times \dots \times A_k | \mathbf{Y} \sim Q_{D'}) dt, \quad (4.22)$$

where $\mathbf{Y}^{\bar{D}}$ represents the projection of the random vector \mathbf{Y} onto the dimensions indicated by the members of the set \bar{D} . Furthermore, assuming that the shift distributions possess densities $(q_D)_{D \subset \mathbb{D}}$, the cross-cumulant density is given by

$$\kappa_{i_1 \dots i_k}^X(\tau_1, \dots, \tau_{k-1}) = \lambda \sum_{D' \supset \bar{D}} p_{D'} \int q_{D'}^{\bar{D}}(t, t + \tau_1, \dots, t + \tau_{k-1}) dt, \quad (4.23)$$

where $q_{D'}^{\bar{D}}$ indicates the k^{th} order joint marginal density of $q_{D'}$ in the dimensions of \bar{D} .

Proof. First, as noted in Eq. (4.10), we can rewrite the distributional representation of Theorem 4.3.1 (Eq. (4.18)) as

$$\begin{pmatrix} X_{i_1}(A_{i_1}) \\ \vdots \\ X_{i_k}(A_{i_k}) \end{pmatrix} =_{\text{distr}} \begin{pmatrix} \sum_{i_1 \in D \subset \bar{D}} \zeta_D(A_1, \dots, A_N) \\ \vdots \\ \sum_{i_k \in D \subset \bar{D}} \zeta_D(A_1, \dots, A_N) \end{pmatrix}, \quad (4.24)$$

where

$$\zeta_D(A_1, \dots, A_N) = \sum_{\substack{D' \supset D \\ (\bar{D} \setminus D) \cap D' = \emptyset}} \xi(D'; A_1, \dots, A_N). \quad (4.25)$$

The processes ζ_D are comprised of a sum of all of the processes $\xi(D')$ (defined in Theorem 0) such that D' contains all of the indices D , but no other indices which are part of the subset \bar{D} under consideration. These sums are non-overlapping, implying that the ζ_D are also independent and Poisson.

Using the representation of Eq. (4.24), we first find that

$$\begin{aligned} \kappa(X_{i_1}(A_1), \dots, X_{i_k}(A_k)) &= \kappa \left[\sum_{i_1 \in D_1 \subset \bar{D}} \zeta_{D_1}, \dots, \sum_{i_k \in D_k \subset \bar{D}} \zeta_{D_k} \right] \\ &= \sum_{i_1 \in D_1 \subset \bar{D}} \dots \sum_{i_k \in D_k \subset \bar{D}} \kappa[\zeta_{D_1}, \dots, \zeta_{D_k}]. \end{aligned}$$

4.3. CUMULANT STRUCTURE OF A GTAS PROCESS

where we suppressed the dependence of the variables ζ_D on the subsets A_i . The first equality in the previous equation is simply the representation defined in Eq. (4.25), and the second is from the multilinear property of cumulants (property (C1) of cumulants from Chapter 2). Note that the sums are over the sets D_1, \dots, D_k satisfying the given conditions. Recall that, by construction, the Poisson processes ζ_D (see Eq. (4.25)) are independent for distinct marking sets. Accordingly, the cumulant $\kappa[\zeta_{D_1}, \dots, \zeta_{D_k}]$ is zero unless $D_1 = \dots = D_k$, by property (C2) of cumulants given in Chapter 2 — that is,

$$\kappa[\zeta_{D_1}(A_1, \dots, A_N), \dots, \zeta_{D_k}(A_1, \dots, A_N)] = \begin{cases} \kappa_k(\zeta_{\bar{D}}(A_1, \dots, A_N)), & D_j = \bar{D} \text{ for each } j, \\ 0, & \text{otherwise.} \end{cases}$$

Hence,

$$\kappa(X_{i_1}(A_1), \dots, X_{i_k}(A_k)) = \kappa_k(\zeta_D(A_1, \dots, A_N)) = \mathbf{E}[\zeta_D(A_1, \dots, A_N)], \quad (4.26)$$

where we have again used that all cumulants of a Poisson-distributed random variable are equal to its mean.

For what follows, taking $D_0, D' \subset \mathbb{D}$ fixed with $D_0 \subset D'$, the sets $M(D, D'; A_1, \dots, A_N)$ with $D_0 \subset D \subset D'$ are disjoint, and

$$\cup_{D_0 \subset D \subset D'} M(D, D'; A_1, \dots, A_N) = B_1 \times \dots \times B_N \quad \text{with} \quad B_i = \begin{cases} A_i, & i \in D_0, \\ \mathbb{R}, & i \notin D_0. \end{cases} \quad (4.27)$$

In particular, note the independence of the above union from D' .

Substituting Eq. (4.25) into Eq. (4.26), we have

$$\begin{aligned}
 \kappa(X_{i_1}(A_1), \dots, X_{i_k}(A_k)) &= \sum_{D \supset \bar{D}} \mathbf{E} [\xi(D; A_1, \dots, A_k)] \\
 &= \lambda \sum_{D \supset \bar{D}} \sum_{D' \supset D} p_{D'} \nu(Q_{D'}) (M(D, D'; A_1, \dots, A_N)) \\
 &= \lambda \sum_{D' \supset \bar{D}} p_{D'} \sum_{\bar{D} \subset D \subset D'} \nu(Q_{D'}) (M(D, D'; A_1, \dots, A_N)) \\
 &= \lambda \sum_{D' \supset \bar{D}} p_{D'} \nu(Q_{D'}) (\cup_{\bar{D} \subset D \subset D'} M(D, D'; A_1, \dots, A_N)) \\
 &= \lambda \sum_{D' \supset \bar{D}} p_{D'} \int P(t + \mathbf{Y}^{\bar{D}} \in A_1 \times \dots \times A_k | \mathbf{Y} \sim Q_{D'}) dt,
 \end{aligned}$$

where the third equality above is a simple exchange of the order of summation, and the fourth equality follows from the additivity of the measure $\nu(Q_{D'})$ over the disjoint sets $M(D, D'; A_1, \dots, A_N)$. Finally, the fifth equality makes use of the independence of the set union on the fourth line from the set D' as indicated by Eq. (4.27), the definition of the measure $\nu(Q_{D'})$ in Eq. (4.17) and the value of the set union given in Eq. (4.27).

This completes the proof of Eq. (4.22), and Eq. (4.23) follows from the definition of the cross-cumulant density in Eq. (2.13). \square

An immediate corollary of Theorem 4.3.3 is a simple expression for the infinite-time-window cumulants, obtained by integrating the cumulant density across all time lags τ_i . From Eq. (4.23), we have

$$\gamma_{i_1 \dots i_k}^{\mathbf{X}}(\infty) = \int \dots \int \kappa_{i_1 \dots i_k}^{\mathbf{X}}(\tau_1, \dots, \tau_{k-1}) d\tau_{k-1} \dots d\tau_1 = \lambda \sum_{D' \supset \bar{D}} p_{D'} \cdot 1 = \lambda \bar{p}_{\bar{D}}. \quad (4.28)$$

This shows that the infinite window spike count cumulants $\gamma_{i_1 \dots i_k}^{\mathbf{X}}(\infty)$ for a GTaS process should be non-increasing with respect to the ordering of sets \bar{D} , i.e.,

$$\gamma_{i_1 \dots i_k i_{k+1}}^{\mathbf{X}}(\infty) \leq \gamma_{i_1 \dots i_k}^{\mathbf{X}}(\infty).$$

4.3. CUMULANT STRUCTURE OF A GTAS PROCESS

We have shown that the cumulant structure of the GTaS model is fully solvable in terms of model parameters, and exhibited its utility in generating spike trains with pre-determined joint temporal correlation structures. As exhibited in Section 4.2.3, the GTaS framework can be used to explore the properties of the input-output transfer for complex networks. The GTaS framework presented in this chapter will hopefully serve as an invaluable tool for researchers in this capacity.

Introduction to Linear Response

Theory

Analysis of coupled neuronal networks is generally quite difficult [70–72, 123, 124, 182, 217, 284, 285]. For example, in networks of integrate-and-fire neurons, only first moments (firing rates) can be determined analytically [169, 219, 280]. Doing so requires one to solve for fixed points of the F-I function which relates output firing rate to mean input current [167]. The problem of solving for second moments of the spiking output of integrate-and-fire neurons is known to be intractable. Precise determination of even second order dependencies requires novel application of partial differential equation methodologies to the Fokker-Planck equations describing the system [180, 231].

In this chapter, we exhibit a linear response method in which single cell properties can be utilized in order to develop an accurate approximation of second-order statistics of spiking neuron models. We appeal to the diffusion approximation (Section 3.3) in order

to render tractable the determination of marginal statistics [167, 169]. We first review concepts of firing rate linear response theory, which yields an analytical approximation of the time-dependent firing rate (or PSTH) of a neuron receiving noisy input. We then introduce a linear approximation of neuronal activity which supplies directly an analytical approximation of correlations in a general recurrent, noisy neuronal network [278]. We next generalize previous work [221, 222] to derive the necessary quantities to allow application of our approximation to neuronal networks with both current-based and conductance-based synapses. More general applications of this theory, and a more detailed examination of its accuracy are relegated to subsequent chapters.

In what follows, we will consider model neurons of the exponential integrate-and-fire variety (defined in Section 3.1.2) as a proxy for the ideas we present, though many of the principles are more general. In particular, the approximation of correlations in a general spiking neuronal network which we present depends explicitly on knowledge of the shape and strength of interactions, in addition to the firing rate linear response function and the covariance structure in the absence of interactions. For any system in which these quantities are known, either exactly (such as in the case of Ornstein-Uhlenbeck systems of linear stochastic differential equations [88]) or approximately (either via experimentation [9, 146, 149] or simulation [197]), the concepts we present may be applicable. In addition, the material on calculation of firing statistics in Section 5.3 is general to all integrate-and-fire neuron models which are encompassed by an appropriate choice of the function $\psi(V)$ present in the definition of the membrane potential dynamics.

5.1 Firing rate linear response theory

Consider an EIF neuron receiving as current input a fixed signal $X(t)$, with a stochastically fluctuating membrane potential evolving according to

$$\tau_m \dot{V} = -(V - E_L - \psi(V)) + E_\xi + \sqrt{2\sigma_\xi^2 \tau_m} \xi(t) + X(t). \quad (5.1)$$

Here, $\xi(t)$ is a standard white noise process. The input X is taken to have a vanishing temporal average ($\mathbf{E}_t[X] = 0$) and to exhibit fluctuations which are not too strong relative to the noisy background signal $\sqrt{2\sigma_\xi^2 \tau_m} \xi(t)$. Thresholding the membrane potential V yields an output spike train

$$y(t) = \sum_j \delta(t - t_j),$$

with realizations of y being in 1 – 1 correspondence with realizations of the noise ξ . See Chapter 3 for a more complete definition and discussion of integrate-and-fire neuron models.

Averaging over the distribution of ξ yields the time-dependent firing rate $r(t)$. Using firing rate linear response theory, we can achieve an approximation of the firing rate of the form [38, 169, 197, 224]

$$r(t) \approx r_0 + (A * X)(t). \quad (5.2)$$

Here, r_0 is the (constant) stationary firing rate in the absence of the fixed signal $X(t)$, and $A(t)$ is the *linear response function* for the neuron ($A(t)$ may alternatively be referred to as the *firing rate response function*, or *firing rate impulse response function*). We illustrate the firing rate approximation of Eq. (5.2) in Figure 5.1.

The function $A(t)$ is proportional to the first-order approximation of the spike-triggered average of the neuron with respect to the noise signal $\xi(t)$, and is hence equivalent to the

optimal Weiner kernel is the presence of $\xi(t)$ — this relationship can be exploited in order to estimate the linear response function in experimental settings [13, 119], or through simulation of complex neuron models [63]. The Fourier transform $\tilde{A}(\omega)$ of $A(t)$ is known as the *susceptibility*.

A common method of determining the kernel $A(t)$ is to first determine $\tilde{A}(\omega)$. For response to a fluctuating input current, the susceptibility is determined by the amplitude and phase shift of the firing rate in response to a sinusoidal variation of the current, and can be determined thusly both in experiments and simulations of complex neuron models. For integrate-and-fire neuron models such as those considered here, the linear response function can be solved for numerically, to arbitrary precision, by solving a backwards boundary-value ordinary differential equation (see Section 5.3).

We emphasize that, while the linear response function depends implicitly on the model parameters $(\tau_m, E_L, E_\xi, \sigma_\xi)$, it is independent of the input signal $X(t)$. In particular, $A(t)$ is sensitive to the resting potential (the sum $E_L + E_\xi$). Further, it should be noted that the presence of the fluctuating background signal ξ is crucial to the accuracy of the approximation in Eq. (5.2), as it is the noise which linearizes the average firing response.

5.2 Linear response approximation of correlations

Except in highly simplified micro-circuits (such as a pair of cells with unidirectional synaptic coupling or receiving a common input [198]), the linear response approximation of firing rates in Eq. (5.2) cannot yield directly an approximation of the cross-covariance function between two neurons. In essence, there is a loss of information regarding the relative time-courses of the neuronal activity upon taking averages — in particular, by taking the

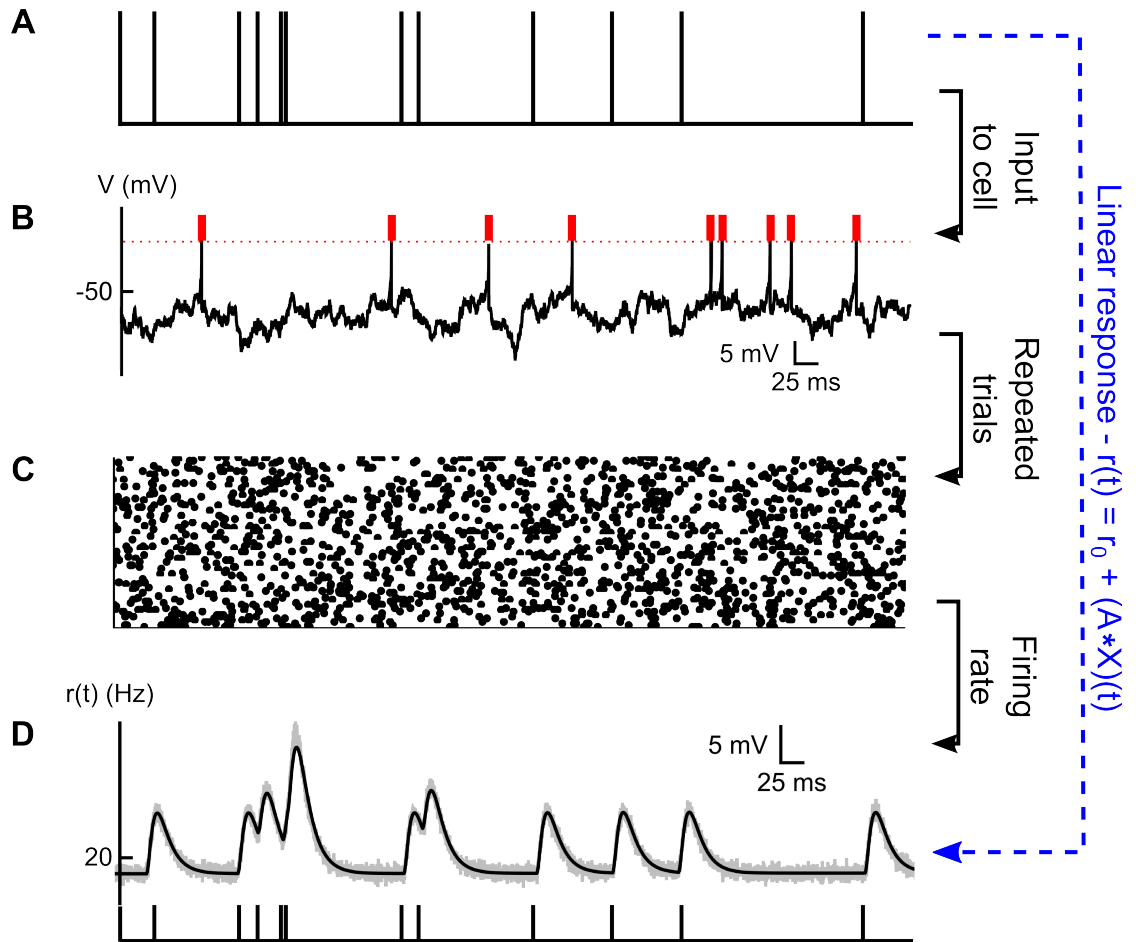


Figure 5.1: **Depicting the firing rate linear response approximation Eq. (5.2).** (A) A spike train is generated and supplies an input current to an exponential integrate-and-fire neuron. (B) The membrane potential of the neuron is driven by intrinsic white noise fluctuations and the spike train in panel A. Each realization of the intrinsic noise corresponds to a realization of the output spike train (red ticks). (C) Fixing the input spike train, repeat the simulation in panel B many times for independent realizations of the intrinsic noise process, generating a raster plot. A dot in the raster indicates a spike in that time bin (horizontal axis) for a specific trial (vertical axis). (D) Averaging the output spike train across trials yields the time-dependent firing rate, or PSTH (grey indicates the Monte Carlo estimation of the PSTH, and black is the theoretical prediction). Spikes in the fixed input spike train shown in panel A (repeated at the bottom of panel D for ease of comparison) drive deviations in the (constant) background firing rate, a quantity determined by the mean and variance of the intrinsic noise.

average which yields the firing rate, we have retained only the marginal probability of observing spikes from that neuron. The dependencies in the firing rate on, for example, the activity of other neurons cannot be recovered.

To remedy this, we generalize the approach of [167], and instead of approximating the time-dependent firing rate in response to a fixed signal $X(t)$, we approximate the time-dependent spiking activity. In particular, we postulate that the trial-by-trial firing response $y(t)$ of the neuron to the signal $X(t)$ is given by

$$y(t) \approx y_0(t) + (A * X)(t), \quad (5.3)$$

where $A(t)$ is again the firing rate response function, and $y_0(t)$ should be viewed as a realization of the output of a neuron with membrane potential obeying Eq. (5.1) with $X(t) \equiv 0$.

If we were to assume Eq. (5.3) holds exactly, this would be equivalent to making an assumption of perfect linearity on the input-output transfer of the neuron in response to the signal $X(t)$, indicated by the superimposition of the linear filtering of $X(t)$ on top of the normal EIF dynamics of $y_0(t)$. We note that averaging Eq. (5.3) across realizations of the underlying driving noise process $\xi(t)$ returns exactly Eq. (5.2), and in this sense, the ansatz in Eq. (5.3) can be viewed as a partial repealing of the average which yields the time-dependent firing rate of the neuron in response to $X(t)$.

5.2.1 Independent noise

We will first apply the linear response ansatz in Eq. (5.3) to a network of exponential integrate-and-fire (EIF) neurons receiving independent white noise and exhibited current-based synaptic interactions, as described in Chapter 3. Briefly, in this setting the membrane potential V_i of the i^{th} cell of the network evolves according to

$$\tau_m \dot{V}_i = -(V_i - E_L - \psi(V_i)) + E_{\xi,i} + \mathbf{E}_t[f_i] + \sqrt{2\sigma_{\xi,i}^2 \tau_m} \xi_i(t) + (f_i(t) - \mathbf{E}_t[f_i]), \quad (5.4)$$

where $\mathbf{E}_t[\cdot]$ indicates a temporal average, and

$$f_i(t) = \sum_j \mathbf{W}_{ij} (\alpha_j * y_j)(t). \quad (5.5)$$

Here, \mathbf{W}_{ij} is the synaptic weight of the connection from neuron j to neuron i , α_j is the synaptic filter applied to the output of neuron j (assumed to have unit area). Unless otherwise specified, synaptic filters are given by delayed alpha functions. The form of such function for a time constant τ_{syn} and delay τ_d is

$$\alpha(t) = \frac{1}{\tau_{\text{syn}}} \exp\left[-\frac{t - \tau_d}{\tau_{\text{syn}}}\right] \Theta(t - \tau_d), \quad (5.6)$$

where $\Theta(t)$ is the Heaviside step function. The stochastic process y_j again represents the spiking output acquired by thresholding the membrane potential of cell j . We further assume that the signals $\xi_i(t)$ are independent (this assumption can be relaxed — see Section 5.2.2).

Thus, in the network setting, we have replaced the fixed input signal $X(t)$ of the previous case with the mean-subtracted, synaptically-filtered output of the network itself, dictating that any proper approximation of the firing activity should be *self-consistent*. Note that the addition and subtraction of $\mathbf{E}_t[f_i]$ in Eq. (5.4) is to allow us to compute linear response to the fluctuations in the synaptic input about its mean value, which can greatly improve the accuracy of the approximation [167].

The linear response ansatz Eq. (5.3) in the network case then takes the form¹

$$\mathbf{y}(t) \approx \mathbf{y}_0(t) + (\mathbf{K} * [\mathbf{y} - \mathbf{r}])(t), \quad \text{where} \quad \mathbf{K}_{ij}(t) = \mathbf{W}_{ij}(A_i * \alpha_j)(t). \quad (5.7)$$

The filter \mathbf{K}_{ij} , which consists of a convolution of the linear response function A_i of the downstream cell i with the synaptic filter $\mathbf{W}_{ij}\alpha_j$ applied to output of the upstream cell j , captures the linear response of cell i to the output of cell j . At first glance, the approximation of Eq. (5.7) may seem somewhat strange, as we are approximating a vector of point processes $\mathbf{y}(t)$ with a vector of “hybrid” processes, composed both of points in $\mathbf{y}_0(t)$ as well as a smooth component $(\mathbf{K} * \mathbf{y})(t)$. Clearly the comparison is poor at the resolution of individual realizations, but we will instead focus on the matching of statistical properties of this approximation — particularly at second order.

We can also arrive at the approximation Eq. (5.7) by a slightly more intuitive road. Above, we discussed Eq. (5.3), and its close relation to the more rigorous approximation of the firing rate in Eq. (5.2). Keeping this discussion in mind, we next define a series of approximations $\mathbf{y}^{(n)}$ for $n \geq 1$ by

$$\mathbf{y}^{(n)}(t) = \mathbf{y}_0(t) + (\mathbf{K} * \mathbf{y}^{(n-1)})(t), \quad \text{where} \quad \mathbf{y}^{(0)}(t) \equiv \mathbf{y}_0(t). \quad (5.8)$$

For instance, we can regard $\mathbf{y}^{(1)}(t)$ as a first approximation of the effects of coupling, in that $\mathbf{y}^{(1)}(t)$ accounts only for first order effects of the synaptic architecture in $\mathbf{K}(t)$. If we consider the cross-covariance functions of the processes $\mathbf{y}^{(1)}(t)$, we would arrive at approximations to the true cross-covariance functions for the network which are precisely equivalent to those postulated in [198]. These approximations ignore, in particular, any

¹If $\mathbf{X}(t), \mathbf{Y}(t)$ are $n \times m$ and $m \times p$ matrices of integrable functions, respectively, we define the $n \times p$ matrix convolution $(\mathbf{X} * \mathbf{Y})(t)$ by

$$(\mathbf{X} * \mathbf{Y})_{ij}(t) = \sum_{k=1}^m (\mathbf{X}_{ik} * \mathbf{Y}_{kj})(t).$$

perturbation to correlations due to paths within the network architecture longer than a single synapse.

Continuing this logic, the approximation $\mathbf{y}^{(n)}(t)$ can be viewed as accounting for (via a linear approximation) the effects of paths within the neuronal network up to length n , and the cross-covariance functions between these processes would reflect the correlating effects of such *network motifs*. This becomes further apparent if we expand the recursive approximation Eq. (5.8), giving

$$\mathbf{y}^{(n)}(t) = \mathbf{y}_0(t) + \sum_{i=1}^n (\mathbf{K}^i * \mathbf{y}_0)(t), \quad (5.9)$$

where the matrix powers in Eq. (5.9) are defined with respect to matrix convolutions. The term in the sum on the right-hand side of Eq. (5.9) involving the power $\mathbf{K}^i(t)$ captures precisely those linear perturbations to activity attributable to length i directed chains through the network architecture.

Finally, defining $\mathbf{y}^\infty(t) = \lim_n \mathbf{y}^{(n)}(t)$, it is not hard to show that the paths of this limit converge pointwise (and uniformly over finite intervals) to our approximation of $\mathbf{y}(t)$ given self-consistently in Eq. (5.7) — that is,

$$\mathbf{y}^\infty(t) = \mathbf{y}_0(t) + (\mathbf{K} * [\mathbf{y}^\infty - \mathbf{r}])(t). \quad (5.10)$$

Thus, the linear response approximation of firing activity can be viewed as a linear approximation in which we take account of linear perturbations to activity of all orders in the synaptic architecture. We illustrate the iterative approximation approach in Figure 5.2.

The limit in Eq. (5.10) — and the approximation in Eq. (5.7) — are only valid when $|\int \mathbf{K}(t)dt| < 1$. This condition guarantees linear stability of the system. In the context of spiking neurons, one can interpret this condition to mean that a spike elicited by any neuron within the system does not reverberate indefinitely; rather, its impact on the network

activity will converge to zero as time proceeds.

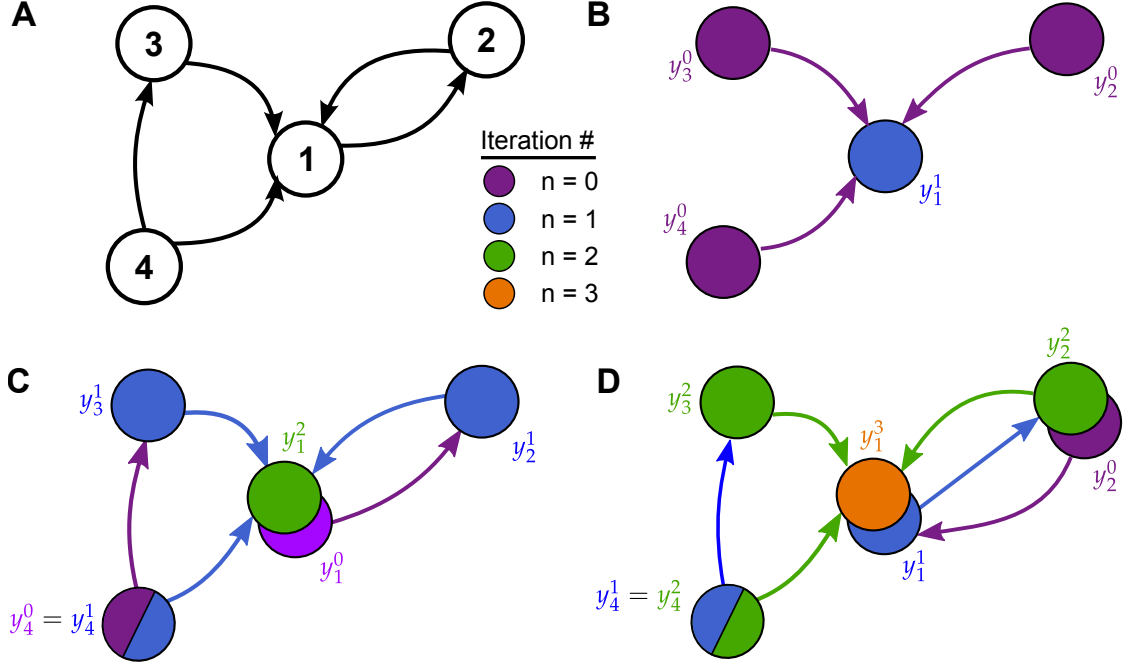


Figure 5.2: **Equations (5.8) and (5.9) give rise to an iterative approximation of network activity.** (A) We approximate the activity y_1 of cell 1, embedded in the depicted recurrent microcircuit. (B) The first approximation y_1^1 of the activity of neuron 1 reflects only the effect of input from the uncoupled approximations y_j^0 of activity for its afferent partners. (C) The second approximation y_1^2 of the activity of neuron 1 now reflects the effects of length two chains through the circuit. In particular, the output of neuron 1 now reflects the impact of its own activity ($y_1^0 \rightarrow y_2^1 \rightarrow y_1^2$), and the approximation of neuron 1's activity now also reflects the indirect input from neuron 4 through neuron 3. (D) The difference between higher order approximations and the second order approximation will be improved resolution of the recurrent loop between cells 1 and 2. At each step, effects due to a longer chain through this loop will be included, and owing to this recurrence, the approximation does not converge in finitely many iterations.

Applying the Fourier transform to Eq. (5.7), convolutions turn to multiplication, and we can solve the resulting linear equation for $\tilde{\mathbf{y}}(\omega)$:

$$\tilde{\mathbf{y}}(\omega) \approx (\mathbf{I} - \tilde{\mathbf{K}}(\omega))^{-1} \tilde{\mathbf{y}}_0(\omega). \quad (5.11)$$

Considering the product of this approximating process with its complex conjugate, we

arrive at an approximation for the cross-spectral structure of the spiking output for the network (see Eq. (2.5)):

$$\mathbf{S}^y(\omega) = \mathbf{E} \left[\overline{\mathbf{y}(\omega)} \mathbf{y}^T(\omega) \right] \approx \left(\mathbf{I} - \overline{\tilde{\mathbf{K}}(\omega)} \right)^{-1} \mathbf{S}_0^y(\omega) \left(\mathbf{I} - \tilde{\mathbf{K}}^T(\omega) \right)^{-1}, \quad (5.12)$$

where

$$\mathbf{S}_0^y(\omega) = \mathbf{E} \left[\overline{\mathbf{y}_0(\omega)} \mathbf{y}_0^T(\omega) \right].$$

and the over-line in Eq. (5.12) indicates a complex conjugate without a transpose. Under the assumptions of independence of the noise vector ξ , $S_0^y(\omega)$ is a diagonal matrix with entries given by

$$(\mathbf{S}_0^y)_{ii}(\omega) = S_{\text{EIF}} \left(\omega; E_{\xi,i} + \mathbf{E}_t[f_i], \sqrt{2\sigma_{\xi,i}^2 \tau_m} \right), \quad (5.13)$$

where we have defined the scalar quantity $S_{\text{EIF}}(\omega; \mu, \sigma)$ to be the spectrum of an EIF neuron receiving white noise input of mean μ and standard deviation σ (we omit the many other parametric dependencies). Like the linear response function, this “unperturbed spectrum” can be measured through simulation or experiments, or determined numerically for the case of general integrate-and-fire neurons [169, 222], a technique we describe in Section 5.3.1.3.

Thus, Eq. (5.12) provides an analytical approximation of the second-order correlation structure of a general, noisy neuronal network (a problem which has no tractable, exact solution, for instance, in the case of integrate-and-fire neuron models). Furthermore, this approximation is given in terms of known (or determinable) marginal properties of the neurons (A_i, S_0^y) and the synaptic architecture (\mathbf{W}, α_i) , reflecting directly the impact of each on the second-order correlation structure of the network.

In Figure 5.3, we compare cross-covariance functions for 3 pairs of EIF neurons within a randomly connected network of both excitatory and inhibitory cells. The three pairs of

neurons were selected randomly, with one each from the categories of excitatory-excitatory, excitatory-inhibitory, and inhibitory-inhibitory pairs. Errors in the linear response approximations of the cross-covariance functions indicate a departure from linearity of the input-output transfer for neurons in the network. In Section 6.4, we will more closely examine the validity of the linear response approximation to correlations in a few situations, in hope of gaining a general notion of when we can expect the approximation to be accurate.

5.2.1.1 Calculation of the linearization point

The precision of the linear response theory, both of correlations and firing rates, requires that the value of the uncoupled spectrum (Eq. (5.13)) as well as the firing rate response function depend on the temporal average of the synaptic input. Here, we address the computation of this average.

Consider a network of EIF neurons receiving independent white noise input of mean μ and intensity σ , and with some synaptic coupling, as in Eq. (5.4). As we assume the synaptic output of the explicitly modeled network to be weighted by the matrix \mathbf{W} and convolved with unit-area synaptic kernels (Eq. (5.5)), it is not hard to show that

$$\mathbf{E}_t[f_i] = \mathbf{W}^{(i)} \mathbf{r},$$

where $\mathbf{W}^{(i)}$ is the i^{th} row of the matrix \mathbf{W} and \mathbf{r} is the vector of output firing rates of the (coupled) network. However, the output firing rates \mathbf{r} are not trivial to calculate, and clearly must depend in turn on the average synaptic inputs. If $r_{EIF}(\mu, \sigma)$ gives the F-I curve for an EIF neuron receiving white noise input of mean μ and intensity σ , then

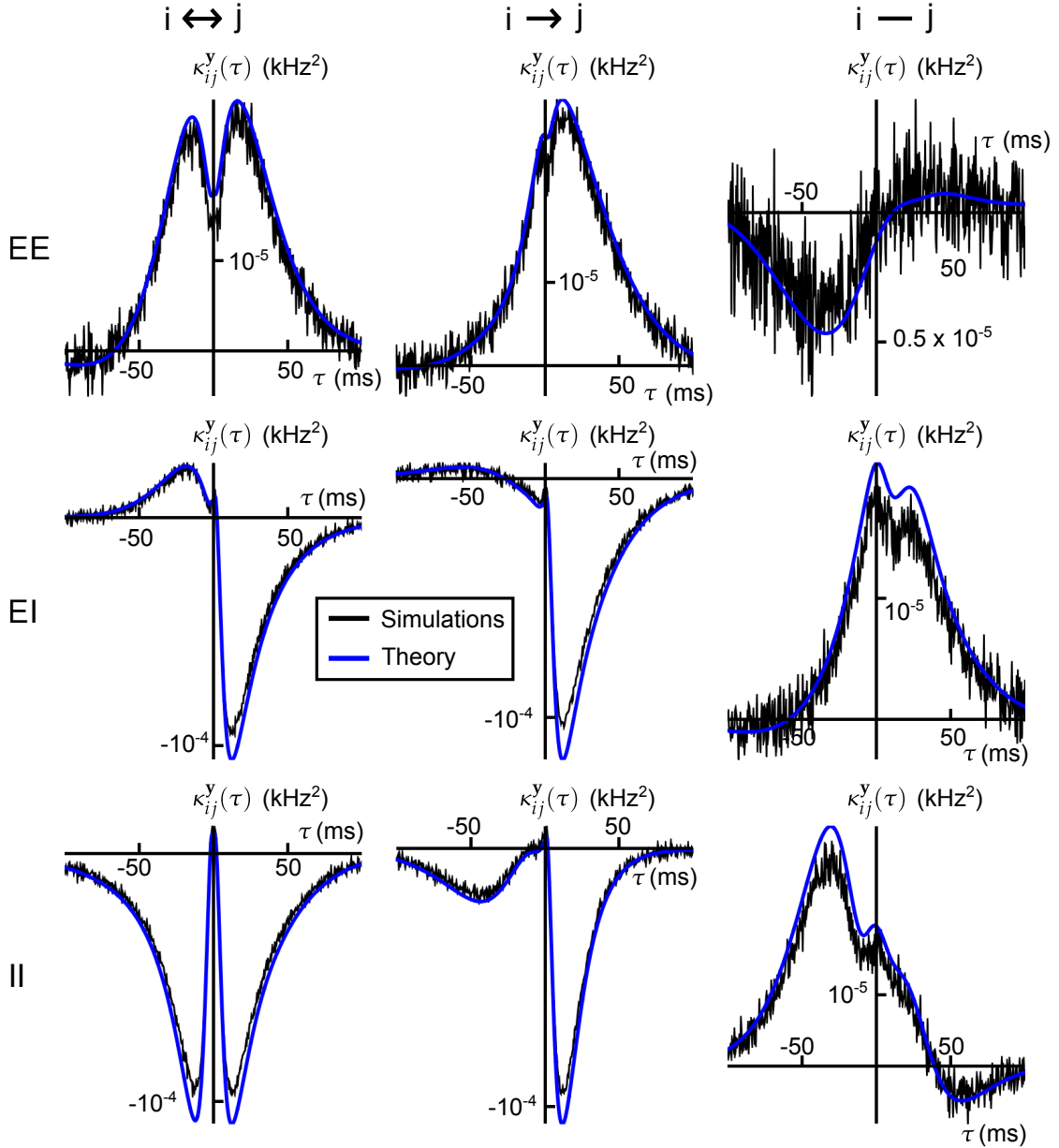


Figure 5.3: **Illustrating the the accuracy of the linear response approximation of correlations in a random network.** Comparison of Monte Carlo estimation of second order cross-cumulant densities (black lines) with their linear response approximations (blue lines, Eq. (5.12)) for nine neuron pairs from a size $N = 100$ random network consisting of 80 excitatory and 20 inhibitory cells. The connection probability was 0.2. A cross-cumulant density is exhibited for one example neuron pair from each of nine possible pairings of neuron classes (EE, EI, II) and first order connectivity (bidirectional, unidirectional or none).

the output firing rates \mathbf{r} of this coupled network satisfy the system of non-linear, self-consistent equations

$$\mathbf{r} = r_{EIF}(\mu + \mathbf{E}_t[\mathbf{f}], \sigma), \quad \text{where} \quad \mathbf{E}_t[\mathbf{f}] = \mathbf{W}\mathbf{r}.$$

Generally, the convexity of the F-I curve will allow this equation to be solved most easily by simple fixed point iteration [167]. The uncoupled firing rate $\mathbf{r}_{uncoup} = r_{EIF}(\mu, \sigma)$ serves as an appropriate starting point for this iteration. Generally, this can be far from the true firing rate of a neuron within a network.

5.2.2 Correlated noise

In the preceding section, we considered linear response of correlations for networks being driven by independent white noise fluctuations. We can relax this assumption, allowing correlations that are not too strong in these noise sources. The equations for the membrane potential evolution become (compare with Eq. (5.4))

$$\begin{aligned} \tau_m \dot{V}_i = & -(V_i - E_L - \psi(V_i)) + E_{\xi,i} + \mathbf{E}_t[f_i] + \sqrt{2\sigma_{\xi,i}^2 \tau_m} (\sqrt{1-c}\xi_i(t) + \sqrt{c}\xi_c(t)) \\ & + (f_i(t) - \mathbf{E}_t[f_i]). \end{aligned} \quad (5.14)$$

Here, each $\xi_i(t)$ and $\xi_c(t)$ are independent standard white noise sources. Thus, the noise to cell i ,

$$\sqrt{1-c}\xi_i(t) + \sqrt{c}\xi_c(t),$$

will also be a standard white noise, now pairwise correlated with correlation coefficient c across neurons.

The linear response approximation of correlations is formulated similarly as in the previous case, with minor adjustments made for the correlated noise sources. First, a

naive application of the linear response ansatz Eq. (5.3) to the dynamics in Eq. (5.14), setting

$$X_i(t) = \sqrt{c\sigma_{\xi,i}^2\tau_m}\xi_c(t) + (f_i(t) - \mathbf{E}_t[f_i]),$$

yields an approximation of the output spiking correlations in this network which is identical schematically to Eq. (5.12). However, the matrix $S_0^y(\omega)$ is no longer diagonal, and has entries given by

$$(\mathbf{S}_0^y)_{ij}(\omega) = \begin{cases} S_{\text{EIF}}\left(\omega; E_{\xi,i} + \mathbf{E}[f_i], \sqrt{2(1-c)\sigma_{\xi,i}^2\tau_m}\right) + 2c|\tilde{A}_i(\omega)|^2\sigma_{\xi,i}^2\tau_m, & i = j, \\ 2c\tilde{A}_i^*(\omega)\tilde{A}_j(\omega)\sigma_{\xi,i}\sigma_{\xi,j}\tau_m, & i \neq j. \end{cases} \quad (5.15)$$

There is an apparent correction which can be made to the linear response approximation of correlations in this case: The diagonal entries of S_0^y given in Eq. (5.15) are approximating the power spectrum of EIF neurons receiving white noise input of mean $E_{\xi,i} + \mathbf{E}[f_i]$ and intensity $\sqrt{2(1-c)\sigma_{\xi,i}^2\tau_m + 2c\sigma_{\xi,i}^2\tau_m} = \sqrt{2\sigma_{\xi,i}^2\tau_m}$. Thus, we can improve the linear response approximation of correlations for the correlated noise system by setting in Eq. (5.15)

$$(\mathbf{S}_0^y)_{ii}(\omega) = S_{\text{EIF}}\left(\omega; E_{\xi,i} + \mathbf{E}[f_i], \sqrt{2\sigma_{\xi,i}^2\tau_m}\right). \quad (5.16)$$

This adjustment of the linearization point in the linear response theory was first noted in [167]. The linearization point of the firing rate response function should be adjusted likewise.

The linear response theory is perturbative in the input correlations as it is in the coupling, and precise only in the case that the system is uncoupled and input correlations are zero. It is not clear *a priori* at what point the linear response theory will fail as a function of the magnitude of input correlations, and in general, the answer will be dependent on the parameters of the system to which the theory is applied. We note only that it is clear

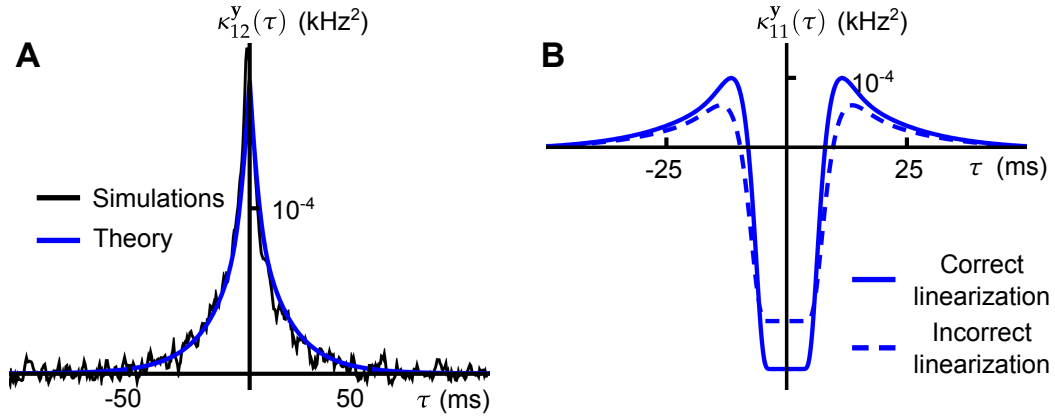


Figure 5.4: **Linear response of correlations for common input.** (A) Comparison of second order cross-cumulant density from simulations and theory (see Eq. (5.15)) for a pair of neurons receiving common white noise input. The input correlation was $c = 0.25$ and the infinite window correlation between the spiking output of the neurons was ≈ 0.21 . (B) Comparison of the steady-state auto-covariance density (δ -peak removed) for the one of the neurons without (Eq. (5.15)) and with (Eq. (5.16)) the adjustment to the power spectrum acquired via a naive linear response application.

the approximation must fail when $c = 1$. Consider an example system consisting of two symmetrically coupled neurons with identical parameters (i.e., leak potentials, etc.), under the assumption of perfectly correlated intrinsic noise and identical initial conditions the spiking output of the two cells should be identical, a prediction not matched by the linear response theory.

5.2.3 Conductance-based synaptic interactions

The theory presented in Section 5.2.1 is valid for the application of linear response theory to systems exhibiting current-based synaptic dynamics. When synapses are conductance-based, a slightly different formulation is necessary. We will present the methodology for a single neuron, and the extension to network applications will be nearly identical to the theory presented for current synapses.

Beginning with a neuron modeled under the diffusion approximation (see Eq. (3.4)), assume additionally that the neuron receives excitatory ($f_E(t)$) and inhibitory ($f_I(t)$) synaptic conductance inputs so that the membrane potential evolves according to

$$\begin{aligned} \tau_{eff} \dot{V}(t) = & -(V - V_{L,eff} - \psi(V)) + \sqrt{2\sigma_{eff}^2(V)} \tau_{eff} \xi(t) \\ & + \frac{\delta f_E(t)}{g_{eff}} (E_E - V) + \frac{\delta f_I(t)}{g_{eff}} (E_I - V). \end{aligned} \quad (5.17)$$

The presence of the additional synaptic input requires adjustment of the effective time constant and rest potential, essentially repeating the algebraic rearrangement of Section 3.3.1. These constants are now given by

$$\begin{aligned} g_{eff} = & g_L + (C_m \mu_E + \mathbf{E}_t[f_E]) + (C_m \mu_I + \mathbf{E}_t[f_I]), \quad \tau_{eff} = \frac{C_m}{g_{eff}}, \\ V_{L,eff} = & \frac{g_L E_L + (C_m \mu_E + \mathbf{E}_t[f_E]) E_E + (C_m \mu_I + \mathbf{E}_t[f_I]) E_I}{g_{eff}}. \end{aligned} \quad (5.18)$$

Because we assume the synaptic input is coming from the local network — the network explicitly modeled — we assume it has finite variance (i.e., it does not include a white component), so that the effective noise intensity $\sigma_{eff}(V)$ is unchanged. We remind the reader that the variation $\delta f(t)$ of a process $f(t)$ is defined by

$$\delta f(t) = f(t) - \mathbf{E}_t[f].$$

Application of linear response to a system exhibiting conductance-based synapses is slightly different in that, in this case, the response properties of a neuron are no longer expressible in terms of a single linear response function. Instead, each neuron possesses two response functions — one for excitatory input (A_E), and one for inhibitory (A_I). It is instructive to first consider the linear response approximation to the firing rate of the neuron to the inputs f_E, f_I :

$$r(t) \approx r_0 + (A_E * \delta f_E)(t) + (A_I * \delta f_I)(t).$$

As in the current-based case considered in Section 5.1, r_0 is the steady-state firing rate of the neuron in the absence of *fluctuations* in the synaptic inputs (i.e., $\delta f_E = \delta f_I \equiv 0$).

Similarly, the linear response approximations of correlations for conductance-based systems begins by posing an approximation to the spiking activity which mimics the firing rate approximation,

$$y(t) \approx y_0(t) + (A_E * \delta f_E)(t) + (A_I * \delta f_I)(t).$$

Application in the network case is essentially identical to the current-based case presented in Section 5.2.1, with the key difference being the form of the matrix of response filters $\mathbf{K}(t)$ (see Eq. (5.7)). In the conductance-based case, this matrix is given by

$$\mathbf{K}_{ij}(t) = \begin{cases} \mathbf{W}_{ij}(A_{E,i} * \alpha_j)(t), & j \in E, \\ \mathbf{W}_{ij}(A_{I,i} * \alpha_j)(t), & j \in I, \end{cases}$$

where $A_{E,i}, A_{I,i}$ are the excitatory and inhibitory response kernels of cell i , and $j \in E$ or $j \in I$ conditions on whether the presynaptic cell j is excitatory or inhibitory. In Figure 5.5, we exhibit the accuracy of the linear response approximation of the cross-cumulant density for a pair of excitatory neurons reciprocally coupled via conductance-based synapses.

5.3 Calculation of firing statistics for IF neurons

To this point, we have taken for granted knowledge of the firing statistics (firing rates, susceptibility and unperturbed spectra) of the neuron models to which we apply the linear response theory of correlations. As previously mentioned, these quantities are measurable, both in experiments, as well as in simulations for complex models by similar principles. In the case of the integrate-and-fire neuron models considered herein, these quantities can be calculated numerically.

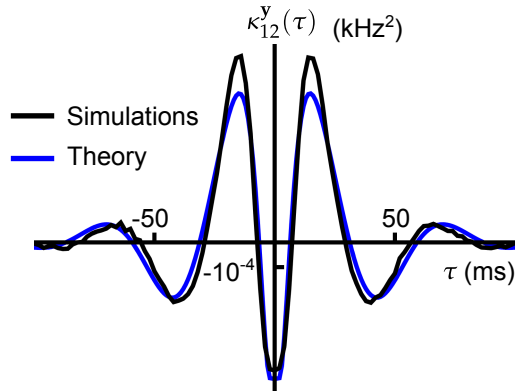


Figure 5.5: Exhibiting the linear response approximation of correlations for conductance-based synapses. Comparison of the theoretical prediction (blue) with the Monte Carlo estimation (black) of the second-order cross cumulant density of a pair of excitatory neurons reciprocally coupled via conductance-based synapses.

Previous analyses derived expressions for some marginal firing statistics of the linear [38, 168, 169, 253], quadratic and exponential [80] integrate-and-fire neuron models. Typically, these analyses lead to expressions for the marginal firing statistics in terms of error functions and parabolic cylinder functions. However, these functions can be computationally expensive to evaluate accurately, and further, these derivations were highly complex and difficult to generalize across neuron models. Richardson [221, 222] introduced a method which nearly perfectly approximates these quantities for general integrate-and-fire models driven by white noise. The statistics are given as solutions of simple boundary value ordinary differential equations derived directly from the Fokker-Planck equations for the evolution of the membrane potential of the neuron model. In Section 5.3.1, we review the results of [221, 222]. In Section 5.3.2, we present one important generalization necessary for the calculation of correlations in neuronal networks exhibiting conductance-based interactions.

5.3.1 Review of existing results

5.3.1.1 Fokker-Planck formalism

Consider a single EIF neuron, evolving in response to a time-varying rest potential $E(t)$ with membrane dynamics

$$\tau_m \dot{V} = -(V - E_L - \psi(V)) + E(t) + \sqrt{2\sigma_\xi^2 \tau_m} \xi(t), \quad (5.19)$$

possessing a firing threshold V_{th} and an absolute refractory period τ_{ref} . Fluctuations in the rest potential can be driven by synaptic inputs, for example. The membrane potential distribution $P(V, t)$ quantifies the probability of finding the membrane potential of such a neuron near the potential V at time t , and $J(V, t)$ is the probability flux across V at time t . The continuity equation [88, 227] relates the two quantities via

$$\frac{\partial P}{\partial t} + \frac{\partial J}{\partial V} = \delta(t - t_0) P_{init}(V) + r(t) \delta(V - V_r) - r(t - \tau_{ref}) \delta(V - V_{th}). \quad (5.20)$$

Here, $P_{init}(V) = P(V, t_0)$ sets the initial distribution of the membrane potential, and the other two terms on the right-hand side account for flux due to the threshold, reset and absolute refractory period. The firing rate $r(t) = J(V_{th}, t)$ is simply the probability flux across threshold at a given time. In addition, the distribution and flux satisfy the relation

$$\tau_m J = (E(t) + \psi(V) - V)P - \sigma_\xi^2 \frac{\partial P}{\partial V}. \quad (5.21)$$

The membrane potential V lives on the domain $(-\infty, V_{th}]$. The method presented by Richardson [221, 222] transforms this into a boundary value problem on a bounded domain by imposing a reflecting boundary at a potential V_{lb} ($J(V_{lb}, t) = 0$). Placed sufficiently low, this reflecting boundary has a negligible impact on the solution of Eqs. (5.20, 5.21). In the presence of the lower reflecting boundary, the membrane potential is

instead limited to the domain $(V_{lb}, V_{th}]$, and the correct normalization of the probability density P is given by

$$\int_{V_{lb}}^{V_{th}} P(V, t) dV + \int_{t-\tau_{ref}}^t r(t') dt' = 1, \quad (5.22)$$

which states that the proportion of an ensemble of neurons evolving according to the dynamics of Eq. (5.19) which are in non-refractory (first term) and refractory (second term) states at any time t sum to unity.

5.3.1.2 Solving for the steady-state firing rate

In the stationary state, under the assumption of a constant rest potential $E(t) = E_0$, initial conditions are forgotten and probability no longer flows with time (i.e., $\frac{\partial P}{\partial t} = 0$). From Eqs. (5.20, 5.21), the steady-state probability $P_0(V)$ and flux $J_0(V)$ satisfy the pair of first-order differential equations

$$\begin{aligned} -\frac{\partial J_0}{\partial V} &= r_0 \delta(V - V_{th}) - r_0 \delta(V - V_r), \\ -\frac{\partial P_0}{\partial V} &= \frac{1}{\sigma_\xi^2} [\tau_m J_0 + (V - E_L - E_0 - \psi(V)) P_0]. \end{aligned}$$

The boundary conditions for the system are $P_0(V_{th}) = 0$, $J_0(V_{th}) = r_0$, where r_0 is the stationary firing rate for the neuron. In particular, the solution to the system depends on the firing rate, which is not known *a priori*. Richardson [221, 222] gets around this issue by setting

$$p_0 = \frac{P_0}{r_0}, \quad j_0 = \frac{J_0}{r_0},$$

so that these scaled quantities satisfy the pair of differential equations

$$\begin{aligned} -\frac{\partial j_0}{\partial V} &= \delta(V - V_{th}) - \delta(V - V_r), \\ -\frac{\partial p_0}{\partial V} &= \frac{1}{\sigma_\xi^2} [\tau_m j_0 + (V - E_L - E_0 - \psi(V)) p_0]. \end{aligned} \quad (5.23)$$

A convenient scheme is suggested in [221, 222] for the backward integration of these equations from V_{th} to the reflecting boundary V_{lb} .

In steady-state, Eq. (5.22) becomes

$$\int_{V_{\text{lb}}}^{V_{\text{th}}} P_0(V) dV + \tau_{\text{ref}} r_0 = r_0 \left(\int_{V_{\text{lb}}}^{V_{\text{th}}} p_0(V) dV + \tau_{\text{ref}} \right) = 1.$$

Therefore, once the solution to the system in Eq. (5.23) has been found numerically, the firing rate is given by

$$r_0 = \left(\int_{V_{\text{lb}}}^{V_{\text{th}}} p_0(V) dV + \tau_{\text{ref}} \right)^{-1}.$$

5.3.1.3 Solving for the spectrum $S_{\text{EIF}}(\omega)$

A similar method can be employed for the determination of the steady-state power spectrum of the neuron with dynamics as described by Eq. (5.19). Again assume that the rest potential is constant ($E(t) = E_0$). The idea will be to solve for the first-passage time density of the neuron, then utilize well-known identities for renewal point processes in order to determine the power spectrum of the neuron.

The general first-passage time density is the distribution of times it takes the neuron to reach the firing threshold V_{th} starting from some initial distribution of values at a time $t = t_0$. We are interested in the particular first-passage time density $f(t)$ which we define to be the distribution of times to reach the threshold V_{th} starting from the spike reset potential V_r at time $t = \tau_{\text{ref}}$. Similar to Eqs. (5.20, 5.21), we can write [222]

$$\begin{aligned} -\frac{\partial J}{\partial V} &= \frac{\partial P}{\partial t} + f(t)\delta(V - V_{\text{th}}) - \delta(t - \tau_{\text{ref}})\delta(V - V_r), \\ -\frac{\partial P}{\partial V} &= \frac{1}{\sigma_\xi^2} [\tau_m J + (V - E_L - E_0 - \psi(V))P]. \end{aligned}$$

Because of the presence of the time-derivative $\frac{\partial P}{\partial t}$, which cannot be neglected in this case,

it is convenient to consider these equations in the frequency domain, where we have

$$\begin{aligned} -\frac{\partial \tilde{J}}{\partial V} &= 2\pi i \omega \tilde{P} + \tilde{f}(\omega) \delta(V - V_{\text{th}}) - e^{-2\pi i \omega \tau_{\text{ref}}} \delta(V - V_{\text{r}}), \\ -\frac{\partial \tilde{P}}{\partial V} &= \frac{1}{\sigma_{\xi}^2} [\tau_m \tilde{J} + (V - E_L - E_0 - \psi(V)) \tilde{P}]. \end{aligned} \quad (5.24)$$

The first equality above used the identity

$$\mathcal{F} \left[\frac{df}{dt} \right] (\omega) = 2\pi i \omega \mathcal{F} [f] (\omega).$$

Next, dividing each of \tilde{P}, \tilde{J} into two parts, one of which is proportional to \tilde{f} , and one which is not,

$$\tilde{P} = \tilde{f} \tilde{p}_f + \tilde{p}_0, \quad \tilde{J} = \tilde{f} \tilde{j}_f + \tilde{j}_0,$$

gives a decoupled pair of two-dimensional first order ODEs: one for $(\tilde{p}_f, \tilde{j}_f)$,

$$\begin{aligned} -\frac{\partial \tilde{j}_f}{\partial V} &= 2\pi i \omega \tilde{p}_f + \delta(V - V_{\text{th}}), \\ -\frac{\partial \tilde{p}_f}{\partial V} &= \frac{1}{\sigma_{\xi}^2} [\tau_m \tilde{j}_f + (V - E_L - E_0 - \psi(V)) \tilde{p}_f], \end{aligned}$$

with initial conditions $\tilde{p}_f(V_{\text{th}}) = 0, \tilde{j}_f(V_{\text{th}}) = 1$ (since $f(t) = J(V_{\text{th}}, t)$), and another for $(\tilde{p}_0, \tilde{j}_0)$,

$$\begin{aligned} -\frac{\partial \tilde{j}_0}{\partial V} &= 2\pi i \omega \tilde{p}_0 - e^{2\pi i \omega \tau_{\text{ref}}} \delta(V - V_{\text{r}}), \\ -\frac{\partial \tilde{p}_0}{\partial V} &= \frac{1}{\sigma_{\xi}^2} [\tau_m \tilde{j}_0 + (V - E_L - E_0 - \psi(V)) \tilde{p}_0], \end{aligned}$$

with initial conditions $\tilde{p}_0(V_{\text{th}}) = \tilde{j}_0(V_{\text{th}}) = 0$. These two allied systems can be solved by the same numerical scheme utilized in the steady-state case of Section 5.3.1.2. Once the solution is obtained, the zero-flux condition at V_{lb} implies $\tilde{J}(V_{\text{lb}}, \omega) = 0$ for every ω , so that

$$\tilde{f}(\omega) = -\frac{\tilde{j}_0(V_{\text{lb}}, \omega)}{\tilde{j}_f(V_{\text{lb}}, \omega)}.$$

Having obtained the Fourier-transformed first-passage time density, identities for renewal point processes [90] (such as the presently considered integrate-and-fire neuron) give that

$$S_{\text{EIF}}(\omega; E_L + E_0, \sqrt{2\sigma_{\xi,i}^2 \tau_m}) = \begin{cases} \pi r_0 \delta(\omega), & \omega = 0, \\ r_0 \left(1 + 2\mathcal{R} \left[\frac{\tilde{f}(\omega)}{1 - \tilde{f}(\omega)} \right] \right), & \omega \neq 0, \end{cases} \quad (5.25)$$

where $\mathcal{R}[\cdot]$ indicates the real part of the argument. To obtain the auto-correlation function (the cross-cumulant density between a process with itself — see Chapter 2), the spectrum should be solved for at a range of frequency values. The Fourier transform then yields the auto-correlation by the Wiener-Khinchin theorem (Eq. (2.6)).

5.3.1.4 Susceptibility to current modulation

Richardson [221, 222] exhibited how to apply the method utilized above for determination of the firing rate and spectra to obtain the linear response to periodic modulation of system parameters, including the noise potential and amplitude. As we are interested in linear response approximations of coupling between neurons, it is the latter on which we focus.

In particular, suppose that the parameter $E(t)$ now undergoes periodic (complex) oscillations about a mean value E_0 , i.e.,

$$E(t) = E_0 + E_1 e^{2\pi i \omega t}.$$

Then, expanding the time-dependent firing rate $r(t) = J(V_{\text{th}}, t)$ to first order in the amplitude of modulation E_1 , we write

$$r(t) = r_0 + \hat{r}_E e^{2\pi i \omega t},$$

where r_0 is the stationary firing rate for constant $E(t) = E_0$ as determined in Section 5.3.1.2, and the amplitude and phase shift of the firing rate modulation is captured in the quantity $\hat{r}_E(\omega) = E_1 \tilde{A}(\omega)$. The susceptibility $\tilde{A}(\omega)$ is the same one appearing in the linear response ansatz Eq. (5.3) and the subsequent analysis.

Note that the periodic fluctuations in the firing rate are complex (i.e., they have both real and imaginary components), owing to the complex nature of the fluctuations in the parameter E . This turns out to be a convenient assumption for the derivation of the firing statistics — one should think of it as simultaneous consideration of two systems, one of which is driven cosinusoidally, and the other driven sinusoidally.

The probability density and flux can likewise be expressed to first order in the strength of resting potential fluctuation E_1 as

$$P = P_0 + \hat{P}_E e^{2\pi i \omega t}, \quad J = J_0 + \hat{J}_E e^{2\pi i \omega t}.$$

Substituting these first-order approximations of P and J into Eqs. (5.20, 5.21) and collecting the first order terms (i.e., those proportional to $e^{2\pi i \omega t}$) gives that the first-order responses \tilde{P}_E, \tilde{J}_E satisfy the equations

$$\begin{aligned} -\frac{\partial \hat{J}_E}{\partial V} &= 2\pi i \omega \hat{P}_E + \hat{r}_E \delta(V - V_{\text{th}}) - \hat{r}_E e^{-2\pi i \omega \tau_{\text{ref}}} \delta(V - V_r), \\ -\frac{\partial \hat{P}_E}{\partial V} &= \frac{1}{\sigma_\xi^2} [\tau_m \hat{J}_E + (V - E_L - E_0 - \psi(V)) \hat{P}_E - E_1 P_0], \end{aligned} \quad (5.26)$$

with boundary conditions $\tilde{P}_E(V_{\text{th}}) = 0$ and $\tilde{J}_E(V_{\text{th}}) = \tilde{r}_E$.

We can perform a separation similar to that of Section 5.3.1.3 by writing

$$\hat{P}_E = \hat{r}_E \hat{p}_r + E_1 \hat{p}_E, \quad \hat{J}_E = \hat{r}_E \hat{j}_r + E_1 \hat{j}_E.$$

Substituting these values into Eq. (5.26) and collecting terms proportional to \hat{r}_E and E_1

yields a pair of two-dimensional ODEs, one for (\hat{p}_r, \hat{j}_r) ,

$$\begin{aligned} -\frac{\partial \hat{j}_r}{\partial V} &= 2\pi i \omega \hat{p}_r + \delta(V - V_{\text{th}}) - e^{-2\pi i \omega \tau_{\text{ref}}} \delta(V - V_r), \\ -\frac{\partial \hat{p}_r}{\partial V} &= \frac{1}{\sigma_\xi^2} [\tau_m \hat{j}_r + (V - E_L - E_0 - \psi(V)) \hat{p}_r], \end{aligned}$$

with boundary conditions $\hat{p}_r(V_{\text{th}}) = 0, \hat{j}_r(V_{\text{th}}) = 1$, and another for (\hat{p}_E, \hat{j}_E) ,

$$\begin{aligned} -\frac{\partial \hat{j}_E}{\partial V} &= 2\pi i \omega \hat{p}_E, \\ -\frac{\partial \hat{p}_E}{\partial V} &= \frac{1}{\sigma_\xi^2} [\tau_m \hat{j}_E + (V - E_L - E_0 - \psi(V)) \hat{p}_E - P_0]. \end{aligned}$$

with boundary conditions $\hat{p}_E(V_{\text{th}}) = \hat{j}_E(V_{\text{th}}) = 0$. Once again applying the zero-flux condition at V_{lb} gives

$$\tilde{A}(\omega) = -\frac{\hat{j}_E(V_{\text{lb}}, \omega)}{\hat{j}_r(V_{\text{lb}}, \omega)}.$$

As in the case of the power spectrum, the linear response kernel $A(t)$ can be acquired by solving the system of ODEs determining $\tilde{A}(\omega)$ for a range of ω values and taking an inverse Fourier transform.

5.3.2 Derivation of firing statistics for conductance synapses

As discussed in Section 5.2.3, application of linear response theory to the approximation of correlations in systems which exhibit conductance-based synapses requires the determination of two linear response functions per neuron — one each for excitatory and inhibitory inputs. In particular, the necessary linear response functions are those for response to fluctuations in the steady-state conductance (just as the application for current-based synapses necessitated the determination of the linear response function to variations in the resting potential which, up to a scaling factor, is equivalent to the response function to variations in the steady-state input current).

For convenience, we restate here the dynamics of the conductance-based neuron under the diffusion approximation (given in Eq. (5.17)):

$$\tau_{eff}\dot{V}(t) = V_{L,eff} - V + \sqrt{2\sigma_{eff}^2(V)\tau_{eff}}\xi(t) + \frac{\delta f_E(t)}{g_{eff}}(E_E - V) + \frac{\delta f_I(t)}{g_{eff}}(E_I - V).$$

The values of the effective time constant and rest potential are given in Eq. (5.18), and the effective noise intensity is given in Eq. (3.5).

The corresponding continuity equation is identical to Eq. (5.20), and the flux is given by [88, 227]

$$\tau_{eff}J = \left[V_{L,eff} - V + \frac{\delta f_E(t)}{g_{eff}}(E_E - V) + \frac{\delta f_I(t)}{g_{eff}}(E_I - V) \right] P - \frac{\partial}{\partial V} \left[\sigma_{eff}^2(V)P \right]. \quad (5.27)$$

Differentiating the product in Eq. (5.27) and collecting terms, we have

$$\begin{aligned} \tau_{eff}J = & \left[V - V_{L,eff} + \left(\frac{\delta f_E(t)}{g_{eff}} + 2\tau_{eff}\sigma_E^2 \right) (E_E - V) \right. \\ & \left. + \left(\frac{\delta f_I(t)}{g_{eff}} + 2\tau_{eff}\sigma_I^2 \right) (E_I - V) \right] P - \sigma_{eff}^2(V) \frac{\partial P}{\partial V}. \end{aligned} \quad (5.28)$$

5.3.2.1 Solving for the steady-state firing rate and spectrum

The determination of the stationary firing rate of the neuron proceeds exactly as in the current-based case (Section 5.3.1.2). First, assume the excitatory and inhibitory synaptic conductances are constant — $f_E(t) = \mathbf{E}_t[f_E] = f_{E0}$ and similarly for $f_I(t)$ — so that the variations $\delta f_E(t)$ and $\delta f_I(t)$ are identically zero. The equations for the steady-state flux J_0 and probability density P_0 are then

$$\begin{aligned} -\frac{\partial J_0}{\partial V} &= r_0\delta(V - V_{th}) - r_0\delta(V - V_r), \\ -\frac{\partial P_0}{\partial V} &= \frac{1}{\sigma_{eff}^2(V)} \left\{ \tau_{eff}J_0 + \left[V - V_{L,eff} + 2\tau_{eff}\sigma_E^2(V - E_E) + 2\tau_{eff}\sigma_I^2(V - E_I) \right] P_0 \right\}. \end{aligned} \quad (5.29)$$

This system of ODEs can be solved for the stationary firing rate r_0 exactly as in Section 5.3.1.2.

Likewise, the spectrum is determined by first computing the Fourier-transformed first-passage time density with a method identical to that exhibited in Section 5.3.1.3. The pertinent flux and probability density differential equations are (compare with Eq. (5.24))

$$\begin{aligned} -\frac{\partial \tilde{J}}{\partial V} &= 2\pi i \omega \tilde{P} + \tilde{f}(\omega) \delta(V - V_{\text{th}}) - e^{-2\pi i \omega \tau_{\text{ref}}} \delta(V - V_r), \\ -\frac{\partial \tilde{P}}{\partial V} &= \frac{1}{\sigma_{\text{eff}}^2(V)} \left\{ \tau_{\text{eff}} \tilde{J} + \left[V - V_{L,\text{eff}} - \psi(V) + 2\tau_{\text{eff}} \sigma_E^2 (V - E_E) + 2\tau_{\text{eff}} \sigma_I^2 (V - E_I) \right] \tilde{P} \right\}. \end{aligned}$$

5.3.2.2 Linear response to mean conductance modulation

The general methodology for derivation of the excitatory and inhibitory conductance linear response kernels is again similar to that exhibited for current-based synapses (see Section 5.3.1.4). The excitatory and inhibitory kernels are determined separately by posing harmonic modulation of the excitatory and inhibitory conductances separately. We will exhibit the method for the excitatory kernel, and the derivation of the inhibitory kernel is identical.

Suppose that the excitatory conductance is given a periodic variation of the form

$$f_E(t) = f_{E0} + f_{E1} e^{2\pi i \omega t}$$

while the inhibitory conductance is constant in time ($f_I(t) = \mathbf{E}_t[f_I] = f_{I0}$). Note that $\mathbf{E}_t[f_E] = f_{E0}$ and $\delta f_E(t) = f_{E1} e^{2\pi i \omega t}$. We expand the firing rate, probability density and flux to first order in f_{E1} , giving, similar to the current-based case considered above,

$$r(t) = r_0 + \hat{r}_{f_E} e^{2\pi i \omega t},$$

with similar expansions for P and J . Substituting these first order expansions into the continuity and flux equations (Eqs. (5.20 and 5.28)) and collecting first order terms (again,

those proportional to $e^{2\pi i\omega t}$ gives the following system for the linear responses of the firing rate, density and flux:

$$\begin{aligned}
 -\frac{\partial \hat{J}_{f_E}}{\partial V} &= 2\pi i\omega \hat{P}_{f_E} + \hat{r}_{f_E} \delta(V - V_{\text{th}}) - \hat{r}_{f_E} e^{-2\pi i\omega \tau_{\text{ref}}} \delta(V - V_r), \\
 -\frac{\partial \hat{P}_{f_E}}{\partial V} &= \frac{1}{\sigma_{eff}^2(V)} \left\{ \tau_{eff} \hat{J}_{f_E} + \left[V - V_{L,eff} - \psi(V) + 2\tau_{eff} \sigma_E^2 (V - E_E) \right. \right. \\
 &\quad \left. \left. + 2\tau_{eff} \sigma_I^2 (V - E_I) \right] \hat{P}_{f_E} + \frac{g_{E1}}{g_{eff}} (V - E_E) P_0 \right\}.
 \end{aligned} \tag{5.30}$$

Here, P_0 is the solution to the ODE in Eq. (5.29). Employing the same technique as Section 5.3.1.4, we write

$$\hat{P}_{f_E} = \hat{r}_{f_E} \hat{p}_r + f_{E1} \hat{p}_{f_E}, \quad \hat{J}_{f_E} = \hat{r}_{f_E} \hat{j}_r + f_{E1} \hat{j}_{f_E}.$$

Substituting these decompositions into Eq. (5.30) again yields a pair of two-dimensional, first order ODEs which can be integrated backwards from threshold V_{th} to the lower bound V_{lb} . The excitatory response function is then given by

$$\tilde{A}_E(\omega) = -\frac{\hat{j}_{f_E}(V_{\text{lb}})}{\hat{j}_r(V_{\text{lb}})}.$$

The inhibitory response function can be derived likewise.

Chapter 6

Analysis of Neuronal Networks Using Linear Response

Novel experimental techniques reveal the simultaneous activity of larger and larger numbers of neurons. As a result there is increasing interest in the structure of cooperative – or *correlated* – activity in neural populations, and in the possible impact of such correlations on the neural code. A fundamental theoretical challenge is to understand how the architecture of network connectivity along with the dynamical properties of single cells shape the magnitude and timescale of correlations. In what follows, we consider applications of the linear response theory of correlations introduced in Chapter 5, aiming to highlight the importance of this theory as an invaluable tool in tackling these challenges..

The linear response approximation of correlations will be shown to admit an expansion in powers of the matrices that describe the network architecture. This expansion can be readily interpreted in terms of paths between different cells. We apply our results to large excitatory-inhibitory networks, and demonstrate first how precise *balance* — or lack

thereof — between the strengths and timescales of excitatory and inhibitory synapses is reflected in the overall correlation structure of the network. We then derive explicit expressions for the average correlation structure in randomly connected networks. These expressions help to identify the important factors that shape coordinated neural activity in such networks. We briefly consider applications of the linear response theory to analysis of correlations within distance-dependent networks.

We conclude this chapter by conducting a thorough error analysis of the linear response theory of correlations. We explore the dependence of the match between theory and simulations on the dynamical operating point of the cell as well as on the strength of interactions. We also consider the failure of the linear response theory to yield accurate predictions of third order dependencies amongst spiking neurons. The question of whether there exists a consistent correction to the predictions of third order correlations acquired from the linear response theory is unresolved, and of great significance for future applications.

6.1 Path expansion of correlations

Recall the iterative construction of the linear response approximation to activity, as was illustrated in the previous chapter, and in particular in Figure 5.2. As explained around Eq. (5.9), terms in this expansion of the output of the coupled network captured linear perturbations to activity due to synaptic paths of increasing length. This decomposition of activity into path contributions suggests a similar decomposition of correlations.

Recall the linear response approximation of the second order correlation structure

given in Eq. (5.12), which we restate here for convenience:

$$\mathbf{S}^y(\omega) = \left(\mathbf{I} - \overline{\tilde{\mathbf{K}}(\omega)}\right)^{-1} \mathbf{S}_0^y(\omega) \left(\mathbf{I} - \tilde{\mathbf{K}}^T(\omega)\right)^{-1}. \quad (6.1)$$

For ease of notation, we will say that the output spectra are equal to their linear response approximation, denoted by the equality in Eq. (6.1). The reader should bear in mind this is still an approximation. Under the assumption of linear stability of the network under which the iterative approximation was also formed (i.e., $\Psi(\tilde{\mathbf{K}}(\omega)) < 1$ for all ω), we can expand the matrix inverses in Eq. (6.1) in a von Neumann series, obtaining

$$\mathbf{S}^y(\omega) = \sum_{n,m=0}^{\infty} \left(\overline{\tilde{\mathbf{K}}(\omega)}\right)^n \mathbf{S}_0^y(\omega) \left(\tilde{\mathbf{K}}^T(\omega)\right)^m. \quad (6.2)$$

The terms of this series expansion correspond to contributions to correlations of *motifs* of varying orders within the network architecture. The *order* of a motif refers to the number of connections which form the motif. In particular, the $(i, j)^{th}$ entry of the matrix term

$$\left(\overline{\tilde{\mathbf{K}}(\omega)}\right)^n \mathbf{S}_0^y(\omega) \quad (6.3)$$

corresponds to contributions to correlations between the pair of cells (i, j) from length n chains through the network which begin at cell j and terminate at cell i . We depict a chain motif in Figure 6.1A. Similarly, the $(i, j)^{th}$ entry of the $(n + m)^{th}$ order term

$$\left(\overline{\tilde{\mathbf{K}}(\omega)}\right)^n \mathbf{S}_0^y(\omega) \left(\tilde{\mathbf{K}}^T(\omega)\right)^m \quad (6.4)$$

yields the contribution to correlations between the pair of cells (i, j) from $(n + m)^{th}$ order diverging motifs which connect a common source neuron to cell i via a length n chain, and cell j via a length m chain, as depicted in Figure 6.1B. In what follows, we will explore some applications of linear response theory, including some elementary applications of the linear response path expansion of correlations. In the next chapter, we present a more significant application.

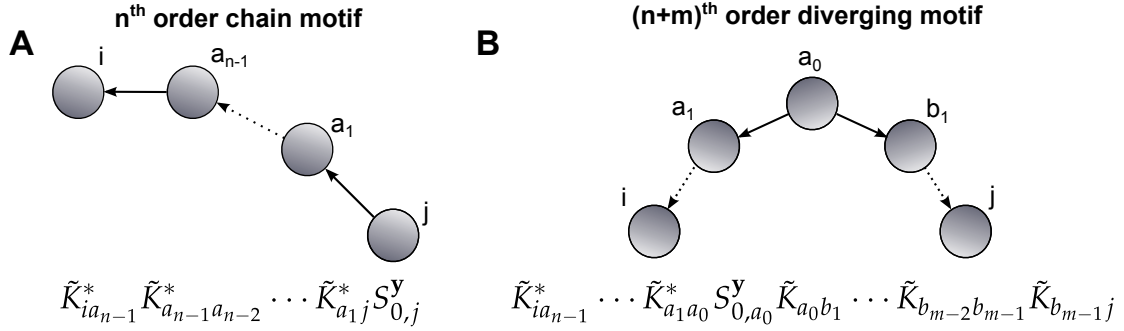


Figure 6.1: **Motifs appearing in the linear response diagrammatic expansion of correlations given in Eq. (6.2).** **(A)** An n^{th} order chain motif in a recurrent network connecting the pair of cells (i, j) . Within the linear response path expansion of correlations (Eq. (6.2)), the contributions to correlations of such motifs are captured by the term in Eq. (6.3). **(B)** An $(n + m)^{\text{th}}$ order diverging motif which contributes to the correlation (i, j) in a recurrent network. Within the linear response path expansion of correlations (Eq. (6.2)), the contributions to correlations of such motifs are captured by the term in Eq. (6.4).

6.2 Linear response application to coupled microcircuits

To illustrate the use of linear response theory in analyzing correlations in coupled neuronal networks, we first consider a pair of simple microcircuits. In the case of small networks, we can solve exactly and explicitly the linear response approximation of correlations given in Eq. (6.1).

6.2.1 Feed-forward inhibitory microcircuit

The first microcircuit we consider is a feed-forward inhibitory (FFI) microcircuit. Feed-forward inhibition is believed to be a central mechanism utilized within cortical networks in order to *gate* synaptic inputs, shaping integration windows and increasing spike precision [24, 76, 86, 186, 208, 294]. The circuit consists of two excitatory E_1 and E_2 with a monosynaptic coupling from E_1 to E_2 . In addition, there is a second-order chain connection from E_1 to E_2 through a third, inhibitory cell I . Activation of the neuron E_1 provides

simultaneous activation of both cells E_2 and I . If the inhibitory connection is strong, then the cell E_2 only has a short time in which to spike before the inhibition will prevent firing (this is the integration window), causing it to forget about the input from E_1 .

The circuit is shown on left in Figure 6.2A. In Figure 6.2B, we compare the linear response approximation of the second order cross-cumulant density between the cells E_2 and I .

In the FFI circuit, the interaction matrix $\tilde{\mathbf{K}}$ takes the form

$$\tilde{\mathbf{K}}(\omega) = \begin{pmatrix} 0 & 0 & 0 \\ \tilde{K}_{E_2E_1}(\omega) & 0 & \tilde{K}_{E_2I}(\omega) \\ \tilde{K}_{IE_1}(\omega) & 0 & 0 \end{pmatrix},$$

where we have indexed the cells in the order (E_1, E_2, I) — for instance, the $(2, 1)$ entry corresponds to the interaction kernel for the synapse $E_1 \rightarrow E_2$. To simplify notation, we will omit further expression of the dependence of spectral quantities on the frequency ω .

In this instance, the matrix $\tilde{\mathbf{K}}$ is nilpotent of order three (that is, $\tilde{\mathbf{K}}^3 = 0$), which is a reflection of the non-recurrent nature of the synaptic architecture of the microcircuit. As a result, the matrix inverses appearing in Eq. (6.1) can be expanded as

$$\left(\mathbf{I} - \tilde{\mathbf{K}}\right)^{-1} = \left(\mathbf{I} + \tilde{\mathbf{K}} + \tilde{\mathbf{K}}^2\right) = \begin{pmatrix} 1 & 0 & 0 \\ \tilde{K}_{E_2E_1} + \tilde{K}_{E_2I}\tilde{K}_{IE_1} & 0 & \tilde{K}_{E_2I} \\ \tilde{K}_{IE_1} & 0 & 0 \end{pmatrix}. \quad (6.5)$$

Substituting Eq. (6.5) — and the corresponding, similar expansion of $(\mathbf{I} - \tilde{\mathbf{K}}^T)^{-1}$ — into Eq. (6.1) yields an explicit approximation of the cross-spectra for all neuron pairs within the FFI network in terms of the individual interaction kernels as well as the uncoupled spectra of the constituent neurons.

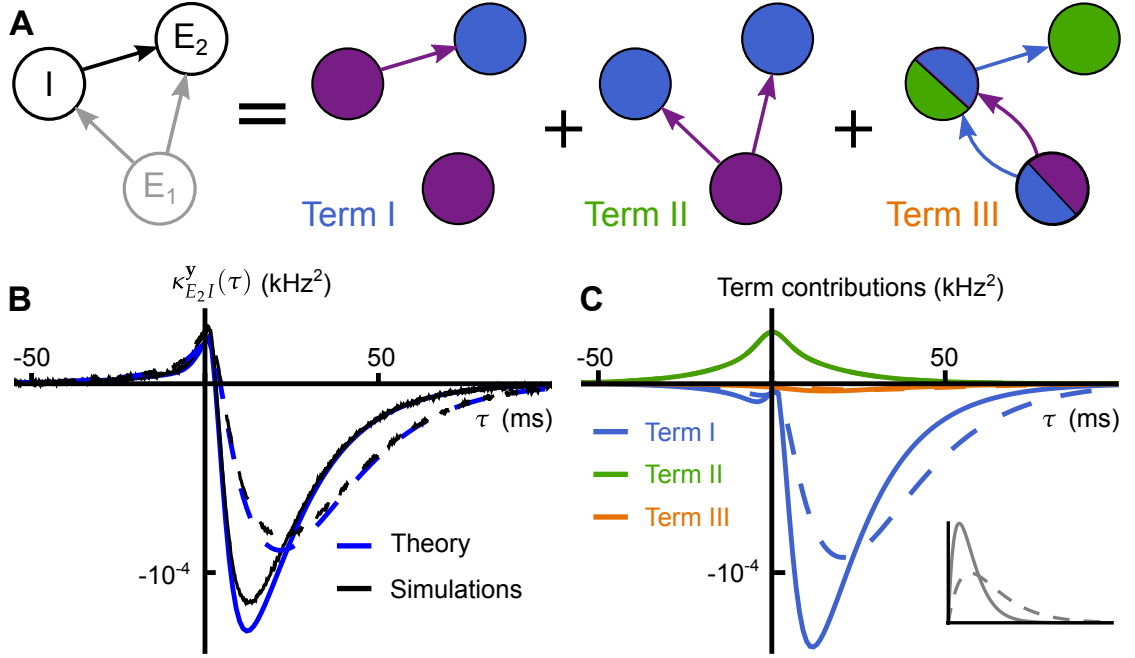


Figure 6.2: **Linear response path expansion of correlations in a feed-forward inhibitory (FFI) microcircuit.** (A) Linear response path expansion of the second order correlations for cells (E_2, I) in the FFI microcircuit. Each of the three terms appearing in the finite expansion correspond to the contribution of a different motif, and their values are denoted in Eq. (6.6). (B) Comparison of the linear response approximation of correlations with Monte Carlo estimation of the second-order cross-cumulant density for the pair (E_2, I) in the FFI microcircuit. Results are plotted for two values of the inhibitory time constant τ_I . The solid line corresponds to $\tau_I = 5$ ms, and the dashed line to $\tau_I = 10$ ms. (C) Plot of the three contributions to the cross-cumulant density for the pair (E_2, I) as determined from the linear response expansion of their correlation structure (Eq. (6.6)). Solid and dashed lines again correspond to values for the two different inhibitory synaptic time constants. The inset shows the two inhibitory synaptic kernels.

For instance, the cross-spectrum for the pair (E_2, I) is given by

$$\begin{aligned}
 S_{E_2 I}^y &= \tilde{K}_{E_2 I}^* S_{0, I}^y + \tilde{K}_{E_2 E_1}^* \tilde{K}_{I E_1} S_{0, E_1}^y + \tilde{K}_{E_2 I}^* |\tilde{K}_{I E_1}|^2 S_{0, E_1}^y \\
 &= \underbrace{(\tilde{A}_{E_2} \tilde{\beta}_{E_2 I})^*}_{I} S_{0, I}^y + \underbrace{(\tilde{A}_{E_2} \tilde{\beta}_{E_2 E_1})^* (\tilde{A}_I \tilde{\beta}_{I E_1})}_{II} S_{0, E_1}^y + \underbrace{(\tilde{A}_{E_2} \tilde{\beta}_{E_2 I})^* |\tilde{A}_I \tilde{\beta}_{I E_1}|^2}_{III} S_{0, E_1}^y, \quad (6.6)
 \end{aligned}$$

where the uncoupled spectra $S_{0, \cdot}^y$ are equal to the corresponding entries of \mathbf{S}_0^y and \tilde{A} are the susceptibility functions (see Chapter 5). The functions $\beta_{ij}(t) = \mathbf{W}_{ij} \alpha_j(t)$ are the weighted

synaptic kernels (see Eq. (5.5)) so that the $\tilde{\beta}_{ij}(\omega)$ are their Fourier transforms.

Equation (6.6) provides intuition about how the joint response of cells E_2 and I is shaped by the features of the network — namely, the synaptic architecture and marginal dynamical properties of the individual neurons. At first order, term I corresponds to the effect of the direction connection from cell I to E_2 . The second order term II captures the correlating effect of the common input arriving to each cell from neuron E_1 . Lastly, term III approximates the contribution to correlations between cells E_2 and I due to the interaction of the synapse connection $E_1 \rightarrow I$ and the two-synapse pathway from E_1 to E_2 through neuron I . This diverging motif provides an indirect source for common input. We plot the temporal domain contributions of these three terms in Figure 6.2C.

In order to gain insight into how synaptic properties can shape the correlation structure within the FFI microcircuit, we varied the time constant τ_I governing the synaptic dynamics of the connection $I \rightarrow E_2$. First, we compare theory and simulations for two values of the time constant in Figure 6.2B. Note that the slower inhibitory time constant results in an elongated cross-cumulant density.

Referring to Figure 6.2C, the linear response decomposition of the correlations reveals that the effect of changing the time constant on the cross-cumulant density is primarily reflected in the first order term (light blue lines). Referring to Eq. (6.6), we see that term I includes a factor $\tilde{\beta}_{E_2 I}$. This frequency-domain multiplication becomes a convolution in the temporal domain. Decreasing τ_I sharpens the synaptic filter resulting in a corresponding decrease in the timescale of the first order term I, and hence, in the cross-cumulant density as well. The decrease in the cross-cumulant density at values $\tau > 0$ implies the aforementioned gating of the output of cell E_2 by cell I , tightening the timing dependencies between the outputs of these two cells. [78, 118, 145, 198, 288].

At second order, term II in Eq. (6.6) captures the effect of the common input to the two cells. This contribution does not involve the inhibitory synaptic kernel, and is therefore unaffected by the change to the synaptic time constant. At third-order, term III in Eq. (6.6) is similarly smoothed as the first order term, though its contribution is significantly smaller. We note that, in general, higher order contributions need not be negligible, a fact we illustrate in the next example.

6.2.2 Bi-directional excitatory microcircuit

Experiments conducted on rats have revealed that bidirectional synaptic interactions between pairs of neurons are significantly more common than would be expected for truly random (i.e., Erdős-Rényi) cortical connectivity [121, 179, 255, 260]. Thus, it is important to understand how mutual connectivity between neurons shapes their correlation structure. To this end, we consider the linear response approximation to the correlation structure for a pair of reciprocally-connected excitatory neurons E_1 and E_2 (Figure 6.3A, left).

In this case, we have

$$\tilde{\mathbf{K}} = \begin{pmatrix} 0 & \tilde{K}_{E_1 E_2} \\ \tilde{K}_{E_2 E_1} & 0 \end{pmatrix},$$

so that

$$(\mathbf{I} - \tilde{\mathbf{K}})^{-1} = \frac{1}{1 - \tilde{K}_{E_1 E_2} \tilde{K}_{E_2 E_1}} (\mathbf{I} + \tilde{\mathbf{K}}).$$

Substituting this matrix inverse into Eq. (6.1) yields the following approximation to the

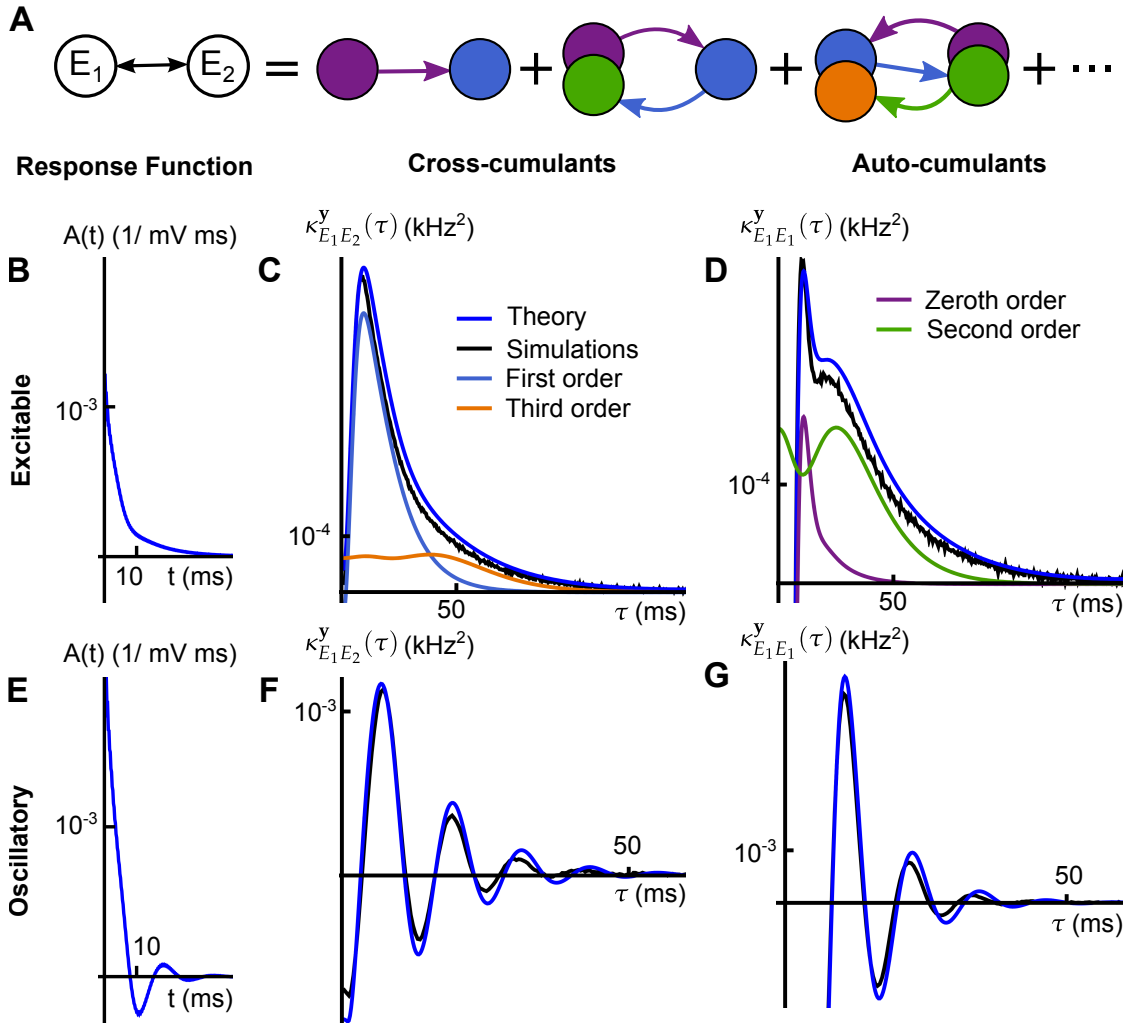


Figure 6.3: **Linear response path expansion of correlations in a bidirectional excitatory microcircuit.** (A) The cross-cumulant density of the two cells can be represented in terms of contributions from an infinite sequence of submotifs (See Eq. (6.8)). Though we show only a few “chain” motifs in one direction, one should note that there will also be contributions to the cross-cumulant from chain motifs in the reverse direction in addition to indirect common input motifs (See Figure 6.1). (B), (E) Linear response kernels in the excitable (B) and oscillatory (E) regimes. (C), (F) Comparison of the cross-cumulant density computed from Monte Carlo simulation and linear response theory (from Eq. (6.7)) with first and third order contributions (from Eq. (6.8)) in the excitable (C) and oscillatory (F) regimes. (D), (G) Comparison of the auto-cumulant density computed from Monte Carlo simulation and linear response theory (from Eq. (6.7)) with zeroth and second order contributions (from Eq. (6.8)) in the excitable (D) and oscillatory (G) regimes.

matrix of cross-spectra for the microcircuit

$$\begin{aligned}
 \mathbf{s}^y &= \frac{1}{|1 - \tilde{K}_{E_1 E_2} \tilde{K}_{E_2 E_1}|^2} (\mathbf{I} + \overline{\tilde{\mathbf{K}}}) \begin{pmatrix} S_{0,E_1}^y & 0 \\ 0 & S_{0,E_2}^y \end{pmatrix} (\mathbf{I} + \tilde{\mathbf{K}}^T) \\
 &= \frac{1}{|1 - \tilde{K}_{E_1 E_2} \tilde{K}_{E_2 E_1}|^2} \begin{pmatrix} S_{0,E_1}^y + |\tilde{K}_{E_1 E_2}|^2 S_{0,E_2}^y & \tilde{K}_{E_1 E_2}^* S_{0,E_2}^y + \tilde{K}_{E_2 E_1} S_{0,E_1}^y \\ \tilde{K}_{E_1 E_2} S_{0,E_2}^y + \tilde{K}_{E_2 E_1}^* S_{0,E_1}^y & S_{0,E_2}^y + |\tilde{K}_{E_2 E_1}|^2 S_{0,E_1}^y \end{pmatrix}.
 \end{aligned} \tag{6.7}$$

In contrast to the previous example, the linear response approximation of the second order correlation structure does not terminate at finite order in the interaction matrix $\tilde{\mathbf{K}}$ owing to the non-polynomial prefactor. This is a reflection of the non-nilpotency of $\tilde{\mathbf{K}}$, or equivalently, the existence of directed chains of infinite length through this circuit (allowing for repetition of connections).

Following our exploration of the impact of synaptic dynamics on neuronal correlation structure in the previous example, we will now investigate the effect of the marginal firing rate dynamics on correlations in the context of the bidirectional excitatory microcircuit. To this end, we placed the neurons in two regimes — the first was an *excitable* regime where, in the absence of input from its synaptic partner, the firing rate of each neuron is relatively low, but the membrane potential lives close to the firing threshold much of the time (Figure 6.3B-D). In the excitable regime, firing is highly irregular (ISI CV ≈ 0.98). We also placed the neurons in an *oscillatory* regime, characterized by strong, regular firing in the absence of input from the other neuron (ISI CV ≈ 0.31). Synaptic input from the other neuron in the circuit tended only to slightly perturb spike times in this regime. The firing regime of the neuron was set by manipulating the mean of the intrinsic fluctuations provided to each cell, which directly determines the rest potential of the neuron. When the rest potential is not too far below threshold, the neuron is excitable, and when it is near or above the firing threshold, oscillatory activity results.

In a linear response theory applications, these changes in firing regime of the neurons are reflected in the linear response function A of each neuron, as well as in their uncoupled power spectra S_0^y . To gain a better understanding of the impact of the alteration of the firing regime on the marginal spiking dynamics, we present the firing rate linear response functions for a neuron in the excitable regime (Figure 6.3B) as well as the oscillatory regime (Figure 6.3E). Notably, the response function for the neuron in the oscillatory regime exhibits a resonance absent in that of the excitable neuron, a reflection of the natural firing frequency of the neuron.

Returning to the approximation of correlations between these two neurons given in Eq. (6.7), expanding the prefactor allows us to express the cross-spectrum between E_1 and E_2 as an infinite series:

$$S_{E_1 E_2}^y = \sum_{n,m=0}^{\infty} (\tilde{K}_{E_1}^* \tilde{K}_{E_2}^*)^n (\tilde{K}_{E_1} \tilde{K}_{E_2})^m \left(\tilde{K}_{E_1 E_2}^* S_{0,E_1}^y + \tilde{K}_{E_2 E_1} S_{0,E_2}^y \right). \quad (6.8)$$

Paths within the synaptic architecture of this microcircuit which contribute to the cross-correlations between the two neurons (see Figure 6.1) must originate from one of the two cells, and the two branches must terminate each at a different cell. This implies that one of the branches must be of odd length (one branch connects the root cell with itself), and the other of even length (connecting the root cell to the other cell). Hence, all contributions to the correlations *between* the two cells are from paths of odd order. This is reflected in Eq. (6.8), where each term of the expansion consists of a multiplication of an odd number of interaction kernels \tilde{K} . We depict three of the contributing motifs in Figure 6.3A. Similar reasoning shows that only even order motifs will contribute to the linear response approximation of the coupled power spectra (i.e., the auto-cumulants or auto-correlations of neurons in the circuit).

We compare the linear response approximation of correlations to results obtained via

Monte Carlo estimation in Figure 6.3. The match is excellent in both regimes. We also present in Figure 6.3 some lower order contributions to the second order cross- and auto-cumulant densities for neurons in the bidirectional excitatory microcircuit. Results for excitable neurons are in panels C and D, while those for oscillatory neurons are in panels F and G. For the excitable neurons, we see that third order contributions to the cross-cumulant density of the two neurons (orange line, panel C), while small in comparison to their first order counterparts (light blue line, panel C), are certainly not insignificant, which was the case in the FFI circuit (Figure 6.2).

Likewise, Figure 6.3D exhibits that, for neurons in the excitable regime, second order contributions to the auto-correlation are of similar magnitude to the zeroth order terms (i.e., the uncoupled spectra S_0^y). These second order contributions arise from two sources — first, the resonance exhibited away from $\tau = 0$ is the signature of the neurons detection of its own output (i.e., the contribution of the length two chain connecting the neuron to itself). In addition, the synaptic input from the other cell in the circuit acts as “common input” to a cell, supplying a peak in this contribution near $\tau = 0$ in analogy to the peak in the cross-cumulant density induced by common input to a pair of distinct neurons (green line, Figure 6.2C). For neurons in the oscillatory regime, the first (in the case of the cross-cumulant) and zeroth (in the case of the auto-cumulant) order terms are dominant, so we do not bother to plot higher order contributions.

In the oscillatory regime, higher order contributions to the cross- and auto-cumulants were small relative to first order contributions and are therefore not shown in panels F and G of Figure 6.3. In addition, the network’s symmetry implies that cross-cumulant densities are symmetric, and we only show these functions for positive lags. The long window spike count correlation coefficient $\rho_{E_1 E_2}(\infty)$ between the two cells was ≈ 0.8 in

the excitable regime and ≈ 0.5 in the oscillatory regime.

6.3 Linear response applications to large networks

The full power of the present approach becomes evident when analyzing the activity of networks larger than the microcircuits considered to this point. We again illustrate the accuracy and utility of the linear response theory using several examples.

In all-to-all networks where inhibition and excitation are tuned to be precisely balanced, the theory reveals that the only contributions to correlations are from local paths — specifically, from first order (direct) interactions and second order common input. If this balance is broken, terms appear in the linear response expansion of correlations which correspond to longer paths (and hence, higher order motifs). One immediate consequence is that a relative increase in inhibition can lead to elevated network synchrony in such networks.

Following our treatment of the simple, all-to-all case, we also consider two other large network examples. In random Erdős-Rényi networks, we exhibit how linear response allows for the derivation of accurate approximations of the average temporal structure of the cross-cumulant density. In the final pair of examples, we treat very large networks with distance-dependent connectivity, exploring the relationship between interneuronal distance and correlation in their activity. As a side note, these examples also demonstrate the computational expediency of the linear response theory of correlations relative to traditional Monte Carlo methods for determining the structure of temporal dependencies in complex neuronal networks.

6.3.1 All-to-all networks

Consider an all-to-all coupled network of N neurons with identical membrane and spiking parameters¹. Of these cells, N_E make excitatory, and N_I make inhibitory synaptic connections. The excitatory cells are assigned indices $1, 2, \dots, N_E$, and the inhibitory cells indices $N_E + 1, N_E + 2, \dots, N$, where $N = N_E + N_I$. We assume that all excitatory (resp. inhibitory) synapses have identical weights $W_E = \frac{G_E}{N_E}$ (resp. $W_I = \frac{G_I}{N_I}$). Synaptic kernels are given by alpha functions (Eq. (5.6)) with time constant $\tau_E = 10$ ms (resp. $\tau_I = 5$ ms). The constants G_E, G_I set the overall strength of excitation and inhibition in the network.

In this case, the interaction matrix $\tilde{\mathbf{K}}$ can be written in block form as

$$\tilde{\mathbf{K}} = \tilde{A}\tilde{\boldsymbol{\beta}}, \quad \text{where} \quad \tilde{\boldsymbol{\beta}} = \begin{pmatrix} \tilde{\boldsymbol{\beta}}_E \mathbf{1}_{N_E N_E} & \tilde{\boldsymbol{\beta}}_I \mathbf{1}_{N_E N_I} \\ \tilde{\boldsymbol{\beta}}_E \mathbf{1}_{N_E N_I} & \tilde{\boldsymbol{\beta}}_I \mathbf{1}_{N_I N_I} \end{pmatrix}.$$

In the previous expression, $\mathbf{1}_{N_1 N_2}$ is the $N_1 \times N_2$ matrix of ones, $\tilde{\boldsymbol{\beta}}_X = W_X \tilde{\alpha}_X$ is the weighted synaptic kernel applied to the output of cells in class $X \in \{E, I\}$ (assumed identical within each class), and \tilde{A} is the common susceptibility network for each cell in the network. Autaptic synapses (i.e., synapses from a cell to itself) are included in order to greatly simplify the analysis. We show in Figure 6.4 that their inclusion has negligible impact.

Define the quantities $\tilde{\varphi}_E = N_E \tilde{\boldsymbol{\beta}}_E$, $\tilde{\varphi}_I = N_I \tilde{\boldsymbol{\beta}}_I$, and $\tilde{\varphi} = \tilde{\varphi}_E + \tilde{\varphi}_I$. A simple inductive argument gives that, for every $k \geq 1$, we have

$$\tilde{\mathbf{K}}^k = \tilde{A}^k \tilde{\varphi}^{k-1} \tilde{\boldsymbol{\beta}}.$$

In addition, direct matrix multiplication yields

$$\overline{\tilde{\mathbf{K}}\tilde{\mathbf{K}}^T} = \tilde{\varphi}_c \mathbf{1}_{NN}, \quad \text{where} \quad \tilde{\varphi}_c = N_E |\tilde{\boldsymbol{\beta}}_E|^2 + N_I |\tilde{\boldsymbol{\beta}}_I|^2,$$

¹Consideration of identical neurons implies equivalency of their uncoupled spectra as well as their firing rate linear response functions in the absence of coupling.

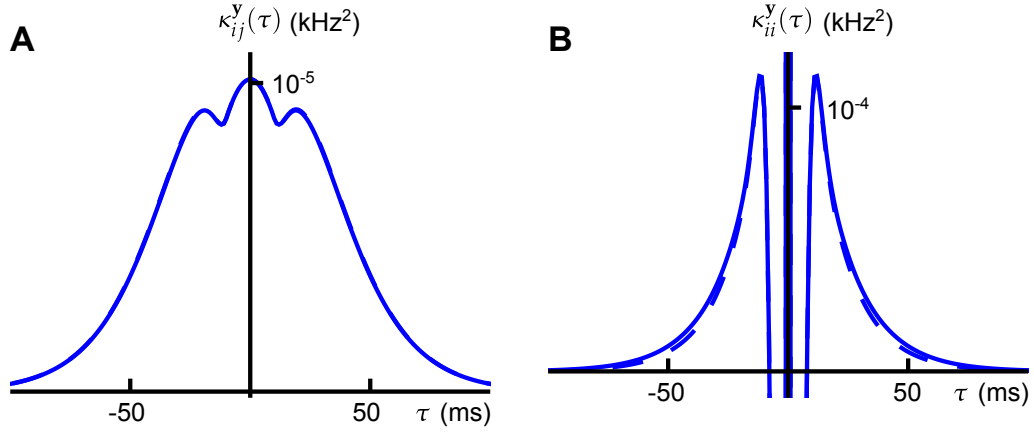


Figure 6.4: **Inclusion of autaptic connections in the all-to-all network has a negligible impact on correlations.** (A) Comparison of the linear response theory prediction of a second order cross-cumulant density in an all-to-all network of size $N = 100$ with (solid line) and without (dashed line) autaptic connections. Relative L^2 difference was approximately 0.0043 (the two lines are almost exactly on top of one another). (B) Same as panel A, for a second order auto-cumulant density. Relative L^2 difference was approximately 0.0016.

which allows for direct calculation of the matrix products $(\bar{\mathbf{K}})^n (\tilde{\mathbf{K}})^m$ when $n, m \neq 0$,

$$(\bar{\mathbf{K}})^n (\tilde{\mathbf{K}})^m = \tilde{A}^{n*} \tilde{A}^l \tilde{\varphi}^{(n-1)*} \tilde{\varphi}^{m-1} \tilde{\varphi}_c \mathbf{1}_{NN}. \quad (6.9)$$

Note that the dynamical homogeneity assumption implies that we can write $\mathbf{S}_0^y = S_0^y \mathbf{I}$ — i.e., all cells have a common uncoupled power spectrum. Substituting Eq. (6.9) into Eq. (6.1) gives

$$\begin{aligned} \mathbf{S}^y &= S_0^y \sum_{n,m=0}^{\infty} (\bar{\mathbf{K}})^n (\tilde{\mathbf{K}})^m \\ &= S_0^y \left[\left(\frac{\tilde{A}}{1 - \tilde{A}\tilde{\varphi}} \right)^* \bar{\boldsymbol{\beta}} + \left(\frac{\tilde{A}}{1 - \tilde{A}\tilde{\varphi}} \right) \tilde{\boldsymbol{\beta}}^T \left| \frac{\tilde{A}}{1 - \tilde{A}\tilde{\varphi}} \right|^2 \tilde{\varphi}_c \mathbf{1}_{NN} + \mathbf{I}_N \right]. \end{aligned} \quad (6.10)$$

Thus, due to the block structure of the matrices in Eq. (6.10), the cross-spectrum between two cells in the network depends only on the class (excitatory or inhibitory of the two cells),

$$S_{ij}^y |_{i \in X, j \in Y} = S_0^y \left[\left(\frac{\tilde{A}}{1 - \tilde{A}\tilde{\varphi}} \right)^* \frac{\tilde{\varphi}_Y^*}{N_Y} + \left(\frac{\tilde{A}}{1 - \tilde{A}\tilde{\varphi}} \right) \frac{\tilde{\varphi}_X}{N_X} + \left| \frac{\tilde{A}}{1 - \tilde{A}\tilde{\varphi}} \right|^2 \tilde{\varphi}_c + \delta_{ij} \right], \quad (6.11)$$

where $X, Y \in \{E, I\}$.

In Eq. (6.11) the first term represents the effects of all directed chains originating at cell j and terminating at cell i , and from cell j to cell i for the second term. To see this, one can expand the denominators of these terms as power series in $\tilde{A}\tilde{\varphi}$. The third term represents the effects of direct and indirect common inputs to the two neurons, an observation reached by similarly expanding the denominator of this term as a product of power series in each of $(\tilde{A}\tilde{\varphi})^*$ and $\tilde{A}\tilde{\varphi}$. In Figure. 6.5A, we highlight a few of these contributing motifs.

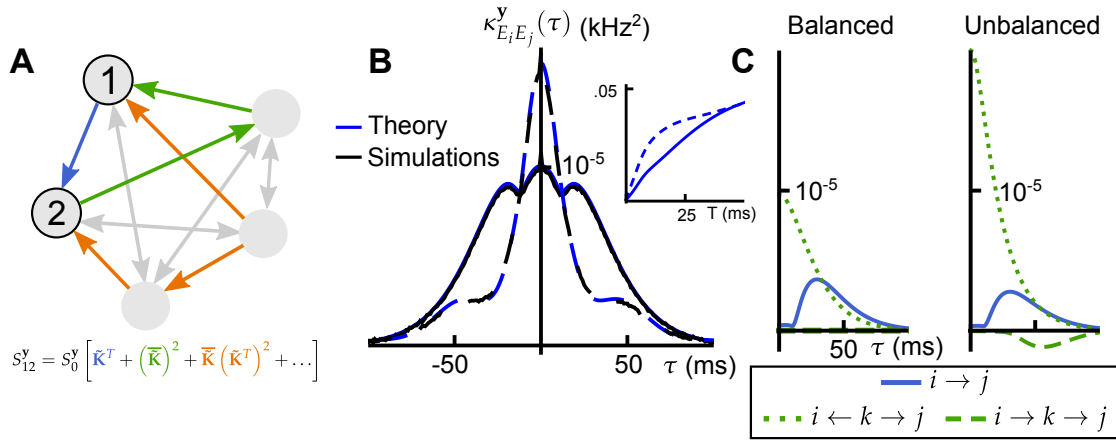


Figure 6.5: **Linear response theory of correlations in all-to-all networks, and the importance of higher order motifs.** (A) Some of the submotifs contributing to correlations in the all-to-all network. (B) Comparison of Monte Carlo estimation cross-cumulant density between two excitatory cells in an all-to-all network with the linear response theoretical prediction obtained using Eq. (6.11) (Solid lines – precisely tuned network with $\tilde{\varphi} \equiv 0$ [$G_E = -G_I = 140$ mV·ms, $\tau_E = \tau_I = 10$ ms], dashed – non-precisely tuned network with $\tilde{\varphi} \neq 0$ [$G_E = 168$ mV·ms, $G_I = -210$ mV·ms, $\tau_E = 10$ ms, $\tau_I = 5$ ms]). The population sizes were $N_E = 80, N_I = 20$. (C) Comparison of first and second order contributions to the cross-correlation function in panel A in the precisely tuned (left) and non-precisely tuned (right) network. In both cases, the long window correlation coefficient $\rho_{ij}^y(\infty)$ was 0.05. The blue line indicates the contribution due to the direct connection between the two cells, while the dotted green line captures contributions due to second order chain motifs, and the dashed green line second order diverging motifs (common input).

When excitation and inhibition are tuned for precise balance in both strength and the speed of their synaptic dynamics, the temporal averages of the excitatory and inhibitory

currents cancel each other, and we have $\tilde{\varphi} = \tilde{\varphi}_E + \tilde{\varphi}_I = 0$. Using $\tilde{\varphi} = 0$ in Eq. (6.11) yields

$$S_{ij}^y |_{i \in X, j \in Y} = S_0^y \left[\tilde{A}^* \frac{\tilde{\varphi}_Y^*}{N_Y} + \tilde{A} \frac{\tilde{\varphi}_X}{N_X} + |\tilde{A}|^2 \tilde{\varphi}_c + \delta_{ij} \right]. \quad (6.12)$$

Effects of direct connections between the cells are captured by the first two terms, while those of direct common inputs to the pair are captured by the third term. Interestingly, contributions from any other submotif of the synaptic architecture precisely cancel, and do not appear in the linear response approximation of correlations. In other words, *in the precisely balanced case, only local interactions contribute to correlations.*

To understand this cancelation intuitively, consider the contribution of directed chains originating at a given excitatory neuron, j . For $\tau > 0$, the cross cumulant density, $\kappa_{ij}^y(\tau)$, is directly determined by the expected change in firing rate of cell j given a spike in cell i τ units of time in the past (see Eq. (2.14)). By the symmetry of the all-to-all connectivity and assumed joint stationarity of the network activity, the firing of cell j has an equal probability of eliciting a spike in any excitatory or inhibitory cell in the network. Due to the precise synaptic balance, the postsynaptic current generated by the elicited spikes in the excitatory population will cancel the postsynaptic current due to elicited spikes in the inhibitory population on average. The contribution of other motifs cancel in a similar way.

In Figure 6.5B, we show the impact of breaking this excitatory-inhibitory balance on cross-correlation functions. We increased the strength and speed of the inhibitory synapses relative to excitatory synapses. For comparison purposes, we held constant the long window correlation coefficients $\rho_{ij}^y(\infty)$ between excitatory pairs by increasing both the excitatory and inhibitory weights (note that, by symmetry, all excitatory pairs should have the same correlation coefficient). Moreover, the degree of network synchrony, characterized by the short window correlation coefficients, is increased (See Figure 6.5B inset).

Intuitively, a spike in one of the excitatory cells transiently increases the likelihood of spiking in all other cells in the network. Since inhibition in the network is stronger and faster than excitation, these additional spikes will transiently decrease the likelihood of spiking in twice removed cells.

Linear response theory allows us to confirm this heuristic observation, and quantify the impact of the imbalance on second order statistics. Expanding Eq. (6.11) for two excitatory cells to second order in coupling strength, we find

$$S_{E_i E_j}^y = S_0^y \left[\tilde{A}^* \frac{\tilde{\varphi}_E^*}{N_E} + \tilde{A} \frac{\tilde{\varphi}_E}{N_E} + |\tilde{A}|^2 \tilde{\varphi}_c + \underbrace{(\tilde{A}^*)^2 \tilde{\varphi}^* \frac{\tilde{\varphi}_E^*}{N_E}} + \underbrace{\tilde{A}^2 \tilde{\varphi} \frac{\tilde{\varphi}_E}{N_E}} + \delta_{ij} \right] + \mathcal{O}(\|\tilde{\mathbf{K}}\|^3). \quad (6.13)$$

Compared to the balanced case, there is no longer a complete cancellation between contributions of chains involving excitatory and inhibitory cells, and the two underlined terms appear as a result (compare with Eq. (6.12)). These terms capture the effects of all length two chains between cells E_i or E_j , starting at one and terminating at the other.

The relative strengthening of inhibition implies that chains of length two provide a negative contribution to the cross-correlation function at short times (*cf.* [288] and the dashed green lines in Figure 6.5C). Additionally, the impact of direct common input to cells E_i and E_j on correlations is both larger in magnitude (because we increased the strength of both connection types) and sharper (the faster inhibitory time constant means common inhibitory inputs induce sharper correlations). These changes are reflected in the shape of the second order, common input term $|\tilde{A}|^2 \tilde{\varphi}_c$ in Eq. (6.13) (see dotted green lines in Figure 6.5C).

In sum, breaking the balance between excitation and inhibition via stronger, faster inhibitory synapses enhances synchrony, moving a greater proportion of the covariance mass closer to $\tau = 0$ (See Figure 6.5B). To illustrate this effect in terms of underlying connectivity motifs, we show the contributions of length two chains and common input in

both the precisely tuned and non-precisely tuned cases in Figure 6.5C. A similar approach would allow us to understand the impact of a wide range of changes in cellular or synaptic dynamics on the structure of correlations across networks.

6.3.2 Random networks

Connectivity in cortical neuronal networks is typically sparse, and connection probabilities can follow distinct rules depending on area and layer [250]. The present theory allows us to consider arbitrary architectures, as we now illustrate.

We consider a randomly connected network of N_E excitatory and N_I inhibitory cells coupled with probability p . To simplify the analysis, every cell receives exactly pN_E excitatory and pN_I inhibitory inputs. Thus, having fixed in-degree (that is, the number of inputs is fixed and constant across cells), each cell receives an identical level of mean synaptic input. In addition, we continue to assume that cells are identical in their individual dynamical properties. Therefore, the response of each cell in the network is described by the same linear response kernel. The excitatory and inhibitory connection strengths are $G_E/(pN_E)$ and $G_I/(pN_I)$, respectively. The timescales of excitation and inhibition were allowed to differ, but are again identical for cells within each class. We note that the above restrictions are not general limitations of the linear response theory of correlations, but are pertinent to the identities we derive below.

When network connectivity is random, the approximation of network correlations (Eq. (6.1)) depends on the realization of the weight matrix \mathbf{W} . For a fixed realization of \mathbf{W} , the linear response approximation Eq. (6.1) can be solved numerically to approximate the correlation structure (See Figure 6.6A). However, the cross-cumulant density between a pair of cells of given types has a form which is easy to analyze when only leading order

terms in $1/N$ are retained. In what follows, we will derive these forms conditioned only on the class (i.e., excitatory or inhibitory) of the two cells involved (Proposition 6.3.1).

Following this, we derive the same average further conditioned on the first order connectivity of the pair in question (Proposition 6.3.2). This additional information leads to a significant reduction in variability in the linear response prediction of the average cross-cumulant density amongst pairs of neurons within the network. These results are suggestive of an idea which will be explored more fully in the linear response application of Chapter 7: Given some minimal characterizations of the synaptic architecture and marginal neuronal dynamics in a local cortical network, linear response theory can allow one to gain insight into the average structure of correlations in that area.

6.3.2.1 Average cross-cumulant densities in the random network

Proposition 6.3.1. *In the random network described in the open to Section 6.3.2, the average cross-spectrum for two cells of given types is*

$$\mathbf{E} \left\{ S_{ij}^y \right\}_{i \in X, j \in Y} = S_0^y \left[\left(\frac{\tilde{A}}{1 - \tilde{A}\tilde{\varphi}} \right)^* \frac{\tilde{\varphi}_Y^*}{N_Y} + \left(\frac{\tilde{A}}{1 - \tilde{A}\tilde{\varphi}} \right) \frac{\tilde{\varphi}_X}{N_X} + \left| \frac{\tilde{A}}{1 - \tilde{A}\tilde{\varphi}} \right|^2 \tilde{\varphi}_c \right] + \mathcal{O}(1/N^2), \quad (6.14)$$

when $i \neq j$, where $\mathbf{E} \{ \cdot \}$ represents an average over realizations of the weight matrix \mathbf{W} . In addition, the average power spectrum ($i = j$) is given by

$$\mathbf{E} \left\{ S_{ii}^y \right\}_{i \in X} = S_0^y \left[1 + \left(\frac{\tilde{A}}{1 - \tilde{A}\tilde{\varphi}} \right) \frac{\tilde{\varphi}_X}{N_X} + \left(\frac{\tilde{A}}{1 - \tilde{A}\tilde{\varphi}} \right)^* \frac{\tilde{\varphi}_X^*}{N_X} + \left| \frac{\tilde{A}}{1 - \tilde{A}\tilde{\varphi}} \right|^2 \tilde{\varphi}_c + |\tilde{A}|^2 \tilde{\varphi}_c \left(\frac{1-p}{p} \right) \right] + \mathcal{O}(1/N^2). \quad (6.15)$$

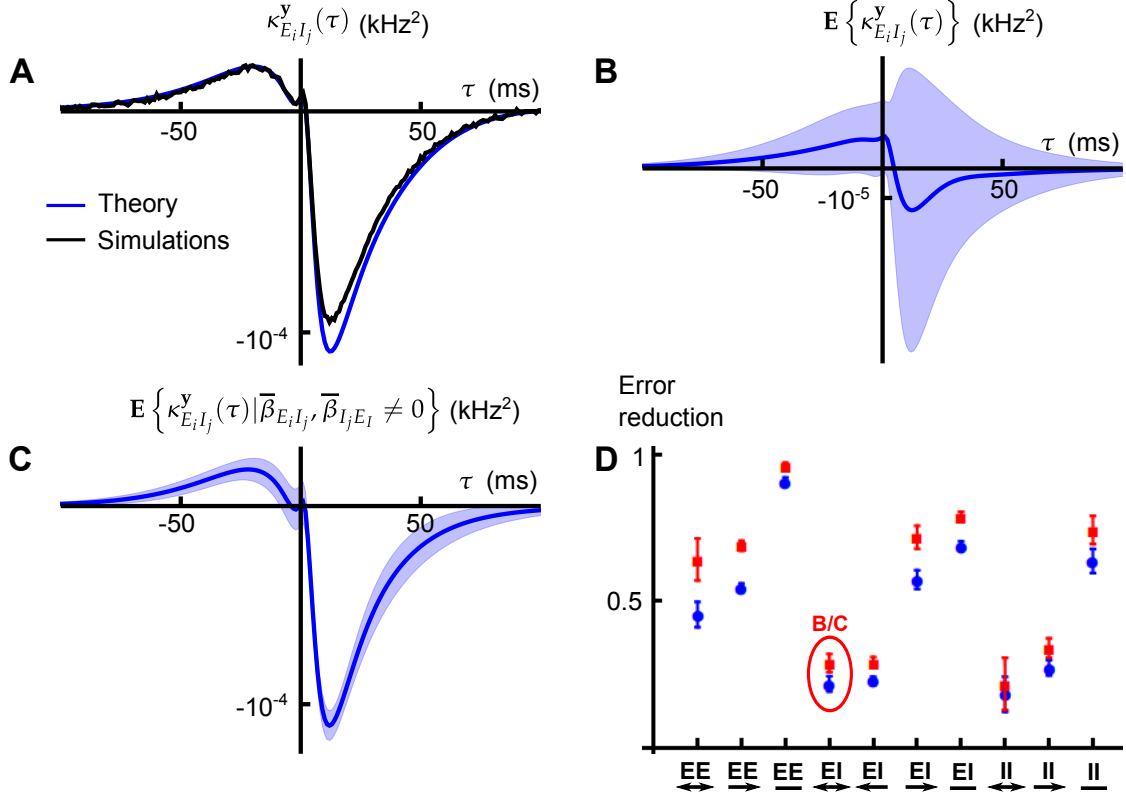


Figure 6.6: **Application of the linear response to a random network reveals the average second order temporal correlation structure.** (A) A comparison of numerically obtained excitatory-inhibitory cross-correlations to the approximation given by Eq. (6.31). (B) Mean and standard deviation for the distribution of correlation functions for excitatory-inhibitory pairs of cells. (Solid line – mean cross-correlation, shaded area – one standard deviation from the mean, calculated using bootstrapping in a single network realization). (C) Mean and standard deviation for the distribution of cross-correlation functions conditioned on cell type *and* first order connectivity for a reciprocally coupled excitatory-inhibitory pair of cells. (Solid line – mean cross-correlation function, shaded area – one standard deviation from the mean found by bootstrapping). (D) Average reduction in L^2 error between cross-correlation functions and their respective first-order conditioned averages, relative to the error between the cross-correlations and their cell-type averages. Blue circles give results for a precisely tuned network, and red squares for a network with stronger, faster inhibition. Error bars indicate two standard errors above and below the mean. G_E, G_I, τ_E, τ_I for panels A-C are as in the precisely tuned network of Figure 6.5, and the two networks of panel D are as in the networks of the same figure.

Proof. Under the given assumptions, the interaction matrix $\tilde{\mathbf{K}}$ takes the form

$$\tilde{\mathbf{K}}(\omega) = \tilde{A}(\omega)\tilde{\boldsymbol{\beta}}(\omega) \quad \text{where} \quad \tilde{\boldsymbol{\beta}}(\omega) = \begin{pmatrix} \frac{G_E}{pN_E}\tilde{\alpha}_E(\omega)\mathbf{R}_{N_EN_E} & \frac{G_I}{pN_I}\tilde{\alpha}_I(\omega)\mathbf{R}_{N_EN_I} \\ \frac{G_E}{pN_E}\tilde{\alpha}_E(\omega)\mathbf{R}_{N_IN_E} & \frac{G_I}{pN_I}\tilde{\alpha}_I(\omega)\mathbf{R}_{N_IN_I} \end{pmatrix}, \quad (6.16)$$

and $\mathbf{R}_{N_1N_2}$ is a random $N_1 \times N_2$ matrix of 0's and 1's, with pN_2 chosen non-zero entries on each row. Note that entries of $\tilde{\mathbf{K}}(\omega)$ are independent except within the rows of each block. Moving forward, we will suppress dependencies on ω for notational purposes. The derived expressions can be assumed to hold for each ω .

In the following, $\mathbf{E}\{\cdot\}$ is an average over realizations of the random adjacency matrices \mathbf{R}_{XY} . We define $\tilde{\varphi}_X$ to be

$$\begin{aligned} \tilde{\varphi}_X &= \sum_{k_0 \in X} \mathbf{E}\{\tilde{\beta}_{k_1k_0}\} = N_X \mathbf{E}\{\tilde{\beta}_{k_1k_0}\}_{k_0 \in X} \\ &= N_X \left(\frac{G_X}{pN_X} \tilde{\alpha}_E \right) p \\ &= G_X \tilde{\alpha}_X, \end{aligned} \quad (6.17)$$

where we have used the subscript notation $k_0 \in X$ to denote that the cell with index k_0 belongs to class $X = E$ or $X = I$. Note that the definition of $\tilde{\varphi}_X$ is independent of the index k_1 chosen, and can alternatively be defined as the same value via a simple sum without expectations as we assumed in-degrees to be fixed. We also define the quantity $\tilde{\varphi}$ as

$$\tilde{\varphi} = \sum_{k_0} \mathbf{E}\{\tilde{\beta}_{k_1k_0}\} = \tilde{\varphi}_E + \tilde{\varphi}_I = G_E \tilde{\alpha}_E + G_I \tilde{\alpha}_I, \quad (6.18)$$

and $\tilde{\varphi}_c$ as

$$\begin{aligned} \tilde{\varphi}_c &= \sum_{k_0} \mathbf{E}\{\tilde{\beta}_{k_1k_0}\tilde{\beta}_{l_1k_0}^*\} \\ &= N_E \mathbf{E}\{\tilde{\beta}_{k_1k_0}\tilde{\beta}_{l_1k_0}^*\}_{k_0 \in E} + N_I \mathbf{E}\{\tilde{\beta}_{k_1k_0}\tilde{\beta}_{l_1k_0}^*\}_{k_0 \in I} \\ &= N_E \left| \frac{G_E}{pN_E} \tilde{\alpha}_E \right|^2 p^2 + N_I \left| \frac{G_I}{pN_I} \tilde{\alpha}_I \right|^2 p^2 \\ &= \frac{1}{N_E} |\tilde{\varphi}_E|^2 + \frac{1}{N_I} |\tilde{\varphi}_I|^2. \end{aligned} \quad (6.19)$$

We note that the definition of $\tilde{\varphi}_c$ is independent of the indices k_1, l_1 , so long as $k_1 \neq l_1$. To understand this calculation, as we sum over k_0 , we will sum over N_E excitatory cells and N_I inhibitory cells. For each value of k_0 , conditioned on the type of cell being $k_0 \in X$, the squared absolute value of the matrix entry will be $|\frac{\tilde{\varphi}_X}{pN_E}|^2$ with probability p^2 (the probability both connections are "on"), and zero otherwise.

Approximate independence of the entries of $\tilde{\beta}$ Consider a pair of cells with indices i, j in the random network. From Eq. (6.1), we again series expand the linear response approximation to the correlation between cells i and j as

$$\begin{aligned} \mathbf{E} \left\{ S_{ij}^y \right\}_{i \in X, j \in Y} &= S_0^y \mathbf{E} \left\{ \left[\left(\mathbf{I} - \overline{A\tilde{\beta}} \right)^{-1} \left(\mathbf{I} - \tilde{A\tilde{\beta}} \right)^{-T} \right]_{ij} \right\}_{i \in X, j \in Y} \\ &= S_0^y \sum_{n,m=0}^{\infty} \tilde{A}^{n*} \tilde{A}^m \mathbf{E} \left\{ \left[\left(\overline{\tilde{\beta}} \right)^n \left(\tilde{\beta}^T \right)^m \right]_{ij} \right\}_{i \in X, j \in Y}. \end{aligned} \quad (6.20)$$

We will assume that the spectral radius $\Psi(\tilde{A\tilde{\beta}}) < 1$, and thus, this series converges.

The assumption of fixed in-degrees means that there are dependencies between the entries of \mathbf{W} (and hence, $\tilde{\beta}$) inside each row of each block of the matrix which are absent in a fully random network. The matrix consists of four blocks, corresponding to the pair types of pre- and post-synaptic cells (EE, EI, IE and II). However, if the network is large and connections are relatively weak, then the entries of the matrix $\tilde{\beta}$ are approximately independent, to leading order in $1/N$. In particular, we will show that

$$\begin{aligned} &\sum_{k_0, \dots, k_{n-1}, l_1, \dots, l_{m-1}=1}^N \left[\mathbf{E} \left\{ \tilde{\beta}_{ik_{n-1}} \tilde{\beta}_{k_{n-1}k_{n-2}} \cdots \tilde{\beta}_{k_1k_0} \tilde{\beta}_{l_1k_0}^* \cdots \tilde{\beta}_{jl_{m-1}}^* \right\} \right. \\ &\quad \left. - \mathbf{E} \left\{ \tilde{\beta}_{ik_{n-1}} \right\} \mathbf{E} \left\{ \tilde{\beta}_{k_{n-1}k_{n-2}} \right\} \cdots \mathbf{E} \left\{ \tilde{\beta}_{k_1k_0} \left(\tilde{\beta}_{l_1k_0}^* \right)^* \right\} \cdots \mathbf{E} \left\{ \left(\tilde{\beta}_{jl_{m-1}}^* \right)^* \right\} \right] \sim \mathcal{O}(1/N^2) \end{aligned} \quad (6.21)$$

holds for $0 < n, m \ll N$. When we do not have $n, m \ll N$, the difference will be small compared to an exponential prefactor which will always accompany these terms, and the relationship still holds.

In Eq. (6.21), we have neglected the conditioning of the cell types of i, j for notation, though this conditioning on cell type can be assumed to always be present. This means that, to lowest order in $1/N$, expectations of powers of $\tilde{\beta}$ can be taken as if all entries of the weight matrix \mathbf{W} were chosen completely independently, and without concern for the fixing of in-degrees. Note that the term $\mathbf{E} \left\{ \tilde{\beta}_{k_1 k_0} (\tilde{\beta}_{l_1 k_0})^* \right\}$ is not factored — these two terms will not be approximately independent as they both involve a connection originating from the same cell k_0 , meaning they will (when the connections are present) have the same value for any k_0 . Instead, these terms will be replaced by contributions in terms of $\tilde{\varphi}_c$, as we have from Eq. (6.19),

$$\sum_{k_0} \mathbf{E} \left\{ \tilde{\beta}_{k_1 k_0} (\tilde{\beta}_{l_1 k_0})^* \right\} = \tilde{\varphi}_c \quad \forall k_1, l_1.$$

In what follows, we prove Eq.(6.21) by considering various conditions on the values of n, m relative to the network size N . In particular, in cases 3 and 4, we assume that n, m are small enough so that the following approximations hold,

$$\begin{aligned} P(N-1, n-1) &\sim N^{n-1} + \mathcal{O}(N^{n-2}) \\ P(N-1, n+m-1) &\sim N^{n+m-1} + \mathcal{O}(N^{n+m-2}), \end{aligned} \tag{6.22}$$

where $P(x, y)$ stands for the number of permutations of y elements chosen from a pool of x , without replacement. Terms in the series expansion of correlations Eq. (6.2) will decay exponentially with an upper bound proportional to $\Psi(\tilde{\mathbf{K}})^{n+m}$, where $\psi(\tilde{\mathbf{K}})$ is the spectral radius of the matrix $\tilde{\mathbf{K}} = \tilde{A}\tilde{\beta}$. The spectral radius of $\tilde{\mathbf{K}}$ will typically vary with ω , so we assume the existence of a uniform bound below unity for all ω . We then assume that by the time the approximations in Eq. (6.22) are no longer valid, the order $n+m$ is large enough so as to make the contributions of the remaining tail of the series not significant. Numerical investigation confirms this to be a reasonable assumption for the networks we consider.

- **Case 1:** $n = 1, m = 0$

These values of n, m correspond to the correlating effects of direct synaptic interactions between pairs of cells. In this case, Eq. (6.21) is trivially satisfied. We have, by definition of $\tilde{\varphi}_E, \tilde{\varphi}_I$, that

$$\mathbf{E} \left\{ \tilde{\beta}_{ij} \right\}_{i \in X, j \in Y} = \frac{\tilde{\varphi}_Y}{N_Y}, \quad (6.23)$$

as the total amount of input from cells of class Y is $\tilde{\varphi}_Y$. This, in turn, implies that the expected impact of a single connection is as stated in Eq. (6.23).

- **Case 2:** $n = m = 1$

These values of n, m correspond to the correlating effects of direct shared inputs to pairs of cells in the network. In this case, we can find the exact value of $\mathbf{E} \left\{ \left[\tilde{\beta} \tilde{\beta}^T \right]_{ij} \right\}$. First, suppose $i \neq j$. From the definition of $\tilde{\varphi}_c$ (Eq. (6.19)), we have

$$\mathbf{E} \left\{ \left[\tilde{\beta} \tilde{\beta}^T \right]_{ij} \right\}_{i \in X, j \in Y} = \sum_{k=1}^N \mathbf{E} \left\{ \tilde{\beta}_{ik}^* \tilde{\beta}_{jk} \right\} = \tilde{\varphi}_c. \quad (6.24)$$

Similarly, if $i = j$, we find

$$\mathbf{E} \left\{ \left[\tilde{\beta} \tilde{\beta}^T \right]_{ii} \right\}_{i \in X} = \sum_{k=1}^N \mathbf{E} \left\{ |\tilde{\beta}_{ik}|^2 \right\} = N_E \left| \frac{G_E}{pN_E} \tilde{\alpha}_E \right|^2 p + N_I \left| \frac{G_I}{pN_I} \tilde{\alpha}_I \right|^2 p = \frac{\tilde{\varphi}_c}{p}. \quad (6.25)$$

- **Case 3:** $2 \leq n \ll N, m = 0$

These values of n, m correspond to correlating effects of directed chains between cells in the network which are short relative to the size of the network. Following Eq. (6.21), for terms of this form we must examine the sum

$$\sum_{k_1, \dots, k_{n-1}=1}^N \left[\mathbf{E} \left\{ \tilde{\beta}_{ik_{n-1}} \cdots \tilde{\beta}_{k_2 k_1} \tilde{\beta}_{k_1 j} \right\} - \mathbf{E} \left\{ \tilde{\beta}_{ik_{n-1}} \right\} \cdots \mathbf{E} \left\{ \tilde{\beta}_{k_2 k_1} \right\} \mathbf{E} \left\{ \tilde{\beta}_{k_1 j} \right\} \right]. \quad (6.26)$$

Counting indices, we first note that there will be N^{n-1} terms in this sum. If all of the initial indices (which correspond to rows) are distinct, the corresponding entries

of $\tilde{\beta}$ are independent, and there is no contribution to the sum in Equation (6.26). The number of terms which factor (and cancel) due to being chosen from distinct rows will be at least the number of ways to pick different arrangements of $n - 1$ distinct integers from $1, \dots, i - 1, i + 1, \dots, N$, or $P(N - 1, n - 1)$. If $n \ll N$, then $P(N - 1, n - 1) = N^{n-1} + \mathcal{O}(N^{n-2})$, so that only $\mathcal{O}(N^{n-2})$ terms do not cancel.

Recall that each entry of $\tilde{\beta}$ is proportional to $1/N^n$ owing to the $1/N$ scaling of the connections. This implies that the error introduced by assuming independence of matrix entries when averaging is $\mathcal{O}(1/N^2)$. Hence, to leading order in $1/N$, we find

$$\begin{aligned}
 \mathbf{E} \left\{ \left[\tilde{\beta}^n \right]_{ij} \right\}_{i \in X, j \in Y} &= \sum_{k_1, \dots, k_{n-1}=1}^N \mathbf{E} \{ \tilde{\beta}_{ik_{n-1}} \cdots \tilde{\beta}_{k_2 k_1} \tilde{\beta}_{k_1 j} \}_{i \in X, j \in Y} \\
 &= \sum_{k_1, \dots, k_{n-1}=1}^N \mathbf{E} \{ \tilde{\beta}_{ik_{n-1}} \} \cdots \mathbf{E} \{ \tilde{\beta}_{k_2 k_1} \} \mathbf{E} \{ \tilde{\beta}_{k_1 j} \}_{i \in X, j \in Y} + \mathcal{O}(1/N^2) \\
 &= \left(\sum_{k_{n-1}} \mathbf{E} \{ \tilde{\beta}_{ik_{n-1}} \} \right) \cdots \left(\sum_{k_1} \mathbf{E} \{ \tilde{\beta}_{k_2 k_1} \} \right) \mathbf{E} \{ \tilde{\beta}_{k_1 j} \}_{i \in X, j \in Y} + \mathcal{O}(1/N^2) \\
 &= \tilde{\varphi}^{n-1} \frac{\tilde{\varphi}_Y}{N_Y} + \mathcal{O}(1/N^2).
 \end{aligned} \tag{6.27}$$

In factoring the sum in the second-to-last equality, we used that the expectation of an entry of $\tilde{\beta}$ depends only on the class of the pre-synaptic cell (the second index). Similarly, we find that

$$\mathbf{E} \left\{ \left[\left(\tilde{\beta}^T \right)^m \right]_{ij} \right\}_{i \in X, j \in Y} = \tilde{\varphi}^{m-1} \frac{\tilde{\varphi}_X}{N_X} + \mathcal{O}(1/N^2).$$

- **Case 4:** $3 \leq n + m \ll N$, and $n, m \neq 0$

These values of n, m correspond to direct and indirect common input motifs in the network. As stated in the proof for case 3 above, a sufficient condition for the terms to factor as in Eq. (6.21) is the independence of the matrix entries involved. This will

certainly be true if the entries come from different rows of $\tilde{\beta}$, i.e., if all of the second indices in Eq. (6.21) have distinct second entries,

$$i \neq k_{n-1} \neq k_{n-2} \neq \cdots \neq k_1 \neq l_1 \neq \cdots \neq l_{m-1} \neq j.$$

Note that since k_0 does not appear as a row index, its value has no bearing on the dependence of the matrix entries (this leads to the multiplicative factor N scaling the permutation below). In addition, as explained in case 2, this term does not factor. The number of ways we can choose such distinct indices is equal to the number of ways in which we can choose $n + m - 2$ indices distinctly, from the set $\{1, \dots, N\} \setminus \{i, j\}$. So long as $n + m \leq N$, there are $P(N - 2, n + m - 2)$ such combinations.

Thus, the number of terms which factor due to independence and do not contribute to the sum in Eq. (6.21) is $NP(N - 2, n + m - 2)$, where the factor N results from the fact that we can perform the factorization for all values of k_0 . If we also have that $n + m - 1 \ll N$, then $NP(N - 2, n + m - 2) \sim N^{n+m-1} + \mathcal{O}(N^{n+m-2})$. It follows that, out of the N^{n+m-1} terms comprising this sum only at most $\mathcal{O}(N^{n+m-2})$ do not cancel. Since each term in the sum is scaled by $1/N^{m+m}$, this implies that the difference is again only $\mathcal{O}(1/N^2)$. Thus, when $n + m \ll n$, we have

$$\begin{aligned} & \mathbf{E} \left\{ \left[\left(\tilde{\beta} \right)^n \left(\tilde{\beta}^T \right)^m \right]_{ij} \right\}_{i \in X, j \in Y} \\ &= \sum_{k_0, \dots, k_{n-1}, l_1, \dots, l_{m-1}=1}^N \mathbf{E} \left\{ \tilde{\beta}_{ik_{n-1}}^* \tilde{\beta}_{k_{n-1}k_{n-2}}^* \cdots \tilde{\beta}_{k_1k_0}^* \tilde{\beta}_{l_1k_0} \cdots \tilde{\beta}_{jl_{m-1}} \right\} \\ &= \sum_{k_0, \dots, k_{n-1}, l_1, \dots, l_{m-1}=1}^N \left[\mathbf{E} \left\{ \tilde{\beta}_{ik_{n-1}}^* \right\} \mathbf{E} \left\{ \tilde{\beta}_{k_{n-1}k_{n-2}}^* \right\} \right. \\ & \quad \left. \cdots \mathbf{E} \left\{ \tilde{\beta}_{k_1k_0}^* \tilde{\beta}_{l_1k_0} \right\} \cdots \mathbf{E} \left\{ \tilde{\beta}_{jl_{m-1}} \right\} \right] + \mathcal{O}(1/N^2). \end{aligned} \tag{6.28}$$

Again noting that the expected value of an entry of $\tilde{\beta}$ is independent of the row

index, we have

$$\begin{aligned}
 \mathbf{E} \left\{ \left[\left(\tilde{\beta} \right)^n \left(\tilde{\beta}^T \right)^m \right]_{ij} \right\}_{i \in X, j \in Y} &= \left(\sum_{k_{n-1}} \mathbf{E} \left\{ \tilde{\beta}_{ik_{n-1}}^* \right\} \right) \left(\sum_{k_{n-2}} \mathbf{E} \left\{ \tilde{\beta}_{k_{n-1}k_{n-2}}^* \right\} \right) \\
 &\cdots \left(\sum_{k_0} \mathbf{E} \left\{ \tilde{\beta}_{k_1k_0}^* \tilde{\beta}_{l_1k_0} \right\} \right) \cdots \left(\sum_{l_{m-1}} \mathbf{E} \left\{ \tilde{\beta}_{jl_{m-1}} \right\} \right) + \mathcal{O}(1/N^2) \\
 &= \tilde{\varphi}^{(n-1)*} \tilde{\varphi}^{m-1} \tilde{\varphi}_c + \mathcal{O}(1/N^2).
 \end{aligned} \tag{6.29}$$

Note that the second equality in Eq. (6.28) is not exactly valid if $i = j$, as the first and last terms ($\tilde{\beta}_{i,k_{n-1}}$ and $\tilde{\beta}_{i,l_{m-1}}$) are no longer independent. However, it is not difficult to verify that the difference is provably only $\mathcal{O}(1/N^2)$, so Eq. (6.29) remains valid.

- **Case 5:** n, m not significantly smaller than N

The counting arguments employed in cases 3 and 4 are no longer valid when n, m are not significantly smaller than N , as the corresponding differences of the form in Eq. (6.21) will begin to feature too many entries from common rows, breaking the permutation approximations we used in the preceding analysis.

However, as explained prior to the consideration of case 1, we assume that terms for which the counting arguments fail are rendered negligible in their contribution to the linear response expansion of correlations, owing to the exponential decay of the terms in the series.

Finally, applying Eqs. (6.23–6.28) to Eq. (6.20) yields the following expression when

$i \neq j$:

$$\begin{aligned}
 \mathbf{E} \left\{ S_{ij}^y \right\}_{i \in X, j \in Y} &= S_0^y \left[\left(\sum_{n=1}^{\infty} \tilde{A}^n \tilde{\varphi}^{n-1} \right)^* \frac{\tilde{\varphi}_Y^*}{N_Y} + \left(\sum_{m=1}^{\infty} \tilde{A}^m \tilde{\varphi}^{m-1} \right) \frac{\tilde{\varphi}_X}{N_X} \right. \\
 &\quad \left. + \left(\sum_{n,m=1}^{\infty} (\tilde{A}^n \tilde{\varphi}^{n-1})^* (\tilde{A}^m \tilde{\varphi}^{m-1}) \right) \tilde{\varphi}_c \right] + \mathcal{O}(1/N^2) \\
 &= S_0^y \left[\left(\frac{\tilde{A}}{1 - \tilde{A}\tilde{\varphi}} \right)^* \frac{\tilde{\varphi}_Y^*}{N_Y} + \left(\frac{\tilde{A}}{1 - \tilde{A}\tilde{\varphi}} \right) \frac{\tilde{\varphi}_X}{N_X} + \left| \frac{\tilde{A}}{1 - \tilde{A}\tilde{\varphi}} \right|^2 \tilde{\varphi}_c \right] + \mathcal{O}(1/N^2).
 \end{aligned} \tag{6.30}$$

When $i = j$, an additional correction term enters at second order owing to the fact that in the random network, when computing the correlation between a neuron and itself, it does not share a random amount of common input with itself, but a deterministic amount given by the in-degree and strength of connections. Hence, the terms corresponding to common input are scaled upwards in strength as seen in Eq. (6.25) and we have for $i = j$

$$\begin{aligned}
 \mathbf{E} \left\{ S_{ii}^y \right\}_{i \in X} &= S_0^y \left[\left(\sum_{n=1}^{\infty} \tilde{A}^n \tilde{\varphi}^{n-1} \right)^* \frac{\tilde{\varphi}_X^*}{N_X} + \left(\sum_{m=1}^{\infty} \tilde{A}^m \tilde{\varphi}^{m-1} \right) \frac{\tilde{\varphi}_X}{N_X} + |\tilde{A}|^2 \frac{\tilde{\varphi}_c}{p} \right. \\
 &\quad \left. + \left(\sum_{\substack{n,m=1 \\ n+m \geq 3}}^{\infty} (\tilde{A}^n \tilde{\varphi}^{n-1})^* (\tilde{A}^m \tilde{\varphi}^{m-1}) \right) \tilde{\varphi}_c \right] + \mathcal{O}(1/N^2) \\
 &= S_0^y \left[1 + \left(\frac{\tilde{A}}{1 - \tilde{A}\tilde{\varphi}} \right)^* \frac{\tilde{\varphi}_X^*}{N_X} + \left(\frac{\tilde{A}}{1 - \tilde{A}\tilde{\varphi}} \right) \frac{\tilde{\varphi}_X}{N_X} \right. \\
 &\quad \left. + \left| \frac{\tilde{A}}{1 - \tilde{A}\tilde{\varphi}} \right|^2 \tilde{\varphi}_c + |\tilde{A}|^2 \tilde{\varphi}_c \left(\frac{1-p}{p} \right) \right] + \mathcal{O}(1/N^2).
 \end{aligned}$$

□

Proposition 6.3.1 shows that, to leading order in $1/N$, the mean cross-spectrum between two cells in given classes equals that in the all-to-all network (*cf.* Eq. (6.11)). Therefore, our previous discussion relating network architecture to the shape of cross-correlations in the all-to-all network extends to the average correlation structure in the

random network for large N .

Pernice *et al.* [205] derived expressions similar to Eq. (6.14) for the correlation functions in networks of interacting *Hawkes processes* [111, 112], which are linear, self-exciting point processes with history-dependent intensities. They assumed that either the network is regular (i.e., both in- and out-degrees are fixed) or has a sufficiently narrow degree distribution. Our analysis depends on having fixed in-degrees, and we do not assume that networks are fully regular. Both approaches lead to results that hold approximately (for large enough N) when the in-degree is not fixed.

6.3.2.2 Reducing uncertainty of average correlations by conditioning on connectivity

As Figure 6.6B shows there is large variability around the mean excitatory-inhibitory cross-correlation function given by the leading order term of Eq. (6.14). Therefore, understanding the average cross-correlation between cells of given types does not necessarily provide much insight into the mechanisms that shape correlations on the level of individual cell pairs. Instead, we examine the average correlation between a pair of cells conditioned on their first order (direct) connectivity.

Proposition 6.3.2. *The average cross-spectrum for a pair of cells with indices $i \neq j$, conditioned on the value of the direct connections between them is*

$$\mathbf{E} \left\{ S_{ij}^y | \tilde{\beta}_{ij}, \tilde{\beta}_{ji} \right\}_{i \in X, j \in Y} = S_0^y \left[\tilde{A}^* \tilde{\beta}_{ij}^* + \tilde{A} \tilde{\beta}_{ji} + \left(\frac{\tilde{A}^2 \tilde{\varphi}}{1 - \tilde{A} \tilde{\varphi}} \right)^* \frac{\tilde{\varphi}_Y^*}{N_Y} + \left(\frac{\tilde{A}^2 \tilde{\varphi}}{1 - \tilde{A} \tilde{\varphi}} \right) \frac{\tilde{\varphi}_X}{N_X} + \left| \frac{\tilde{A}}{1 - \tilde{A} \tilde{\varphi}} \right|^2 \tilde{\varphi}_c \right] + \mathcal{O}(1/N^2). \quad (6.31)$$

Here we set $\tilde{\beta}_{ij} = 0$ if we condition on the absence of a connection $j \rightarrow i$, and $\tilde{\beta}_{ij} = \tilde{\beta}_Y/p$ if we condition on its presence. The term $\tilde{\beta}_{ji}$ is set similarly.

Proof. Our strategy will be to first make use of the fact that the results shown in the proof of Proposition 6.3.1 for the approximate independence of connections still hold. Then, in Eqs (6.32–6.35), we show that the factored expectations are unchanged by conditioning on the value of the connections to leading order in $1/N$. These two observations will prove Proposition 6.3.2. As an example, we consider the case of conditioning on the connectivity of a pair of excitatory cells ($\tilde{\beta}_{ij}$ and $\tilde{\beta}_{ji}$, where $i, j \in E$), and the proofs for conditions on the presence or absence of connections of other classes is nearly identical.

First, we can solve for the expectation of an outgoing connection from cell i (with an identical conclusion holding for cell j):

$$\begin{aligned}
 \mathbf{E} \{ \tilde{\beta}_{ai} | \tilde{\beta}_{ij}, \tilde{\beta}_{ji} \}_{i,j \in E,a} &= \begin{pmatrix} \text{Probability that cell} \\ a \text{ is excitatory} \end{pmatrix} \begin{pmatrix} \text{Expected value of } \tilde{\beta}_{ai} \\ \text{if } a \text{ is excitatory} \end{pmatrix} \\
 &+ \begin{pmatrix} \text{Probability that cell} \\ a \text{ is inhibitory} \end{pmatrix} \begin{pmatrix} \text{Expected value of } \tilde{\beta}_{ai} \\ \text{if } a \text{ is inhibitory} \end{pmatrix} \\
 &= \frac{N_E}{N} \left(\frac{G_E}{pN_E} \tilde{\alpha}_E \right) \left(p + \frac{1 - \delta_{\tilde{\beta}_{ji},0} - p}{N_E} \right) + \frac{N_I}{N} \left(\frac{G_E}{pN_E} \tilde{\alpha}_E \right) p \\
 &= \frac{\tilde{\varphi}_E}{N_E} + \frac{(1 - \delta_{\tilde{\beta}_{ji},0} - p)G_E}{pN^2} \\
 &= \frac{\tilde{\varphi}_E}{N_E} + \mathcal{O}(1/N^2),
 \end{aligned} \tag{6.32}$$

where the subscript a denotes an average over all possible values of the index a . The term

$$p + \frac{1 - \delta_{\tilde{\beta}_{ji},0} - p}{N_E}$$

represents the fraction of connections cell i will make onto other excitatory cells which are expected to be present. Because we fix the in-degree when generating graphs in this example, this fraction depends on the value of $\tilde{\beta}_{ji}$. In particular, it will be greater or less than p , the connection probability, depending on whether the connection $i \rightarrow j$ is on ($\tilde{\beta}_{ji} \neq 0$) or off ($\tilde{\beta}_{ji} = 0$), respectively.

As an example, if the connection $j \rightarrow i$ is “on”, the expected number of outgoing connections from j to excitatory cells which will be on is $1 + p(N_E - 1)$, as unconditioned outgoing connections (i.e., $\tilde{\beta}_{ki}$ for $k \neq j$) are multiples of Bernoulli random variables. Note that the first-order conditioned expected value coincides with the unconditioned expected value to leading order in $1/N$ (compare Eq. (6.32) with Eq. (6.23)).

We also have that

$$\begin{aligned} \sum_b \mathbf{E} \{ \tilde{\beta}_{ab} | \tilde{\beta}_{ij}, \tilde{\beta}_{ji} \}_{i,j \in E} &= \mathbf{E} \left\{ \left(\sum_b \tilde{\beta}_{ab} \right) \middle| \tilde{\beta}_{ij}, \tilde{\beta}_{ji} \right\}_{i,j \in E} = \tilde{\varphi} \quad \text{and} \\ \sum_{b \in X} \mathbf{E} \{ \tilde{\beta}_{ab} | \tilde{\beta}_{ij}, \tilde{\beta}_{ji} \}_{i,j \in E} &= \mathbf{E} \left\{ \left(\sum_{b \in X} \tilde{\beta}_{ab} \right) \middle| \tilde{\beta}_{ij}, \tilde{\beta}_{ji} \right\}_{i,j \in E} = \tilde{\varphi}_X \end{aligned} \quad (6.33)$$

for any a , agreeing with the values of the same quantities found in the absence of conditioning on connection values (cf. Eqs. (6.17, 6.18)). We have fixed the in degree so that the fact that certain connections are present or absent has no bearing on the expected input to a particular cell.

We can also solve for the value of $\tilde{\varphi}_c$ when we condition on the first order connectivity of two excitatory cells:

$$\begin{aligned} \tilde{\varphi}_{EE,c} &= \mathbf{E} \left\{ \left[\tilde{\beta} \tilde{\beta}^T \right]_{ij} \middle| \tilde{\beta}_{ij}, \tilde{\beta}_{ji} \right\}_{i \in E, j \in E} \\ &= \sum_{k=1}^N \mathbf{E} \{ \tilde{\beta}_{ik} \tilde{\beta}_{jk} | \tilde{\beta}_{ij}, \tilde{\beta}_{ji} \} \\ &= \sum_{k \neq i, j} \mathbf{E} \{ \tilde{\beta}_{ik} \tilde{\beta}_{jk} | \tilde{\beta}_{ij}, \tilde{\beta}_{ji} \} + \mathbf{E} \{ \tilde{\beta}_{ii} \tilde{\beta}_{ji} | \tilde{\beta}_{ij}, \tilde{\beta}_{ji} \} + \mathbf{E} \{ \tilde{\beta}_{ij} \tilde{\beta}_{jj} | \tilde{\beta}_{ij}, \tilde{\beta}_{ji} \} \\ &= \sum_{k \neq i, j} \mathbf{E} \{ \tilde{\beta}_{ik} \tilde{\beta}_{jk} | \tilde{\beta}_{ij}, \tilde{\beta}_{ji} \} + \tilde{\beta}_{ji} \mathbf{E} \{ \tilde{\beta}_{ii} | \tilde{\beta}_{ij}, \tilde{\beta}_{ji} \} + \tilde{\beta}_{ij} \mathbf{E} \{ \tilde{\beta}_{jj} | \tilde{\beta}_{ij}, \tilde{\beta}_{ji} \} \\ &= (N_E - 2) \left(\frac{G_E}{pN_E} \tilde{\alpha}_E \right)^2 p_i p_j + N_I \left(-\frac{G_I}{pN_I} \tilde{\alpha}_I \right)^2 p^2 \\ &\quad + \tilde{\beta}_{ij} \left(\frac{G_E}{pN_E} \tilde{\alpha}_E \right) p_i + \tilde{\beta}_{ji} \left(\frac{G_E}{pN_E} \tilde{\alpha}_E \right) p_j, \end{aligned} \quad (6.34)$$

where we define p_i to be the probability that an excitatory connection $k \rightarrow i$ exists when $k \neq j$ conditioned on the value of $\tilde{\beta}_{ij}$. This can be explicitly calculated as

$$p_i = \begin{cases} \frac{pN_E - 1}{N_E - 1}, & \text{if } \tilde{\beta}_{ij} \neq 0, \\ \frac{pN_E}{N_E - 1}, & \text{if } \tilde{\beta}_{ij} = 0, \end{cases}$$

with identical calculations holding for p_j for the probability of an excitatory connection $k \rightarrow j$ when $k \neq i$. In either case, it is easy to see that $p_i = p + \mathcal{O}(1/N)$. Substituting these identities into Eq. (6.34) and comparing with Eq. (6.19), we have

$$\tilde{\varphi}_{EE,c} = \tilde{\varphi}_c + \mathcal{O}(1/N^2). \quad (6.35)$$

Like the first order terms in Eqs (6.32, 6.33), the expected common input $\tilde{\varphi}_c$ is unchanged to leading order in $1/N$ by conditioning on the first order connectivity of a pair of cells.

The results established in the proof of Proposition 6.3.1 regarding the approximate independence of entries of $\tilde{\beta}$ (Eq. (6.21)) still hold. Equations (6.32-6.35) reveal that, to leading order in $1/N$, there will be no change to the expectation of terms higher than first order in Eq. (6.20) as a result of the conditioning. Hence, the only difference occurs at first order, where we are replacing average connection values with known connection values. Finally, applying Eq. (6.21) and Eqs. (6.32-6.35) to Eq. (6.20), we obtain Eq. (6.31).

□

Although Eq. (6.31) appears significantly more complicated than the cell-type averages given in Eq. (6.14), they only differ in the first order terms $S_0^y \tilde{A}^* \tilde{\beta}_{ij}^*$ and $S_0^y \tilde{A} \tilde{\beta}_{ji}$. The magnitude of expected contributions from all higher order motifs is unchanged and coincides with those in the all-to-all network.

Figure 6.6C shows the mean cross-correlation function for excitatory-inhibitory pairs

with bidirectional coupling. Taking into account the mutual coupling significantly reduces variability (Compare with Figure 6.6B). To quantify this improve, we calculate the mean reduction in variability when correlation functions are computed conditioned on the connectivity between the cells. For a single network, the relative decrease in variability can be quantified using

$$\mu_{\text{error}} = \frac{1}{N_T} \sum_{\substack{(i,j) \in T \\ i > j}} \frac{\|\kappa_{ij}^y(\tau) - \kappa_T^{\text{FOC}}(\tau)\|_2}{\|\kappa_{ij}^y(\tau) - \kappa_T^{\text{CT}}(\tau)\|_2},$$

where T represents the collection of all pairs of cells of a given type and pairwise connectivity (in the present example these are reciprocally coupled excitatory-inhibitory pairs), and N_T is the number of pairs of that type in the network. The function $\kappa_T^{\text{CT}}(\tau)$ is the leading order approximation of average correlations given only the type of cells in T (as in Eq. (6.14)), and $\kappa_T^{\text{FOC}}(\tau)$ the leading order approximation to average correlations conditioned on the first order connectivity of class T (as in Eq. (6.31)). We make use of the norm $\|\cdot\|_2$ defined by $\|f\|_2 = (\int |f|^2)^{1/2}$. Figure 6.6D shows μ_{error} averaged over twenty networks. In particular, compare the reduction in variability when conditioning on bidirectional coupling between excitatory-inhibitory pairs shown in Figures 6.6B,C, with the corresponding relative error in Figure 6.6D (circled in red).

6.3.3 Distance-dependent networks

Distance-dependent features of cortical connectivity have been observed in a variety of settings [114, 204, 213, 260]. In auditory and visual cortices, for example, it has been observed that neurons preferentially form synapses with partners with similar tuning preferences [22, 164, 199, 302]. In addition, computational studies have attempted to explain the role of distance-dependent connectivity in shaping neuronal activity [154, 157, 258].

Here, we present some preliminary results acquired via the application of linear response theory in two networks with distance-dependent connectivity. We believe these results are suggestive of some interesting paths for future exploration of applications of the linear response theory of correlations.

The first network we consider is a spatially one-dimensional “circular boxcar” network. In particular, we consider a network of N_E excitatory and N_I inhibitory integrate-and-fire neurons. Each neuron was assigned a preferred orientation ϕ_i . Within each class (excitatory and inhibitory), the preferred orientations of class members were spread uniformly about the unit circle. Connectivity weights were set as

$$\mathbf{W}_{ij} = \begin{cases} w_E, & j \in E, d(\phi_i, \phi_j) \leq \theta_E, \\ w_I, & j \in I, d(\phi_i, \phi_j) \leq \theta_I, \\ 0, & \text{otherwise,} \end{cases} \quad (6.36)$$

where $d(\phi_i, \phi_j)$ is the angular distance around the circle. The constants θ_X set the connectivity radii for neurons of each class. This type of connectivity is loosely based on models of orientation selectivity in visual cortex [258].

The distance-dependent synaptic architecture not surprisingly generates a corresponding distance-dependent correlation structure. In Figure 6.7A, we compare the relationship between tuning distance and the pairwise long-window spike count correlation (Eq. (2.12)) obtained using the linear response theory (Eq. (6.1)) with that acquired via Monte Carlo simulation. The parameters of the network were such that excitation was stronger and more localized than inhibition. As a result, nearby neurons were strongly positively correlated, while neurons at intermediate distances became significantly negatively correlated. In Figure 6.7B, we plot the distance-correlation curve accounting for interactions only up to certain orders (acquired from Eq. (6.2)). Interestingly, there are significant contributions

from non-local interactions from motifs of fifth order and above.

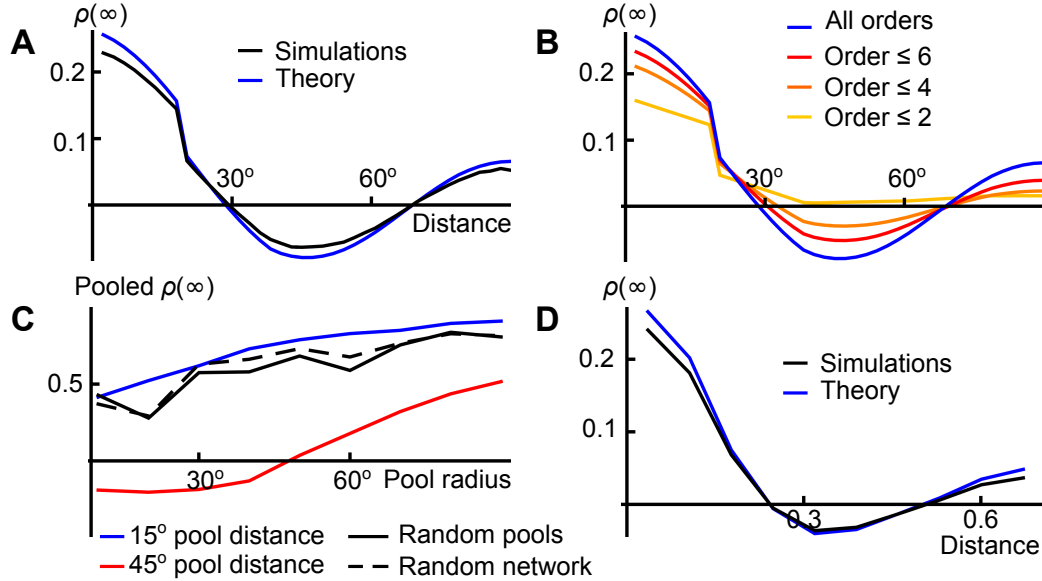


Figure 6.7: **Spiking correlation structure within distance-dependent neuronal networks.** (A) Exhibiting the relationship between pairwise asymptotic spike count correlation coefficients (Eq. (2.12)). The blue line indicates the linear response prediction (Eq. (6.1)) while black indicates the estimation of the distance-correlation relationship acquired from Monte Carlo simulation. The “circular boxcar” network was of size $N = 100$ with $N_E = 80$, and the synaptic footprints were $\sigma_E = 20^\circ, \sigma_I = 60^\circ$. (B) Decomposition of the linear response prediction of the distance-correlation relationship in panel A into contributions up to specified orders (acquired using Eq. (6.2)). (C) Correlation between the pooled (summed) spiking outputs of the circular boxcar network. Pools were formed as collections of neurons with preferred orientations falling within an interval of length twice the pool radius. The network was approximately radially symmetric, and thus, only the relative positions of the pools (compare blue and red lines), as opposed to the absolute positions, mattered in determining pooled correlation. Black lines indicate values obtained by pooling randomly from the circular boxcar network (solid black line) and pooling randomly from a random network (i.e., one without distance-dependent architecture – broken black line). (D) Same as panel A, but for a “planar boxcar” network. The planar network was of size $N = 1000$ with $N_E = 800$. The distance metric was Euclidean, and we set $\sigma_E = 0.15, \sigma_I = 0.4$.

In Table 6.1, we contrast the mean and standard deviation of correlations in the

distance-dependent network with that of a random network possessing similar connection strengths and connection probability, but lacking the distance-dependence in the connectivity. The mean correlation between cells in the two networks is similar, but the variation in correlation values is much smaller for a random network — a direct reflection of the strong local variations in spike count correlation is visible in Figure 6.7A.

Network type	Theory	Simulation
Circular boxcar ($N = 100$)	0.0346 ± 0.1022	0.0332 ± 0.0903
Random ($N = 100$)	0.0481 ± 0.0240	0.0402 ± 0.0252
Planar boxcar ($N = 1000$)	0.0094 ± 0.0773	0.0075 ± 0.0719
Random ($N = 1000$)	0.0097 ± 0.0073	0.0091 ± 0.0140

Table 6.1: **Mean and standard deviation of the distribution of excitatory-excitatory pairwise correlations in structured and random networks.** The values in circular and planar boxcar networks are from the same data as Figure 6.7.

As an example, we considered the correlation of pooled collections of neurons within the distance-dependent network in Figure 6.7C [232, 233]. In particular, we formed pools by summation of all excitatory neurons with preferred orientations which fell within two pools of increasing radius (note that the approximate radial symmetry of the network made only the relative positions of the pools important). The correlation between two nearby pools (blue line) was significantly larger than that between two distant pools (red line). In both cases, correlation increases with pool radius as the growing pools encompass more neurons with positive correlations amongst them. If the output of this ring network feeds forward in a spatially-dependent manner (as is posited in the aforementioned models of orientation selectivity in V1), then the level of pooled correlation could strongly modulate the activity of the downstream network.

We also plot in Figure 6.7C, the pooled correlation when pools of matching size are formed by a random selection of neurons from the ring network without regard to preferred orientations (solid black line). The level of pooled correlation is very similar to that

obtained by likewise sampling from a truly random network (i.e., one without distance-dependent connectivity). This is not too surprising, as we have been shown in [232] that mean correlation is a strong determinant of pooled correlation, and the mean correlations are similar between the circular and random networks (Table 6.1).

We also considered a spatially extended, two-dimensional network. Neurons were assigned a location on the 2-torus instead of the 1-torus as in the previous example. The network connectivity was constructed similarly (see Eq. (6.36)), and the distance metric was Euclidean distance. In Figure 6.7, we plot the distance-correlation relationship for this “planar boxcar” network. The “planar boxcar” label given to the network owes to the nature of the distance-dependent connectivity in this example, in which neurons synapsed onto all other cells within a specified radius of their location at the same strength. Nearby cells were again strongly positively correlated, with negative correlations introduced at intermediate distances. In Table 6.1, we give the mean and standard deviation of correlations for this network, and for comparison, the same for a similarly defined random network. Again, mean correlations are of comparable magnitudes, but in this much larger network ($N = 1000$, compared with $N = 100$ for the boxcar network), the variation in correlations is increased by an order of magnitude owing to the spatial structure.

6.4 Validity of the linear response approximation

A natural question at this point is when the linear response theory gives accurate approximations to the correlation structure. There are two factors that determine the consistency of the linear response theory with the true spiking correlations: First, we must be in a regime where the firing rate approximation of Eq. (5.2) is valid. The linear response ansatz given by Eq. (5.3) relies on the average effect of an input being a “good” (in some sense)

imitator of the true effect of an input; therefore, failure of the rate (first order) approximation necessarily implies failure of the correlation (second order) approximation. The first order approximation will be valid when the *fluctuations* in the input signal $X(t)$ are not too large compared to intensity of the intrinsic noise ξ . In particular, one general requirement is that each neuron respond linearly not only to individual synaptic inputs, but also to its summed synaptic input, implying that, for example, the summed strengths of excitatory and inhibitory inputs must be appropriately “weak.”

On the other hand, the first order theory does not supply the second order approximation of correlations by rigorous argument except in the case of a pair of cells with a unidirectional synaptic interaction between them. Thus, it is not completely clear when the additional step of using the linear response theory to approximate correlations should fail in networks with non-trivial synaptic structure.

A detailed theoretical error analysis is infeasible due to the non-rigorous nature of the linear response approximation of correlations. In general, though, we observed that the accuracy of the linear response theory of correlations showed the same trends as the firing rate theory: it was improved for weaker perturbations (i.e., weaker coupling and input correlations) and stronger intrinsic noise.

6.4.1 Accuracy of linear response in the all-to-all network of Figure 6.5

First, we examined the limits of linear response theory in predicting time-dependent firing activity (the peri-stimulus time histogram, or PSTH) in the balanced, all-to-all network considered in Figure 6.5. We generated 100 realizations of Poisson spiking processes, each 2s in duration. We designated 80 to be excitatory and 20 to be inhibitory, to emulate the input received by a cell in the all-to-all network. These point processes were convolved

with weighted alpha functions (see Eq. (5.6)), and used to drive an EIF neuron which was also receiving a white, fluctuating background input.

As exhibited in Figure 5.1, we averaged over realizations of background noise to obtain the time-dependent firing intensity of this post-synaptic cell. We quantified the agreement between the result obtained by numerical simulation and the approximation obtained using linear response theory by computing the Pearson correlation coefficient between the two. This was performed over a range of input noise intensities and connection weights to obtain the density plot in Figure 6.8A. In agreement with the expectation that noise linearizes responses and improves the linear response approximation, the agreement is best when noise is strong and connections weak, and worst for weak noise and strong connections. Notably, for a large range of parameters, the linear response prediction of the PSTH was quite good, with Pearson correlation coefficients above 80%.

Approximating time-dependent firing activity (PSTH) is only a part of approximating network correlations. Network effects can further limit the accuracy of the approximation given by Eq. (5.12). We therefore compared numerically obtained cross-correlation functions with those given by Eq. (6.11) at four points (indicated by black dots in Figure 6.8A). The results shown in Figure 6.8B indicate that the trends in cross-correlations and PSTH approximation errors are similar. In particular, for connection strengths still stronger than those used in the paper (red dot), the match between theory and simulations is excellent at both noise levels tested.

However, in networks, large connection strengths (over 10x those used in Figure 6.5) can cause the approximation of cross-correlations to be worse than what would be expected from the agreement in firing rate prediction. In particular, note that the relative L^2

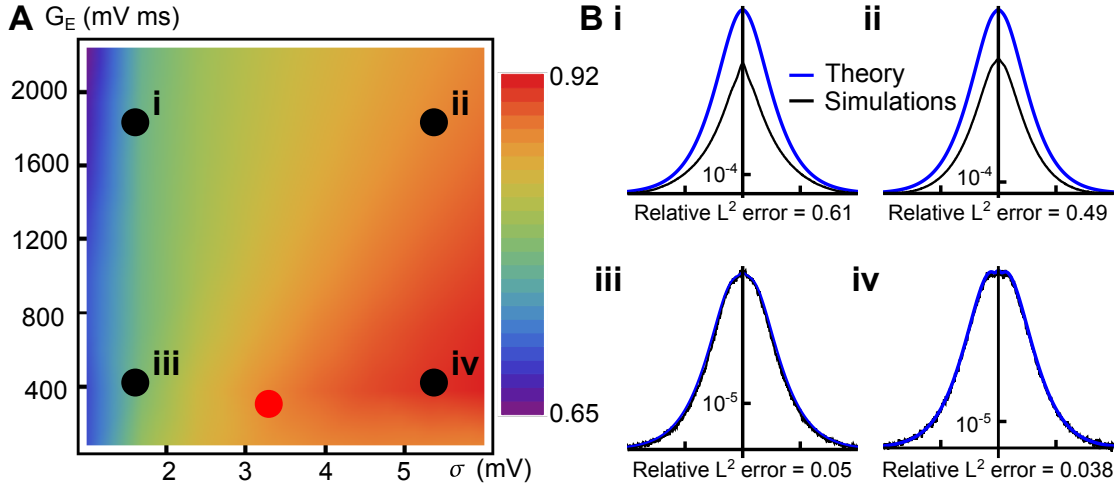


Figure 6.8: **Error analysis of the linear response theory.** (A) The Pearson correlation coefficient between the time-dependent firing activity (PSTH) calculated from Monte Carlo simulations and linear response theory for an array of σ (noise intensity) and G_E (total excitatory/inhibitory connection weight) values for a single EIF neuron receiving 80 excitatory and 20 inhibitory Poisson inputs at 17 Hz, convolved with alpha synaptic kernels (see Eq. (5.6)). These inputs emulated the total drive received by a neuron in the precisely balanced, all-to-all network considered in Figure 6.5. A higher correlation indicates a closer match between simulations and theory. The red dot indicates the parameters used for Figure 6.5. (B) The cross-correlation function between two excitatory cells in the precisely balanced, all-to-all network from Monte Carlo simulations and linear response theory at four points in (σ, G_E) space, indicated by the black dots in panel A.

error² between theoretical and numerical predictions was much lower for cases (iii), (iv) when connection strengths were weak. Nevertheless, in the case of strong connectivity (examples (i), (ii)), the relative error was significantly reduced in the high noise case (ii). It is possible that a significant portion of the increase in error could be tied to an increase in the input variability when the input comes from a (generally correlated) recurrent network.

²The relative L^2 error between the linear response-predicted correlation C^∞ and the Monte Carlo prediction C was defined as $error = \|C^\infty - C\|_2 / \|C\|_2$.

6.4.2 Accuracy of the linear response theory in different firing regimes

The accuracy of the linear response could also potentially depend on the firing regime of the responding neuron. To explore this possibility, we revisit the FFI microcircuit considered in Figure 6.2. We varied the effective rest potential $E_L + E_{\xi,i}$ of the downstream excitatory cell E_2 , while keeping the remaining parameters fixed. The linear response prediction and Monte Carlo estimated cross-cumulant densities for the pair (E_2, I) are shown in Figure 6.9 at three values of the effective rest potential.

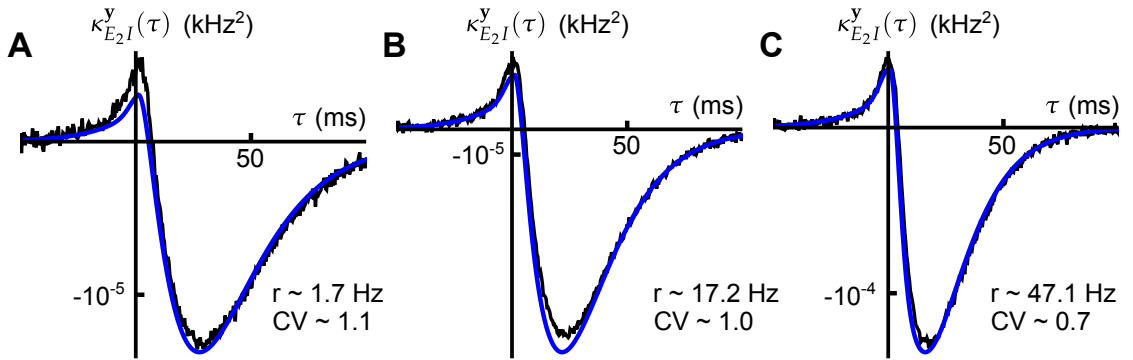


Figure 6.9: **The performance of linear response theory in various firing regimes.** For the feed-forward inhibitory microcircuit considered in the manuscript (see Figure 6.2), we varied the effective rest potential $E_L + E_{\xi,i}$ (see Eq. (5.4) and Figure 6.2) to the cell E_2 between three values — (A) $E_L + E_{\xi,i} = -59$ mV, (B) $E_L + E_{\xi,i} = -54$ mV (this is the value used in Figure 6.2), (C) $E_L + E_{\xi,i} = -49$ mV. Insets give the firing rate and the coefficient of variation of the interspike interval distribution of cell E_2 .

For comparison, we have also included the CV of the ISI distribution for the cell E_2 . The three chosen parameter values lead to three quantitatively and qualitatively different firing behaviors. In particular, when the effective rest potential is -59 mV, firing is spontaneous, but rare (rate ~ 1.7 Hz, CV ~ 1.1). Although the error does seem to increase as firing rates decreases, the theory still performs well even for very low-rate spiking. We suspect that part of this error is due to the propensity of linear response theory to predict negative (nonphysical) firing rates when rates are low but connections are strong.

6.4.3 Failure of the linear response theory of correlations at third order

To this point, we have only considered linear response as applied to the estimation of *second order* cross-cumulant measures. We also attempted to apply linear response theory to approximate third order cross-cumulant densities. However, we found that there are serious issues with such applications. We will present a pair of examples revealing somewhat distinct issues presented by the theory when applied to third order correlations amongst spiking neurons.

There is still an open question as to whether a correction can be posed which could account, to some extent, for these discrepancies. One possible avenue of future research is to attempt an extension of the rigorous derivation of the second order correlation structure of Hawkes processes [111, 112] to third order. The second order correlation structure of a vector Hawkes process has a form very reminiscent of the linear response approximation to correlations given in Eq. (6.1). If the form of the third order correlations for Hawkes processes could be determined, this could suggest a beneficial alteration of the naive linear response approximation of the third order correlation structure.

6.4.3.1 Linear response theory of third order correlations

Recall that the starting point for the linear response approximation of second order correlations in Eq. (6.1) was a linear approximation of the spectra $\tilde{\mathbf{y}}(\omega)$ of the point processes $\mathbf{y}(t)$ representing the output of the modeled network (*cf.* Eq. (5.11)). For each process y_i , we can write

$$\tilde{y}_i(\omega) = \tilde{\mathbf{L}}_i(\omega)\tilde{\mathbf{y}}_0(\omega) = \sum_{n=1}^N \tilde{L}_{in}(\omega)\tilde{y}_{0,n}(\omega), \quad (6.37)$$

where $\tilde{\mathbf{L}}_i(\omega)$ is the i^{th} row of the matrix $\tilde{\mathbf{L}}(\omega) = (\mathbf{I} - \tilde{\mathbf{K}}(\omega))^{-1}$.

Given the spectra $\tilde{\mathbf{y}}(\omega)$, the bispectrum (see Eq.(2.5)) for a subset of three of these processes can be written

$$S_{ijk}^y(\omega_1, \omega_2) = \mathbf{E} [\tilde{y}_i^*(\omega_1 + \omega_2) \tilde{y}_j(\omega_1) \tilde{y}_k(\omega_2)].$$

Substituting Eq. (6.37) into the previous expression gives

$$S_{ijk}^y(\omega_1, \omega_2) = \sum_{n_1, n_2, n_3=1}^N \tilde{L}_{in_1}^*(\omega_1 + \omega_2) \tilde{L}_{jn_2}(\omega_1) \tilde{L}_{kn_3}(\omega_2) S_{0,ijk}^y(\omega_1, \omega_2), \quad (6.38)$$

where the functions

$$S_{0,ijk}^y(\omega_1, \omega_2) = \mathbf{E} [\tilde{y}_{0,i}^*(\omega_1 + \omega_2) \tilde{y}_{0,j}(\omega_1) \tilde{y}_{0,k}(\omega_2)]$$

are the “uncoupled bispectra” of the network. Under the assumption of independent uncoupled activity, \mathbf{S}_0^y is a diagonal tensor. We note that Eq. (6.38) can be re-expressed in tensor notation as as

$$\begin{aligned} \mathbf{S}^y(\omega_1, \omega_2) &= \mathbf{E} \left[\overline{\tilde{\mathbf{y}}(\omega_1 + \omega_2)} \otimes \tilde{\mathbf{y}}(\omega_1) \otimes \tilde{\mathbf{y}}(\omega_2) \right] \\ &= \mathbf{E} \left[\overline{\tilde{\mathbf{L}}(\omega_1 + \omega_2) \tilde{\mathbf{y}}_0(\omega_1 + \omega_2)} \otimes \tilde{\mathbf{L}}(\omega_1) \tilde{\mathbf{y}}_0(\omega_1) \otimes \tilde{\mathbf{L}}(\omega_2) \tilde{\mathbf{y}}_0(\omega_2) \right] \\ &= \left[\overline{\tilde{\mathbf{L}}(\omega_1 + \omega_2)} \otimes \tilde{\mathbf{L}}(\omega_1) \otimes \tilde{\mathbf{L}}(\omega_2) \right] \cdot \mathbf{S}_0^y(\omega_1, \omega_2), \end{aligned} \quad (6.39)$$

where \otimes indicates a tensor product.

To our knowledge, the uncoupled bispectra \mathbf{S}_0^y cannot be determined analytically for integrate-and-fire neurons even in the absence of correlated input. In the second order case, the derivation relies heavily on a second order identity relating the first-passage time density of a renewal process to its power spectrum (see Eq. (5.25)). In the absence of an equivalent identity at third order, the uncoupled spectra of the EIF neurons composing the systems under consideration must be determined by other means. In what follows, before computing linear response approximations to third order correlation structures, we computed by Monte Carlo simulation an approximation of the uncoupled bispectra \mathbf{S}_0^y .

6.4.3.2 Three cell excitatory microcircuit

The first example we considered was a feed-forward excitatory microcircuit consisting of three neurons. The weight matrix was of the form

$$\mathbf{W} = \begin{pmatrix} 0 & 0 & 0 \\ w_E & 0 & 0 \\ w_E & w_E & 0 \end{pmatrix}.$$

That is, the connectivity was $1 \rightarrow 2, 1 \rightarrow 3, 2 \rightarrow 3$. In Figure 6.10, we compare the Monte Carlo-estimated cross-cumulant density for the triplet $(1, 2, 3)$ (panel A) to the naive linear response estimation of the same (panel B) calculated using Eq. (6.39).

There are significant qualitative and quantitative errors in the linear response approximation. In particular, the true cross-cumulant density exhibits a sharp peak in the region $\tau_2 > \tau_1 > 0$. Recall that the third order cross-cumulant density measures the excess rate of spiking above what would be predicted from lower order (first and second in the present example) cumulants. Therefore, this peak indicates an elevated likelihood to observe firing events ordered as $1 \rightarrow 2 \rightarrow 3$, a feature which is not captured by the linear response theory.

6.4.3.3 Two cell bidirectional inhibitory microcircuit

We also evaluated the linear response approximation to third order correlations for a two-cell, bidirectional inhibitory microcircuit. The weight matrix had the form

$$\mathbf{W} = \begin{pmatrix} 0 & w_I \\ w_I & 0 \end{pmatrix}.$$

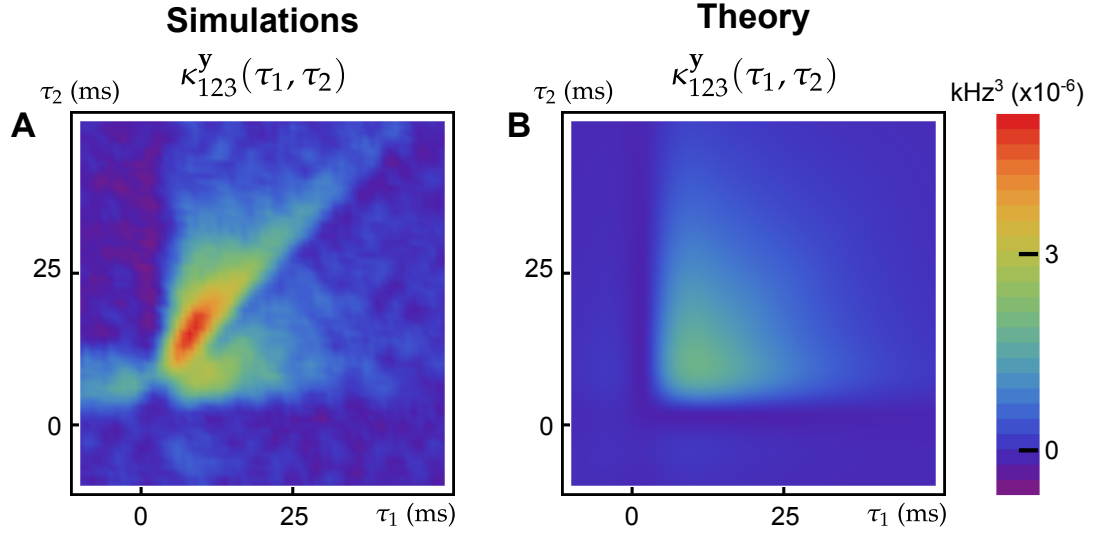


Figure 6.10: **Linear response fails to capture third order correlations even qualitatively.** (A) Monte Carlo-estimated third order cross-cumulant density for the triplet (1, 2, 3) in the 3-cell excitatory microcircuit described in Section 6.4.3.2. Colors indicate function values at the corresponding lags τ_1 (horizontal axis) and τ_2 (vertical axis) — see color bar (far right). (B) Same as panel A, but displays the linear response approximation to the third-order cross-cumulant density derived by an two-dimensional inverse Fourier transform of Eq. (6.39).

In this case, we calculated the third-order cross-cumulant density for the triplet (1, 2, 1), which included the first cell twice. Interestingly, as we exhibit in Figure 6.11, the linear response approximation of the third order correlations failed, but in a very different way than was observed for the three-cell system considered in Section 6.4.3.2.

As explained in the discussion surrounding Eq. (2.16), the cross-cumulant density $\kappa_{121}^y(\tau_1, \tau_2)$ can generally be written as

$$\kappa_{121}^y(\tau_1, \tau_2) = \delta(\tau_2)\kappa_{12}^y(\tau_1) + \text{“non-singular contributions”}.$$

In Figure 6.11A, we plot the second order cross-cumulant density for the pair (1, 2) and the singular contribution predicted by the linear response theory (scaled to real units). Half of the correlation function is effectively missing from the linear response prediction.

In addition, as Figure 6.11B,C show, half of the non-singular, “true” third order features are missing as well. Interestingly, the half that is present is accurately reproduced, both qualitatively and quantitatively. This suggests that a correction may be possible, but we have not yet determined what that correction should be.

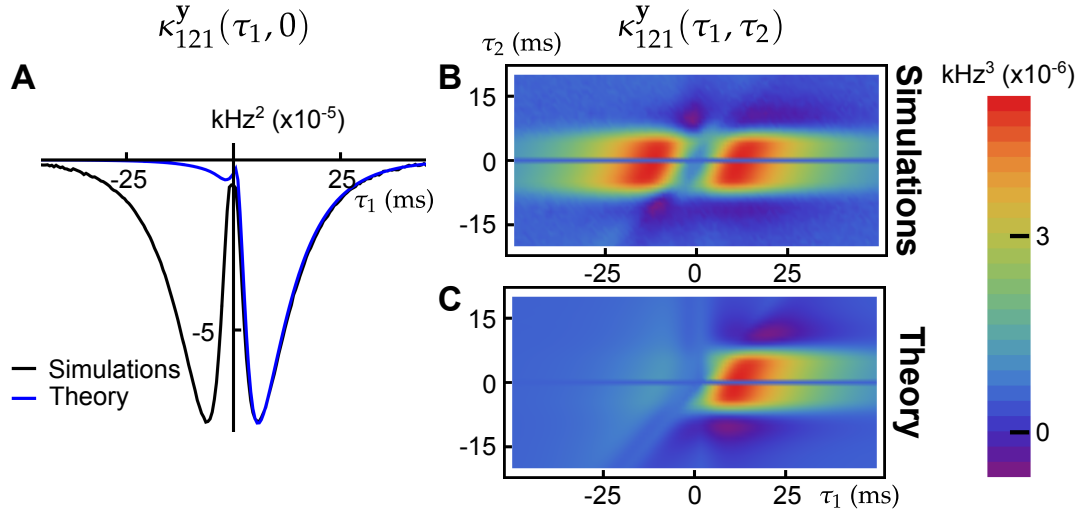


Figure 6.11: **Linear response theory captures “half” of the third-order correlations in a bidirectional inhibitory microcircuit.** (A) Comparing the singular contribution calculated from Monte Carlo simulation (black line) with the linear response prediction (blue line). Note that for $\tau_1 > 0$, the blue and black lines lie almost exactly on top of each other. (B) Monte Carlo-estimated third order cross-cumulant density for the triplet (1, 2, 1) in the 2-cell inhibitory microcircuit described in Section 6.4.3.3. Colors indicate function values at the corresponding lags τ_1 (horizontal axis) and τ_2 (vertical axis) — see color bar (far right). (C) Same as panel A, but displays the linear response approximation to the third-order cross-cumulant density obtained from a two-dimensional inverse Fourier transform of Eq. (6.39).

Motif Cumulants and Average Correlations

The aim of the field of *connectomics* is to produce detailed maps of cortical connectivity [261, 262]. Thanks to rapid technological advancement in the areas of electrical recording [67, 289], optogenetics [10, 172] and photostimulation [200, 286], the neuroscientific community has made amazing strides in mapping neural circuitry. However, as mentioned in Section 3.3, the human brain, is currently estimated to possess on the order of 100 billion (10^{11}) neurons making 100 trillion (10^{14}) synapses with each other. For this reason, a detailed mapping and modeling of the full neuronal architecture of mammalian brains will not be achieved in the foreseeable future.

The cause is not lost — experimental studies are already revealing a wealth of information about the *statistics* of connectivity in various cortical regions [260, 273, 295]. These experimental efforts place the burden on theorists to explore what can be inferred about

the nature of cortical activity from these available data. In the present chapter, we will introduce measures of neuronal connectivity known as *motif cumulants* [127, 128, 309]. Figure 1.3 portrays the role that motif cumulants can play in shaping the global dynamical properties of a neuronal network. An Erdős-Rényi network model can be equivalently defined as a network model having zero expected motif cumulants above first order, and deviations from this model equate to the introduction of non-zero motif cumulants.

Applying the linear response theory of Chapters 5 and 6, we will achieve an expansion of average correlations within a network of integrate-and-fire neurons in terms of these motif cumulants [127, 128]. In particular, we utilize this expansion to express average correlation as a function of the frequency (probability of observation) of second order motifs within the synaptic architecture. We depict the second order motifs for a network with a single class of cells in Figure 7.1. Embedded within this result is the observation that, in networks admitting a linear description, the second order cross-cumulant structure can be determined from knowledge of relatively few dynamical and synaptic architectural statistics. The theory presented in this chapter reveals explicitly the nature of the ties between dynamics and network topology.

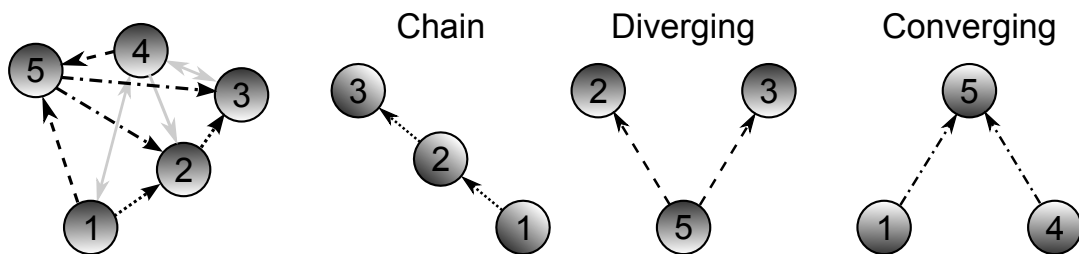


Figure 7.1: **Second order motifs within a recurrent network.** (Left) Second order submotifs — motifs involving two connections and at most three cells — are embedded within the graph of a network. (Right) The three types of second order motifs: chain, diverging and converging.

7.1 Graphical structure of neuronal networks

7.1.1 Preliminaries

We will again consider coupled networks of N exponential integrate-and-fire neurons. To facilitate the analysis in this chapter, we will make some simplifying assumptions: First, we will assume the cells in our networks to be dynamically identical — in the context of the linear response theory, this implies identical susceptibility functions $\tilde{A}(\omega)$ and identical uncoupled power spectra $S_0^y(\omega)$. Furthermore, we will assume the strength of synaptic interactions to be constant within neuron classes: For a network consisting of a single population in which we do not distinguish between types or classes of neurons, this means we can express the synaptic weight matrix as

$$\mathbf{W} = w\mathbf{W}^0,$$

where \mathbf{W}^0 is the adjacency matrix of the network (i.e., $W_{ij}^0 = 1$ if there is a connection $j \rightarrow i$, and is zero otherwise).

Finally, we will consider all spectral quantities to be evaluated at $\omega = 0$ (and accordingly omit all dependencies on ω). This corresponds to the consideration of spike count cross-cumulants over infinitely long windows (see Eq. (2.18) and the surrounding discussion). In general, the analysis presented in this chapter can be performed at each frequency in order to analyze the full second order temporal cumulant structure.

Rajan and Abbot [209] derived an asymptotic (large N) characterization of the spectral radius of the weight matrix for a general excitatory-inhibitory neuronal network. In particular, they found that for an Erdős-Rényi network consisting of N_E excitatory (resp. N_I inhibitory) cells making synapses with weight w_E (resp. w_I), there would be a single

eigenvalue at $pN_E w_E + pN_I w_I$, characterizing the average strength of an interaction, and the remaining eigenvalues would be randomly randomly in the circle with radius

$$\sqrt{p(1-p)(N_E w_E^2 + N_I w_I^2)}.$$

Motivated by these findings, we quantify the strength of interactions across a distribution of random networks by associating with the class a so-called *Erdős-Rényi spectral radius* $\Psi_{\text{ER}}(\tilde{A}w)$ by

$$\Psi_{\text{ER}}(\tilde{A}w) = |\tilde{A}| \max \left\{ |pN_E w_E + pN_I w_I|, \sqrt{p(1-p)(N_E w_E^2 + N_I w_I^2)} \right\}. \quad (7.1)$$

Here, p is the expected connection probability across the distribution of networks. In general, a higher value of $\Psi_{\text{ER}}(\tilde{A}w)$ indicates stronger interactions between cells *on average*, and the performance of the linear response theory is generally better on classes of networks with relatively small $\Psi_{\text{ER}}(\tilde{A}w)$.

7.1.1.1 Graph generation

In this chapter, we will make use of random, non-Erdős-Rényi graphs (i.e., graph edges are not placed independently from each other). Here, we present more details on how we generate network samples with fixed connection probability, but different frequencies of second order motifs.

First, the degree distribution method consists of initially generating a sample of in and out degrees from a truncated power law distribution with density, following [309],

$$f(d) = \begin{cases} C_1 d^{\gamma_1}, & 0 \leq d \leq L_1, \\ C_2 d^{\gamma_2}, & L_1 \leq d \leq L_2, \\ 0, & \text{otherwise,} \end{cases}$$

where d is the in- or out-degree. The two marginal distributions of in and out degree are then coupled using a Gaussian copula with correlation coefficient ρ to generate the in- and out-degree list. The parameters $\rho, L_1/L_2, L_2, \gamma_1 > 0, \gamma_2 < 0$ are randomly and uniformly sampled for each network, separately for in and out degrees.

We also use the SONET method [309] for generating single population networks. In concept, the sampling distribution of the SONET algorithm is similar to that of the maximum entropy graph distribution: Given only the connection probability and second order motif frequency, we try to generate the “most random” network satisfying these moment constraints. However, instead of drawing the connections from a Gibbs distribution as in a proper maximum entropy method, we make use of a dichotomized, N^2 -dimensional multivariate Gaussian distribution. The SONET algorithm allows us to sample from the entire range of possible first and second order motif frequencies. Network samples generated using both methods cover the range of motif frequency observed experimentally in cortical circuits [260, 309].

7.1.2 Second order motif cumulants

Briefly, a motif is defined as a subgraph of the network architecture. To quantify the frequency of a motif in a given realization of the random synaptic architecture, we first count the number of times the motif occurs, then normalize by the number of occurrences possible in a network of that size. For instance, the first order motif cumulant is simply the empirical connection probability p , given by

$$p = \frac{1}{N} \mathbf{u}^T \mathbf{W}^0 \mathbf{u} = \frac{1}{N^2} \sum_{i,j} W_{ij}^0, \quad (7.2)$$

where we have defined the N -vector \mathbf{u} by $\mathbf{u} = \frac{1}{\sqrt{N}}\mathbf{1}_{N_1}$. Here, $\mathbf{1}_{N_1N_2}$ is the $N_1 \times N_2$ matrix of all ones. Note that if $\langle \mathbf{X} \rangle$ indicates the entry-wise average of the matrix \mathbf{X} , then

$$\langle \mathbf{X} \rangle = \frac{1}{N} \mathbf{u}^T \mathbf{X} \mathbf{u}.$$

The prevalence of second order motifs is assessed similarly. For instance, the frequency of second order diverging motifs (see Figure 7.1) is measured by

$$\begin{aligned} q_{\text{div}} &= \frac{1}{N^2} \mathbf{u}^T \mathbf{W}^0 \mathbf{W}^{0T} \mathbf{u} - p^2 \\ &= \frac{1}{N} \langle \mathbf{W}^0 \mathbf{W}^{0T} \rangle - p^2 \\ &= \frac{1}{N^3} \sum_{i,j,k} \mathbf{W}_{ik}^0 \mathbf{W}_{jk}^0 - p^2. \end{aligned} \tag{7.3}$$

Motif cumulants for second order chain and converging motifs are defined likewise,

$$\begin{aligned} q_{\text{ch}} &= \frac{1}{N^2} \mathbf{u}^T \left(\mathbf{W}^0 \right)^2 \mathbf{u} - p^2 \\ &= \frac{1}{N} \mathbf{u}^T \left(\mathbf{W}^{0T} \right)^2 \mathbf{u} - p^2 \\ &= \frac{1}{N} \langle \left(\mathbf{W}^0 \right)^2 \rangle - p^2, \end{aligned} \tag{7.4}$$

$$\begin{aligned} q_{\text{con}} &= \frac{1}{N^2} \mathbf{u}^T \mathbf{W}^{0T} \mathbf{W}^0 \mathbf{u} - p^2 \\ &= \frac{1}{N} \langle \mathbf{W}^{0T} \mathbf{W}^0 \rangle - p^2. \end{aligned} \tag{7.5}$$

In the limit of large population size, the empirical connection probability p of an Erdős-Rényi network converges to the statistical connection probability p_{stat} used to define the model with probability one, by the strong law of large numbers. Similarly, the probability of observation of any second order motif necessarily converges to p^2 . Thus, the subtraction of p^2 in the definitions (7.3–7.5) specifies these quantities to be measurements of the frequency of the corresponding second order motif *in excess* (or deficit) of what would be naively predicted from lower order — in the present case, just first order — motif frequencies. In other words, given only the first order motif cumulant (the connection probability)

and lacking any knowledge of the graphical dependencies, the *best guess* one can make for the probability of seeing a given second order motif is p^2 — i.e., to assume connections are independent. It is this normalization which suggests the interpretation of q_{div} as a motif *cumulant*.

Relation between motif cumulants and the degree distribution It is important to note that the second order motif cumulants defined in Eqs. (7.3–7.5) are not independent, and generally cannot be manipulated independently. These quantities do jointly possess three degrees of freedom, given by their relationship to moments of the degree distributions [101, 127, 128, 236],

$$q_{\text{div}} = \frac{1}{N^2} \mathbf{var} [d^{\text{out}}], \quad q_{\text{con}} = \frac{1}{N^2} \mathbf{var} [d^{\text{in}}], \quad \text{and} \quad q_{\text{ch}} = \frac{1}{N^2} \mathbf{cov} [d^{\text{out}}, d^{\text{in}}].$$

The stated variances and covariances are sample moments of the network degree distribution.

7.1.3 Motif moments and higher order cumulants

7.1.3.1 Single population networks

In anticipation of subsequent analyses, we will now establish some additional notation, and define higher order motif cumulants. First, we define a *motif moment* to be the empirical probability of observing a specified motif, without removal of lower order contributions. For an (n, m) diverging motif (see Figure 6.1 and the surrounding discussion), the motif moment $\mu_{n,m}$ is simply defined as

$$\mu_{n,m} = \frac{1}{N^{n+m-1}} \left\langle \left(\mathbf{W}^0 \right)^n \left(\mathbf{W}^{0T} \right)^m \right\rangle = \frac{1}{N^{n+m}} \mathbf{u}^T \left(\mathbf{W}^0 \right)^n \left(\mathbf{W}^{0T} \right)^m \mathbf{u}. \quad (7.6)$$

Motif moments μ_n corresponding to length n chains are given by $\mu_n = \mu_{n,0} = \mu_{0,n}$.

The relationship between motif moments and motif cumulants is analogous to that between moments and cumulants of random variables. In particular, we define motif cumulants implicitly via expanded forms of motif moments. Letting

$$\mathcal{C}(n) = \left\{ \{n_1, \dots, n_t\} : \sum_i n_i = n, n_i > 0 \right\}$$

be the collection of all compositions (*ordered* partitions) of N , we set for $n, m \geq 1$

$$\mu_n = \sum_{\{n_1, \dots, n_t\} \in \mathcal{C}(n)} \left(\prod_{i=1}^t \kappa_{n_i} \right), \quad (7.7)$$

$$\mu_{n,m} = \sum_{\substack{\{n_1, \dots, n_t\} \in \mathcal{C}(n) \\ \{m_1, \dots, m_s\} \in \mathcal{C}(m)}} \left(\prod_{i=1}^{t-1} \kappa_{n_i} \right) (\kappa_{n_t, m_s} + \kappa_{n_t} \kappa_{m_s}) \left(\prod_{j=1}^{s-1} \kappa_{m_j} \right). \quad (7.8)$$

In evaluating the motif cumulant $\mu_{n,m}$, we adopt the convention that $(\prod_{i=1}^{t-1} \kappa_{n_i}) = 1$ if $t = 1$, and likewise if $s = 1$.

The construction of motif moments from cumulants has a familiar interpretation: estimating the probability of a joint event from the probability of its constituents. Figure 7.2 demonstrates this for two example motifs. Each term in the diagrammatic expansion arises from a cumulant. The first order term gives the probability assuming independence of each connection, and the subsequent terms give corrections from excess occurrences of second, and then higher order, submotifs. Hence, each motif cumulant $\kappa_{n,m}$ captures “pure” higher order connectivity statistics.

Referring to definitions given in Eqs. (7.2), (7.3) and (7.4), it is not difficult to check that

$$p = \kappa_1, \quad q_{\text{div}} = \kappa_{1,1}, \quad \text{and} \quad q_{\text{ch}} = \kappa_2.$$

General motif moments can also be expressed explicitly in terms of the adjacency matrix, which is the subject of the next proposition.

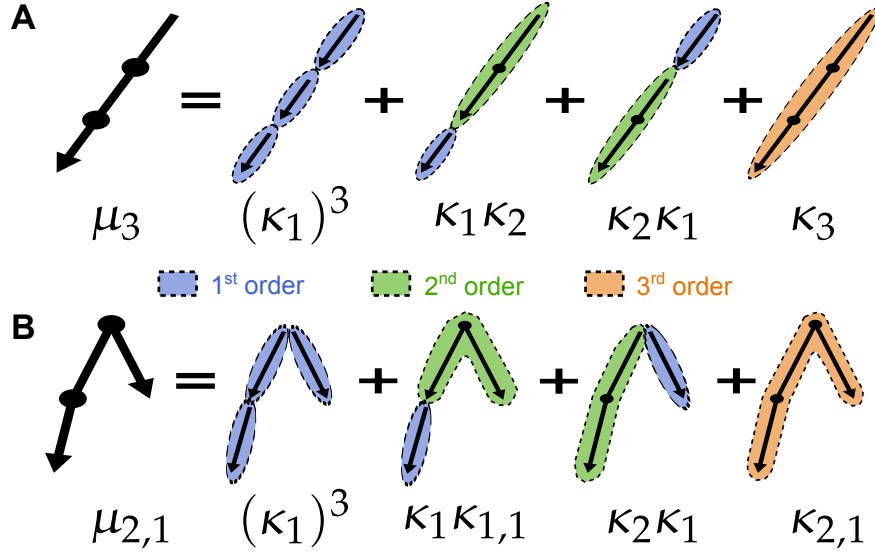


Figure 7.2: **Diagrammatic expansion of the probability of occurrence for motifs.** (A) The probability of observing a third order chain motif, μ_3 , can be expanded in terms of empirical motif cumulants of lesser or equal order. (B) Same as panel A, but for a third order diverging motif, $\mu_{2,1}$.

Proposition 7.1.1. Let \mathbf{W}^0 be the adjacency matrix for a size N network consisting of a single class of cells. Define $\mathbf{H} = \mathbf{u}\mathbf{u}^T$ and $\mathbf{\Theta} = \mathbf{I} - \mathbf{H}$. Define $\mathbf{W}_n^\theta = [(\mathbf{W}^0 \mathbf{\Theta})^{n-1} \mathbf{W}^0]$. If the motif cumulants $\kappa_n, \kappa_{n,m}$ are defined implicitly by Eqs. (7.7, 7.8) then we also have for $n, m \geq 1$ that

$$\kappa_n = \frac{1}{N^n} \mathbf{u}^T \mathbf{W}_n^\theta \mathbf{u}, \quad (7.9)$$

$$\kappa_{n,m} = \frac{1}{N^{n+m}} \mathbf{u}^T \mathbf{W}_n^\theta \mathbf{\Theta} \mathbf{W}_m^\theta \mathbf{u}. \quad (7.10)$$

Proof. First, recall that from Eq. (7.6), we have

$$\mu_n = \frac{1}{N^n} \mathbf{u}^T (\mathbf{W}^0)^n \mathbf{u}.$$

Substituting $\mathbf{I} = \mathbf{\Theta} + \mathbf{H}$ between every subsequent appearance of the adjacency matrix \mathbf{W}^0 gives

$$\mu_n = \frac{1}{N^n} [\mathbf{W}^0 (\mathbf{\Theta} + \mathbf{H})]^{n-1} \mathbf{W}^0 \mathbf{u}. \quad (7.11)$$

Next, we expand across every sum $\Theta + \mathbf{H}$ in Eq. (7.11) and collect consecutive products of \mathbf{W}^0 and Θ into terms of the form $\mathbf{W}_{n_i}^\theta$. Noting the obvious bijection between a composition of the integer n , i.e., $\{n_1, \dots, n_t\} \in \mathcal{C}(n)$, and a term of the form

$$\left[\prod_{i=1}^{t-1} (\mathbf{W}_{n_i}^\theta \mathbf{H}) \right] \mathbf{W}_{n_t}^\theta.$$

we can write (substituting $\mathbf{H} = \mathbf{u}\mathbf{u}^T$)

$$\begin{aligned} \mu_n &= \frac{1}{N^n} \mathbf{u}^T \left\{ \sum_{\{n_1, \dots, n_t\} \in \mathcal{C}(n)} \left[\prod_{i=1}^{t-1} (\mathbf{W}_{n_i}^\theta \mathbf{H}) \right] \mathbf{W}_{n_t}^\theta \right\} \mathbf{u} \\ &= \frac{1}{N^n} \sum_{\{n_1, \dots, n_t\} \in \mathcal{C}(n)} \left[\prod_{i=1}^t (\mathbf{u}^T \mathbf{W}_{n_i}^\theta \mathbf{u}) \right]. \end{aligned} \quad (7.12)$$

If $t = 1$, we define the product $\left[\prod_{i=1}^{t-1} (\mathbf{W}_{n_i}^\theta \mathbf{H}) \right] = \mathbf{I}$.

Now, we will establish Eq. (7.9) by induction. Note that this equation holds trivially for $n = 1$, as from Eqs. (7.6, 7.7) we have, noting that the only decomposition of $n = 1$ is $\{1\}$,

$$\kappa_1 = \mu_1 = \frac{1}{N} \mathbf{u}^T \mathbf{W}^0 \mathbf{u} = \frac{1}{N} \mathbf{u}^T \mathbf{W}_1^\theta \mathbf{u}.$$

Next, assume that Eq. (7.9) holds for all $n < p$. That is, we have

$$\kappa_n = \frac{1}{N^n} \mathbf{u}^T \mathbf{W}_n^\theta \mathbf{u}, \quad n < p. \quad (7.13)$$

From Eq. (7.12) we can write

$$\mu_p = \frac{1}{N^p} \left\{ \mathbf{u}^T \mathbf{W}_p^\theta \mathbf{u} + \sum_{\{n_1, \dots, n_t\} \in \mathcal{C}(p)}^* \left[\prod_{i=1}^t (\mathbf{u}^T \mathbf{W}_{n_i}^\theta \mathbf{u}) \right] \right\},$$

where the notation \sum^* indicates a sum over all partitions not consisting of a single element (i.e., $t > 1$). Substituting Eq. (7.13) into the previous expression next gives that

$$\mu_p = \frac{1}{N^p} \mathbf{u}^T \mathbf{W}_p^\theta \mathbf{u} + \sum_{\{n_1, \dots, n_t\} \in \mathcal{C}(p)}^* \left[\prod_{i=1}^t \kappa_{n_i} \right].$$

Noting that Eq. (7.7) can be written

$$\mu_p = \kappa_p + \sum_{\{n_1, \dots, n_t\} \in \mathcal{C}(p)}^* \left[\prod_{i=1}^t \kappa_{n_i} \right],$$

comparing the previous two expressions yields that

$$\kappa_p = \frac{1}{N^p} \mathbf{u}^T \mathbf{W}_p^\theta \mathbf{u}.$$

In sum, Eq. (7.9) holding for $n < p$ implies that it holds for $n = p$. By induction, Eq. (7.9) holds for all n .

Equation (7.10) is established likewise. Starting from Eq. (7.6), substituting $\mathbf{I} = \Theta + \mathbf{H}$ between every subsequent appearance of the adjacency matrix \mathbf{W}^0 gives

$$\mu_{n,m} = \frac{1}{N^{n+m}} \mathbf{u}^T \left[\mathbf{W}^0 (\Theta + \mathbf{H}) \right]^{n-1} \mathbf{W}^0 (\Theta + \mathbf{H}) \mathbf{W}^{0T} \left[(\Theta + \mathbf{H}) \mathbf{W}^{0T} \right]^{m-1} \mathbf{u}. \quad (7.14)$$

By expanding across all sums of $\Theta + \mathbf{H}$ except the central one (between the terms $\mathbf{W}^0, \mathbf{W}^{0T}$), and noting that there is an obvious bijection between a pair of compositions of the integers n and m , i.e., $\{n_1, \dots, n_t\} \in \mathcal{C}(n), \{m_1, \dots, m_s\} \in \mathcal{C}(m)$, and a term of the form

$$\left[\prod_{i=1}^{t-1} (\mathbf{W}_{n_i}^\theta \mathbf{H}) \right] \left[\mathbf{W}_{n_t}^\theta (\Theta + \mathbf{H}) \mathbf{W}_{m_s}^\theta \right] \left[\prod_{j=1}^{s-1} (\mathbf{H} \mathbf{W}_{m_j}^\theta) \right],$$

we can write (substituting $\mathbf{H} = \mathbf{u} \mathbf{u}^T$)

$$\begin{aligned} \mu_{n,m} &= \frac{1}{N^{n+m}} \mathbf{u}^T \left\{ \sum_{\substack{\{n_1, \dots, n_t\} \in \mathcal{C}(n) \\ \{m_1, \dots, m_s\} \in \mathcal{C}(m)}}} \left[\prod_{i=1}^{t-1} (\mathbf{W}_{n_i}^\theta \mathbf{H}) \right] \left[\mathbf{W}_{n_t}^\theta (\Theta + \mathbf{H}) \mathbf{W}_{m_s}^\theta \mathbf{u} \right] \left[\prod_{j=1}^{s-1} (\mathbf{H} \mathbf{W}_{m_j}^\theta) \right] \right\} \mathbf{u} \\ &= \frac{1}{N^{n+m}} \sum_{\substack{\{n_1, \dots, n_t\} \in \mathcal{C}(n) \\ \{m_1, \dots, m_s\} \in \mathcal{C}(m)}}} \left[\prod_{i=1}^{t-1} (\mathbf{u}^T \mathbf{W}_{n_i}^\theta \mathbf{u}) \right] \left[\mathbf{u}^T \mathbf{W}_{n_t}^\theta (\Theta + \mathbf{u} \mathbf{u}^T) \mathbf{W}_{m_s}^\theta \mathbf{u} \right] \left[\prod_{j=1}^{s-1} (\mathbf{u}^T \mathbf{W}_{m_j}^\theta \mathbf{u}) \right] \\ &= \sum_{\substack{\{n_1, \dots, n_t\} \in \mathcal{C}(n) \\ \{m_1, \dots, m_s\} \in \mathcal{C}(m)}}} \left[\prod_{i=1}^{t-1} \left(\frac{1}{N^{n_i}} \mathbf{u}^T \mathbf{W}_{n_i}^\theta \mathbf{u} \right) \right] \left[\frac{1}{N^{n_t+m_s}} \mathbf{u}^T \mathbf{W}_{n_t}^\theta (\Theta + \mathbf{u} \mathbf{u}^T) \mathbf{W}_{m_s}^\theta \mathbf{u} \right] \\ &\quad \cdot \left[\prod_{j=1}^{s-1} \left(\frac{1}{N^{m_j}} \mathbf{u}^T \mathbf{W}_{m_j}^\theta \mathbf{u} \right) \right]. \end{aligned} \quad (7.15)$$

If $t = 1$, we again define the product $[\prod_{i=1}^{t-1} (\mathbf{W}_{n_i}^\theta \mathbf{H})] = \mathbf{I}$ and likewise if $s = 1$.

We now prove Eq. (7.10) by induction, taking as true Eq. (7.9). First, when $n = m = 1$, the only compositions are trivial (i.e., $\mathcal{C}(1) = \{\{1\}\}$). Equations (7.8) and (7.15) give in this case that

$$\mu_{1,1} = \kappa_{1,1} + \kappa_1^2 = \frac{1}{N^2} \mathbf{u}^T \mathbf{W}_1^\theta \Theta \mathbf{W}_1^\theta \mathbf{u} + \left(\frac{1}{N} \mathbf{u}^T \mathbf{W}_1^\theta \mathbf{u} \right)^2.$$

Since Eq. (7.7) for $n = 1$ provides the equality

$$\kappa_1 = \frac{1}{N} \mathbf{u}^T \mathbf{W}_1^\theta \mathbf{u},$$

we have that

$$\kappa_{1,1} = \frac{1}{N^2} \mathbf{u}^T \mathbf{W}_1^\theta \Theta \mathbf{W}_1^\theta \mathbf{u}.$$

Hence, Eq. (7.8) holds for $n = m = 1$. Next, fix a pair of integers (p, q) with $(p, q) > (1, 1)$, where the inequality $(n, m) < (p, q)$ is defined such that $n \leq p$ and $m \leq q$, with at least one inequality holding strictly. Assume Eq. (7.8) is true for all $(n, m) < (p, q)$. That is, in these cases,

$$\kappa_n = \frac{1}{N^n} \mathbf{u}^T \mathbf{W}_n^\theta \mathbf{u} \quad (\text{by Eq. (7.7)}) \quad \text{and} \quad \kappa_{n,m} = \frac{1}{N^{n+m}} \mathbf{u}^T \mathbf{W}_n^\theta \Theta \mathbf{W}_m^\theta \mathbf{u}. \quad (7.16)$$

From Eq. (7.15), we can write

$$\begin{aligned} \mu_{p,q} = & \sum_{\substack{\{n_1, \dots, n_t\} \in \mathcal{C}(p) \\ \{m_1, \dots, m_s\} \in \mathcal{C}(q)}}^* \left[\prod_{i=1}^{t-1} \left(\frac{1}{N^{n_i}} \mathbf{u}^T \mathbf{W}_{n_i}^\theta \mathbf{u} \right) \right] \left[\frac{1}{N^{n_t+m_s}} \mathbf{u}^T \mathbf{W}_{n_t}^\theta (\Theta + \mathbf{u} \mathbf{u}^T) \mathbf{W}_{m_s}^\theta \mathbf{u} \right] \\ & \cdot \left[\prod_{j=1}^{s-1} \left(\frac{1}{N^{m_j}} \mathbf{u}^T \mathbf{W}_{m_j}^\theta \mathbf{u} \right) \right] + \frac{1}{N^{p+q}} \left[\mathbf{u}^T \mathbf{W}_p^\theta \Theta \mathbf{W}_q^\theta \mathbf{u} + \left(\mathbf{u}^T \mathbf{W}_p^\theta \mathbf{u} \right) \left(\mathbf{u}^T \mathbf{W}_q^\theta \mathbf{u} \right) \right], \end{aligned}$$

where the notation \sum^* indicates a sum over all partitions in $\mathcal{C}(p)$ and $\mathcal{C}(q)$ not *both* consisting of a single element (i.e., t, s are not simultaneously equal to 1). Substituting in

Eq. (7.16) gives that

$$\mu_{p,q} = \frac{1}{N^{p+q}} \mathbf{u}^T \mathbf{W}_p^\theta \Theta \mathbf{W}_q^\theta \mathbf{u} + \kappa_p \kappa_q + \sum_{\substack{\{n_1, \dots, n_t\} \in \mathcal{C}(p) \\ \{m_1, \dots, m_s\} \in \mathcal{C}(q)}}^* \left(\prod_{i=1}^{t-1} \kappa_{n_i} \right) (\kappa_{n_t, m_s} + \kappa_{n_t} \kappa_{m_s}) \left(\prod_{j=1}^{s-1} \kappa_{m_j} \right).$$

In addition, Eq. (7.8) can be written

$$\mu_{n,m} = \kappa_{p,q} + \kappa_p \kappa_q + \sum_{\substack{\{n_1, \dots, n_t\} \in \mathcal{C}(n) \\ \{m_1, \dots, m_s\} \in \mathcal{C}(m)}}^* \left(\prod_{i=1}^{t-1} \kappa_{n_i} \right) (\kappa_{n_t, m_s} + \kappa_{n_t} \kappa_{m_s}) \left(\prod_{j=1}^{s-1} \kappa_{m_j} \right).$$

Comparing the previous two expressions yields that

$$\kappa_{p,q} = \frac{1}{N^{p+q}} \mathbf{u}^T \mathbf{W}_p^\theta \Theta \mathbf{W}_q^\theta \mathbf{u},$$

i.e., Eq. (7.10) holds for $(n, m) = (p, q)$. Therefore, Eq. (7.10) holds for $(n, m) = (1, 1)$ and if it holds for $(n, m) < (p, q)$, then it holds for $(n, m) = (p, q)$. By induction, Eq. (7.10) holds for all $(n, m) \geq (1, 1)$, completing the proof. \square

The motif moments and cumulants defined in Eqs. (7.9–7.10) involve diverging and chain motifs of the type depicted in Figure 6.1. The astute reader may wonder at this point why no converging motifs are being considered. The answer is that such motifs simply do not appear in the linear response approximation of correlations. Below, we will verify this independence of correlations on converging motifs which is generally true for linearly interacting networks.

7.1.3.2 Motif cumulants in networks with multiple subpopulations

Neuronal network models often possess natural divisions into subpopulations. For example, neuronal populations can be divided according to the polarity of interactions between neurons (i.e., into excitatory and inhibitory neurons). In addition, neurons of different

types have been observed to exhibit a wide range of synaptic and electrophysiological properties [18]. We next extend the concept of motif cumulants presented in Section 7.2.1 for a single homogeneous population to networks consisting of distinguishable subpopulations.

One immediate complication which arises in the consideration of motif cumulants in the context of networks with multiple subpopulations is the combinatorial explosion of the number of motifs embedded within the network architecture of a given order. For example, there are twenty distinct second order motifs for a network consisting of two distinct populations, as opposed to three for a single population (see Figure 7.1). The twenty motifs include three motif types, and $2^3 = 8$ possible choices for each type, including four redundant motifs — for example, the motifs $E \leftarrow E \rightarrow I$ and $I \leftarrow E \rightarrow E$ are equivalent. Diagrams of these twenty motifs are shown in Figure 7.3.

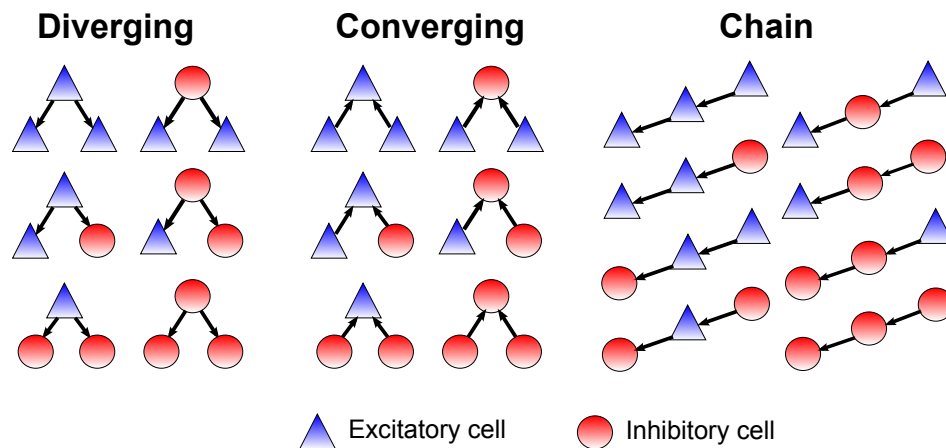


Figure 7.3: **Second order motifs in a two population network.** In a two population network, twenty different second order motifs can be defined depending on the motif type (converging, diverging or chain) as well as the subpopulation identity of each neuron in the motif. In this case, the two populations, represented by different colored shapes, are excitatory and inhibitory neurons.

When considering the situation of multiple subpopulations, it is natural to also consider the blockwise-averaged correlation. To fix ideas, we will consider a two-class network consisting of excitatory and inhibitory cells, but the theory is certainly more general, and extensions to more subpopulations are natural. In this case, take our size N network to consist of N_E excitatory cells and $N_I = N - N_E$ inhibitory cells. Define the $N \times 2$ matrix \mathbf{U} as

$$\mathbf{U} = \begin{bmatrix} \frac{1}{\sqrt{N_E}} \mathbf{1}_{N_E 1} & \mathbf{0} \\ \mathbf{0} & \frac{1}{\sqrt{N_I}} \mathbf{1}_{N_I 1} \end{bmatrix}.$$

In addition, define the blockwise average $\langle \mathbf{X} \rangle_B$ of an $N \times N$ matrix \mathbf{X} as the 2×2 matrix

$$\langle \mathbf{X} \rangle_B = \begin{bmatrix} \langle \mathbf{X}_{EE} \rangle & \langle \mathbf{X}_{EI} \rangle \\ \langle \mathbf{X}_{IE} \rangle & \langle \mathbf{X}_{II} \rangle \end{bmatrix},$$

where \mathbf{X}_{YZ} indicates the corresponding $N_Y \times N_Z$ block of \mathbf{X} and $\langle \mathbf{X}_{YZ} \rangle$ is a normal entry-wise matrix average. We note that

$$\langle \mathbf{X} \rangle_B = \mathbf{D} \mathbf{U}^T \mathbf{X} \mathbf{U} \mathbf{D},$$

where

$$\mathbf{D} = \begin{bmatrix} 1/\sqrt{N_E} & 0 \\ 0 & 1/\sqrt{N_I} \end{bmatrix}.$$

Motif moments are defined analogously to the single population case (see Eq. (7.6)) as

$$\boldsymbol{\mu}_{n,m} = \frac{1}{N^{n+m-1}} \left\langle (\mathbf{W})^n (\mathbf{W}^T)^m \right\rangle_B = \frac{1}{N^{n+m-1}} \mathbf{D} \mathbf{U}^T (\mathbf{W})^n (\mathbf{W}^T)^m \mathbf{U} \mathbf{D}. \quad (7.17)$$

Note that motif moments (and, accordingly, cumulants) are now matrices, as opposed to scalars when defined for a single population, and more importantly, are defined in terms of the *weight* matrix, as opposed to the adjacency matrix. The reasoning behind this choice is simple — when considering multiple populations, a natural difference one can pose

between the populations is different synaptic efficacies. In the present case, excitatory and inhibitory synapses should, at minimum, differ in sign (polarity). In the presence of heterogeneous synaptic weighting, the adjacency matrix is generally less meaningful to the determination of network dynamics than the weight matrix. As a result, motifs, like the connections they involve, can also now possess a strength or polarity which depends on the classes of the cells embedded in the motif.

In parallel with and with slight modification to Eqs. (7.7) and (7.8) in the single population situation, motif moments and cumulants are implicitly related in the multiple subpopulation case as

$$\boldsymbol{\mu}_n = \sum_{\{n_1, \dots, n_t\} \in \mathcal{C}(n)} \left[\left(\prod_{i=1}^{t-1} \boldsymbol{\kappa}_{n_i} \mathbf{E} \right) \boldsymbol{\kappa}_{n_t} \right], \quad (7.18)$$

$$\boldsymbol{\mu}_{n,m} = \sum_{\substack{\{n_1, \dots, n_t\} \in \mathcal{C}(n) \\ \{m_1, \dots, m_s\} \in \mathcal{C}(m)}} \left(\prod_{i=1}^{t-1} \boldsymbol{\kappa}_{n_i} \mathbf{E} \right) (\boldsymbol{\kappa}_{n_t, m_s} + \boldsymbol{\kappa}_{n_t} \mathbf{E} \boldsymbol{\kappa}_{m_s}) \left(\prod_{j=1}^{s-1} \mathbf{E} \boldsymbol{\kappa}_{m_j} \right), \quad (7.19)$$

where

$$\mathbf{E} = \frac{1}{N} \mathbf{D}^{-2} = \begin{bmatrix} N_E/N & 0 \\ 0 & N_I/N \end{bmatrix}.$$

The matrix \mathbf{E} interleaves products of cumulant terms to ensure that the correct scaling is applied for the diagrammatic expansion of motif moments as in Figure 7.2 — in short, this accounts for the probabilities of selecting cells of each population.

Finally, a direct extension of Proposition 7.1.1 gives the following explicit definition of motif cumulants for multiple subpopulations [127, 128],

$$\boldsymbol{\kappa}_n = \frac{1}{N^{n-1}} \mathbf{D} \mathbf{U}^T \mathbf{W}_n^\theta \mathbf{U} \mathbf{D}, \quad (7.20)$$

$$\boldsymbol{\kappa}_{n,m} = \frac{1}{N^{n+m-1}} \mathbf{D} \mathbf{U}^T \mathbf{W}_n^\theta \Theta \mathbf{W}_m^{\theta T} \mathbf{U} \mathbf{D}, \quad (7.21)$$

where we have $\Theta = \mathbf{I} - \mathbf{U}\mathbf{U}^T$ and, in a slight deviation from the single population case, $\mathbf{W}_n^\theta = [\mathbf{W}\Theta]^{n-1} \mathbf{W}$. Importantly, note that motif cumulants in this multipopulation case, like their moment counterparts, are given in terms of the synaptic weight matrix, and not the synaptic adjacency matrix. Thus, in the multipopulation case, the entries of the motif cumulant $\kappa_{n,m}$ should be interpreted as the expected weight of an (n, m) diverging motif *in excess* of what one would predict given access to expected weights of lower order submotifs comprising the (n, m) diverging motif.

The second order motif cumulants $\kappa_{1,1}$ and κ_2 for two populations can be tied explicitly to scalar motif frequencies as were defined in the single population case [127]. First, assuming that synaptic strengths are constant within each class and depend only on the presynaptic cell, we can write

$$\mathbf{W} = \begin{bmatrix} w_E \mathbf{W}_{EE}^0 & w_I \mathbf{W}_{EI}^0 \\ w_E \mathbf{W}_{IE}^0 & w_I \mathbf{W}_{II}^0 \end{bmatrix},$$

where \mathbf{W}_{XZ}^0 is the adjacency matrix for connections from cells in class Z to those in class X . Letting $p_{XZ} = \langle \mathbf{W}_{XZ}^0 \rangle$ represent the corresponding connection probability, we define the quantity $q_{\text{div}}^{XY,Z}$ to be the second order motif cumulant for diverging motifs with a presynaptic cell in class Z and postsynaptic cells of type X, Y , where $X, Y, Z \in \{E, I\}$, i.e.,

$$q_{\text{div}}^{XY,Z} = \frac{1}{N_Z} \langle \mathbf{W}_{XZ}^0 \mathbf{W}_{YZ}^{0T} \rangle - p_{XZ} p_{YZ}. \quad (7.22)$$

Compare the definition in Eq. (7.22) with that for the corresponding single population quantity in Eq. (7.3). Similar expressions define $q_{\text{con}}^{XY,Z}$, the motif cumulant for converging motifs emanating from cells of classes X and Y and terminating in a cell of class Z , and q_{ch}^{XYZ} , the motif cumulant for second order chain motifs which originate from a cell of class Z , terminate in a cell of class X , passing through an intermediate cell of class Y .

7.2. MOTIF CUMULANTS DETERMINE AVERAGE SECOND ORDER CORRELATION

The motif cumulant $\kappa_{1,1}$ can be expressed in terms of scalar second order motif cumulants as

$$\kappa_{1,1} = \begin{bmatrix} \frac{N_E}{N} w_E^2 q_{\text{div}}^{EE,E} + \frac{N_I}{N} w_I^2 q_{\text{div}}^{EE,I} & \frac{N_E}{N} w_E^2 q_{\text{div}}^{EI,E} + \frac{N_I}{N} w_I^2 q_{\text{div}}^{EI,I} \\ \frac{N_E}{N} w_E^2 q_{\text{div}}^{IE,E} + \frac{N_I}{N} w_I^2 q_{\text{div}}^{IE,I} & \frac{N_E}{N} w_E^2 q_{\text{div}}^{II,E} + \frac{N_I}{N} w_I^2 q_{\text{div}}^{II,I} \end{bmatrix}. \quad (7.23)$$

The form of this matrix makes intuitive sense: Take, for example, the entry corresponding to the EE block:

$$\frac{N_E}{N} w_E^2 q_{\text{div}}^{EE,E} + \frac{N_I}{N} w_I^2 q_{\text{div}}^{EE,I}.$$

The first term above is a product of the weight of a diverging motif from an excitatory cell (w_E^2) with the excess probability of seeing such a motif which terminates in two excitatory cells, finally modulated by the probability of selecting an E cell as the “root” cell in the diverging motif. The second term is interpreted likewise, and the sum arises as a result of the law of total expectation. We can similarly expand the motif cumulant κ_2 in terms of the quantities q_{ch}^{XYZ} .

7.2 Motif cumulants determine average second order correlation

We next apply the linear response theory of Chapters 5 and 6 in order to explore the relationship between average spiking correlation in a neuronal network and the motif cumulants defined in the previous section. In particular, we will show that motif cumulants of only first and second order can almost completely account for the impact of network architecture on average correlation in several classes of random networks. Through the linear response theory, we will arrive at an explicit approximation of average correlation for an integrate-and-fire network in terms of motif cumulants of all orders.

7.2.1 Single population networks

Figure 7.4 exhibits the relationship between second order motif frequencies and average correlation in a network consisting of a single class of excitatory cells. In Figure 7.4A, we plot average correlation as a function of the three second order motif frequencies defined in Eqs. (7.3–7.5). The data reveal a strong, positive dependence on the frequency of second order chain motifs. Likewise, we observe a positive (but somewhat weaker) dependence on the frequency of diverging motifs. Finally, there seems to be a negligible dependence on the frequency of converging motifs. We confirmed these qualitative observations by performing linear regression on the data, and the coefficients of this regression for the second order motif frequencies are displayed in Figure 7.4B.

We derive an analytical form for the relationships between average covariance and second order motif frequencies suggested in Figure 7.4. We again return to the linear response path expansion of second order correlations given in Eq. (6.2). Under the simplifying assumptions outlined in Section 7.1.1, we have $\tilde{\mathbf{K}} = \tilde{A}w\mathbf{W}^0$ and $\mathbf{S}_0^y = S_0^y\mathbf{I}$. Thus, we can express the path expansion for a single population network as

$$\frac{\mathbf{S}^y}{S_0^y} = \sum_{n,m=0}^{\infty} (\tilde{A}w)^{n+m} (\mathbf{W}^0)^n (\mathbf{W}^{0T})^m. \quad (7.24)$$

A first approach is to simply truncate Eq. (7.24) at second order in motif *moments*, thereby ignoring completely contributions to covariances of all motifs higher than second order. Doing so yields the following approximation of average covariance in terms of first and second order motif cumulants,

$$\frac{\langle \mathbf{S}^y \rangle}{S_0^y} = \frac{\mathbf{1} \mathbf{u}^T \mathbf{S}^y \mathbf{u}}{N S_0^y} \approx \frac{1}{N} + 2\tilde{A}wp + 3N (\tilde{A}w)^2 p^2 + N (\tilde{A}w)^2 q_{\text{div}} + 2N (\tilde{A}w)^2 q_{\text{ch}}. \quad (7.25)$$

The approximation of Eq. (7.25) is susceptible to large systematic errors in networks with strong synaptic interactions (for a complete discussion, see [127]).

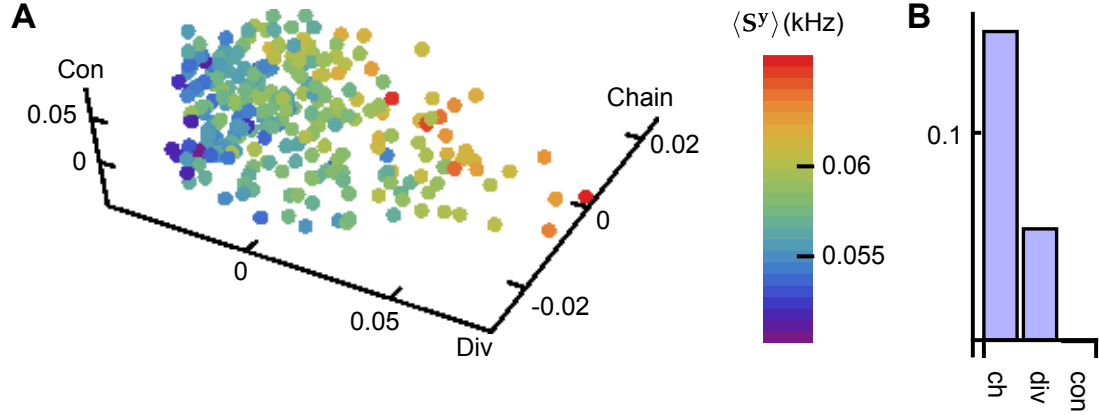


Figure 7.4: **The relationship between second order motif frequencies and average correlation in excitatory-only EIF networks.** (A) Three dimensional scatter plot of average correlations obtained from Monte Carlo simulation of excitatory-only networks of exponential integrate-and-fire neurons, given as a function of second order motif frequencies. The x , y and z coordinates indicate the quantities q_{div} , q_{ch} and q_{con} , respectively. The color of a point indicates the average second order covariance calculated for that network (see color bar). Each of the 265 points displayed corresponds to an adjacency matrix of size $N = 100$ sampled randomly according to the methods prescribed in Section 7.1.1.1. Second order motif frequencies were calculated from the adjacency matrices as in Eqs. (7.3–7.5), and the effective interaction strength was $\Psi_{\text{ER}}(\hat{A}w) = 0.2$ (see Eq. (7.1)). The average spiking correlation coefficient ranged from 0.0036 to 0.0078 in the networks considered. (B) Linear regression coefficients which relate average second order covariance obtained from Monte Carlo simulation of the integrate-and-fire network to the frequencies of second order motifs in this dataset.

We next derive a correction to the approximation Eq. (7.25) which similarly depends only on first and second order motif cumulants, but also includes in the estimate contributions to covariances of motifs higher than second order. This correction depends on the following proposition:

Proposition 7.2.1. *Let \mathbf{H} be the rank-1 orthogonal projection matrix generated by the unit vector $\mathbf{u} = \frac{1}{\sqrt{N}}\mathbf{1}_{N1}$, i.e., $\mathbf{H} = \mathbf{u}\mathbf{u}^T$, and $\Theta = \mathbf{I} - \mathbf{H}$. For any $N \times N$ matrix \mathbf{B} , let*

$$\mathbf{B}_n^\theta = (\mathbf{B}\Theta)^{n-1} \mathbf{B} = \underbrace{\mathbf{B}\Theta\mathbf{B} \cdots \Theta\mathbf{B}}_{n \text{ factors of } \mathbf{B}}.$$

7.2. MOTIF CUMULANTS DETERMINE AVERAGE SECOND ORDER CORRELATION

If the spectral radii $\Psi(\mathbf{B}) < 1$ and $\Psi(\mathbf{B}\Theta) < 1$, then

$$\sum_{n,m=0}^{\infty} \mathbf{u}^T \mathbf{B}^n \mathbf{B}^{mT} \mathbf{u} = \left(1 - \sum_{n=1}^{\infty} \mathbf{u}^T \mathbf{B}_n^{\theta} \mathbf{u}\right)^{-2} \left(1 + \sum_{n,m=1}^{\infty} \mathbf{u}^T \mathbf{B}_n^{\theta} \Theta \mathbf{B}_m^{\theta T} \mathbf{u}\right) \left(1 - \sum_{m=1}^{\infty} \mathbf{u}^T \mathbf{B}_m^{\theta T} \mathbf{u}\right)^{-1}.$$

Proof. Omitted. A detailed proof can be found in [127]. \square

Taking an entry-wise average of Eq. (7.24) gives

$$\frac{\langle \mathbf{S}^y \rangle}{S_0^y} = \frac{1}{N} \frac{\mathbf{u}^T \mathbf{S}^y \mathbf{u}}{S_0^y} = \frac{1}{N} \sum_{n,m=0}^{\infty} \mathbf{u} (\tilde{A}w)^{n+m} (\mathbf{W}^0)^n (\mathbf{W}^{0T})^m \mathbf{u}^T.$$

Thus, applying Proposition 7.2.1 with $\mathbf{B} = \tilde{A}w\mathbf{W}^0$, assuming that the spectral radius conditions are satisfied, we can write

$$\begin{aligned} \frac{\langle \mathbf{S}^y \rangle}{S_0^y} &= \frac{1}{N} \left(1 - \sum_{n=1}^{\infty} (\tilde{A}w)^n \mathbf{u}^T \mathbf{W}_n^{\theta} \mathbf{u}\right)^{-1} \left(1 + \sum_{n,m=1}^{\infty} (\tilde{A}w)^{n+m} \mathbf{u}^T \mathbf{W}_n^{\theta} \Theta \mathbf{W}_m^{\theta T} \mathbf{u}\right) \\ &\quad \cdot \left(1 - \sum_{m=1}^{\infty} (\tilde{A}w)^m \mathbf{u}^T \mathbf{W}_m^{\theta T} \mathbf{u}\right)^{-1}. \end{aligned}$$

Substituting the explicit forms of motif cumulants (Eqs. (7.9) and (7.10)) into the previous expression gives

$$\begin{aligned} \frac{\langle \mathbf{S}^y \rangle}{S_0^y} &= \frac{1}{N} \left(1 - \sum_{n=1}^{\infty} (N\tilde{A}w)^n \kappa_n\right)^{-1} \left(1 + \sum_{n,m=1}^{\infty} (N\tilde{A}w)^{n+m} \kappa_{n,m}\right) \\ &\quad \cdot \left(1 - \sum_{m=1}^{\infty} (N\tilde{A}w)^m \kappa_m\right)^{-1}. \end{aligned} \tag{7.26}$$

Retaining only those terms which involve cumulants up to order two (namely, $\kappa_1, \kappa_{1,1}$ and κ_2) in Eq. (7.26), and substituting the definitions $q_{\text{div}} = \kappa_{1,1}, q_{\text{ch}} = \kappa_2$ gives the following approximation of average correlations in terms of first and second order cumulants [127, 128]:

$$\frac{\langle \mathbf{S}^y \rangle}{S_0^y} = \frac{1}{N} \frac{1 + (N\tilde{A}w)^2 q_{\text{div}}}{\left[1 - (N\tilde{A}w) p - (N\tilde{A}w)^2 q_{\text{ch}}\right]^2}. \tag{7.27}$$

7.2. MOTIF CUMULANTS DETERMINE AVERAGE SECOND ORDER CORRELATION

Truncation of Eq. (7.26) at a certain motif *cumulant* order improves upon similar truncations of Eq. (7.24) at a certain motif *moment* order (or, equivalently, a certain motif order) by attempting to account for the contributions of motifs of *all* orders. This is done by approximating the probability of observing these higher order motifs in terms of the probabilities of observing lower order motifs which compose the higher order motifs (see Figure 7.2). In the special case of Eq. (7.27), we approximate the probability of observing these motifs exclusively in terms of first and second order motif frequencies.

In Figure 7.5A, we compare the predictions of average correlation obtained from the “cumulant resummation” approximation in Eq. (7.27) with that obtained from Monte Carlo simulation of a network of EIF neurons. As shown in Figure 7.5B, the motif cumulant resummation approximation accurately captures the dependencies of average covariance on second order motif cumulants observed from simulations. We emphasize that the present analysis of average spiking covariance in integrate-and-fire networks, particularly the explicit expression of average correlations in terms of the graph architecture, is not generally tractable. These results are made possible here by the synthesis of the linear response theory of correlations presented in Chapters 5 and 6 with the graph-theoretical analysis of Section 7.1.

7.2.2 Multi-population networks

The expression of average correlation can be extended to networks consisting of multiple homogeneous populations. We focus on presenting clearly the theory for two subpopulations, and the requirements of extension to more than two subpopulations are immediate.

Figure 7.6 reveals the dependence between second order motif frequencies in the two

7.2. MOTIF CUMULANTS DETERMINE AVERAGE SECOND ORDER CORRELATION

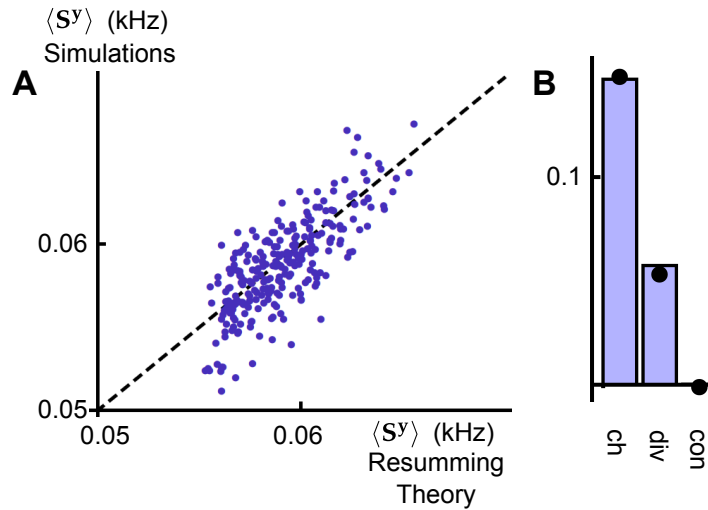


Figure 7.5: Accuracy of the “cumulant resummation” approximation of average covariance in excitatory-only EIF networks. (A) Scatter plot of average correlation obtained from the motif cumulant resummation approximation (horizontal axis, see Eq. (7.27)) against that obtained from Monte Carlo simulation of the integrate-and-fire network (vertical axis). The dashed line represents the diagonal, and each of the 265 points corresponds to one of the networks considered in Figure 7.4. (B) Coefficients of the least squares linear regression of average covariance against the frequency of second order motif frequencies for the 265 networks considered in panel A. Bars represent the values obtained by performing the regression on the prediction of average covariance obtained from the motif cumulant resummation approximation Eq. (7.27), and dots indicate the values obtained by considering the average covariances obtained from simulations (same data as Figure 7.4B).

population, excitatory-inhibitory network. Mirroring our findings for the single population case (see Figure 7.4), we found that chain motifs are the strongest determinant of average correlation amongst the second order motifs, while the dependence on diverging motifs is weaker but still positive, and there is a negligible dependence on converging motifs. As discussed in Section 7.1.3.2, certain motifs now possess a “polarity”; for example, a second order chain motif involving two excitatory (positive) connections will have a positive contribution to correlation. On the other hand, a chain motif consisting of an excitatory (positive) and inhibitory (negative) connection will contribute negatively to

correlations.

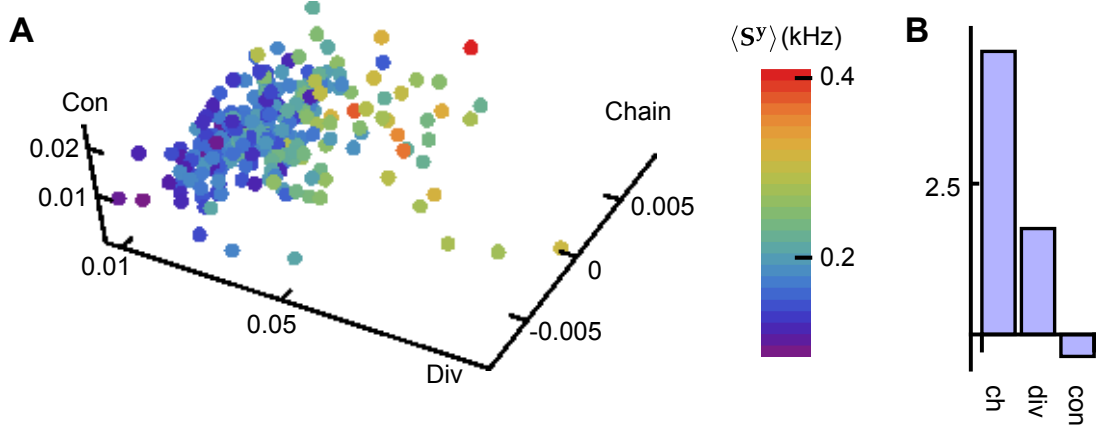


Figure 7.6: **The relationship between second order motif frequencies and average correlation in EIF networks with excitatory and inhibitory neurons.** (A) Three dimensional scatter plot of average correlations obtained from Monte Carlo simulation of an excitatory-only network of EIF neurons, given as a function of weighted linear combinations of second order motif frequencies. The x , y and z coordinates indicate weighted linear combinations of diverging, chain and converging motifs, respectively. The weightings are explained in a technical note within Section 7.2.2. The color of a point indicates the average second order covariance calculated for that network (see color bar). Each of the 265 points displayed corresponds to an adjacency matrix of size $N = 100$ ($N_E = 80$) sampled randomly according to the methods prescribed in Section 7.1.1.1. The effective interaction strength was $\Psi_{ER}(\tilde{A}w) \approx 0.234$ (see Eq. (7.1)). The average spiking correlation coefficient ranged from 0.015 to 0.055 in the networks considered. (B) Linear regression coefficients which relate average second order covariance obtained from Monte Carlo simulation of the EIF network to the weighted linear combinations of second order motif frequencies on the axes in panel A for the 265 networks considered in panel A.

Analogous to the single population expansion of average correlation in terms of motif cumulants in Eq. (7.26), the blockwise average correlations for the network with multiple subpopulations can be expressed as [127, 128]

$$\frac{\langle \mathbf{S}^y \rangle}{S_0^y} = \frac{1}{N} \left(\mathbf{I} - \sum_{n=1}^{\infty} (N\tilde{A})^n \boldsymbol{\kappa}_n \mathbf{E} \right)^{-1} \left(\mathbf{E}^{-1} + \sum_{n,m=1}^{\infty} (N\tilde{A})^{n+m} \boldsymbol{\kappa}_{n,m} \right) \cdot \left(\mathbf{I} - \sum_{m=1}^{\infty} (N\tilde{A})^m \mathbf{E} \boldsymbol{\kappa}_m^T \right)^{-1}, \quad (7.28)$$

7.2. MOTIF CUMULANTS DETERMINE AVERAGE SECOND ORDER CORRELATION

where all variables are defined in Section 7.1.3.2. The derivation of this expansion is essentially identical to that for the single population case, relying on a higher dimensional analog of Proposition 7.2.1, and we omit it.

Truncating Eq. (7.28) at second cumulant order, retaining only factors which involve the cumulants $\kappa_1, \kappa_{1,1}$ and κ_2 , gives

$$\frac{\langle \mathbf{S}^y \rangle}{S_0^y} = \frac{1}{N} \left(\mathbf{I} - N\tilde{A}\kappa_1\mathbf{E} - (N\tilde{A})^2 \kappa_2\mathbf{E} \right)^{-1} \left(\mathbf{E}^{-1} + (N\tilde{A})^2 \kappa_{1,1} \right) \cdot \left(\mathbf{I} - N\tilde{A}\mathbf{E}\kappa_1^T - (N\tilde{A})^2 \mathbf{E}\kappa_2^T \right)^{-1}. \quad (7.29)$$

Equation (7.29) yields an approximation of average blockwise correlation for the multi-population network, extending the single population result. Eq. (7.27). In Figure 7.7, we check the performance of the multipopulation motif cumulant resumming approximation Eq. (7.29) for calculating the three different blockwise averages in an excitatory-inhibitory network of EIF neurons.

We next performed a least squares linear regression of the average correlation against the frequencies of the twenty motifs displayed in Figure 7.3. Figure 7.7B compares the values of the largest eight of the twenty regression coefficients obtained from the motif cumulant resumming approximation in Eq. (7.29) and Monte Carlo simulations. The motif cumulant resumming approximation captures dependencies in average covariance on the individual motif frequencies. Note that the motifs displayed are all chain and diverging motifs — the dependencies on converging motifs were not significant, paralleling our findings in the single population example.

Technical note on generation of Figure 7.6 Performing least squares linear regression of average covariance against the twenty second order motif frequencies in the two-population

7.2. MOTIF CUMULANTS DETERMINE AVERAGE SECOND ORDER CORRELATION

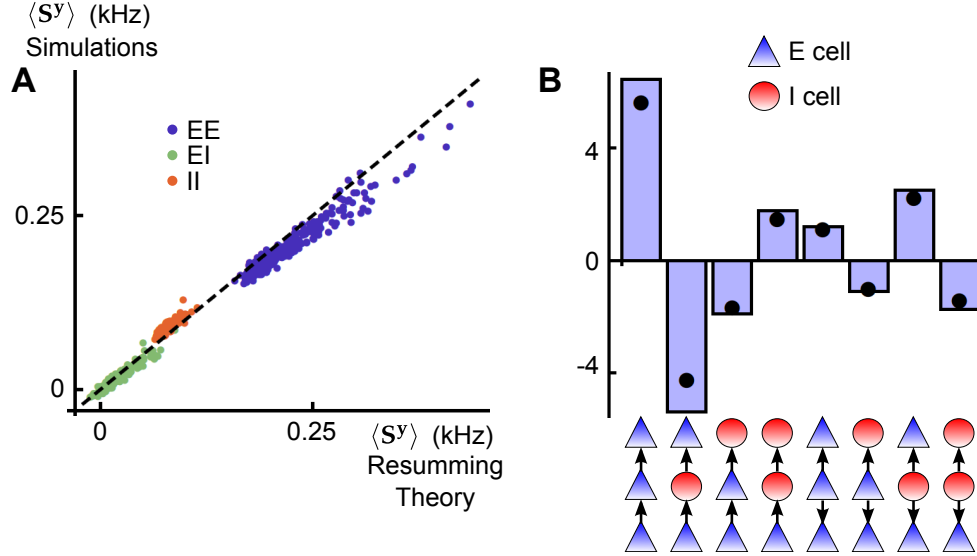


Figure 7.7: Accuracy of the “cumulant resummung” approximation of average covariance in EIF networks with excitatory and inhibitory neurons. (A) Scatter plot of average correlation obtained from the motif cumulant resummung approximation (horizontal axis, see Eq. (7.27)) against that obtained from Monte Carlo simulation of the EIF networks (vertical axis). The dashed line represents the diagonal, and each of the 265 points corresponds to one of the networks considered in Figure 7.6. (B) The eight largest coefficients of the least squares linear regression of average covariance against the frequency of second order motif frequencies for the 265 networks considered in panel A. Bars represent the values obtained by performing the regression on the prediction of average covariance obtained from the motif cumulant resummung approximation Eq. (7.27), and dots indicate the values obtained by considering the average covariances obtained from simulations. The motifs corresponding to each regression coefficient are indicated by the graphics along the horizontal axis — for example, the first motif listed is the $E \rightarrow E \rightarrow E$ chain motif, and the last is the $E \leftarrow I \rightarrow I$ diverging motif. No converging motif regression coefficients are shown, as they were generally much smaller in magnitude for the presented motifs.

network yields a relation of the form

$$\frac{\langle S^y \rangle}{S_0^y} = \sum_{X,Y,Z \in \{E,I\}} k_{\text{ch}}^{XYZ} q_{\text{ch}}^{XYZ} + \sum_{X,Y,Z \in \{E,I\}} k_{\text{div}}^{XY,Z} q_{\text{div}}^{XY,Z} + \sum_{X,Y,Z \in \{E,I\}} k_{\text{con}}^{XY,Z} q_{\text{div}}^{XY,Z}. \quad (7.30)$$

In order to aid in the visualization of the dependence of average covariance on these motifs in Figure 7.6, we plotted average covariance against weighted linear combinations of these motif frequencies. As an example, consider chain motifs. We weighted each

7.2. MOTIF CUMULANTS DETERMINE AVERAGE SECOND ORDER CORRELATION

chain motif first by the probability of observation of that type of chain motif within all chain motifs (thus inducing factors of $f_E = N_E/N$ and $f_I = N_I/N$ in the weighted motif strength), as well as the relative strength and sign of the specific connections involved.

The weighted chain motif strength Q_{ch} (the quantity on the y -axis in Figure 7.6) is given by

$$Q_{\text{ch}} = \sum_{X,Y,Z \in \{E,I\}} \frac{w_Z w_Y}{w_E w_E} f_X f_Y f_Z q_{\text{ch}}^{XYZ}.$$

We remind the reader that q_{ch}^{XYZ} indicates the second order motif cumulant corresponding to chain motifs connecting the classes X, Y and Z as $Z \rightarrow Y \rightarrow X$, and w_E, w_I are the (signed) strengths of excitatory and inhibitory connections in the network, respectively. The weight of q_{ch}^{XYZ} involves the weights w_Y and w_Z , corresponding to the weight of the two synapses involved in the motif. The factors f_X, f_Y, f_Z account for the probability of picking cells of the type involved in the motif, so that the product of the three gives the probability of selecting a chain motif consisting of cells in that particular arrangement.

Efficient encoding of the ego-rotational axis in the fly brain

Coupling between sensory neurons impacts their tuning properties and the correlation of their responses to external stimuli. How such coupling affects motor commands and ultimately behavior remains unclear. In this chapter, we investigate the role of neuronal coupling during visual processing using a biophysical model of the vertical system (VS) cell network in the blow fly. These neurons are thought to encode the horizontal rotation axis over the course of rapid free flight manoeuvres, such as those executed while cruising or for pursuit behaviors. This presents to the VS network and its efferents a problem of *marginalization* (see Figure 1.4C and [175]) — neurons within the visual system must attempt to remove or reduce “unimportant” variability, representing the angle of rotation in its collective response with sufficient fidelity.

A prominent feature of the vertical system is the strong electrical coupling between its neurons. We computed optimal linear and non-linear Bayesian estimators from the VS

cell population response to rotating natural and artificial visual scenes. Surprisingly, and in contrast to the predictions of previous heuristic studies [56, 68, 292], our analysis shows that coupling between VS cells has no impact on the quality of encoding in their response. The result holds both for steady-state and transient responses, contrary to the intuition gained from suboptimal decoders considered previously.

However, anatomical and electrophysiological findings suggest that several downstream neurons driving motor responses to ego-rotation receive inputs primarily from a small subset of VS cells [100, 268, 296–298]. These downstream neurons must therefore decode information about the axis of rotation from a partial readout of the VS population response. In this case, coupling significantly increases encoding efficiency, leading to near-optimal estimates from a subpopulation readout. We explain our findings in terms of the dynamical transformation between visual inputs and the vertical system response in the presence of electrical coupling. Thus, coupling at one level of the fly visual system allows for near-optimal decoding from partial information at the subsequent, pre-motor level. Our conclusions are suggestive of more general principles, and can provide insight into efficient processing of sensory information in other organisms.

8.1 Modeling the vertical system response to optic flow

8.1.1 Model of the VS network

Our study is based on a model of the vertical system tangential cells closely based on that of [30]. Here, we will briefly describe the model, and note the differences between the specific implementations. Parameters not explicitly stated, and details of the model not discussed are identical to those given by [30].

Simulations proceeded by first projecting a random image onto the surface of a sphere. We considered images which consist of randomly arranged bars of varying sizes, as well as random checkerboard images and compositions of natural scenes. Spherical images involving natural scenes were generated by choosing six frames at random from a subset of the van Hateren dataset [283], arranging these on the faces of a cube, then projecting the cube onto the surface of the sphere [30]. Spherical images were rotated about a horizontal axis, thereby generating a pattern of optic flow (Figure 8.1A). Details on image and optic flow stimulus generation are given in Section 8.1.2.

The rotated image sequences ('optic flow stimuli') were first filtered by an array of vertically oriented local motion detectors (LMDs or 'Reichardt detectors'; [29, 99, 215]). The LMDs were spaced approximately evenly on the surface of the sphere. There were 5,000 per hemisphere, corresponding approximately to the number of facets on the left and right eyes [116]. For the Reichardt detector model utilized by [30], the input to a single detector is composed of luminance signals from two vertically-aligned pixels separated by an elevation of 2° . First-order filtered low- and high-pass versions of the input from the two pixels are cross-multiplied and then subtracted (Figure 8.1B). A negative (resp. positive) detector response reflects upward (resp. downward) motion. The downward and upward components are separately weighted according to the dendritic receptive field (RF) of each cell, and activate the dendritic compartment of the VS model neurons as excitatory and inhibitory conductances, respectively. Dendritic receptive fields were vertically-centered Gaussians, with horizontal standard deviation 15° , and vertical standard deviation 60° (see Figure 8.1C and [30]). Hence each cell effectively sampled the entire vertical surround above and below its receptive field center. Receptive field centers are given in Figure 1.4A. Note that maximal excitation and inhibition occurs at azimuthal rotation angles approximately orthogonal to the centers of the receptive field.

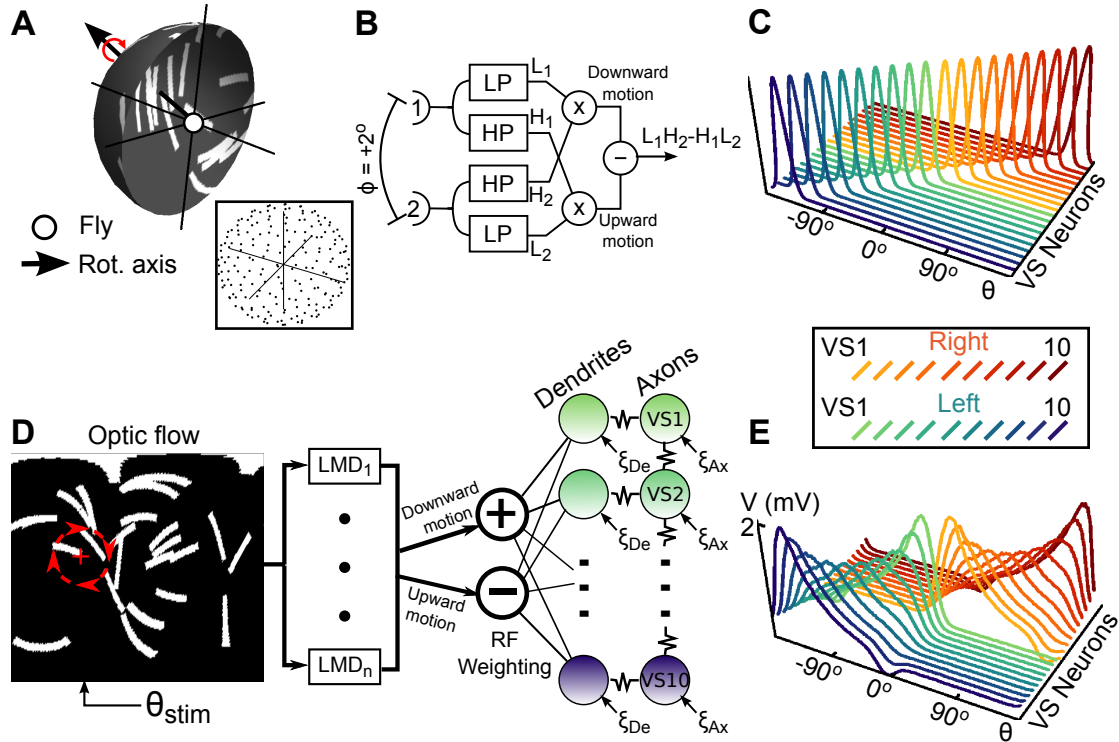


Figure 8.1: Schematic of the VS network model. (A) Spherical image rotation sequences (red curved arrow) were presented to the model of the fly vertical system (VS). The rotation axis in the equatorial plane is characterized by its azimuth, θ_{stim} . Lower right inset shows how the Reichardt detectors were arrayed on the surface of the sphere. (B) Schematics of the Reichardt detector. LP and HP indicate first order low- and high- pass linear filters, respectively, while \times and $-$ represent elementary signal multiplication and subtraction steps. Each detector was assembled from two subunits separated by an elevation of 2° . (C) Horizontal cross sections of the dendritic receptive fields for the VS neurons. The frontmost curve is for the left-side VS10 neuron (see panel E, upper inset). (D) The model is an assembly of a number of components: The optic flow stimulus is generated by rotations of spherical images, and is filtered by the local motion detectors (LMDs). The LMD output is separated into upward and downward components which are mapped to inhibitory ($-$), and excitatory ($+$) conductances, respectively, onto the dendrites of the VS neurons. Conductances are weighted by the position of the LMD with respect to the VS cell receptive fields (see C). Resistor symbols indicate electrical coupling of compartments, and ξ_{Ax} , resp. ξ_{De} , are independent, intrinsic noise sources to the axons, resp. dendrites, of VS cells. (E) Steady-state membrane potential of the twenty coupled VS neurons ($g_{gap} = 1 \mu S$) in response to stimulation by a horizontal grating with constant downward velocity. The input was a narrow, 10° wide strip centered at angle θ . The responses were obtained by sweeping the strip 360° around the visual field. Upper inset details color scheme and cell ordering for panels C and E.

Lastly, the axonal compartments of adjacent, ipsilateral VS neurons are electrically coupled to each other. Figure 8.1D shows a schematic of the model processing stages. Figure 8.1E shows the response of each VS neuron to downward stimulation in a narrow (10° wide) vertical strip which was swept across the visual field.

The axonal and dendritic membrane potentials for the VS neurons in each hemisphere evolve according to:

$$\begin{aligned} C_m \frac{d\mathbf{V}_{Ax}}{dt} &= -G_{Ax} \mathbf{V}_{Ax}(t) + g_{Ax-Den} \mathbf{V}_{De}(t) + \sqrt{\sigma_{Ax}^2 \tau_{Ax}} \boldsymbol{\xi}_{Ax}(t), \\ C_m \frac{d\mathbf{V}_{De}}{dt} &= -G_{De}(t) \mathbf{V}_{De}(t) + g_{Ax-Den} \mathbf{V}_{Ax}(t) + \mathbf{I}(t) + \sqrt{\sigma_{De}^2 \tau_{De}} \boldsymbol{\xi}_{De}(t). \end{aligned} \quad (8.1)$$

Here \mathbf{V}_{Ax} and \mathbf{V}_{De} are vectors whose entries correspond to the 10 axonal and dendritic voltages, respectively. The full VS model consists of two copies of this system, representing the activity of the system in the left and right hemispheres. The two systems differ parametrically only in their receptive field centers (see Figure 1.4A and Figure 8.1C). The parameter g_{Ax-Den} sets the conductance for the coupling of the axonal and dendritic compartments of each neuron, while C_m is the membrane capacitance and $g_{L,Ax}$, $g_{L,De}$ are the leak conductances of each compartment. The membrane time constant of each compartment is $\tau_X = C_m/g_{L,X}$, $X = Ax, De$. The resting potential of each compartment is zero. Following a perturbation from rest, the membrane potential decays exponentially back to the resting potential with a characteristic timescale τ_X . Intrinsic variability is modeled by standard white noise processes $\boldsymbol{\xi}_{Ax}(t)$, $\boldsymbol{\xi}_{De}(t)$, and σ_{Ax} , σ_{De} set the noise intensities.

The input current to the dendrite of cell i is given by $I_i(t) = E_E g_{E,i}(t) + E_I g_{I,i}(t)$, where $g_{E,i}(t)$ is the excitatory conductance to cell i induced by the optic flow stimulus, E_E is the associated reversal potential, and likewise for the inhibitory quantities $g_{I,i}(t)$ and E_I . The matrix $G_{De}(t)$ is diagonal with entries given by

$$G_{De,ii}(t) = g_{L,De} + g_{Ax-Den} + g_{E,i}(t) + g_{I,i}(t), \quad i = 1, \dots, 10.$$

The matrix G_{Ax} has entries given by

$$G_{Ax,ij} = \begin{cases} g_{L,Ax} + g_{Ax-Den} + g_{gap} + g_{inh} & i = j = 1 \text{ or } 10, \\ g_{L,Ax} + g_{Ax-Den} + 2g_{gap} & 2 \leq i = j \leq 9, \\ -g_{gap} & i = j + 1 \text{ or } i = j - 1, \\ -g_{inh} & i = 1, j = 10 \text{ or } i = 10, j = 1. \end{cases} \quad (8.2)$$

Here, g_{gap} sets the strength of the axo-axonal gap junction coupling between adjacent, ipsilateral VS neurons. One difference between our simulation protocol and that of [30] is that we generated visual inputs at time steps of 1 ms, but integrated Eq. (8.1) at a smaller time step of 0.01 ms to guarantee numerical accuracy. We first calculated the conductances elicited by the optic flow stimulus at the coarser time step, then linearly interpolated to obtain a realization of the conductance at the finer timescale. Typical responses of the uncoupled and coupled systems to rotation of a random bar image at $\theta_{stim} = 90^\circ$ are shown in Figure 8.2A and Figure 8.2B, respectively. Central to the ability of the VS population to encode the axis of rotation is the fact that the magnitude of the response of a VS neuron depends strongly (but non-linearly) on the rotational velocity of the visual stimulus within its receptive field.

When we consider the efficiency with which the rotation axis is encoded in the VS axonal responses, we take the output of the system to be temporal averages of the axonal membrane potential. For transient responses, the VS output is

$$\bar{\mathbf{V}}_{Ax}^{tr}(T) = \frac{1}{T} \int_0^T \mathbf{V}_{Ax}(t) dt, \quad \text{where } \mathbf{V}_{Ax}(0) = \mathbf{V}_{De}(0) = \mathbf{0}. \quad (8.3)$$

In particular, when considering transient responses, we assume the system starts from rest (0 mV) at the beginning of the period over which we average. Similarly, steady-state

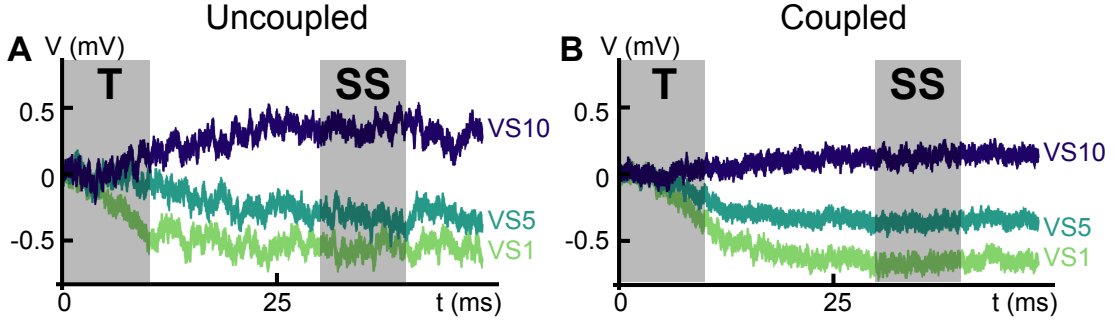


Figure 8.2: **A typical response of the VS network (A)** Plot of the temporal response of the left-side VS1, VS5 and VS10 neurons in the uncoupled system ($g_{\text{gap}} = 0 \mu\text{S}$) to the rotation of a natural scene stimulus (see Figure 1.4B). Shaded boxes labeled **T** and **SS** indicate time intervals 10 ms in duration over which we average the VS axonal responses to obtain the transient average, $\bar{V}_{\text{Ax}}^{\text{tr}}(T)$, and the steady-state average $\bar{V}_{\text{Ax}}^{\text{ss}}(T)$, respectively. **(B)** Same as panel A, but for the coupled system ($g_{\text{gap}} = 1 \mu\text{S}$).

responses are given as

$$\bar{V}_{\text{Ax}}^{\text{ss}}(T) = \frac{1}{T} \int_{\tau_{\text{ss}}}^{\tau_{\text{ss}}+T} \mathbf{V}_{\text{Ax}}(t) dt, \quad \text{where } \tau_{\text{ss}} = 30 \text{ ms.} \quad (8.4)$$

In contrast to the transient response defined above, the steady-state response is defined so that, at the beginning of the integration period (τ_{ss}), the entire VS system is (approximately) in steady-state. It should be noted that despite the very fast time constants the VS model neurons possess, they do not immediately reach steady-state, as it takes some time for the motion detector-filtered stimulus impinging on the VS dendrites to equilibrate. In Figure 8.2, the shaded boxes indicate the periods over which we obtain the transient and steady-state responses.

It has been observed that there is a functionally mutually inhibitory interaction between the end cells (VS1 and VS10) in each hemisphere, believed to be implemented by electrical coupling of VS7-10 to an inhibitory cell Vi which forms a chemical synapse onto the ipsilateral VS1 cell, and electrical coupling of VS1 to an inhibitory cell Vi2 which

forms a chemical synapse onto the ipsilateral VS10 cell [30, 98]. Following [292], we implemented this functionally mutually inhibitory (or “repulsive”) coupling using a negative-conductance gap-junction between VS1 and VS10 (g_{inh} in Eq. (8.2)) instead of explicitly modeling the V_i cell. Our findings do not depend qualitatively on the presence of this connection (results not shown). When we change the strength of the axo-axonal gap junction coupling amongst VS neurons, this repulsive coupling is scaled accordingly. Unless otherwise specified, we set $g_{\text{inh}} = -0.06g_{\text{gap}}$.

For simplicity, we did not model several known functional and anatomical properties of VS cells, such as the rotational structure of their receptive fields [152, 153] or dendro-dendritic connections with the dCH neuron [98]. These properties and their impact on the VS network are currently the subject of electrophysiological investigations [126], but are not expected to significantly affect our conclusions. Previous computational studies of the VS network have made similar simplifying assumptions [56, 68, 142, 292].

8.1.2 Generation of images and optic flow patterns

Optic flow patterns were generated by first projecting various types of random images onto the surface of the unit sphere. We considered three classes of random images: random bar images, random checkerboard images, and natural scenes (see Figure 1.4B for examples of each type of image). In the first two cases, images were binary — pixel intensities were either 0 or 1 — and for natural scenes, pixel intensities varied continuously between 0 and 1. All images were discretized at 1° increments in spherical coordinates. Throughout, images were random and distinct across trials.

Random bar images were parameterized by the number of bars, as well as bar width

and length. When generating a bar image, each bar was generated by first randomly placing an initial line segment of the specified bar width on the surface of the unit sphere. We then translated this segment along the direction of the length of the bar by rotation about the appropriate axis, turning “on” all pixels along the path touched by the rotating segment. Bar images utilized in generating the presented results (i.e., Figures 8.4–8.7, 8.11) contained 25 bars of length 40° and width 5° . Choosing bars with different dimensions or changing the number of bars affected our findings only quantitatively and not qualitatively (results not shown).

For checkerboard images, we defined a coarse discretization of the image consisting of $4^\circ \times 4^\circ$ squares, and randomly set all pixels within a square to be zero or one, independently across squares. Lastly, for natural images, we first took a subcollection of one hundred natural scenes from the van Hateren dataset [282]. We then randomly selected six (with replacement) of these one hundred images, projected them onto the sides of a cube, which was itself then projected onto a sphere, mimicking the approach of [30].

The sequences of images comprising optic flow patterns were generated by rotation of the sphere about a horizontal axis (we did not consider translatory motion). At a given positive time, the value of a pixel was set equal to the value of the pixel obtained by a reversal of the rotation to the original image. The rotational velocity was constant across simulations and set to $500^\circ/s$, falling well within the parameters of typical motion of the fly during flight [66]. This value is also consistent with the range of values considered in previous computational studies of the VS network [56, 68, 142, 292].

8.2 Implementation of estimators for the rotational axis

In order to quantify the fidelity of encoding of the ego-rotational axis within the VS axonal population response, we implement a pair of probabilistic estimators. First, for our analysis of the steady-state responses, we make use of the optimal linear estimator (OLE, see [238]) — the linear estimator which exhibits the lowest mean-square error of prediction amongst all linear estimators. In Section 8.2.1, we present an explicit definition of the OLE, along with some details of how it was applied to the VS axonal responses.

Our primary interest, however, will be in the more behaviorally-relevant transient responses. When we analyze the transient encoding of the axis of rotation, we implemented an approximation the true minimum mean-square estimator (MMSE), defined as the expected value over the posterior distribution of the stimulus. The MMSE is globally optimal across all estimators in the mean-square sense. However, even with the benefit of modern computational power, it is not feasible to directly estimate distribution functions for continuous variates with more than a very few dimensions. For this reason, in order to implement the MMSE, we must first formulate an approximation of the stimulus posterior distribution and, thus, the joint distribution of VS axonal responses.

Two popular approaches to this problem used in computational neuroscience are to fit a maximum entropy distribution that matches a set of empirical statistics of the data [74, 134, 194, 235, 251], or to apply copulas [190]. We chose the latter approach, which is common in the valuation of financial derivatives, but has not been widely applied in neuroscience (see, however, [23, 195, 196]). One advantage of the copula approach is that it allows us to use the true (empirical) marginal distributions in the fit — the copula serves strictly as a fittable model for the dependence structure amongst the marginal responses.

We outline our method for approximating the joint distribution using copulas, and provide an evaluation of the distributional fit in Section 8.2.2. In Section 8.2.3, we briefly explain how our approximation of the joint distribution of VS axonal responses is used to implement the MMSE.

8.2.1 Optimal linear estimator

In the following three sections, the reader should keep in mind that the random vector $\bar{\mathbf{V}}$ is a surrogate for the time-averaged axonal response. For the present section involving the optimal linear estimator, applications will involve the steady-state averaged axonal response $\bar{\mathbf{V}}_{\text{Ax}}^{\text{ss}}$ defined in Eq. (8.4). In the subsequent sections where we consider the application of copulas to computation of the minimum mean-square estimator (MMSE), we will be referring to the transient averaged axonal response $\bar{\mathbf{V}}_{\text{Ax}}^{\text{tr}}$ which is defined in Eq. (8.3).

For our analysis of the steady-state encoding of the axis of rotation, we applied an optimal linear estimator, the linear estimator which minimizes the expected value of the squared error under the posterior distribution [238]. Given an M -dimensional stimulus vector \mathbf{s} encoded in the N -dimensional variable response $\bar{\mathbf{V}} = (\bar{V}_1, \dots, \bar{V}_N)^T$ of a neuronal system (where T denotes transposition), the tuning curve for the i^{th} neuron is the scalar-valued function

$$\mu_i(\mathbf{s}) = \mathbf{E} [\bar{V}_i | \mathbf{s}] = \int d\bar{\mathbf{V}} \bar{V}_i P(\bar{\mathbf{V}} | \mathbf{s}).$$

The center of mass for the i^{th} neuron is the vector

$$\mathbf{L}_i = \mathbf{E} [\mathbf{s} \mu_i(\mathbf{s})] = \int d\mathbf{s} \mathbf{s} \mu_i(\mathbf{s}),$$

and the second moment of the responses of the i^{th} and j^{th} neurons (averaged across stimulus values) is

$$Q_{ij} = \int d\mathbf{s} d\bar{\mathbf{V}} \bar{V}_i \bar{V}_j P(\bar{\mathbf{V}}|\mathbf{s}) P(\mathbf{s}),$$

where $P(\mathbf{s})$ is the prior distribution for the stimulus. Throughout this work, we assume a uniform prior distribution of stimulus rotation angles. Given an observed response $\bar{\mathbf{V}}_{\text{obs}}$, the optimal linear estimator has the form

$$\hat{\mathbf{s}} = L^T Q^{-1} \bar{\mathbf{V}}_{\text{obs}},$$

where $L = [\mathbf{L}_1 | \dots | \mathbf{L}_N]^T$ is an $N \times M$ matrix obtained by concatenating the M -dimensional column vectors $\mathbf{L}_1, \dots, \mathbf{L}_N$ [238]. As long as the joint distribution $P(\bar{\mathbf{V}}, \mathbf{s})$ of responses ($\bar{\mathbf{V}}$) and stimuli (\mathbf{s}) possesses finite first and second moments, the matrix Q is invertible. Implementation of the optimal linear estimator requires measurement of only first and second moments. It is thus considerably simpler to obtain than, for instance, the true minimum mean-square estimator defined in Section 8.2.3. The optimal linear estimator and the minimum mean-square estimator coincide only when the joint distribution $P(\bar{\mathbf{V}}, \mathbf{s})$ is Gaussian, which is not generally true for the system we consider.

In our applications, the stimulus vector \mathbf{s} was assumed to be a two-dimensional unit vector representing the angle of rotation by

$$\mathbf{s}(\theta_{\text{stim}}) = (\cos(\theta_{\text{stim}}), \sin(\theta_{\text{stim}}))^T.$$

The estimated angle $\hat{\theta}_{\text{stim}}^{\text{OLE}}$ was determined by assuming $\hat{\mathbf{s}}$ possessed the same form, and setting

$$\hat{\theta}_{\text{stim}}^{\text{OLE}} = \arg(\hat{\mathbf{s}}).$$

8.2.2 Modeling the joint distribution of VS axonal responses using copulas

For our analysis of the transient state encoding of the axis of rotation, we applied the true minimum mean-square estimator (MMSE). However, even with the benefit of modern computational power, it is not feasible to directly estimate probability distribution functions for continuous variates with more than a few dimensions. For this reason, in order to implement the MMSE, we must first formulate an approximation of the joint probability distribution of VS axonal responses.

Two approaches to this problem are to fit a maximum entropy distribution that matches a set of empirical statistics of the data [74, 134, 194, 235, 251], or to apply copulas [190]. We chose the latter approach, which is common in the valuation of financial derivatives, but has not been widely applied in neuroscience (see, however, [23, 195, 196]). One advantage of the copula approach is that it allows us to use the true (empirical) marginal probability distributions in the fit — the copula serves strictly as a fittable model for the dependence structure amongst the marginal responses.

To fix ideas, we remind the reader that ultimately we will fit a copula to the averaged transient VS axonal response, $\bar{\mathbf{V}}_{\text{Ax}}^{\text{tr}}(T)$, which is defined in Eq. (8.3). Thus, we consider a random vector $\bar{\mathbf{V}} = (\bar{V}_1, \dots, \bar{V}_N)^T$ with cumulative distribution function $F(\bar{v}_1, \dots, \bar{v}_N)$. A copula for the distribution function F is an N -variable function C for which

$$F(\bar{v}_1, \dots, \bar{v}_N) = C(F_1(\bar{v}_1), \dots, F_N(\bar{v}_N)), \quad (8.5)$$

where $F_i(\cdot)$ is the marginal cumulative probability distribution function for the variable $\bar{V}_i, i = 1, \dots, N$. Sklar's Theorem guarantees the existence of the copula C for any distribution F with marginals $\{F_i\}_{i=1}^N$ (cf. [190], Theorem 2.10.9). If F is continuous, C is

unique. From Eq. (8.5), it is clear that C determines completely the inter-variable dependence structure contained in the distribution F .

Note that an N -dimensional copula is equivalent to a distribution function on the N -dimensional unit hypercube $[0, 1]^N$ with uniform marginals: Define the random vector $\mathbf{U} = (U_1, \dots, U_N)$ where $U_i = F_i(\bar{V}_i)$. The probability integral transform implies that each U_i is a marginally uniformly distributed random variable (e.g., [84], Sect. 11.8). The copula $C(u_1, \dots, u_N)$ for $\bar{\mathbf{V}}$ has an equivalent definition as the distribution function of \mathbf{U} .

As is the case for the distribution function F of $\bar{\mathbf{V}}$, the ‘curse of dimensionality’ prevents us from directly approximating the corresponding copula C . A common approach is to select a parametrized copula family which can then be fit most easily via the maximum likelihood principle [307]. We applied the Gaussian copula [305], which takes the form

$$C_{\Sigma}^{\text{Gauss}}(u_1, \dots, u_N) = \Phi_{\Sigma} \left(\Phi^{-1}(u_1), \dots, \Phi^{-1}(u_N) \right). \quad (8.6)$$

Here Φ_{Σ} is the joint Gaussian distribution function with correlation matrix Σ (i.e., $\Sigma_{ii} = 1$ for each i) and Φ is the standard univariate Gaussian distribution function. Given independent identically distributed samples of a random vector $\bar{\mathbf{V}} = (\bar{V}_1, \dots, \bar{V}_N)^T$ with marginals $\{F_i\}$, the value of the correlation Σ_{ij} which is consistent with application of the maximum likelihood principle to second moments can be shown to equal [31]

$$\hat{\Sigma}_{ij} = \text{corr}[\Phi^{-1}(F_i(\bar{V}_i)), \Phi^{-1}(F_j(\bar{V}_j))], \quad 1 \leq i, j \leq N, \quad (8.7)$$

where $\text{corr}(x, y)$ denotes the correlation coefficient of x and y [305].

We fit a Gaussian copula to the transient response of the system, $\bar{\mathbf{V}}_{\text{Ax}}^{\text{tr}}(T)$, defined in Eq. (8.3). In order to test the goodness of the fit distribution, we selected twenty random subsets of three left-side VS neurons, and associated with each subset a random stimulus

rotation angle. We then sampled the marginal copula for each subset (i.e., $C(u_i, u_j, u_k)$ with $u_i = F_i(\bar{V}_i)$ in Eq. (8.5)), comparing it with the fit copula utilized in the MMSE calculations outlined in the next section (Eqs. (8.6), (8.7)). We compared the empirically observed and fit copula distribution values at 1,000 equally spaced points in the unit cube of the form $(0.1i, 0.1j, 0.1k)$, $1 \leq i, j, k \leq 10$. In Figure 8.3A, we present a probability-probability (P-P) plot of the true (empirical) copula values against the fit values. In other words, letting C^{true} and C^{fit} indicate the true and fit copula distribution functions for three randomly selected left-side VS neurons in the system presented a rotation at a random stimulus angle, Figure 8.3 presents a scatter plot of the 1,000 points

$$\left\{ \left(C^{\text{fit}}(0.1i, 0.1j, 0.1k), C^{\text{true}}(0.1i, 0.1j, 0.1k) \right) : 1 \leq i, j, k \leq 10 \right\}.$$

We also computed for each of the twenty subsets and for all 1,000 sample points the relative error between the probabilities from the true and fit copula distributions. In particular, we defined for each point

$$\epsilon_{ijk}^{\text{rel}} = \frac{|C^{\text{true}}(0.1i, 0.1j, 0.1k) - C^{\text{fit}}(0.1i, 0.1j, 0.1k)|}{C^{\text{true}}(0.1i, 0.1j, 0.1k) + C^{\text{fit}}(0.1i, 0.1j, 0.1k)}, \quad 1 \leq i, j, k \leq 10. \quad (8.8)$$

Since the probabilities lie within $[0, 1]$ by definition, the relative errors lie also within $[0, 1]$, with a value of 0 indicating a perfect match. In Figure 8.3B, we plot a histogram of the relative errors for all twenty random subsets (thus comprising a total of 20,000 data points). We found the true and fit copula distributions generally agreed quite well. The average relative error across all 20,000 points was ≈ 0.0438 , and 90.3% of relative errors were below 0.1.

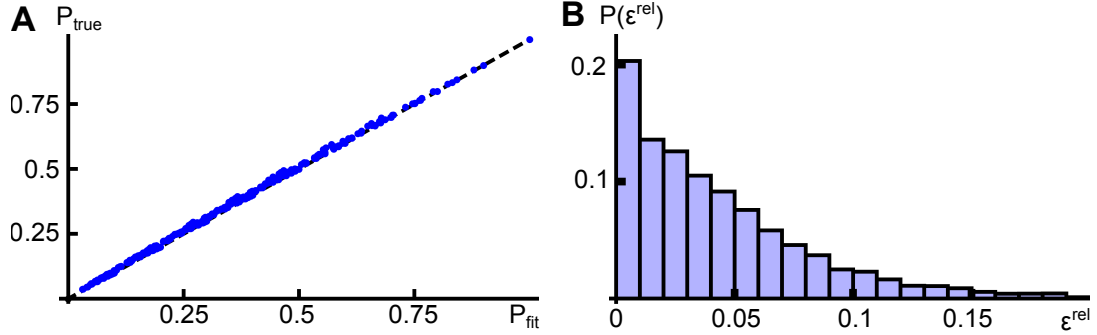


Figure 8.3: **Assessing the copula fit for the transient response distribution (A)** Blue points give a P-P plot of the fit copula (horizontal axis) against the true, empirical copula for a randomly-selected subset of three left-side VS neurons, at a random stimulus angle. We computed the copula probabilities at 1,000 points which divided the unit cube into 1,000 equal sized sub-cubes as described in the text. The black dashed line indicates the diagonal, with agreement between the true and fit models being indicated by the points lying on or near the diagonal. Optic flow presented to the system was generated by the rotation of random bar images, and the copula was fit to the transient response distribution. **(B)** Histogram of relative errors for copula probabilities. Vertical axis represents fractions of points which lie in the corresponding error range on the horizontal axis. We repeated the simulation of panel A, for a total of twenty random pairings of three left-side VS neurons and stimulus angles. We then computed the relative error (see Eq. (8.8)) between the true and fit copula probabilities at the 1,000 equally spaced points within the unit cube for all twenty copula fits, and plotted the errors as a histogram.

8.2.3 Computation of the MMSE

Given a general copula distribution function C as defined in Eq. (8.5), the copula density is defined by

$$c(u_1, \dots, u_N) = \frac{\partial}{\partial u_1} \cdots \frac{\partial}{\partial u_N} C(u_1, \dots, u_N).$$

Applying the chain rule for derivatives, the joint density f corresponding to the distribution F can then be written

$$f(x_1, \dots, x_N) = c(F_1(x_1), \dots, F_N(x_N)) \prod_{i=1}^N f_i(x_i), \quad (8.9)$$

where each f_i is the marginal density corresponding to the distribution F_i . As we will make use of the Gaussian copula, it will be useful to note that the density of the Gaussian

copula can be expressed in closed form as

$$c_{\Sigma}^{\text{Gauss}}(u_1, \dots, u_N) = \frac{1}{\det(\Sigma)} \exp \left[\mathbf{w}^T (\Sigma^{-1} - \mathbf{I}) \mathbf{w} \right], \quad \mathbf{w} = \left[\Phi^{-1}(u_1), \dots, \Phi^{-1}(u_N) \right]^T. \quad (8.10)$$

To approximate minimum mean-square estimation [143], we first simulated the response of the VS network in order to determine an empirical estimate of the marginal distribution functions F_i . Note that we did not assume a parametric form for the marginal distributions, but instead obtained a discrete estimate by binning values of the membrane potential integral at a sufficiently fine resolution. We then separately fit the Gaussian copula to the joint responses.

Both the marginal distributions and the copula were determined as a function of the stimulus rotation angle θ_{stim} at a resolution of 1° . Marginal distribution histograms were approximated from ten thousand samples at each rotation angle, and the copula from one thousand samples. The MMSE was then computed based on 1,600 samples taken at 5° increments.

The MMSE of the axis of rotation is calculated as the mean of the posterior distribution of rotation angles given the axonal membrane potentials. To be precise, given an observed response $\bar{\mathbf{V}}_{\text{Ax}}^{\text{tr}}(T)$, we associated each stimulus angle value θ_{stim} with a corresponding two-dimensional unit vector $\mathbf{s}(\theta_{\text{stim}}) = [\cos(\theta_{\text{stim}}), \sin(\theta_{\text{stim}})]^T$, and defined $\hat{\theta}_{\text{stim}}^{\text{MMSE}}$, the estimate of the MMSE, to be the argument of this vector, averaged over the posterior distribution, i.e.,

$$\hat{\theta}_{\text{stim}}^{\text{MMSE}} = \mathbf{E} \left[\theta_{\text{stim}} \mid \bar{\mathbf{V}}_{\text{Ax}}^{\text{tr}}(T) \right] = \arg \left[\int d\theta_{\text{stim}} \mathbf{s}(\theta_{\text{stim}}) P \left(\theta_{\text{stim}} \mid \bar{\mathbf{V}}_{\text{Ax}}^{\text{tr}}(T) \right) \right].$$

Values of the posterior density $P \left(\theta_{\text{stim}} \mid \bar{\mathbf{V}}_{\text{Ax}}^{\text{tr}}(T) \right)$ were determined using the fit copula and the measured marginal distributions, along with Eqs. (8.9, 8.10). The integral over the

posterior density was calculated via simple Riemann integration at a 1° discretization.

8.3 Steady-state encoding of the axis of rotation

We studied how the azimuth of the angle of body rotation is encoded in the response of the vertical system (VS) neuronal network using the model schematically depicted in Figure 8.1. We first provide a summary system description, and then examine how coupling amongst VS neurons affects their joint dynamics. We then explore the efficiency with which the axis of ego-rotation of the fly may be encoded in the VS population response during flight.

8.4 Dynamical effects of coupling on VS network responses

The effect of coupling on response properties of the VS network has recently received some attention [30, 56, 68, 97, 292]. We first review and expand upon some previous observations pertinent to the present investigation.

Figure 8.4A shows five typical responses of the left-side VS10 neuron to rotations of random bar images about $\theta_{\text{stim}} = 90^\circ$ in the absence (left) and presence (right) of the axo-axonal gap junction coupling. External variability in the optic flow stimulus provided to the system leads to large trial-to-trial fluctuations in responses, even in the absence of intrinsic fluctuations. The efficacy of coupling in reducing external variability is visible even at the resolution of a few trials. In Figure 8.4B, we show that correlations increase significantly when the VS neurons are coupled electrically. Correlations were measured

between steady-state average membrane potential responses for the left-side VS population (the steady-state average is taken to be the average membrane potential over the SS window in panel A).

Throughout Figure 8.4, we depict responses in the absence of intrinsic fluctuations (i.e., $\sigma_{Ax} = \sigma_{De} = 0$), highlighting the effect of coupling on external variability. Figures 8.4C and D show how steady-state tuning (i.e., mean responses) and variance are affected by coupling. First, we note the considerable reduction in external variability owing to coupling. Just as importantly, coupling allows the VS neurons to interpolate their responses [56, 68]. This results in an increase in orientation coverage [93], thereby allowing each cell to individually represent a greater range of stimulus angles in its response. This effect is also observed by comparing the receptive fields in Figure 8.1C with the “effective” tuning curves to strip stimulation shown in Figure 8.1E. Notably, this smoothing effect takes place without a significant decrease in tuning curve amplitude.

8.5 Steady-state encoding of the axis of rotation

The effects of coupling discussed in the previous section point to a potential trade-off: coupling could improve encoding by extending the range of tuning curves, and reducing response variability. On the other hand, increased correlations (redundancy) could potentially reduce total stimulus-related information content. Whether and to what extent this is the case depends heavily on the specifics of the system under consideration [11, 15, 65, 162, 203, 247].

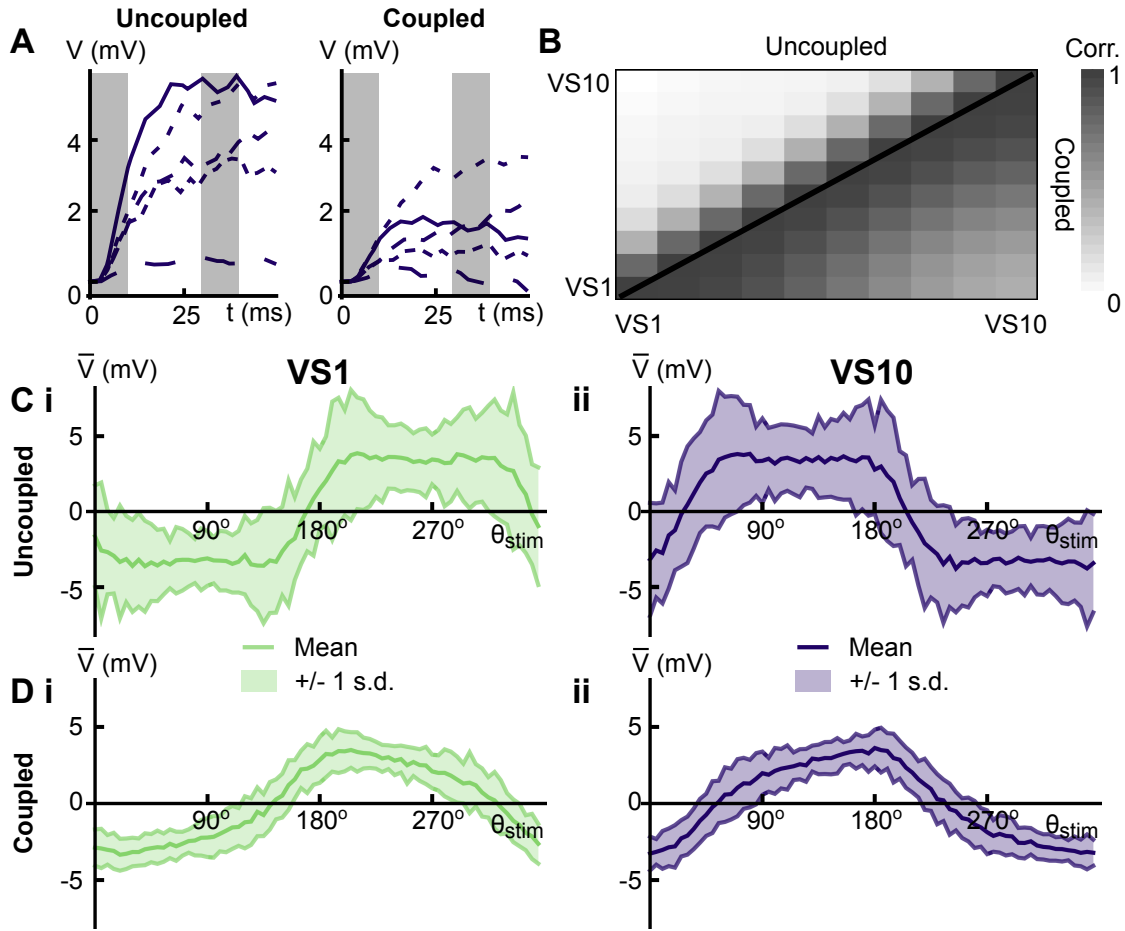


Figure 8.4: **The effect of coupling on VS neuronal dynamics.** (A) (Left) Typical axonal response of the left-side VS10 cell in the uncoupled network ($g_{\text{gap}} = 0 \mu\text{S}$) to rotations of bar images about $\theta_{\text{stim}} = 90^\circ$. Different line types indicate different, randomly generated images. (Right) Same as the left panel, but for the coupled system ($g_{\text{gap}} = 1 \mu\text{S}$). Images rotated to generate optic flow stimuli were the same ones used in the uncoupled system, with matching line types indicating matching image presentations. (B) Correlations for the integrated membrane potential in steady-state for the left-side VS neurons. Values above (resp. below) the diagonal are for the uncoupled (resp. coupled) system. Nearby cells were correlated at levels of approximately 0.7 and 0.97 for the uncoupled and coupled systems, respectively. (C) Steady-state tuning curve (mean response) and variability as a function of rotation angle for (i) VS1 and (ii) VS10 in the uncoupled system. Shaded areas indicate ± 1 s.d. of the response distribution. (D) Same as C, but for the coupled system. All responses and statistics for this figure were generated in the absence of intrinsic fluctuations ($\sigma_{\text{Ax}}, \sigma_{\text{De}} = 0$), and the optic flow stimuli were created by rotations of random bar images (see Section 8.1.2).

Previous studies have made primarily heuristic arguments about the effects of coupling on the encoding of the axis of rotation in steady-state responses (see, for example, [56,292]). We will provide a quantitative answer to this question by studying the error of an optimal linear estimator (see Section 8.2.1) which decodes the steady-state responses of the VS population.

8.5.1 MSE of the OLE is independent of coupling in steady-state

VS neurons do not directly participate in the generation of motor responses, but are electrically coupled to motor neurons [129,269] as well as to prominent descending neurons [100,269,296–298]. The response of these downstream neurons is determined by a temporal filtering of the graded response of the VS population rather than instantaneous values of their membrane potentials. We therefore define the response of the system of VS cells using time-averaged integrals of the graded responses of the VS population, $\bar{\mathbf{V}}_{\text{Ax}}^{\text{ss}}(T)$, as defined in Eq. (8.4). Here T indicates the time scale of integration and the “ss” superscript indicates that the system is in steady-state.

Variability of the axonal response is a consequence of both intrinsic fluctuations and variability in the optic flow stimulus, which reflects the randomness of visual inputs. To evaluate the accuracy with which the angle of rotation is encoded in the averaged response, we implemented an *optimal linear estimator* (OLE; see Section 8.2.1 and [238]). This linear estimator minimizes mean-square error (MSE) under the posterior distribution of the stimulus. The OLE applied in this section is computationally simpler to implement than the true (generally non-linear) mean-square error minimizing estimator. However, as noted at the end of the section, the general conclusions drawn using it apply more

generally. The true mean square minimizing estimator will be considered in the next section, when analyzing the efficiency of encoding of the axis of rotation within transient responses.

The MSE of the OLE as a function of θ_{stim} is shown in Figure 8.5, for three types of images and two integration timescales. The effects of coupling discussed in Section 8.4 suggest that coupling can affect the performance of the OLE. Surprisingly, we found that across image types and integration timescales, the MSE of the OLE in steady-state was independent of the strength of axo-axonal coupling. In panels A and B, we show results for random bar images with integration windows of $T = 10$ ms and $T = 20$ ms, respectively. Panels C and D of Figure 8.5 show the MSE for random checkerboard images and natural scenes, respectively. The statistics of the optic flow generated by images from a given class set the baseline level for the MSE. However, the error was found to be independent of coupling strength for all classes of images tested. We also verified this for different parameters of the random bar images (results not shown — see Section 8.1.2 for details of image generation).

Since the axonal and dendritic compartments were coupled electrically, the dendritic response was affected by the strength of the axo-axonal coupling. However, the impact of coupling on the vector $\mathbf{V}_{\text{De}}(t)$ of dendritic responses was found to be limited to a multiplication of the response by a diagonal matrix (result not shown). Up to this scaling, the time course of the dendritic response is dominated by the synaptic input arriving through the visual pathway which reflects response to the filtered optic flow stimulus. Therefore, to a good approximation, the system can be viewed as hierarchical [68]: The motion detector-filtered optic flow stimulus drives the dendrites, and the dendrites drive the axonal compartments, with the activity at each step determined completely by the response

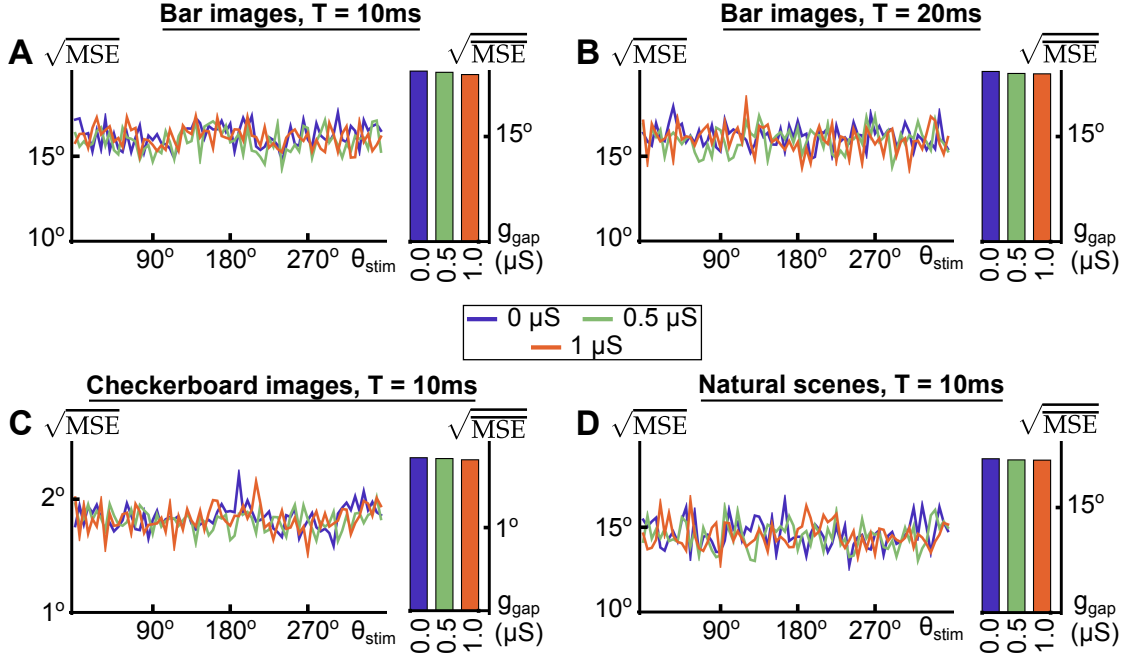


Figure 8.5: **Mean-square error of the OLE for steady-state responses (A)** (Left) Lines indicate the square root of the mean-square error of the OLE for steady-state responses to filtered optic flow stimuli generated by the rotation of random bar images with a $T = 10$ ms window of integration. Line colors correspond to different coupling strengths as indicated by the legend. (Right) Bars represent the square root of the stimulus averaged mean-square error for the data plotted to the left, with bar colors corresponding to line colors. **(B)** Same as A, but for a window of integration of $T = 20$ ms. **(C)** Same as A, but for random checkerboard images. Note the different scaling of the vertical axis. **(D)** Same as A, but for natural scenes. Details regarding image generation and the technique for generating the optic flow presented to the model can be found in Section 8.1.2.

at the preceding stage (along with any intrinsic noise sources). In particular, disregarding intrinsic noise in the system, we have

$$\begin{aligned}
 \bar{\mathbf{V}}_{\text{Ax}}^{\text{ss}}(T) &= \frac{1}{T} \int_0^T ds \mathbf{V}_{\text{Ax}}(s) \\
 &= \frac{1}{T} \int_0^T ds \int_0^\infty du H(u) \mathbf{V}_{\text{De}}(s-u) \\
 &\equiv_D \left[ds \int_0^\infty H(s) \right] \left[\frac{1}{T} \int_0^T ds \mathbf{V}_{\text{De}}(s) ds \right] \\
 &= \mathcal{H} \bar{\mathbf{V}}_{\text{De}}^{\text{ss}}(T), \quad \text{where } \mathcal{H} = \int_0^\infty ds H(s).
 \end{aligned} \tag{8.11}$$

Here, \equiv_D indicates equality in distribution, and $H(s) = C_m^{-1} g_{Ax-Den} \exp[-C_m^{-1} G_{Ax} s] \Theta(s)$ is the exponential filter the axonal system applies to the dendritic response. We note that at positive times, when the Heaviside function $\Theta(s) = 1$, $H(s)$ is a matrix exponential. That the axonal response can be represented by a convolution of a matrix exponential with the dendritic response (second equality) is a general mathematical property of linear systems of differential equations such as those which describe the evolution of \mathbf{V}_{Ax} (see Eq. (8.1)).

The equality in distribution in Eq. (8.11) arises from switching the order of integration and using the time-shift invariance of the dendritic membrane potential distribution under the steady-state assumption. In this case the distributions of $\mathbf{V}_{De}(s - u)$ and $\mathbf{V}_{De}(s)$ agree for all finite u , and the two quantities can be exchanged under an equality in distribution. The dendritic average $\overline{\mathbf{V}}_{De}^{ss}(T)$ is defined analogously to the axonal quantity in Eq. (8.4).

Under the hierarchical assumption, the axonal activity is conditionally independent of the input given the dendritic activity: If the linear transfer exhibited in Eq. (8.11) is invertible, the posterior distribution of the stimulus given the axonal response agrees exactly with the distribution conditioned on the dendritic response. Since $\overline{\mathbf{V}}_{Ax}^{ss}(T) \equiv_D \mathcal{H} \overline{\mathbf{V}}_{De}^{ss}(T)$ for some invertible matrix \mathcal{H} , it follows that

$$P(\theta_{stim} | \overline{\mathbf{V}}_{Ax}^{ss}(T)) = P(\theta_{stim} | \overline{\mathbf{V}}_{De}^{ss}(T)). \quad (8.12)$$

In this situation, there is no change in information due to coupling. This equality holds as long as \mathcal{H} is invertible. Realistic gap junction coupling strengths change the entries in the matrix \mathcal{H} , but do not impact its invertibility. In addition, we found that the dendritic responses were independent of coupling up to an invertible linear scaling factor, implying that the posterior distribution $P(\theta_{stim} | \overline{\mathbf{V}}_{De}^{ss}(T))$ is likewise independent of coupling.

Thus, not only will the performance of the OLE be unaffected by coupling in this case, but the same conclusion holds for more general probabilistic estimators (including the MMSE considered in what follows, all Bayesian estimators and the maximum likelihood estimator).

8.6 Transient encoding of the axis of rotation

During cruising flight in a stationary environment, flies often move along straight-line segments separated by saccadic periods of rapid rotation. These straight-flight segments can occur at rates of up to ten per second and can be as short as 30 ms in duration [25, 240, 282]. Since motor projections of the VS network must pass through intermediate descending neurons [100, 268, 296–298], the representation of ego-rotations for compensatory optomotor responses must take place at an even shorter time scale. Similarly short time scales are likely critical during other natural flying behaviors, such as pursuit and tracking [52, 158]. For realistic rotational velocities, the transient period of the VS cells membrane potential from rest can last upwards of 30 ms (see the time scale of response in Fig. 8.4A), calling into question the behavioral relevance of steady-state responses for a fly in motion. We therefore considered instead time-averaged integrals of the transient response beginning from rest, $\bar{\mathbf{V}}_{Ax}^{\text{tr}}(T)$ (see Eq. (8.3)). Here, T denotes the length of integration window and the “tr” superscript indicates the transient state of the system.

The OLE applied in Section 8.5.1 is only the optimal mean-square Bayesian estimator under the assumption of Gaussianity of the integrated membrane potentials. This assumption does not hold in general, and we therefore implemented the true minimum

mean-square estimator (MMSE) given by

$$\hat{\theta}_{\text{stim}}^{\text{MMSE}} = \mathbf{E} \left[\theta_{\text{stim}} \mid \bar{\mathbf{V}}_{\text{Ax}}^{\text{tr}}(T) \right], \quad (8.13)$$

with the average taken over the posterior distribution of the stimulus, $P(\theta_{\text{stim}} \mid \bar{\mathbf{V}}_{\text{Ax}}^{\text{tr}}(T))$.

Our model VS network is highly complex, and it is not obvious how to parametrize the likelihood $P(\bar{\mathbf{V}}_{\text{Ax}}^{\text{tr}}(T) \mid \theta_{\text{stim}})$. As a result, Eq. (8.13) cannot be evaluated via Markov Chain Monte Carlo (MCMC) methods, or other techniques designed for efficient sampling from probability distributions [228]. We therefore generated samples from the posterior distribution by simulating the model directly. We then compute the integral in Eq. (8.13) after using copulas to approximate the multivariate distribution of the responses (see Sections 8.2.2 and 8.2.3).

8.6.1 MMSE is independent of coupling in the transient state

The MMSE for the angle of rotation estimated from the integrated axonal potentials is shown in Figure 8.6. Surprisingly, the behavior of the MMSE in the transient state was qualitatively identical to that of the OLE in the steady-state (see Figure 8.5). Although the error depended on image statistics, it was again approximately independent of coupling.

The explanation for this behavior turned out to be largely identical to that provided in the steady-state case (see Eq. (8.11)), with one crucial difference: The equality in distribution on the third line of Eq. (8.11) does not hold exactly for transient responses. *A priori* it is not obvious that the equality should hold even approximately. The characteristic response timescales of the VS axonal compartments (and of the system filter H) are given as the product of the membrane capacitances with the inverses of the eigenvalues of G_{Ax} . If these eigenvalues are large enough (i.e., if the VS axonal effective time constants are

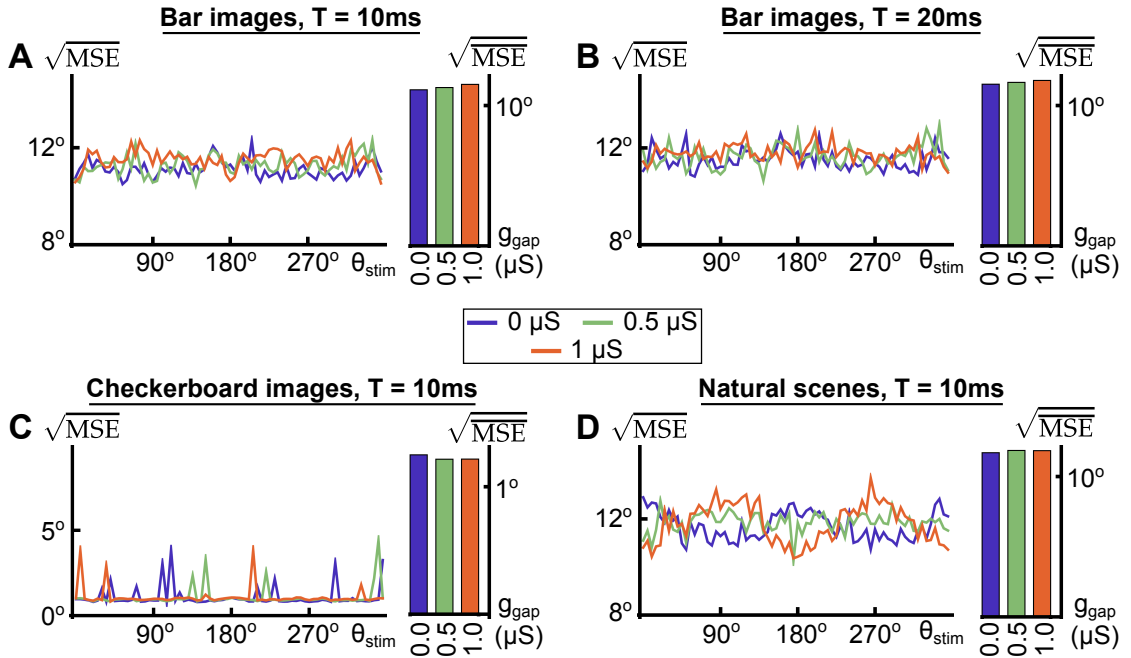


Figure 8.6: **Mean-square error of the MMSE for transient responses (A)** (Left) Lines indicate the square root of the mean-square error of the MMSE for transient responses to filtered optic flow stimuli generated by the rotation of random bar images with a $T = 10$ ms window of integration. Line colors correspond to different coupling strengths as indicated by the legend. (Right) Bars represent the square root of the stimulus averaged mean-square error from the data plotted to the left, with bar colors corresponding to line colors. **(B)** Same as A, but for a window of integration of $T = 20$ ms. **(C)** Same as A, but for random checkerboard images. Note the different scaling of the vertical axis. **(D)** Same as A, but for natural scenes.

fast relative to the window of integration), this equality does hold approximately, owing to a separation of these timescales. In this case, there again exists an invertible linear relationship between the transient axonal average $\bar{V}_{Ax}^{tr}(T)$ and the corresponding dendritic average $\bar{V}_{De}^{tr}(T)$. We emphasize the importance of the separation of timescales effect in this independence of error from coupling for the transient response. It is achieved as a result of the contrast between the extremely fast axonal time constants and the slow evolution of the dendritic response to the filtered optic flow stimulus.

According to [30], the VS axonal compartments have baseline time constants on the order of a millisecond. The effective time constants will thus be even smaller, owing to the axo-dendritic and axo-axonal gap junction synapses [237]. These short integration time constants allow the system to reliably implement the linear transfer relating the dendritic and axonal averages for transient responses, as in Eq. (8.11). To verify this, we carried out linear regression analysis of the dependence between the axonal and dendritic responses. We found R^2 values for individual coordinates in excess of 0.999 for all coupling values ($g_{\text{gap}} = 0, 0.5, 1 \mu\text{S}$) and integration time windows tested ($T = 10, 20 \text{ ms}$) when the intensity of intrinsic noise was set to zero (results not shown). This indicates that transfer is nearly linear in each axonal dimension. The linear regression was performed for random values of θ_{stim} , indicating the independence of this transfer matrix from the stimulus value.

In short, the axonal network uses a very fast system filter to institute a highly reliable linear transfer of the averaged transient dendritic response to the average transient axonal response. As in the steady-state case, the entries of the transfer matrix depend on coupling, but its existence and invertibility do not. Hence, the posterior distribution of the stimulus conditioned on the axonal response is nearly identical to that conditioned on the dendritic response (see Eq. (8.12)), and the latter is approximately independent of coupling [68]. As a result, the estimates (and error) of any probabilistic estimators will not depend significantly on the strength of the axo-axonal gap junction coupling within the VS system.

8.7 The role of coupling

At this point, it is unclear whether coupling between VS neurons has any impact on the quality of encoding of the axis of rotation. While previous studies argued that it could be beneficial [56, 68, 97, 292], our attempts to quantify its impact on optimal encoding efficiency had thus far shown no effect.

A possible answer is found in considering the downstream projections of the vertical system. A pair of prominent premotor descending neurons has been identified within each brain hemisphere. These descending neurons of the ocellar and vertical system (DNOVS) form gap junctions with subsets of the VS cells, and directly innervate motor neurons in the thoracic ganglion of the fly [100, 296–298]. DNOVS1 and DNOVS2 couple electrically to ipsilateral VS neurons, with the strongest coupling to the VS6-7 and VS5-6 neurons, respectively.

Based on this anatomical observation, we thus considered the MMSE based on a partial readout of the VS5-7 neurons from each hemisphere. The results are presented for different images and integration timescales in Figure 8.7, which parallels Figures 8.5 and 8.6 in format. We found that coupling is of great benefit to the accuracy of the MMSE of θ_{stim} given access only to the response of a subpopulation of the VS neurons. Depending on image statistics and the timescale of integration, even moderate levels of coupling resulted in two to three-fold improvements in the square root of the stimulus averaged MSE (bar charts in Figure 8.7).

In order to explain these findings, we return to our discussion of the effects of coupling on the axonal response distribution shown in Figure 8.4 for steady-state responses. The effects on transient responses are qualitatively similar. Increasing coupling causes three

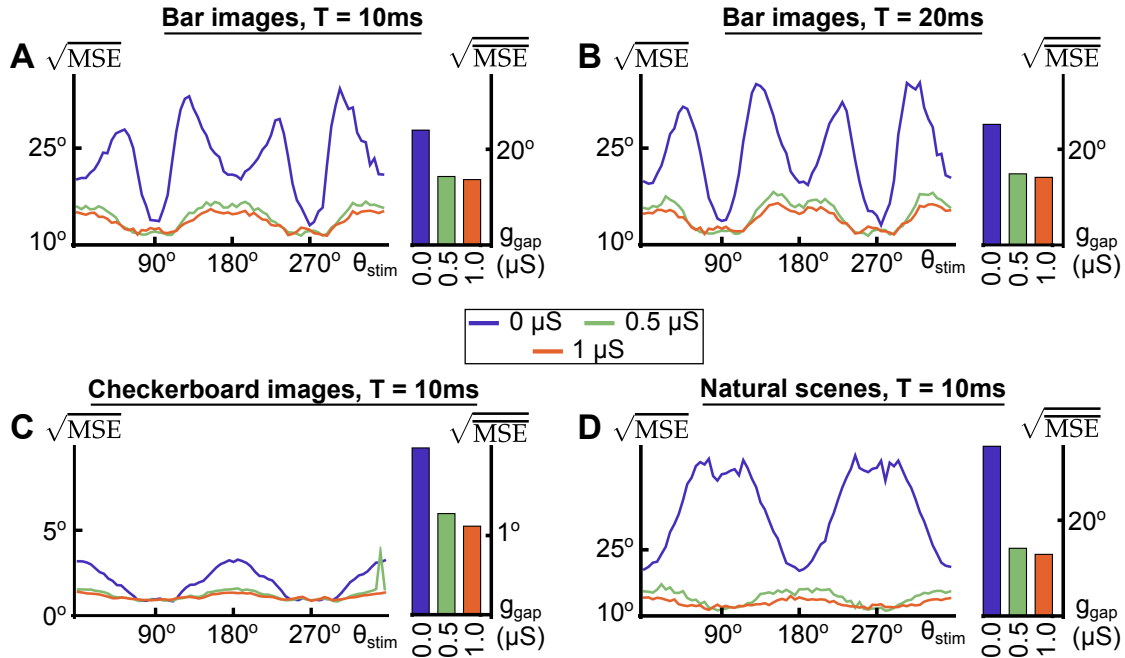


Figure 8.7: **Mean-square error of the MMSE for a partial readout of transient responses** (A) (Left) Lines indicate the square root of the mean-square error of the MMSE for transient responses to filtered optic flow stimuli generated by the rotation of random bar images with a $T = 10\text{ms}$ window of integration. Line colors correspond to different coupling strengths as indicated by the legend. The partial readout was formed from the responses of the VS 5–7 cells on each side. (Right) Bars represent the square root of the stimulus averaged mean-square error from the data plotted to the left, with bar colors corresponding to line colors. (B) Same as A, but for a window of integration of $T = 20\text{ms}$. (C) Same as A, but for random checkerboard images. Note the different scaling of the vertical axis. (D) Same as A, but for natural scenes.

important qualitative changes in the response distribution: First, variability was reduced without diminishing the amplitude of tuning curves, which assists encoding of the axis of rotation (see Figure 8.4C, D).

Next, tuning curves (mean responses) were widened so that each cell individually responds to a wider range of angles. This may only marginally benefit a full readout. On the other hand, for a partial readout, responses can appear marginally identical for stimulus values lying in the flat regions of the tuning curves (e.g., between 45° and 135°

in Figure 8.4Ci). Without coupling, the readout would have to rely entirely on higher order statistics to distinguish these angles. Coupling, on the other hand, smoothed out these non-informative portions of the tuning curves. This increase in orientation coverage allowed nearby stimuli to be distinguished even at the level of individual responses.

Lastly, coupling increases correlations (see Figure 8.4B), potentially reducing the information the population carries about the stimulus [11, 15, 203, 259]. However, this increase in redundancy was favorable to a subpopulation readout, as the marginal distribution of the retained neurons encodes information about the responses of neurons which are hidden to the readout. In other words, although the total stimulus-related information contained in population responses can be reduced, the information carried by an arbitrary subpopulation could simultaneously be increased significantly.

In short, coupling modified the dynamical characteristics of VS population responses in such a way that a near-precise trade-off takes place for a full readout (in which case error is largely independent of coupling). However, as will be elaborated further in Section 8.8 and Figure 8.11 below, for a readout from a subset of the VS cells, these same effects work in harmony to augment encoding efficiency, resulting in the large decrease in MSE with coupling shown in Figure 8.7.

8.7.1 Coupling improves partial decoding in simplified model

We verified the robustness of our findings by qualitatively reproducing them using a simplified and dimensionless Ornstein-Uhlenbeck model (or OU model). The features of the model were set so that only essential characteristics were shared with the full model defined above in Eq. (8.1). In particular, each cell was given a sinusoidal tuning curve (i.e., the mean response depended sinusoidally on the stimulus angle θ_{stim}) to emulate the

characteristic retinotopic responses of the VS network.

We replaced the processed optic flow stimulus input to VS model neurons with simple white noise. To imitate the slow timescale of the dendritic response as received at the axonal terminals, the dendritic compartments were given a significantly slower time constant than the axonal compartment. Lastly, the white noise inputs to the dendritic compartments were assigned a spatially decaying correlation structure to emulate the effects of receptive field overlap. In this setting, we qualitatively replicated our findings for full and partial readouts (Figure 8.8). The model was not precisely tuned, and the result held over a sizable range for all parameters (results not shown).

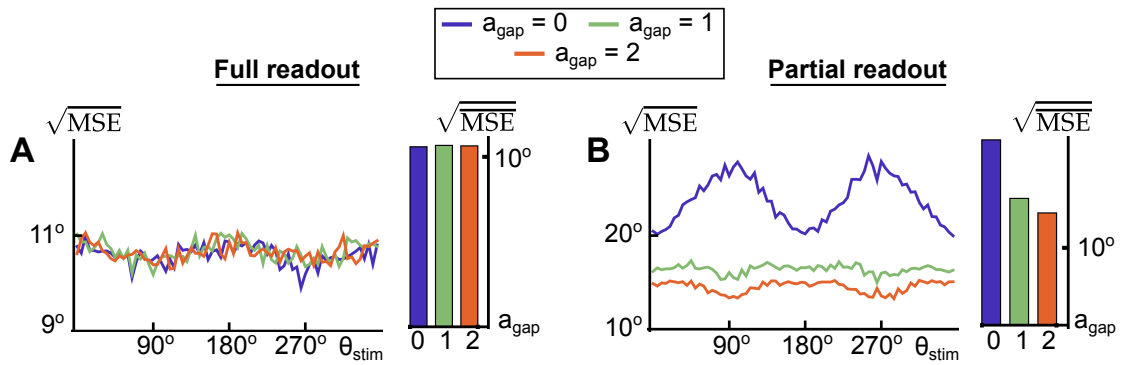


Figure 8.8: **Mean-square error of the MMSE for full and partial readout from an approximating Ornstein-Uhlenbeck system (A)** (Left) Lines indicate the square root of the mean-square error of the OLE for transient responses to filtered optic flow stimuli generated by the rotation of random bar images. Line colors correspond to different coupling strengths between “axon” compartments, as indicated by the legend. (Right) Bars represent the square root of the stimulus averaged mean-square error from the data plotted to the left, with bar colors corresponding to line colors. **(B)** Same as A, but for a partial readout formed from the responses of the cells index 5, 6 and 7 on each side, imitating the partial readout considered in the full system (see Figure 8.7).

We now provide a precise definition of the model. In form, the corresponding Langevin equations for the evolution of the coupled OU processes \mathbf{X}_{Ax} , \mathbf{X}_{De} are similar to those of

the full model (Eq. (8.1)):

$$\begin{aligned}\tau_{\text{Ax,OU}} \frac{d\mathbf{X}_{\text{Ax}}}{dt} &= -A_{\text{Ax}}\mathbf{X}_{\text{Ax}}(t) + a_{\text{Ax-Den}}\mathbf{X}_{\text{De}}(t) + \sqrt{\sigma_{\text{Ax,OU}}^2 \tau_{\text{Ax,OU}}} \boldsymbol{\xi}_{\text{Ax}}(t), \\ \tau_{\text{De,OU}} \frac{d\mathbf{X}_{\text{De}}}{dt} &= -(1 + a_{\text{Ax-Den}})\mathbf{X}_{\text{De}}(t) + a_{\text{Ax-Den}}\mathbf{X}_{\text{Ax}}(t) + \boldsymbol{\mu}(\theta) + \sqrt{\sigma_{\text{De,OU}}^2 \tau_{\text{De,OU}} B_{\text{De}}} \boldsymbol{\xi}_{\text{De}}(t).\end{aligned}$$

Compared with the matrix G_{Ax} defined for the full model in Eq. (8.2), the matrix A_{Ax} has entries given by

$$A_{\text{Ax},ij} = \begin{cases} 1 + a_{\text{Ax-Den}} + a_{\text{gap}} & i = j = 1 \text{ or } 10, \\ 1 + a_{\text{Ax-Den}} + 2a_{\text{gap}} & 2 \leq i = j \leq 9, \\ -a_{\text{gap}} & i = j + 1 \text{ or } i = j - 1. \end{cases}$$

Thus, $\mathbf{X}_{\text{Ax}}, \mathbf{X}_{\text{De}}$ are ten-dimensional processes, and there exists a copy of the system for each hemisphere. The two copies are uncoupled, and differ parametrically only in their receptive field centers, as in the full model. The parameters are labeled in such a way as to facilitate comparisons with their counterparts in the full model. For example, the parameter a_{gap} captures the coupling between neighboring compartments, and the parameter $a_{\text{Ax-Den}}$ the axo-dendritic coupling.

The tuning curves describe the steady-state response in the absence of fluctuations. To coarsely approximate the steady-state responses of the full system, we defined the tuning curves as sinusoids with $\mu_i(\theta) = \sin(\theta - \varphi_i)$, where φ_i indicates the receptive field center of the i^{th} cell. Note that as a result, each cell's response will be extremal at stimulation angles separated by 90° from the cell's receptive field center, as is approximately the case in the detailed VS model — see Figure 8.1E. Responses were taken to be time integrals as for the detailed model.

8.7.2 Comparison of the MMSE with a zero-crossing estimator

Both Cuntz *et al.* [56] and Elyada *et al.* [68] argued heuristically that coupling could increase the accuracy of an estimator which would, given the VS axonal responses, propose the axis of rotation to be defined as a “zero crossing” of the population response. We implemented such an estimator, and assessed the effects of coupling on its accuracy.

We first explicitly define this estimator, a step which was bypassed by the heuristic descriptions of [56, 68]. Our approach will be to define for each cell a *zero angle*, which is intuitively the most likely rotation angle given that the axonal response of the cell is near zero in absolute value. Then, given the population response to a rotation about the stimulus angle θ_{stim} , the estimator searches for consecutive pairs of VS neurons which exhibit a sign change in their responses. Once such a pair is found, the estimator will propose the axis of rotation to be given by an angle in between the zero angles of the two VS neurons. The precise estimate is given by assuming that the responses of the two VS neurons to rotations about θ_{stim} vary linearly with their zero angle, and then solving by linear interpolation for the zero angle of a *hypothetical* VS neuron which would exhibit a zero absolute response to the rotation about θ_{stim} .

More precisely, we define the *zero angle* of the i^{th} cell on each side, $\theta_{X,i}^0$, to be

$$\theta_{X,i}^0 = \underset{\theta_{\text{stim}} \in Q}{\operatorname{argmax}} P(\theta_{\text{stim}} | \bar{V}_{Ax,X,i} \approx 0), \quad X \in \{L, R\}, 1 \leq i \leq 10,$$

where

$$Q = \left\{ \theta_{\text{stim}} \mid \left| \frac{\partial P(\theta_{\text{stim}} | \bar{V}_{Ax,X,i} \approx 0)}{\partial \theta_{\text{stim}}} \right| > 0 \right\}.$$

When defining the zero angle of a VS neuron, we would like this angle to correspond approximately to the center of the receptive field of the neuron. The posterior distribution

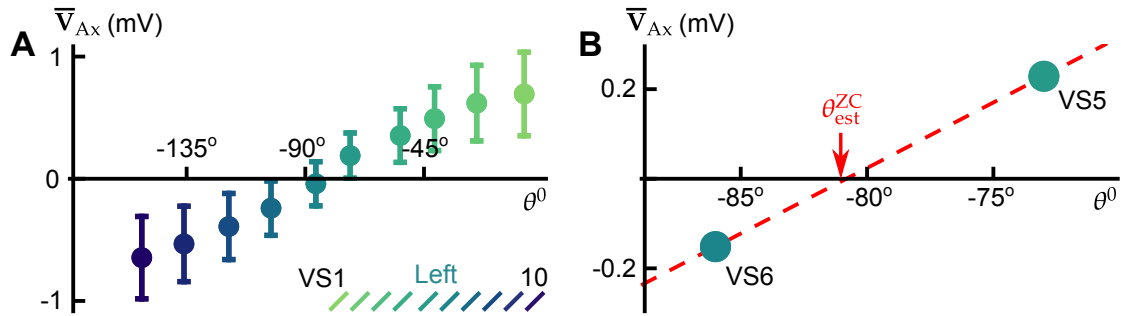


Figure 8.9: **Visualizing the zero-crossing estimator.** (A) Circles indicate the mean axonal response of the left-side VS neurons to a rotation of a random bar image about $\theta_{stim} = -85^\circ$. Error bars indicate 1 standard deviation of the response distribution. The horizontal coordinate of each dot indicates that cell's zero angle θ^0 . (B) On an example realization for the response to rotation about $\theta_{stim} = -85^\circ$, the zero crossing occurred between the VS5 and VS6 cells. These cells had had zero angles of $\theta_{L,5}^0 = -73^\circ$ and $\theta_{L,6}^0 = -87^\circ$, respectively. The zero crossing estimator predicts the angle of rotation to be the zero angle of a hypothetical cell which would exhibit zero response, under the assumption that the response varies linearly with zero angle (red dashed line).

of the stimulus conditioned on a small absolute response for a given VS cell will generally have two relative maxima, roughly corresponding to rotations near the center of the receptive field to the neuron and rotations 180° from the center of the receptive field. In these stimulus ranges, the optic flow crossing the retinotopic receptive field of the cell in question will have low velocity, leading to weak absolute responses. Near the receptive field center of the neuron, the posterior gradient will be positive, owing to the polarity of the synapses through which upward and downward motion separately arrive at the dendrites of a VS neuron (in particular, upward motion inhibits the cell, and downward motion excites, as stated in the model definition of Section 8.1.1), as well as the fact that all rotations we consider would correspond to counter-clockwise rolls of the fly about a given axis. Restriction to the set Q where the derivative of the posterior with respect to the stimulus angle θ_{stim} is positive is designed to resolve this ambiguity in the definition of the

zero angle. We plot the mean and standard deviation of the marginal response distribution for each left-side VS neuron to a rotation of a random bar image about $\theta_{\text{stim}} = -85^\circ$ in Figure 8.9A. The horizontal coordinate of each point indicates the zero angle of each cell.

The estimator first searches for a pair of consecutive VS neurons which exhibit responses $\bar{V}_1 < 0, \bar{V}_2 > 0$, having zero angles θ_1^0, θ_2^0 , where we assume the two cells are labeled such that

$$\theta_2^0 - \theta_1^0 \pmod{360^\circ} \in [0^\circ, 180^\circ).$$

A sufficient condition for such a pair to exist is existence of at least one pair of VS neurons exhibiting positive and negative responses, respectively. Once such a pair is located, the zero-crossing estimate $\theta_{\text{est}}^{\text{ZC}}$ is proposed as the angle associated with the zero potential level for the line connecting (θ_1^0, \bar{V}_1) and (θ_2^0, \bar{V}_2) — i.e., we set

$$\theta_{\text{est}}^{\text{ZC}} = \theta_1^0 + \frac{\theta_2^0 - \theta_1^0}{\bar{V}_2 - \bar{V}_1} (0 - \bar{V}_1).$$

We provide a visualization of this estimation scheme in Figure 8.9B.

It is possible, in the case of a subpopulation readout in the presence of large noise, for example, that all of the considered neurons can exhibit either positive or negative responses. In this case, the estimate is set to be a random angle in $[0^\circ, 360^\circ)$. It may also be that multiple such pairs are found. In this case, the estimate is randomly selected from the values of $\theta_{\text{est}}^{\text{ZC}}$ associated with each pair.

In Figure 8.10, we plot the performance of the zero-crossing estimator. As was predicted by [56, 68], the estimator does benefit from the axo-axonal coupling for a full readout (panel A). However, in the case of a partial readout (panel B), the changes in prediction error with coupling are not significant and the error increases significantly. In all cases,

as one should expect, the estimator is suboptimal when compared to the MMSE, notably so for the case of a subpopulation readout (compare with Figure 8.6A and Figure 8.7A). In general, it is possible to propose various suboptimal estimators which are affected by coupling in different ways — our findings are derived from the application of general Bayesian estimators, and in particular, the optimal mean-square estimator.

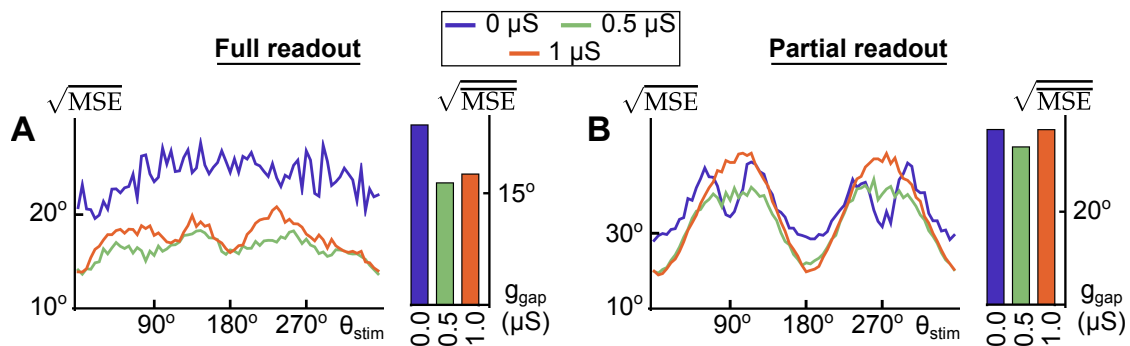


Figure 8.10: **Mean-square error of the MMSE for a full and partial readout, for the zero-crossing estimator.** (A) (Left) Lines indicate the square root of mean-square error of the zero-crossing estimator for transient responses to filtered optic flow generated by the rotation of random bar images with a $T = 10\text{ms}$ window of integration. The readout provided to the estimator consisted of the full VS population response. Line colors correspond to different coupling strengths as indicated by the legend. (Right) Bars represent the square root of the stimulus averaged mean-square error from the data plotted to the left, with bar colors corresponding to line colors. (B) Same as A, but for a partial readout formed from the responses of the VS5–7 cells on each side.

8.8 Factors determining partial decoding improvement

A natural question at this point is whether the efficient encoding of the axis of rotation by a subpopulation can be achieved simply through changes in the marginal responses of the VS cells. Could changes to tuning curves and reduction in variability (see Figure 8.4) completely account for the observed improvements in encoding accuracy? Or is it important that the electrical coupling between VS cells also affects the correlations in their

response? In order to assess the importance of correlations in encoding, it is common to shuffle observations across trials [160, 192, 242].

8.8.1 Trial-to-trial variations vs. tuning curve smoothing

In Figure 8.11, we plot the MSE of the MMSE as a function of the axis of rotation for two coupling strengths, for trial-shuffled data. The bar chart to the right in Figure 8.11 presents the estimation error for the uncoupled and coupled systems, with and without trial-shuffling. Approximately half of the improvement in MSE for the subpopulation readout (dashed bars, Figure 8.11 right) was accounted for by the changes to tuning and variability (gray bar). This demonstrates that the marginal dynamical changes and the shaping of the correlation structure were of nearly equal importance to the efficient subpopulation representation in this example.

8.8.2 Axonal filtering

The encoding of the axis of rotation in the VS response takes on a hierarchical structure, as discussed above and depicted in Figure 1.4C. In particular, the axonal system receives input from the dendritic system, which itself possesses a retinotopic receptive field structure, and thus also encodes the axis of rotation in its response. If only a subset of the VS responses are made known to an estimator, why have ten cells instead of, say, a more economical single cell with the same extended dendritic structure?

To answer this question, we simulated the system with only a single cell (axon) in each hemisphere which received input from all ten dendrites, and left the dendritic structure unchanged. In this case, the axonal response within each hemisphere is now univariate

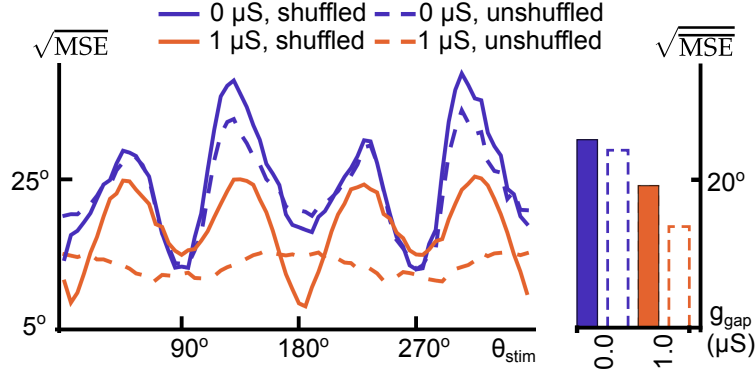


Figure 8.11: **Correlations encode stimulus information in a partial readout** (Left) Solid lines indicate the square root of the mean-square error of the MMSE for trial-shuffled transient responses to filtered optic flow stimuli generated by the rotation of random bar images with a $T = 10$ ms window of integration. Line colors correspond to different coupling strengths as indicated by the legend. Dashed lines indicate the error of the partial readout without shuffling for the same strengths of coupling (same data as Figure 8.7A). The partial readout was formed from the responses of the VS 5–7 cells on each side. (Right) Solid border bars represent the square root of the stimulus averaged mean-square error for the cross-trial shuffled data plotted to the left, with bar colors corresponding to line colors. Dashed border bars indicate the same, but for the non-shuffled data (as in Figure 8.7).

and evolves according to (compare with Eq. (8.1))

$$C_m \frac{dV_{Ax}}{dt} = -(g_{L,Ax} + 10g_{Ax-Den})V_{Ax}(t) + 10g_{Ax-Den} \left[\frac{1}{10} \sum_{i=1}^{10} V_{De,i}(t) \right] + \sqrt{\sigma_{Ax}^2 \tau_{Ax}} \xi_{Ax}(t). \quad (8.14)$$

As Eq. (8.14) reveals, this is essentially equivalent to assuming the single axonal compartment couples to a single dendritic compartment evolving as the average of the ten dendritic compartments in the full model. Naively, one should expect this to be much worse, and we verify this in Figure 8.12, where we compare the error of the MMSE for the single axon system to that of the full, coupled system with a partial readout consisting of the VS5–7 cells (as in Figure 8.7). The average error in the full system is decreased by over a factor of four (compare the solid orange and dashed blue lines, Figure 8.7, right), while the local error is reduced by up to a factor of eight (Figure 8.7, left).

To eliminate the possibility that the improvement is entirely due to the two additional dimensions available when reading out the VS5–7 responses, we also compared the performance of the MMSE for the single axon system to that for the full, coupled system, allowing for a readout of only the VS5 cell. This coupled system is again notably superior to the single axon system (compare Figure 8.7, dashed orange and blue lines). In short, the axonal post-processing of the dendritic input due to coupling is notably distinct from the detrimental pre-processing which takes place for the single axon system, in which a potentially large loss of stimulus-related information results from the averaging of dendritic responses. These results hold for passive dendrites — it is an open question as to whether the single axon system could be rescued by more complex (i.e., nonlinear) dendritic processing.

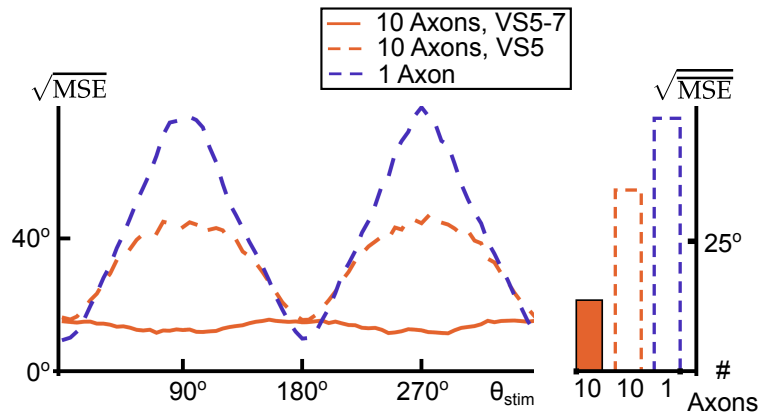


Figure 8.12: **A single cell with large dendritic extent cannot accurately encode the axis of rotation** (Left) Solid orange line indicates the square root of the mean-square error of the MMSE for transient responses to filtered optic flow stimuli generated by the rotation of random bar images with a $T = 10$ ms window of integration, for the full system with a partial readout consisting of the VS5–7 cells in each hemisphere (same data as Figure 8.7A). The dashed orange line is the same as the solid line, except the readout consisted of only the VS5 cell. The dashed blue line indicates the MSE for a system consisting of a single axonal compartment in each hemisphere which couples to all ten of the corresponding dendritic compartments, as described in the text. (Right) Bars represent the square root of the stimulus averaged mean-square error for the systems and readouts of the corresponding lines to the left.

8.8.3 Partial readout subset size and VS cell identity

Finally, we asked to what extent our results depend on the particular subset of the VS population which the MMSE has access to. We randomly selected twenty distinct readouts of sizes up to five (except for readouts of size one, of which there are only ten possible choices). In addition, for readouts of size three, we ensured that the set VS5–7, the readout considered in Figure 8.7, was one of the tested readouts. For each of the chosen readouts, we computed the MSE averaged across values of θ_{stim} .

The results are presented in Figure 8.13. The MSE for the coupled network (panel B) decreases rapidly, essentially leveling off for readouts of two cells or more. Strikingly, for these same readout sizes, there is very little dependence on the particular subset chosen, as indicated by the closeness of the minima and maxima to the average. On the other hand, the average MSE across readouts does not decrease as rapidly for the uncoupled network. Moreover, the MSE for the uncoupled network depends strongly on the identity of the particular subset — though the mean for the uncoupled network is close to that of the coupled network by readouts of size three, the error for the “worst” readout remains greatly elevated by comparison. Coupling is uniformly beneficial to the fidelity of encoding of the axis of rotation in the axonal response. Strikingly, however, the error for the readout of the VS5–7 cells was highest amongst all tested readouts for both the coupled and uncoupled system. Thus, if biological constraints dictate a situation where the rotation angle must be estimated from the response of only these particular neurons, coupling of the VS axonal responses becomes of great importance, as we have illustrated (Figure 8.7). This phenomenon is closely linked to the changes in ‘orientation coverage’ with population size recently reported in pools of orientation selective cortical neurons used to discriminate sinusoidal gratings drifting in different directions [93]. Analogous

coverage changes are a central effect of coupling in the VS network (Figure 8.4).

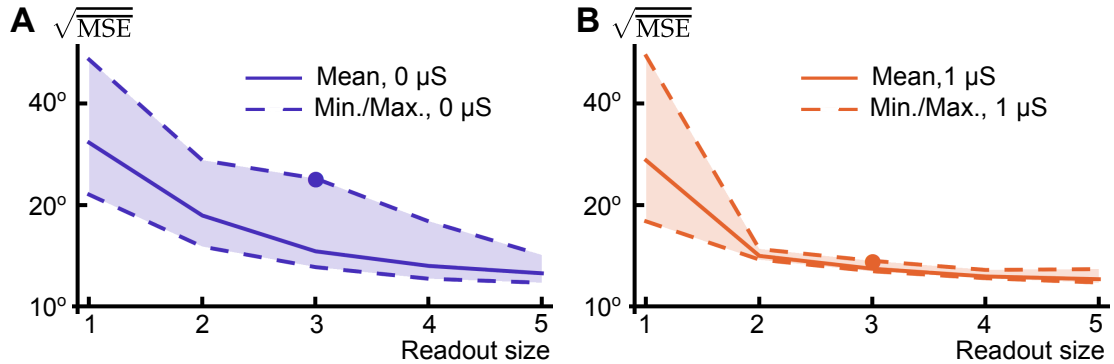


Figure 8.13: **Encoding accuracy depends on cell identities for a partial readout (A)** The solid line indicates the average square root of the mean-square error of the MMSE calculated from transient responses in the uncoupled system. Input to the system consisted of filtered optic flow stimuli generated by the rotation of random bar images with a $T = 10$ ms window of integration. The MSE was averaged across 20 randomly chosen subsets for each readout subset size, except for a size one readout, where we could only consider ten readouts, corresponding to the ten VS cells. Dashed lines indicate the maximum and minimum values of the MSE observed across the randomly chosen subsets. For size three readouts, we ensured that we included the subset consisting of VS5–7 (the same subset used in Figures 8.7), and the filled circle indicates the MSE for this subset. Note the logarithmic scale of the vertical axes. **(B)** Same as panel A, but for the coupled system.

Discussion

This work can be divided into three distinct subjects: First, the Generalized Thinning and Shift model of Chapter 4 presents a powerful tool to computational and experimental neuroscientists who need to better understand how neuronal networks operate on their inputs, and how these operations depend on the fine-scale correlation structure of that input. The linear response theory of correlations in integrate-and-fire networks of Chapters 5 through 7 is invaluable for gaining intuition for how the properties of individual cells, network architecture, and response statistics interact and are shaped by each other. Finally, the analysis of part of the fly visual system given in Chapter 8 revealed a crucial function of coupling within cells detecting rotations of the fly. Our findings may have more general implications.

The Generalized Thinning and Shift model

In Chapter 4, we introduced the Generalization Thinning and Shift (GTaS) model, a general method of generating spike trains with flexible spatiotemporal structure. The GTaS

model is completely analytically tractable: all statistics of interest can be obtained directly from the distributions used to define it. It is based on an intuitive algorithm of selecting and shifting point processes from a “mother” train. Moreover, the GTaS model can be used to easily generate partially synchronous states, cluster firing, cascading chains, and other spatiotemporal patterns of neural activity.

Processes generated by the GTaS model are naturally described by cumulant densities of pairwise and higher orders. This raises the question of whether such statistics are readily computable from data, so that realistic classes of GTaS models can be defined in the first place. One approach is to fit mechanistic models to data, and to use the higher order structure that is generated by the underlying mechanisms [308]. A synergistic blend of other methods with the GTaS framework may also be fruitful — for example, the Cu-BIC framework of [263] could be used to determine relevant marking orders, and the parametrically-described GTaS process could then be fit to allow generation of surrogate data after selection of appropriate classes of shift distributions. When it is necessary to infer higher order structure in the face of data limitations, population cumulants are an option to increase statistical power (albeit at the cost of spatial resolution — see Figure 4.3).

While the GTaS model has flexible higher order structure, it is always marginally Poisson. While throughout the cortex spiking is significantly irregular [122, 245], the level of variability differs across cells, with Fano factors ranging from below 0.5 to above 1.5 [49]. Changes in variability can reflect cortical states and computation [170, 299]. A model that would allow flexible marginal variability would therefore be very useful. Unfortunately, the tractability of the GTaS model is closely related to the fact that the marginal processes are Poisson. For this reason, an immediate generalization does not seem possible.

A number of other models have been used to describe population activity. Maximum

entropy (ME) approaches also result in models with varied spatial activity. ME models are defined based on moments or other averaged features of multivariate spiking activity [235, 241]. Such models are often used to fit purely spatial patterns of activity, though [181, 270] have extended the techniques to treat temporal correlations as well. Generalized linear models (GLMs) have been used successfully to describe spatiotemporal patterns at second [207], and third order [194]. In comparison to the present GTaS method, both GLMs and ME models are more flexible. They feature well-defined approaches for fitting to data, including likelihood-based methods with well-behaved convexity properties. What the GTaS method contributes is an explicit way to generate population activity with explicitly specified high order spatio-temporal structure. Moreover, the lower order cumulant structure of a GTaS process can be modified independently of the higher order structure, though the reverse is not true.

There are a number of possible implications of such spatio-temporal structure for communication within neural networks. In Section 4.2.3, we showed that these temporal correlations can play a role similar to that of spatial correlations established in [156] for determining network input-output transfer. Our model allowed us to examine that impact of such temporal correlations on the network-level gain of a downstream population (cascade amplification factor). Even in a very simple network it was clear that the strength of the response is determined jointly by the temporal structure of the input to the network, and the connectivity within the network. Kuhn *et al.* examined the effect of higher order structure on the firing rate gain of an integrate-and-fire neuron by driving it with a mixture of SIP or MIP processes [156]. However, in these studies, only the spatial structure of higher order activity was varied. The GTaS model allows us to concurrently change the temporal structure of correlations. In addition, the precise control of the cumulants allows us to derive models which are equivalent up to a certain cross-cumulant order, when the

configuration of marking probabilities and shift distributions allow it (as for the SIP and MIP processes of [156], which are equivalent at second order).

Such patterns of activity can be useful when experimentally probing dendritic information processing [89], or investigating the response of neuronal networks to complex patterns of input [141]. Spatiotemporal patterns can also be generated by cell assemblies [17]. The firing in such assemblies can be spatially structured, and this structure may not be reflected in the activity of participating cells. Assemblies can exhibit persistent patterns of firing, sometimes with millisecond precision [109]. The GTaS framework is well suited to describe exactly such activity patterns. The examples we presented can be easily extended to generate more complex patterns of activity with overlapping cell assemblies, different cells leading the activity, and other variations.

Understanding impact of spatiotemporal patterns on neural computations remains an open and exciting problem. Progress will require coordinating computational, theoretical, and experimental work – the latter taking advantage of novel stimulation techniques. We hope that the GTaS model, as a practical and flexible method for generating high-dimensional, correlated spike trains, will play a significant role along the way.

Analysis of neuronal dependencies through linear response

In Chapters 5 through 7, we have extended and further developed a general theoretical framework that can be used to describe the correlation structure in a network of spiking cells. The application of linear response theory allows us to find tractable approximations of cross-correlation functions in terms of the network architecture and single cell response properties. The approach was originally used to derive analytical approximations to auto- and cross-spectra in an all-to-all inhibitory network in order to study the

population response of the electrosensory lateral line lobe of weakly electric fish [167]. The key approximation relies on the assumption that the activity of cells in the network can be represented by a mixed point and continuous stochastic process, as given in Eq. (5.3). This approximation can be viewed as a generalization of classic Linear-Poisson models of neural spiking: the crucial difference is the replacement of the stationary firing rate by a realization of an integrate-and-fire spiking process. This allows for the retention of the underlying IF spiking activity while additionally posing that neurons act as perfect linear filters of their inputs. An intuitive, iterative construction then leads to the expressions for approximate cross-correlations between pairs of cells given by Eq. (5.12).

The linear response framework of Lindner *et al.* [167] was extended by Marinazzo *et al.* [178] to somewhat more complex networks, and compared with other studies in which networks exhibit collective oscillations. In addition, other works [5, 20, 45] used linear response techniques to study information in the collective response of cells in a network. More recently, Ostojic *et al.* [198] obtained formulas for cross-correlations one would obtain by terminating the iterative construction in Eq. (5.8) at first order ($n = 1$). Their approach captures corrections due to direct coupling (first order terms) and direct common input (second order terms involving second powers of interaction kernels; for further reference, see also [59, 249]). Our approach can be viewed as a generalization that also accounts for length two directed chains, along with all higher order corrections. As Figure 6.3 illustrates, these additional terms can be significant. The present approach also allows us to calculate corrected auto-correlations, in contrast with that of Ostojic *et al.*

Our work is also closely related to that of Pernice *et al.* [205], who analyzed the correlation structure in networks of interacting *Hawkes processes* [111, 112]. Both studies represent correlations between cell pairs in terms of contributions of different connectivity motifs.

While our methods apply directly to integrate-and-fire systems, stationary Hawkes processes are necessarily Poisson in the absence of coupling. As a result, the methods of Pernice *et al.* do not generally apply to integrate-and-fire neuronal networks. Moreover, for simplicity Pernice *et al.* examined only “total” spike count covariances, which are the integrals of the cross-correlation functions. However, as they note, their approach can be extended to obtain the temporal structure of cross-correlations. Similarly, Toyozumi *et al.* [276] derive expressions for cross-correlations in networks of interacting point process models in the Generalized Linear Model (GLM) class. These are very similar to Hawkes processes, but feature a static nonlinearity that shapes the spike emission rate.

To illustrate the power of the present linear response theory in analyzing the factors that shape correlations, we considered a number of simple examples for which the approximation given by Eq. (5.12) is tractable. We showed how the theory can be used both to gain intuition about the network and cell properties that shape correlations, and to quantify their impact. In particular, we explained how only local connections affect correlations in a precisely tuned all-to-all network, and how strengthening inhibition can synchronize spiking activity. In each case, we use comparisons with integrate-and-fire simulations to show that linear response theory makes highly accurate predictions.

It may be surprising that *linear* response theory can be used to provide corrections to cross-correlations of arbitrary order in network connectivity. The key to why this works lies in the accuracy of the linearization. A more accurate approximation could be obtained by including second and higher order corrections to the approximate response of a single cell, as well as corrections to the joint response. While including such terms is formally necessary to capture all contributions of a given order in network connectivity [211, 212], the success of linear response theory suggests that they are small for the cases at hand.

In short, the present approximation neglects higher-order corrections to the approximate response of individual cells, along with all corrections involving joint responses, but accounts for paths through the network of arbitrary length.

As expected from the preceding discussion, simulations suggest that, for IF neurons, our approximations become less accurate as cells receive progressively stronger inputs. The physical reasons for this loss of accuracy could be related to interactions between the “hard threshold” and incoming synaptic inputs with short timescales. Additionally, while the theory will work for short synaptic timescales, it will improve for slower synaptic dynamics, limiting towards being essentially exact in the limit of arbitrarily long synaptic time constants (note the improvement in the approximation for the FFI circuit for the slower timescale exhibited in Figure 6.2). Another important factor is background noise, which is known to improve the accuracy of the linear description of single cell responses. We assume the presence of a white noise background, although it is possible to extend the present methods to colored background noise [6, 81].

We found that linear response theory remains applicable in a wide range of dynamical regimes, including relatively low noise, superthreshold regimes where cells exhibit strong oscillatory behavior. Moreover, the theory can yield accurate approximations of strong correlations due to coupling: for the bidirectionally coupled excitatory circuit of Figure 6.3, the approximate cross-correlations match numerically obtained results even when correlation coefficients are large ($\rho_{E_1 E_2}(\infty) \approx 0.8$ in the excitable regime, ≈ 0.5 in the oscillatory regime). A thorough discussion of the limits of applicability of linear response to the computation of correlations in networks can be found in Section 6.4. There, we show that the approximation is valid over a range of physiological values in the case of the all-to-all network, and that the theory gives accurate predictions in the presence of

low firing rates. We briefly reviewed some preliminary findings which indicate the failure of the linear response theory to accurately describe *third* order correlations. Resolution of this disagreement by the proposition of a consistent correction to the linear response theory is an important open problem.

The limits of linear response approximations of time-dependent firing activity and correlations have been tested in a number of other studies. Ostojic and Brunel [197] examined this accuracy in the relatively simple case of a neuron receiving filtered Gaussian noise in addition to a white background. Chacron *et al.* [45] noted that linear response approaches applied to networks of perfect integrators begin to display significant errors at larger connection strengths. Marinazzo *et al.* [178] remarked on the errors induced by network effects in linear response approximations to correlations in a delayed feedback loop. In particular, these errors were attributed to network effects such as synchrony in the excitatory population. The authors noted that such activity cannot be correctly modeled by a linear approach.

Although we have demonstrated the theory using networks of integrate-and-fire neurons, the approach is widely applicable. The linear response kernel and power spectrum for a general integrate and fire neuron model can be easily obtained [221]. In addition, it is also possible to obtain the rate, spectrum, and susceptibility for modulation of the mean conductance in the case of conductance-based (rather than current-based) synapses (See [223] and Section 3 in Text S1). As the linear response kernel is directly related to the spike triggered average [85, 198], the proposed theoretical framework should be applicable even to actual neurons whose responses are characterized experimentally.

The possibilities for future applications are numerous. For example, one open question is how well the theory can predict correlations in the presence of adaptive currents [223].

In addition, the description of correlations in terms of architecture and response properties suggests the possibility of addressing the difficult inverse problem of inferring architectural properties from correlations [193,198,201,276]. Ostojic *et al.* applied linear response methods to the latter problem. It is our hope that the present approach will prove a valuable tool in moving the computational neuroscience community towards a more complete understanding of the origin and impact of correlated activity in neuronal populations.

The role of coupling in the blow fly vertical system

A fly faces the challenging task of rapidly extracting information about ego-motion from complex patterns of optic flow. In probabilistic terms, the fly's brain must perform real-time marginalization to extract relevant information from visual inputs (Figure 1.4C). We used a simplified, but biophysically realistic model of the vertical cell system (VS) to examine the role of electrical coupling in encoding the azimuthal axis of ego-rotation. We have shown that this parameter can be accurately extracted from the transient response of the VS network, within time windows that are neurally and behaviorally relevant in free flight.

Coupling did not affect the error of probabilistic estimates obtained from the population response (Figures 8.5, 8.6). This surprising result is explained by several changes to the population response. In isolation, some of these changes can be detrimental, while others can be beneficial to encoding (Figure 8.4). Notably, the fast responses of the VS network resulted in an invertible linear transfer from dendritic to axonal responses (Eq. (8.11)). As a consequence, the posterior distribution of the azimuthal angle of rotation was unaffected by coupling. Hence, any Bayesian or maximum-likelihood estimator, including the

OLE and MMSE, are unaffected by coupling.

The DNOVS 1 and 2 are two well-studied, efferent targets of the VS system [100, 296–298]. These neurons project to thoracic ganglia where they contact neck motor neurons involved in head stabilization during flight. Each DNOVS neuron is coupled electrically to multiple VS neurons, exhibiting the strongest connections to only two of them. In total, the DNOVS pair is coupled predominantly to a subset of three VS neurons in each hemisphere.

When we estimated the rotation angle from the response of this subset of three VS neurons, coupling significantly improved encoding accuracy (Figure 8.7). For such a sub-population readout, the transfer from dendritic to axonal membrane potential is linear, but no longer invertible. Hence, the performance of the estimator depends on coupling. The dynamical changes induced by coupling (Figure 8.4) result in a sub-population readout that has fidelity comparable to a full readout. This result depends on the chosen sub-population. Coupling had the greatest impact on the readout from VS5–7 (Figure 8.13).

These results are robust. Model details such as image statistics and the output integration window had only a quantitative impact. We reproduced our findings in an Ornstein-Uhlenbeck system that shared only general features with the full system (Figure 8.8). Post-dendritic processing enabled by the coupling of distinct axonal compartments was crucial to encoding accuracy (Figure 8.12).

Earlier arguments regarding the benefit of coupling were primarily heuristic [68], and generally concerned steady-state responses [56, 292]. By considering dominant eigenmodes, [292] showed that coupling lead to a reliable, lower dimensional representation of VS activity. Rotation about a given azimuthal axis results in depolarization of the potential of VS cells located to one side of the axis, and hyperpolarization in the remaining

cells. This prompted [56] and [68] to propose estimating the axis of rotation by interpolating the responses of the VS cells, and finding a zero crossing.

When we implemented such a zero-crossing estimator and compared it to the MMSE, we found it to be significantly suboptimal. The estimator usually struggled to achieve reasonable encoding accuracy when presented with responses to natural scenes. In this case, responses are generally weaker than those induced by the other image types we considered, and the zero-crossing estimator is more susceptible to noise. Furthermore, coupling could either improve or degrade prediction error, depending on image statistics. When presented with a subpopulation response, the zero crossing estimator fared even worse, generally producing an error several times that of the MMSE in the coupled system.

The MMSE establishes a baseline for the performance of any estimator. While suboptimal estimators can be affected by coupling in different ways, we found consistent results for the MMSE across stimulus conditions. While brains and neurons may not necessarily process information optimally [171], evidence for optimality has been gathered both at the behavioral and neural level (e.g., [73, 77]). In this study, optimal estimators served as an operational benchmark, revealing the potential capabilities of the system under realistic assumptions.

Among previous analyses of optic flow encoding in lobula plate neurons of the fly, two studies stand conceptually close to the current work. Karmeier and collaborators took a Bayesian approach reminiscent of our own to quantify the encoding efficiency of the axis of rotation in the VS population response [142]. Further, they also proposed time integrals of the VS membrane potentials as readout variables, and examined the impact of population size on the ability of the VS system to encode the axis of rotation. We note several important differences: Foremost, [142] did not investigate the effect of VS coupling,

instead focusing on the effects of integration time and input correlations. Furthermore, they used a phenomenological model, in contrast to the biophysically plausible model we considered. More recently, Weber and collaborators applied generalized linear models to assess the benefits of coupling between two optic flow-processing, spiking neurons of the lobula plate (H1 and Vi) for conveying information about optic flow parameters [293].

Our results in the fly VS system are suggestive of more general principles: Consider a neuronal network which encodes an external parameter in its response. Coupling can allow each neuron to represent a greater extent of the parameter space. When downstream targets need to extract information about this parameter from relatively few neuronal projections, the redundancy within their responses can be highly beneficial [266]. As we have shown, such redundancy will not necessarily degrade the performance of an estimator.

We found that changes in correlation structure were important in improving encoding accuracy in the case of a subpopulation readout (Figure 8.11). These findings contrast with the usual discourse on whether neuronal responses should be correlated (to error-correct), or decorrelated (to maximize information transmission; [275]). In the present case, correlations between VS neurons carry information about the responses of unobserved neurons. Electrical synapses are both strong and fast in their effect on subthreshold dynamics relative to their chemical counterparts [303]. They are therefore particularly well-suited for increasing the coverage of a parameter, reducing variability and introducing redundancy.

Many previous theoretical studies examined how changes in neuronal response statistics, such as correlations or tuning curves, impact coding [11, 15, 65, 140, 162, 203, 244, 247, 259]. This approach gives us valuable insights into how information about a stimulus is affected by different aspects of the neural population response. However, it is important to remember that different response statistics are frequently dependent [21, 248]. They are

characterizations of a generally complex system that may be better described in terms of its underlying architecture and the dynamical properties of its input.

These issues relate to a key advantage of our approach: We made no *a priori* assumptions about the statistical form of the VS population response. In particular, we made no assumptions on how the joint activity of VS neurons encodes the axis of rotation. Rather, we considered the responses of a biophysically inspired model to realistic stimuli. The spatiotemporal structure of the input, and the properties of the VS network fully determined its responses. Since we obtained the full joint distribution of responses, we could avoid an ad-hoc analysis (or model) of encoding in the VS response. Instead, we obtained a direct measure of the information available to the animal about the stimulus [93].

There are some manifest avenues for future investigation: For instance, we implemented the readout of the VS population responses as simple temporal averages. However, downstream DNOVS neurons are not perfect integrators. In particular, DNOVS 2 is a spiking neuron, introducing a strong nonlinearity into the processing pathway. Further, the effect of interactions with other neurons of the lobula plate should be investigated [30]. We also did not attempt to determine whether significant information is contained in correlations higher than second order. Application of maximum-entropy approaches could help answer this question [134].

The aerial performance of flies during intrasaccadic flight maneuvers is unmatched in both nature and technology [82], making the study of optic flow processing within the brain of flies and other insects of great general interest. A vertical system, similar to the one examined here, has been identified in the fruit fly, *Drosophila melanogaster*. More broadly, the extraction of information from optic flow is a problem faced by all seeing organisms moving through the world. Understanding how the brain of a fly does this

efficiently, and with so few neurons, can provide insight into the implementations utilized in more complex organisms.

Tying it all together

Animal brains may range widely in their complexity, from the “simplicity” of the roundworm (approximately 300 neurons and 5000 synapses [300]), to the relatively amazing efficiency of the fly brain (containing a few hundred thousand cells [28], all the way to the stunning intricacy of our own human brains (10^{11} neurons and 10^{14} synapses [301]). The study of brains, and specifically the form and function of the subnetworks they contain, is a problem of both immense importance and immense difficulty.

The common thread which weaves the present work together is the focus on the effect of dependencies and interactions amongst neuronal populations in shaping their collective responses. We believe that successful scientific progress towards understanding such relationships rests on three foundational pillars: First, we must develop tools which will allow us to “poke and prod” neurons and networks, increasing our understanding of their general response properties, and pulling back the veil over the underlying structure of these networks. The Generalized Thinning and Shift framework and related approaches can provide such instruments.

Next, given the extreme nature of the complexity of the computational and experimental settings neuroscientists find themselves in, we must strive to better understand how local (observable) properties of networks can shape their response distributions. This is a central function of the linear response theory of correlations. In particular, we showed how motif cumulants — the values of which experimentalists are making increasingly

available for a variety of cortical networks [260] — can accurately predict global dynamical properties. Furthermore, given knowledge of such relationships, there is a potential for flipping them on their heads, thereby drawing conclusions on local network structure (which is generally poorly sampled) from observable, large scale statistics of network activity.

Comprehension of the structure of a network and the dynamics that overlay that structure, and more importantly, their interrelationship, still says nothing of the *function* of the network. This is the final pillar: we must advance our procedures for assessing the role of the dynamics and structure in creating an environment conducive for the network to perform the tasks it is faced with. Crucially, in our analysis of the encoding of the axis of ego-rotation in a biophysically-realistic model of the fly visual system, we avoided *a priori* assumptions of form or function of the population response. As in our study of the fly visual system, embracing this approach will hopefully lead to studies and findings with broader implications.

Appendix A

Notation tables

Symbol	Description
$V_i(t)$	Membrane potential of cell i at time t .
E_L, C_m, g_L, τ_m	Leak reversal potential, membrane capacitance, leak conductance and membrane time constant of a neuron. The latter three are related by $\tau_m = C_m/g_L$.
$E_{\xi,i}, \sigma_{\xi,i}$	Mean and standard deviation of the background noise for cell i .
V_{th}, V_r, τ_{ref}	Membrane potential threshold, reset, and absolute refractory period for cells.
$\psi(v), V_T, \Delta_T$	Spike generating current, soft threshold and spike shape parameters for the IF model [81].
τ_{syn}, τ_d	Synaptic time constant and delay of the synaptic filter applied to the output of a neuron. See an example filter in Eq. (5.6).
\mathbf{W}_{ij}	The $j \rightarrow i$ synaptic weight, proportional to the area under a single post-synaptic current for current-based synapses.
$\tilde{\beta}(t)$	Entries $[\tilde{\beta}(t)]_{ij} = \tilde{\beta}_{ij}(t)$ give the $j \rightarrow i$ synaptic kernel - equals the product of the synaptic weight \mathbf{W}_{ij} and the synaptic filter for outputs of cell j .
$\mathbf{y}(t)$	Vector of spike train outputs of a network, $\mathbf{y}(t) = (y_1(t), \dots, y_N(t))$.
$N_{y_i}(A)$	Spike count for cell i — counts the Number of spikes of the process i with times in the set A . Also referred to as a counting process.

Table A.1: **Notation for neuron models.** Notation used in defining and discussing neuron models.

Symbol	Description
x^*	The complex conjugate $x^* = a - bi$ of a scalar quantity $x = a + bi$, where $a, b \in \mathbb{R}$.
$\bar{\mathbf{X}}$	The complex conjugate (non-transposed) of a matrix or vector \mathbf{X} , defined as an entry-wise scalar conjugate transpose.
$(f * g)(t)$	The convolution of f and g given by $(f * g)(t) = \int_{-\infty}^{\infty} f(s)g(t-s)ds.$
$f(t), \tilde{f}(\omega)$	$\tilde{f}(\omega)$ is the Fourier transform of $f(t)$ with the convention $\tilde{f}(\omega) = \mathcal{F}[f](\omega) \equiv \int_{-\infty}^{\infty} e^{-2\pi i \omega t} f(t) dt$
$\kappa(\mathbf{X})$	Cross-cumulant of a random vector \mathbf{X} defined in Eq. (2.1).
$\kappa_{i_1 i_2 \dots i_k}^{\mathbf{y}}(\tau_1, \dots, \tau_{k-1})$	The k^{th} order cross-cumulant density for the processes $(y_{i_1}, y_{i_2}, \dots, y_{i_k})$, defined in Eq. (2.13) for spike trains and Eq. (2.3) for numerically valued stochastic processes. When \mathbf{y} is replaced by a counting process \mathbf{X} , as in Chapter 4, we refer to the cross-cumulant density of the corresponding spike trains, and not to the density associated with the counting processes themselves.
$S_{i_1 i_2 \dots i_k}^{\mathbf{y}}(\tau_1, \dots, \tau_{k-1})$	The k^{th} order polyspectrum for the processes $(y_{i_1}, y_{i_2}, \dots, y_{i_k})$, defined in Eq. (2.5).
$\gamma_{i_1 i_2 \dots i_k}^{\mathbf{y}}(T), \gamma_{i_1 i_2 \dots i_k}^{\mathbf{y}}(\infty)$	The k^{th} order spike count cross-cumulant for the processes $(y_{i_1}, y_{i_2}, \dots, y_{i_k})$ over windows of length T , and over arbitrarily long windows, defined in Eqs. (2.11) and (2.9).
$\rho_{ij}^{\mathbf{y}}(T)$	Pearson correlation coefficient between the spike counts $N_{y_i}(T)$ and $N_{y_j}(T)$ over windows of length T .
$C(u_1, \dots, u_N), c(u_1, \dots, u_N)$	Copula distribution function and density. Defined in Section 2.2.

Table A.2: **Mathematical notation.** Mathematical notation used in the text.

Symbol	Description
\mathbf{X}	Vector of counting processes associated with a GTaS process.
\mathbb{D}	$\mathbb{D} = \{1, 2, \dots, N\}$ where N is the system size of the GTaS process under consideration.
$(p_D)_{D \subset \mathbb{D}}$	Marking probabilities of a GTaS process.
$(Q_D)_{D \subset \mathbb{D}}, \mathbf{Y}$	Family of shift distributions on \mathbb{R}^N for a GTaS process, and a the random shift vector drawn from these distributions.
$\mathcal{B}(\mathbb{R})$	Borel subsets of the real line \mathbb{R} .
$\xi(D; A_1, \dots, A_N)$	Independent Poisson variables which count points which, after shifting, lie in the sets A_i only along the dimensions corresponding to the indices of D . These counts consist of contributions from subsets marked for $D' \supset D$, but indices in $D' \setminus D$ end up outside the corresponding A_i . Defined in the statement of Theorem 4.3.1.
$\zeta_D(A_1, \dots, A_N)$	Independent Poisson variables which are context-dependent resummations of the variables $\xi(D; A_1, \dots, A_N)$. Defined below Eq. (4.10).
$\kappa_{i_1 \dots i_{k-1}, \text{pop}}^{\mathbf{X}}(\tau_1, \dots, \tau_{k-1})$	Population cumulant density defined in Eq. (2.15).

Table A.3: **Notation for the Generalized Thinning and Shift model.** Notation used in the definition and discussion of the Generalized Thinning and Shift model in Chapter 4.

Symbol	Description
$r_i, r_i(t), A_i(t)$	Stationary rate and linear response kernel for cell i . The latter two are related in Eq. (5.2).
$\mathbf{K}(t)$	The entry $[\mathbf{K}(t)]_{ij} = K_{ij}(t)$ gives the $j \rightarrow i$ interaction kernel - describes how the firing activity of cell i is perturbed by an input spike from cell j . It is defined by $K_{ij}(t) = (A_i * \tilde{\beta}_{ij})(t)$.
$\mathbf{y}_i^n(t)$	The n^{th} order approximation of the activity of cell i in a network which accounts for directed paths through the network graph up to length n ending at cell i . Defined in Eqs. (5.8, 5.9).
$S_{0,i}^y$	The “unperturbed” spectra for cell i , defined as the power spectrum of the i^{th} process in the absence of <i>fluctuations</i> due to input.
$\tilde{\varphi}_{E,I}, \tilde{\varphi}, \tilde{\varphi}_c$	Total excitatory/inhibitory synaptic input, total input, and total common input in the all-to-all and random networks of Chapter 6.
p	Empirical connection probability in a random network.
$\mu_n, \mu_{n,m}$	The <i>motif moment</i> for order length n chain motifs and (n, m) diverging motifs, respectively — quantify the empirical probability of observation for n^{th} order chain motifs and $(n + m)^{\text{th}}$ order, respectively. Motifs are depicted in Figure 6.1. Definition given in Eq. (7.6), and we set $\mu_n = \mu_{n,0} = \mu_{0,n}$.
$\kappa_n, \kappa_{n,m}$	The <i>motif cumulant</i> for length n chain motifs and (n, m) diverging motifs, respectively. Defined implicitly in terms of motif moments in Eqs. (7.7, 7.8), and explicitly in Eq. (7.9, 7.10).
$\rho^{\text{avg}}, \rho_{XY}^{\text{avg}}$	Average spike count correlation coefficient across a network, and average spike count correlation coefficient between cells of classes X and Y , respectively.
$\Psi_{\text{ER}}(\tilde{A}w)$	Erdős-Rényi spectral radius, used as a measure to quantify the average total strength of interactions within realizations of a random network ensemble, defined in Eq. (7.1).

Table A.4: **Notation for linear response theory applications.** Notation used in the applications of linear response theory contained in Chapters 5 through 7.

Bibliography

- [1] L. F. Abbott and P. Dayan. The effect of correlated variability on the accuracy of a population code. *Neural Comput.*, 11(1):91–101, 1999.
- [2] M. Abeles. *Corticonics: Neural circuits of the cerebral cortex*. Cambridge University Press, 1991.
- [3] M. Abeles and Y. Prut. Spatio-temporal firing patterns in the frontal cortex of behaving monkeys. *J Physiol.-Paris*, 90(3):249–250, 1996.
- [4] A. Aertsen, M. Diesmann, and M. O. Gewaltig. Propagation of synchronous spiking activity in feedforward neural networks. *J. Physiol.-Paris*, 90(3):243–247, 1996.
- [5] O. Á. Åkerberg and M. J. Chacron. Noise shaping in neural populations. *Phys. Rev. E*, 79(1):011914, 2009.
- [6] A. K. Alijani and M. J. E. Richardson. Rate response of neurons subject to fast or frozen noise: From stochastic and homogeneous to deterministic and heterogeneous populations. *Phys. Rev. E*, 84(1):011919, 2011.
- [7] S. Amari, H. Nakahara, S. Wu, and Y. Sakai. Synchronous firing and higher-order interactions in neuron pool. *Neural Comput.*, 15(1):127–142, 2003.
- [8] A. M. Amjad, D. M. Halliday, J. R. Rosenberg, and B. A. Conway. An extended difference of coherence test for comparing and combining several independent coherence estimates: theory and application to the study of motor units and physiological tremor. *J. Neurosci. Meth.*, 73(1):69–79, 1997.
- [9] M. Arsiero, H.-R. Lüscher, B. N. Lundstrom, and M. Giugliano. The impact of input fluctuations on the frequency–current relationships of layer 5 pyramidal neurons in the rat medial prefrontal cortex. *J. Neurosci.*, 27(12):3274–3284, 2007.

- [10] G. Aston-Jones and K. Deisseroth. Recent advances in optogenetics and pharmacogenetics. *Brain Res.*, 2013.
- [11] B. B. Averbeck, P. E. Latham, and A. Pouget. Neural correlations, population coding and computation. *Nat. Rev. Neurosci.*, 7(5):358–366, 2006.
- [12] Y. Aviel, E. Pavlov, M. Abeles, and D. Horn. Synfire chain in a balanced network. *Neurocomputing*, 44:285–292, 2002.
- [13] L. Badel, S. Lefort, T. K. Berger, C. C. H. Petersen, W. Gerstner, and M. J. E. Richardson. Extracting non-linear integrate-and-fire models from experimental data using dynamic i–v curves. *Biol. Cybern.*, 99(4):361–370, 2008.
- [14] W. Bair, E. Zohary, and W.T. Newsome. Correlated firing in macaque visual area mt: time scales and relationship to behavior. *J Neurosci*, 21(5):1676–1697, 2001.
- [15] H. B. Barlow. Possible principles underlying the transformation of sensory messages. *Sensory Communication*, pages 217–234, 1961.
- [16] A. K. Barreiro, J. Gjorgjieva, F. Rieke, and E. Shea-Brown. When are feedforward microcircuits well-modeled by maximum entropy methods? *Arxiv preprint*, 2010.
- [17] B. Bathellier, L. Ushakova, and S. Rumpel. Discrete neocortical dynamics predict behavioral categorization of sounds. *Neuron*, 76(2):435–449, 2012.
- [18] D. Battaglia, A. Karagiannis, T. Gallopin, H. W. Gutch, and B. Cauli. Beyond the frontiers of neuronal types. *Front. Neural Circuits*, 7, 2013.
- [19] N. Bauerle and R. Grubel. Multivariate counting processes: copulas and beyond. *Astin Bulletin*, 35(2):379, 2005.
- [20] J. Beck, V. R. Bejjanki, and A. Pouget. Insights from a simple expression for linear Fisher information in a recurrently connected population of spiking neurons. *Neural Comput.*, 23(6):1484–1502, 2011.
- [21] JM Beck, WJ Ma, X Pitkow, PE Latham, and Pouget A. Not noisy, just wrong: the role of suboptimal inference in behavioral variability. *Neuron*, 74(1):30–39, 2012.
- [22] R. Ben-Yishai, R. L. Bar-Or, and H. Sompolinsky. Theory of orientation tuning in visual cortex. *Proc. Natl. Acad. Sci. USA*, 92(9):3844–3848, 1995.
- [23] P. Berkes, F. Wood, and J. Pillow. Characterizing neural dependencies with copula models. *Adv. Neur. In.*, 21:129–136, 2009.
- [24] D. M. Blitz and W. G. Regehr. Timing and specificity of feed-forward inhibition within the LGN. *Neuron*, 45(6):917–928, 2005.

- [25] N. Boeddeker and M. Egelhaaf. A single control system for smooth and saccade-like pursuit in blowflies. *J. Exp. Biol.*, 208(8):1563–1572, 2005.
- [26] A. Borst and S. Bahde. Spatio-temporal integration of motion: A simple strategy for safe landing in flies. *Naturwiss.*, 75(5):265–267, 1988.
- [27] A. Borst and J. Haag. Neural networks in the cockpit of the fly. *J. Comput. Phys. A*, 188(6):419–437, 2002.
- [28] A. Borst, J. Haag, and D. F. Reiff. Fly motion vision. *Ann. Rev. Neurosci.*, 33:49–70, 2010.
- [29] A. Borst, C. Reisenman, and J. Haag. Adaptation of response transients in fly motion vision. II: Model studies. *Vision Res.*, 43(11):1309, 2003.
- [30] A. Borst and F. Weber. Neural action fields for optic flow based navigation: a simulation study of the fly lobula plate network. *PLoS ONE*, 6(1):e16303, 2011.
- [31] E. Bouyé, V. Durrleman, A. Nikeghbali, G. Riboulet, and T. Roncalli. Copulas for finance - A reading guide and some applications. *Available at SSRN 1032533*, 2000.
- [32] T. Branco, B. A. Clark, and M. Häusser. Dendritic discrimination of temporal input sequences in cortical neurons. *Sci. Signal.*, 329(5999):1671, 2010.
- [33] T. Branco and M. Häusser. Synaptic integration gradients in single cortical pyramidal cell dendrites. *Neuron*, 69(5):885–892, 2011.
- [34] R. Brette and W. Gerstner. Adaptive exponential integrate-and-fire model as an effective description of neuronal activity. *J. Neurophysiol.*, 94(5):3637–3642, 2005.
- [35] Romain Brette. Generation of correlated spike trains. *Neural Comput.*, 21(1):188–215, 2009.
- [36] D. R. Brillinger. An introduction to polyspectra. *Ann. Math. Stat.*, pages 1351–1374, 1965.
- [37] E. N. Brown, R. E. Kass, and P. Mitra. Multiple neural spike train data analysis: state-of-the-art and future challenges. *Nat. Neurosci.*, 7(5):456–61, 2004.
- [38] N. Brunel and V. Hakim. Fast global oscillations in networks of integrate-and-fire neurons with low firing rates. *Neural Comput.*, 11(7):1621–1671, 1999.
- [39] N. Brunel and M. C. W. van Rossum. Lapicques 1907 paper: from frogs to integrate-and-fire. *Biol. Cybern.*, 97(5):337–339, 2007.
- [40] A. N. Burkitt. A review of the integrate-and-fire neuron model: II. Inhomogeneous synaptic input and network properties. *Biol. Cybern.*, 95(2):97–112, 2006.

- [41] A. N. Burkitt. A review of the integrate-and-fire neuron model: I. Homogeneous synaptic input. *Biol. Cybern.*, 95(1):1–19, 2006.
- [42] G. Buzsáki. Neural syntax: cell assemblies, synapsesembles, and readers. *Neuron*, 68(3):362–385, 2010.
- [43] N. Cain and E. Shea-Brown. Impact of correlated neural activity on decision-making performance. *Neural Comput.*, 25(2):289–327, 2013.
- [44] C. E. Carr, H. Agmon-Snir, and J. Rinzel. The role of dendrites in auditory coincidence detection. *Nature*, 393(6682):268–272, May 1998.
- [45] M. J. Chacron, A. Longtin, and L. Maler. Delayed excitatory and inhibitory feedback shape neural information transmission. *Phys. Rev. E*, 72(5):051917, 2005.
- [46] C. Chatfield. *The Analysis of Time Series: An Introduction*, volume 59. Chapman and Hall/CRC, 2003.
- [47] B. Y. Chow, X. Han, A. S. Dobry, X. Qian, A. S. Chuong, M. Li, M. A. Henninger, G. M. Belfort, Y. Lin, P. E. Monahan, and E. S. Boyden. High-performance genetically targetable optical neural silencing by light-driven proton pumps. *Nature*, 463(7277):98–102, 2010.
- [48] C. C. Chow and N. Kopell. Dynamics of spiking neurons with electrical coupling. *Neural Comput.*, 12(7):1643–1678, 2000.
- [49] M. M. Churchland, B. M. Yu, J. P. Cunningham, L. P. Sugrue, M. R. Cohen, G. S. Corrado, W. T. Newsome, A. M. Clark, P. Hosseini, B. B. Scott, D. C. Bradley, M. A. Smith, A. Kohn, J. A. Movshon, K. M. Armstrong, T. Moore, S. W. Chang, L. H. Snyder, S. G. Lisberger, N. J. Priebe, I. M. Finn, D. Ferster, S. I. Ryu, G. Santhanam, M. Saghani, and K. V. Shenoy. Stimulus onset quenches neural variability: a widespread cortical phenomenon. *Nat. Neurosci.*, 13(3):369–378, March 2010.
- [50] M. Cohen and W. Newsome. Estimates of the contribution of single neurons to perception depend on timescale and noise correlation. *J. Neurosci.*, 29(20):6635–6648, Dec 2009.
- [51] M. R. Cohen and A. Kohn. Measuring and interpreting neuronal correlations. *Nat. Neurosci.*, 14(7):811–819, 2011.
- [52] T. S. Collett and M. S. Land. Visual control of flight behavior in the hoverfly, *Syrirta pipiens* L. *J. Comp. Physiol.*, 99(1):1–66, 1975.
- [53] B. W. Connors and M. A. Long. Electrical synapses in the mammalian brain. *Annu. Rev. Neurosci.*, 27:393–418, 2004.
- [54] D. R. Cox and V. Isham. *Point Processes*, volume 12. Chapman & Hall/CRC, 1980.

- [55] D. R. Cox and P. A. W. Lewis. Multivariate point processes. *Selected Statistical Papers of Sir David Cox: Volume 1, Design of Investigations, Statistical Methods and Applications*, 1:159, 2006.
- [56] H. Cuntz, J. Haag, F. Forstner, I. Segev, and A. Borst. Robust coding of flow-field parameters by axo-axonal gap junctions between fly visual interneurons. *P. Natl. Acad. Sci. USA*, 104(24):10229–10233, 2007.
- [57] D. J. Daley and D. Vere-Jones. *An Introduction to the Theory of Point Processes: Volume I: Elementary Theory and Methods*, volume 1. Springer, 2002.
- [58] P. Dayan and L. F. Abbott. *Theoretical Neuroscience*, volume 31. MIT Press, 2001.
- [59] J. de la Rocha, B. Doiron, K. Josić E. Shea-Brown, and A. Reyes. Correlation between neural spike trains increases with firing rate. *Nature*, 448(7155):802–806, 2007.
- [60] S. Demarta and A. J. McNeil. The t copula and related copulas. *Int. Stat. Rev.*, 73(1):111–129, 2005.
- [61] A. Destexhe. Conductance-based integrate-and-fire models. *Neural Comput.*, 9(3):503–514, 1997.
- [62] J. D. Dorn and D. L. Ringach. Estimating membrane voltage correlations from extracellular spike trains. *J. Neurophysiol.*, 89(4):2271–2278, 2003.
- [63] S. Druckmann, T. K. Berger, F. Schürmann, S. Hill, H. Markram, and I. Segev. Effective stimuli for constructing reliable neuron models. *PLoS Comput. Biol.*, 7(8):e1002133, 2011.
- [64] A. S. Ecker, P. Berens, G. A. Keliris, M. Bethge, N. K. Logothetis, and A. S. Tolias. Decorrelated neuronal firing in cortical microcircuits. *Science*, 327(5965):584–587, 2010.
- [65] A. S. Ecker, P. Berens, A. S. Tolias, and M. Bethge. The effect of noise correlations in populations of diversely tuned neurons. *J Neurosci*, 31(40):14272–14283, 2011.
- [66] M. Egelhaaf, N. Boeddeker, R. Kern, R. Kurtz, and J. P. Lindemann. Spatial vision in insects is facilitated by shaping the dynamics of visual input through behavioral action. *Front. Neural Circuits*, 6, 2012.
- [67] G. T. Einevoll, F. Franke, E. Hagen, C. Pouzat, and K. D. Harris. Towards reliable spike-train recordings from thousands of neurons with multielectrodes. *Curr. Opin. Neurobiol.*, 22(1):11–17, 2012.
- [68] Y. M. Elyada, J. Haag, and A. Borst. Different receptive fields in axons and dendrites underlie robust coding in motion-sensitive neurons. *Nat. Neurosci.*, 12(3):327–332, 2009.

- [69] G. B. Ermentrout. Type I membranes, phase resetting curves, and synchrony. *Neural Comput.*, 8(5):979–1001, 1996.
- [70] G. B. Ermentrout and J. D. Cowan. A mathematical theory of visual hallucination patterns. *Biol. Cybern.*, 34(3):137–150, 1979.
- [71] G. B. Ermentrout and N. Kopell. Frequency plateaus in a chain of weakly coupled oscillators, I. *SIAM J. Math. Anal.*, 15(2):215–237, 1984.
- [72] G. B. Ermentrout and N. Kopell. Parabolic bursting in an excitable system coupled with a slow oscillation. *SIAM J. Appl. Math.*, 46(2):233–253, 1986.
- [73] M. O. Ernst and M. S. Banks. Humans integrate visual and haptic information in a statistically optimal fashion. *Nature*, 415(6870):429–433, 2002.
- [74] A. Fairhall, E. Shea-Brown, and A. Barreiro. Information theoretic approaches to understanding circuit function. *Curr. Opin. Neurobiol.*, 2012.
- [75] K. Farrow, A. Borst, and J. Haag. Sharing receptive fields with your neighbors: tuning the vertical system cells to wide field motion. *J. Neurosci.*, 25(15):3985–3993, 2005.
- [76] M. Ferrante, M. Migliore, and G. A. Ascoli. Feed-forward inhibition as a buffer of the neuronal input-output relation. *Proc. Natl. Acad. Sci. USA*, 106(42):18004–18009, 2009.
- [77] C. R. Fetsch, A. Pouget, G. C. DeAngelis, and D. E. Angelaki. Neural correlates of reliability-based cue weighting during multisensory integration. *Nat. Neurosci.*, 15(1):146–154, 2012.
- [78] E. E. Fetz and B. Gustafsson. Relation between shapes of post-synaptic potentials and changes in firing probability of cat motoneurons. *J. Physiol.*, 341(1):387, 1983.
- [79] R. Fitzhugh. Impulses and physiological states in theoretical models of nerve membrane. *Biophys. J.*, 1(6):445–466, 1961.
- [80] N. Fourcaud-Trocmé and N. Brunel. Dynamics of the instantaneous firing rate in response to changes in input statistics. *J. Comput. Neurosci.*, 18(3):311–321, 2005.
- [81] N. Fourcaud-Trocmé, D. Hansel, C. van Vreeswijk, and N. Brunel. How spike generation mechanisms determine the neuronal response to fluctuating inputs. *J. Neurosci.*, 23(37):11628–11640, 2003.
- [82] M. A. Frye and M. H. Dickinson. Fly flight: a model for the neural control of complex behavior. *Neuron*, 32(3):385–388, 2001.
- [83] E. J. Furshpan and D. D. Potter. Transmission at the giant motor synapses of the crayfish. *J. Physiol.*, 145(2):289–325, 1959.

- [84] F. Gabbiani and S. J. Cox. *Mathematics for Neuroscientists*. Academic Press, 2010.
- [85] F. Gabbiani and C. Koch. Principles of spike train analysis. In I. Segev and C. Koch, editors, *Methods in Neuronal Modeling*, pages 313–360. MIT Press, Cambridge, 1998.
- [86] L. Gabernet, S. P. Jadhav, D. E. Feldman, M. Carandini, and M. Scanziani. Somatosensory integration controlled by dynamic thalamocortical feed-forward inhibition. *Neuron*, 48(2):315–327, 2005.
- [87] E. Ganmor, R. Segev, and E. Schneidman. Sparse low-order interaction network underlies a highly correlated and learnable neural population code. *Proc. Natl. Acad. Sci. USA*, 108(23):9679–9684, 2011.
- [88] C. W. Gardiner. *Handbook of Stochastic Methods for Physics, Chemistry and the Natural Sciences*. Springer-Verlag, Berlin, 2009.
- [89] S. Gasparini and J. C. Magee. State-dependent dendritic computation in hippocampal CA1 pyramidal neurons. *J. Neurosci.*, 26(7):2088–2100, February 2006.
- [90] W. Gerstner and W. M. Kistler. *Spiking neuron models: Single neurons, populations, plasticity*. Cambridge university press, 2002.
- [91] J. Gjorgjieva, C. Clopath, J. Audet, and J.-P. Pfister. A triplet spike-timing-dependent plasticity model generalizes the Bienenstock–Cooper–Munro rule to higher-order spatiotemporal correlations. *Proc. Natl. Acad. Sci. USA*, 108(48):19383–19388, 2011.
- [92] C. Golgi. The neuron doctrine: theory and facts. *Nobel Lectures: Physiology or Medicine*, 1921:189–217, 1901.
- [93] A. B. A. Graf, A. Kohn, M. Jazayeri, and J. A. Movshon. Decoding the activity of neuronal populations in macaque primary visual cortex. *Nat. Neurosci.*, 14(2):239–245, 2011.
- [94] S. Grün and S. Rotter. *Analysis of parallel spike trains*. Springer, 2010.
- [95] R. Güttig and H. Sompolinsky. The tempotron: a neuron that learns spike timing-based decisions. *Nat. Neurosci.*, 9(3):420–428, 2006.
- [96] D. A. Gutnisky and K. Josic. Generation of spatio-temporally correlated spike-trains and local-field potentials using a multivariate autoregressive process. *J. Neurophysiol.*, December 2009.
- [97] J. Haag and A. Borst. Neural mechanism underlying complex receptive field properties of motion-sensitive interneurons. *Nat. Neurosci.*, 7(6):628–634, 2004.
- [98] J. Haag and A. Borst. Reciprocal inhibitory connections within a neural network for rotational optic-flow processing. *Front. Neurosci.*, 1(1):111, 2007.

- [99] J. Haag, W. Denk, and A. Borst. Fly motion vision is based on reichardt detectors regardless of the signal-to-noise ratio. *P. Natl. Acad. Sci. USA*, 101(46):16333–16338, 2004.
- [100] J. Haag, A. Wertz, and A. Borst. Integration of lobula plate output signals by DNOVS1, an identified premotor descending neuron. *J. Neurosci.*, 27(8):1992–2000, 2007.
- [101] S. Haeusler, K. Schuch, and W. Maass. Motif distribution, dynamical properties, and computational performance of two data-based cortical microcircuit templates. *J. Physiol.-Paris*, 103(1):73, 2009.
- [102] A. Hald. The early history of the cumulants and the Gram-Charlier series. *Int. Stat. Rev.*, 68(2):137–153, 2000.
- [103] X. Han and E. S. Boyden. Multiple-color optical activation, silencing, and desynchronization of neural activity, with single-spike temporal resolution. *PLoS ONE*, 2(3):e299, 2007.
- [104] D. Hansel, G. Mato, and B. Pfeuty. The role of intrinsic cell properties in synchrony of neurons interacting via electrical synapses. In *Phase Response Curves in Neuroscience*, pages 361–398. Springer, 2012.
- [105] D. Hansel and C. van Vreeswijk. How noise contributes to contrast invariance of orientation tuning in cat visual cortex. *J. Neurosci.*, 22(12):5118–5128, 2002.
- [106] B. J. Hansen, M. I. Chelaru, and V. Dragoi. Correlated variability in laminar cortical circuits. *Neuron*, 76(3):590–602, 2012.
- [107] F. B. Hanson and H. C. Tuckwell. Diffusion approximations for neuronal activity including synaptic reversal potentials. *J. Theor. Neurobiol.*, 2:127–153, 1983.
- [108] K. D. Harris. Neural signatures of cell assembly organization. *Nat. Rev. Neurosci.*, 6(5):399–407, 2005.
- [109] K. D. Harris, D. A. Henze, H. Hirase, X. Leinekugel, G. Dragoi, A. Czurkó, and G. Buzsáki. Spike train dynamics predicts theta-related phase precession in hippocampal pyramidal cells. *Nature*, 417(6890):738–741, 2002.
- [110] K. Hausen. *Photoreception and Vision in Invertebrates* (Ali, MA, ed.), 1984.
- [111] A. G. Hawkes. Point spectra of some mutually exciting point processes. *J. Roy. Stat. Soc. B Met.*, 33(3):438–443, 1971.
- [112] A. G. Hawkes. Spectra of some self-exciting and mutually exciting point processes. *Biometrika*, 58(1):83–90, 1971.

- [113] D. O. Hebb. *The organization of behavior: A neuropsychological theory*. Psychology Press, 1949.
- [114] B. Hellwig. A quantitative analysis of the local connectivity between pyramidal neurons in layers 2/3 of the rat visual cortex. *Biol. Cybern.*, 82(2):111–121, 2000.
- [115] R. Hengstenberg. Common visual response properties of giant vertical cells in the lobula plate of the blowfly *Calliphora*. *J. Comput. Phys. A*, 149(2):179–193, 1982.
- [116] R. Hengstenberg. Stabilizing eye/head movements in the blowfly *Calliphora erythrocephala*. In Alain Berthoz, Werner Graf, and Pierre Paul Vidal, editors, *The Head-Neck Sensory Motor System*, chapter 5, pages 49–55. Oxford University Press, 1992.
- [117] R. Hengstenberg, K. Hausen, and B. Hengstenberg. The number and structure of Giant Vertical Cells (VS) in the lobula plate of the blowfly *Calliphora erythrocephala*. *J. Comp. Phys.*, 149(2):163–177, 1982.
- [118] A. Herrmann and W. Gerstner. Noise and the PSTH response to current transients: I. General theory and application to the integrate-and-fire neuron. *J. Comput. Neurosci.*, 11(2):135–151, 2001.
- [119] L. Hertäg, J. Hass, T. Golovko, and D. Durstewitz. An approximation to the adaptive exponential integrate-and-fire neuron model allows fast and predictive fitting to physiological data. *Front. Comput. Neurosci.*, 6, 2012.
- [120] A. L. Hodgkin and A. F. Huxley. A quantitative description of membrane current and its application to conduction and excitation in nerve. *J. Physiol.*, 117(4):500, 1952.
- [121] C. Holmgren, T. Harkany, B. Svennenfors, and Y. Zilberter. Pyramidal cell communication within local networks in layer 2/3 of rat neocortex. *J. Physiol.*, 551(1):139–153, 2003.
- [122] G. R. Holt, W. R. Softky, C. Koch, and R. J. Douglas. Comparison of discharge variability in vitro and in vivo in cat visual cortex neurons. *J. Neurophysiol.*, 75(5):1806–1814, 1996.
- [123] J. J. Hopfield. Neural networks and physical systems with emergent collective computational abilities. *Proc. Natl. Acad. Sci. USA*, 79(8):2554–2558, 1982.
- [124] J. J. Hopfield. Neurons with graded response have collective computational properties like those of two-state neurons. *Proc. Natl. Acad. Sci. USA*, 81(10):3088–3092, 1984.
- [125] J. J. Hopfield. Pattern recognition computation using action potential timing for stimulus representation. *Nature*, 376(6535):33–36, 1995.
- [126] E. Hopp, A. Borst, and J. Haag. Subcellular mapping of dendritic activity in optic flow processing neurons. *Manuscript submitted*, 0(0):0–0, 2013.

- [127] Y. Hu, J. Trousdale, K. Josić, and E. Shea-Brown. Motif statistics and spike correlations in neuronal networks. *J. Stat. Mech.-Theory E.*, 2013(03):P03012, 2013.
- [128] Y. Hu, J. Trousdale, E. Shea-Brown, and K. Josić. Local paths to global coherence: cutting networks down to size. *arXiv preprint arXiv:1212.4239*, 2012.
- [129] S. J. Huston and H. G. Krapp. Nonlinear integration of visual and haltere inputs in fly neck motor neurons. *J. Neurosci.*, 29(42):13097–13105, 2009.
- [130] Y. Ikegaya, G. Aaron, R. Cossart, D. Aronov, I. Lampl, D. Ferster, and R. Yuste. Synfire chains and cortical songs: temporal modules of cortical activity. *Sci. Signal.*, 304(5670):559, 2004.
- [131] E. M. Izhikevich. Simple model of spiking neurons. *IEEE T. Neural Networ.*, 14(6):1569–1572, 2003.
- [132] E. M. Izhikevich. Which model to use for cortical spiking neurons? *IEEE T. Neural Networ.*, 15(5):1063–1070, 2004.
- [133] E. M. Izhikevich. Polychronization: Computation with spikes. *Neural Comput.*, 18(2):245–282, 2006.
- [134] E. T. Jaynes. Information theory and statistical mechanics. *Phys. Rev.*, 106(4):620, 1957.
- [135] L. A. Jeffress. A place theory of sound localization. *J. Comp. Physiol. Psychol.*, 41(1):35–39, 1948.
- [136] P. I. M. Johannesma. Diffusion models for the stochastic activity of neurons. *Neural Netw.*, pages 116–144, 1968.
- [137] D. H. Johnson and I. N. Goodman. Jointly Poisson processes. *arXiv preprint*, 2009.
- [138] P. X. Joris, P. H. Smith, and T. C. T. Yin. Coincidence detection in the auditory system: 50 years after Jeffress. *Neuron*, 21(6):1235–1238, December 1998.
- [139] K. Josić, E. Shea-Brown, B. Doiron, and J. de la Rocha. Stimulus-dependent correlations and population codes. *Neural Comput.*, 21(10):2774–2804, 2009.
- [140] K. Josić, E. Shea-Brown, B. Doiron, and J. de la Rocha. Stimulus-dependent correlations and population codes. *Neural Comput.*, 21(10):2274–2284, 2009.
- [141] I. Kahn, U. Knoblich, M. Desai, J. Bernstein, A. M. Graybiel, E. S. Boyden, R. L. Buckner, and C. I. Moore. Optogenetic drive of neocortical pyramidal neurons generates fMRI signals that are correlated with spiking activity. *Brain Res.*, 2013.
- [142] K. Karmeier, H. G. Krapp, and M. Egelhaaf. Population coding of self-motion: applying Bayesian analysis to a population of visual interneurons in the fly. *J. Neurophysiol.*, 94(3):2182–2194, 2005.

- [143] S. M. Kay. *Fundamentals of statistical signal processing, volume I: Estimation theory*. Prentice Hall, 1993.
- [144] M. G. Kendall, A. Stuart, and J. K. Ord. *The Advanced Theory of Statistics (Volume 1)*. Griffin (3rd Edition), 1969.
- [145] P. A. Kirkwood. On the use and interpretation of cross-correlations measurements in the mammalian central nervous system. *J. Neurosci. Meth.*, 1(2):107, 1979.
- [146] B. W. Knight. The relationship between the firing rate of a single neuron and the level of activity in a population of neurons experimental evidence for resonant enhancement in the population response. *J. Gen. Physiol.*, 59(6):767–778, 1972.
- [147] C. Koch and I. Segev. *Methods in Neuronal Modeling: From Ions to Networks*. MIT Press, 1998.
- [148] J. J. Koenderink. Optic flow. *Vision Res.*, 26(1):161–179, 1986.
- [149] H. Köndgen, C. Geisler, S. Fusi, X.-J. Wang, H.-R. Lüscher, and M. Giugliano. The dynamical response properties of neocortical neurons to temporally modulated noisy inputs in vitro. *Cereb. Cortex*, 18(9):2086–2097, 2008.
- [150] N. Kopell and G. B. Ermentrout. Chemical and electrical synapses perform complementary roles in the synchronization of interneuronal networks. *P. Natl. Acad. Sci. USA*, 101(43):15482–15487, 2004.
- [151] U. Koster, J. Sohl-Dickstein, C. Gray, and B. Olshausen. Higher order correlations within cortical layers dominate functional connectivity in microcolumns. *arXiv preprint q-bio/1301.0050*, 2013.
- [152] H. G. Krapp, B. Hengstenberg, and R. Hengstenberg. Dendritic structure and receptive-field organization of optic flow processing interneurons in the fly. *J. Neurophysiol.*, 79(4):1902–1917, 1998.
- [153] H. G. Krapp and R. Hengstenberg. Estimation of self-motion by optic flow processing in single visual interneurons. *Nature*, 384(6608):463–466, 1996.
- [154] B. Kriener, M. Helias, A. Aertsen, and S. Rotter. Correlations in spiking neuronal networks with distance dependent connections. *J. Comput. Neurosci.*, 27(2):177–200, 2009.
- [155] M. Krumin and S. Shoham. Generation of spike trains with controlled auto- and cross-correlation functions. *Neural Comput.*, 21(6):1642–1664, June 2009.
- [156] A. Kuhn, A. Aertsen, and S. Rotter. Higher-order statistics of input ensembles and the response of simple model neurons. *Neural Comput.*, 15(1):67–101, 2003.

- [157] A. Kumar, S. Rotter, and A. Aertsen. Conditions for propagating synchronous spiking and asynchronous firing rates in a cortical network model. *J. Neurosci.*, 28(20):5268–5280, 2008.
- [158] M. S. Land and T. S. Collett. Chasing behavior of houseflies (*Fannia canicularis*). *J. Comp. Physiol.*, 89(4):331–357, 1974.
- [159] L. Lapicque. Recherches quantitatives sur l'excitation électrique des nerfs traitée comme une polarisation. *J. Physiol. Pathol. Gen.*, 9:620635, 1907.
- [160] P. E. Latham and S. Nirenberg. Synergy, Redundancy, and Independence in Population Codes, Revisited. *J. Neurosci.*, 25(21):5195–5206, 2005.
- [161] P. E. Latham, B. J. Richmond, P. G. Nelson, and S. Nirenberg. Intrinsic dynamics in neuronal networks. I. Theory. *J. Neurophysiol.*, 83(2):808–827, 2000.
- [162] P. E. Latham and Y. Roudi. Role of correlations in population coding. *arXiv preprint arXiv:1109.6524*, 2011.
- [163] D. N. Lee and H. Kalmus. The optic flow field: The foundation of vision [and discussion]. *Philos. T. Roy. Soc. B*, 290(1038):169–179, 1980.
- [164] R. B. Levy and A. D. Reyes. Spatial profile of excitatory and inhibitory synaptic connectivity in mouse primary auditory cortex. *J. Neurosci.*, 32(16):5609–5619, 2012.
- [165] T. J. Lewis and J. Rinzel. Dynamics of spiking neurons connected by both inhibitory and electrical coupling. *J. Comput. Neurosci.*, 14(3):283–309, 2003.
- [166] Timothy J Lewis and Frances K Skinner. Understanding activity in electrically coupled networks using PRCs and the theory of weakly coupled oscillators. In *Phase Response Curves in Neuroscience*, pages 329–359. Springer, 2012.
- [167] B. Lindner, B. Doiron, and A. Longtin. Theory of oscillatory firing induced by spatially correlated noise and delayed inhibitory feedback. *Phys. Rev. E*, 72(6):1–14, 2005.
- [168] B. Lindner and L. Schimansky-Geier. Transmission of noise coded versus additive signals through a neuronal ensemble. *Phys. Rev. Lett.*, 86(14):2934–2937, 2001.
- [169] B. Lindner, L. Schimansky-Geier, and A. Longtin. Maximizing spike train coherence or incoherence in the leaky integrate-and-fire model. *Phys. Rev. E*, 66(3):031916, 2002.
- [170] A. Litwin-Kumar and B. Doiron. Slow dynamics and high variability in balanced cortical networks with clustered connections. *Nat. Neurosci.*, 15(11):1498–1505, September 2012.
- [171] G. E. Loeb. Optimal isn't good enough. *Biol. Cybern.*, 106(11-12):757–765, 2012.

- [172] L. L. Looger and O. Griesbeck. Genetically encoded neural activity indicators. *Curr. Opin. Neurobiol.*, 22(1):18–23, 2012.
- [173] A. Luczak, P. Bartho, and K. D. Harris. Gating of sensory input by spontaneous cortical activity. *J. Neurosci.*, 33(4):1684–1695, January 2013.
- [174] A. Luczak, P. Barthó, S. L. Marguet, G. Buzsáki, and K. D. Harris. Sequential structure of neocortical spontaneous activity in vivo. *Proc. Natl. Acad. Sci. USA*, 104(1):347–352, 2007.
- [175] W. J. Ma, V. Navalpakkam, J. M. Beck, R. van den Berg, and A. Pouget. Behavior and neural basis of near-optimal visual search. *Nat. Neurosci.*, 14(6):783–790, 2011.
- [176] J. H. Macke, P. Berens, A. S. Ecker, A. S. Tolias, and M. Bethge. Generating spike trains with specified correlation coefficients. *Neural Comput.*, 21(2):397–423, February 2009.
- [177] J. H. Macke, M. Opper, and M. Bethge. Common input explains higher-order correlations and entropy in a simple model of neural population activity. *Phys. Rev. Lett.*, 106(20):208102, 2011.
- [178] D. Marinazzo, H. J. Kappen, and S. C. A. M. Gielen. Input-driven oscillations in networks with excitatory and inhibitory neurons with dynamic synapses. *Neural Comput.*, 19(7):1739–1765, 2007.
- [179] H. Markram, J. Lübke, M. Frotscher, A. Roth, and B. Sakmann. Physiology and anatomy of synaptic connections between thick tufted pyramidal neurones in the developing rat neocortex. *J. Physiol.*, 500(Pt 2):409, 1997.
- [180] F. Marpeau, A. Barua, and K. Josić. A finite volume method for stochastic integrate-and-fire models. *J. Comput. Neurosci.*, 26(3):445–457, 2009.
- [181] Olivier Marre, Sami El Boustani, Yves Frégnac, and Alain Destexhe. Prediction of spatiotemporal patterns of neural activity from pairwise correlations. *Phys. Rev. Lett.*, 102(13):138101, 2009.
- [182] W. S. McCulloch and W. Pitts. A logical calculus of the ideas immanent in nervous activity. *B. Math. Biol.*, 5(4):115–133, 1943.
- [183] A. J. McNeil and J. Nešlehová. Multivariate Archimedean copulas, d-monotone functions and \uparrow_1 -norm symmetric distributions. *Ann. Stat.*, pages 3059–3097, 2009.
- [184] M. Meister and M. J. Berry II. The neural code of the retina. *Neuron*, 22(3):435, 1999.
- [185] J. M. Mendel. Tutorial on higher-order statistics (spectra) in signal processing and system theory: Theoretical results and some applications. *Proc. IEEE*, 79(3):278–305, 1991.

- [186] W. Mittmann, U. Koch, and M. Häusser. Feed-forward inhibition shapes the spike output of cerebellar Purkinje cells. *J. Physiol.*, 563(2):369–378, 2005.
- [187] F. Montani, E. Phoka, M. Portesi, and S. R. Schultz. Statistical modelling of higher-order correlations in pools of neural activity. *Physica A*, 392(14):10.1016/j.physa.2013.03.012, 2013.
- [188] C. Morris and H. Lecar. Voltage oscillations in the barnacle giant muscle fiber. *Biophys. J.*, 35(1):193–213, 1981.
- [189] R. B. Nelsen. *An Introduction to Copulas*. Springer Verlag, 1999.
- [190] R. B. Nelsen. *An Introduction to Copulas*. Springer, 2006.
- [191] S. Nirenberg, S. M. Carcieri, A. L. Jacobs, and P. E. Latham. Retinal ganglion cells act largely as independent encoders. *Nature*, 411(6838):698–701, 2001.
- [192] S. Nirenberg and P. E. Latham. Decoding neuronal spike trains: How important are correlations? *Proc. Natl. Acad. Sci. USA*, 100(12):7348–7353, 2003.
- [193] D. Q. Nykamp. A mathematical framework for inferring connectivity in probabilistic neuronal networks. *Math Biosci.*, 205(2):204–251, 2007.
- [194] I. E. Ohiorhenuan, F. Mechler, K. P. Purpura, A. M. Schmid, Q. Hu, and J. D. Victor. Sparse coding and high-order correlations in fine-scale cortical networks. *Nature*, 466(7306):617–621, July 2010.
- [195] A. Onken, S. Grünewälder, M. H. J. Munk, and K. Obermayer. Analyzing short-term noise dependencies of spike-counts in macaque prefrontal cortex using copulas and the flashlight transformation. *PLoS Comput. Biol.*, 5(11):e1000577, 2009.
- [196] A. Onken, S. Grünewälder, M. H. J. Munk, and K. Obermayer. Modeling short-term noise dependence of spike counts in macaque prefrontal cortex. *Adv. Neur. In.*, 21:1233–1240, 2009.
- [197] S. Ostojic and N. Brunel. From spiking neuron models to linear-nonlinear models. *PLoS Comput. Biol.*, 7(1):e1001056, 2011.
- [198] S. Ostojic, N. Brunel, and V. Hakim. How connectivity, background activity, and synaptic properties shape the cross-correlation between spike trains. *J. Neurosci.*, 29(33):10234–10253, 2009.
- [199] A.-M. M. Oswald and A. D. Reyes. Maturation of intrinsic and synaptic properties of layer 2/3 pyramidal neurons in mouse auditory cortex. *J. Neurophysiol.*, 99(6):2998–3008, 2008.

- [200] A. M. Packer, D. S. Peterka, J. J. Hirtz, R. Prakash, K. Deisseroth, and R. Yuste. Two-photon optogenetics of dendritic spines and neural circuits. *Nat. Methods*, 9(12):1202–1205, 2012.
- [201] L. Paninski, Y. Ahmadian, D. G. Ferreira, S. Koyama, K. R. Rad, M. Vidne, J. Vogelstein, and W. Wu. A new look at state-space models for neural data. *J. Comput. Neurosci.*, 29(1):107–126, 2010.
- [202] S. Panzeri, R. S. Petersen, S. R. Schultz, M. Lebedev, and M. E. Diamond. The role of spike timing in the coding of stimulus location in rat somatosensory cortex. *Neuron*, 29(3):769–777, 2001.
- [203] S. Panzeri, S. R. Schultz, A. Treves, and E. T. Rolls. Correlations and the encoding of information in the nervous system. *P. Roy. Soc. Lond. B Bio.*, 266(1423):1001–1012, 1999.
- [204] R. Perin, T. K. Berger, and H. Markram. A synaptic organizing principle for cortical neuronal groups. *P. Natl. Acad. Sci. USA*, 108(13):5419–5424, 2011.
- [205] V. Pernice, B. Staude, S. Cardanobile, and S. Rotter. How structure determines correlations in neuronal networks. *PLoS Comput. Biol.*, 7(5):e1002059, 05 2011.
- [206] J.-P. Pfister and W. Gerstner. Triplets of spikes in a model of spike timing-dependent plasticity. *J. Neurosci.*, 26(38):9673–9682, 2006.
- [207] J. W. Pillow, J. Shlens, L. Paninski, A. Sher, A. M. Litke, E. J. Chichilnisky, and E. P. Simoncelli. Spatio-temporal correlations and visual signalling in a complete neuronal population. *Nature*, 454(7207):995–999, July 2008.
- [208] F. Pouille and M. Scanziani. Enforcement of temporal fidelity in pyramidal cells by somatic feed-forward inhibition. *Science*, 293(5532):1159–1163, 2001.
- [209] K. Rajan and L. F. Abbott. Eigenvalue spectra of random matrices for neural networks. *Phys. Rev. Lett.*, 97(18):188104, 2006.
- [210] S. Ramón y Cajal. *Neuron Theory Or Reticular Theory?: Objective Evidence of the Anatomical Unity of Nerve Cells*. CSIC-Dpto. de Publicaciones, 1954.
- [211] A. V. Rangan. Diagrammatic expansion of pulse-coupled network dynamics in terms of subnetworks. *Phys. Rev. E*, 80(3):036101, 2009.
- [212] A.V. Rangan. Diagrammatic expansion of pulse-coupled network dynamics. *Phys. Rev. Lett.*, 102(15):158101, 2009.
- [213] S. G. Rao, G. V. Williams, and P. S. Goldman-Rakic. Isodirectional tuning of adjacent interneurons and pyramidal cells during working memory: evidence for microcolumnar organization in pfc. *J. Neurophysiol.*, 81(4):1903–1916, 1999.

- [214] G. D. Reddy, K. Kelleher, R. Fink, and P. Saggau. Three-dimensional random access multiphoton microscopy for functional imaging of neuronal activity. *Nat. Neurosci.*, 11(6):713–720, June 2008.
- [215] W. Reichardt. Evaluation of optical motion information by movement detectors. *J. Comp. Phys. A*, 161(4):533–547, 1987.
- [216] A. Renart, N. Brunel, and X.-J. Wang. Mean-field theory of irregularly spiking neuronal populations and working memory in recurrent cortical networks. In J. Feng, editor, *Computational Neuroscience: A Comprehensive Approach*, pages 431–490. CRC Press, Boca Raton, 2004.
- [217] A. Renart, J. de la Rocha, P. Bartho, L. Hollender, N. Parga, A. Reyes, and K. D. Harris. The asynchronous state in cortical circuits. *Science*, 327(5965):587–590, 2010.
- [218] L. M. Ricciardi and L. Sacerdote. The Ornstein-Uhlenbeck process as a model for neuronal activity. *Biol. Cybern.*, 35(1):1–9, 1979.
- [219] L. M. Ricciardi and C. E. Smith. *Diffusion Processes and Related Topics in Biology*. Springer-Verlag Berlin, 1977.
- [220] M. J. E. Richardson. Effects of synaptic conductance on the voltage distribution and firing rate of spiking neurons. *Phys. Rev. E*, 69(5):051918, 2004.
- [221] M. J. E. Richardson. Firing-rate response of linear and nonlinear integrate-and-fire neurons to modulated current-based and conductance-based synaptic drive. *Phys. Rev. E*, 76(2):021919, 2007.
- [222] M. J. E. Richardson. Spike-train spectra and network response functions for nonlinear integrate-and-fire neurons. *Biol. Cybern.*, 99(4):381–392, 2008.
- [223] M. J. E. Richardson. Dynamics of populations and networks of neurons with voltage-activated and calcium-activated currents. *Phys. Rev. E*, 80(2):021928, 2009.
- [224] M. J. E. Richardson, N. Brunel, and V. Hakim. From subthreshold to firing-rate resonance. *J. Neurophysiol.*, 89(5):2538–2554, 2003.
- [225] M. J. E. Richardson and W. Gerstner. Synaptic shot noise and conductance fluctuations affect the membrane voltage with equal significance. *Neural Comput.*, 17(4):923–947, 2005.
- [226] M. J. E. Richardson and R. Swarbrick. Firing-rate response of a neuron receiving excitatory and inhibitory synaptic shot noise. *Phys. Rev. Lett.*, 105(17):178102, 2010.
- [227] H. Risken. *The Fokker-Planck Equation: Methods of Solution and Applications*. Springer Verlag, Berlin, 1996.
- [228] C. P. Robert and G. Casella. *Monte Carlo Statistical Methods*. Springer-Verlag, 2004.

- [229] S. R. Robinson, E. C. Hampson, M. N. Munro, and D. I. Vaney. Unidirectional coupling of gap-junctions between neuroglia. *Science*, 262(5136):1072–1074, 1993.
- [230] R. Romo, A. Hernandez, A. Zainos, and E. Salinas. Correlated neuronal discharges that increase coding efficiency during perceptual discrimination. *Neuron*, 38:649–657, 2003.
- [231] R. J. Rosenbaum, F. Marpeau, J. Ma, A. Barua, and K. Josić. Finite volume and asymptotic methods for stochastic neuron models with correlated inputs. *J. Math. Bio.*, 65(1):1–34, 2012.
- [232] R. J. Rosenbaum, J. Trousdale, and K. Josić. Pooling and correlated neural activity. *Front. Comput. Neurosci.*, 4, 2010.
- [233] R. J. Rosenbaum, J. Trousdale, and K. Josić. The effects of pooling on spike train correlations. *Front. Neurosci.*, 5, 2011.
- [234] S. M. Ross. *Stochastic Processes*. Wiley, 2 edition, 1 1995.
- [235] Y. Roudi, S. Nirenberg, and P. E. Latham. Pairwise maximum entropy models for studying large biological systems: When they can work and when they can't. *PLoS Comput. Biol.*, 5(5):e1000380, 2009.
- [236] A. Roxin. The role of degree distribution in shaping the dynamics in networks of sparsely connected spiking neurons. *Front. Comput. Neurosci.*, 5(8):1–15, 2011.
- [237] M. Rudolph and A. Destexhe. The discharge variability of neocortical neurons during high-conductance states. *Neuroscience*, 119(3):855–874, 2003.
- [238] E. Salinas and L. F. Abbott. Vector reconstruction from firing rates. *J. Comput. Neurosci.*, 1(1):89–107, 1994.
- [239] E. Salinas and T. J. Sejnowski. Correlated neuronal activity and the flow of neural information. *Nat. Rev. Neurosci.*, 2:539–550, 2001.
- [240] C. Schilstra and J. H. van Hateren. Blowfly flight and optic flow. I. Thorax kinematics and flight dynamics. *J. Exp. Biol.*, 202(11):1481–1490, 1999.
- [241] E. Schneidman, M. J. Berry, R. Segev, and W. Bialek. Weak pairwise correlations imply strongly correlated network states in a neural population. *Nature*, 440(20):1007–1012, 2006.
- [242] E. Schneidman, W. Bialek, and M. J. Berry II. Synergy, redundancy, and independence in population codes. *J. Neurosci.*, 23(37):11539–11553, 2003.
- [243] I. Segev, J. Rinzel, and G. M. Shepherd. *The theoretical foundations of dendritic function: the collected papers of Wilfrid Rall with commentaries*. MIT Press, 1994.

- [244] P. Seriès, P. E. Latham, and A. Pouget. Tuning curve sharpening for orientation selectivity: coding efficiency and the impact of correlations. *Nat. Neurosci.*, 7(10):1129–1135, 2004.
- [245] M. N. Shadlen and W. T. Newsome. The variable discharge of cortical neurons: implications for connectivity, computation, and information coding. *J. Neurosci.*, 18(10):3870–3896, 1998.
- [246] M. Shamir and H. Sompolinsky. Nonlinear population codes. *Neural Comput.*, 16(6):1105–1136, June 2004.
- [247] M. Shamir and H. Sompolinsky. Implications of neuronal diversity on population coding. *Neural Comput.*, 18(8):1951–1986, 2006.
- [248] E. Shea-Brown, K. Josić, J. de la Rocha, and B. Doiron. Correlation and synchrony transfer in integrate-and-fire neurons: basic properties and consequences for coding. *Phys. Rev. Lett.*, 100(10):108102, 2008.
- [249] E. Shea-Brown, K. Josić, J. de La Rocha, and B. Doiron. Correlation and synchrony transfer in integrate-and-fire neurons: Basic properties and consequences for coding. *Phys. Rev. Lett.*, 100(10):108102, 2008.
- [250] G. M. Shepherd. *Foundations of the Neuron Doctrine*. Oxford University Press, Oxford, 1991.
- [251] J. Shlens, G. D. Field, J. L. Gauthier, M. Greschner, A. Sher, A. M. Litke, and E. J. Chichilnisky. The structure of large-scale synchronized firing in primate retina. *J. Neurosci.*, 29(15):5022–5031, 2009.
- [252] J. Shlens, G. D. Field, J. L. Gauthier, M. I. Grivich, D. Petrusca, A. Sher, A. M. Litke, and E.J. Chichilnisky. The structure of multi-neuron firing patterns in primate retina. *J. Neurosci.*, 26:8254–8266, 2006.
- [253] G. Silberberg, M. Bethge, H. Markram, K. Pawelzik, and M. Tsodyks. Dynamics of population rate codes in ensembles of neocortical neurons. *J. Neurophysiol.*, 91(2):704–709, 2004.
- [254] W. Singer. Neuronal synchrony: A versatile code review for the definition of relations? *Neuron*, 24:49–65, 1999.
- [255] P. J. Sjöström, G. G. Turrigiano, and S. B. Nelson. Rate, timing, and cooperativity jointly determine cortical synaptic plasticity. *Neuron*, 32(6):1149–1164, 2001.
- [256] A. Sklar. Random variables, joint distribution functions, and copulas. *Kybernetika*, 9(6):449–460, 1973.
- [257] W. R. Softky and C. Koch. The highly irregular firing of cortical cells is inconsistent with temporal integration of random EPSPs. *J. Neurosci.*, 13(1):334–350, 1993.

- [258] D. C. Somers, S. B. Nelson, and M. Sur. An emergent model of orientation selectivity in cat visual cortical simple cells. *J. Neurosci.*, 15(8):5448–5465, 1995.
- [259] H. Sompolinsky, H. Yoon, K. Kang, and M. Shamir. Population coding in neuronal systems with correlated noise. *Phys. Rev. E*, 64(5 Pt 1):051904, 2001.
- [260] S. Song, P. J. Sjöström, M. Reigl, S. Nelson, and D. B. Chklovskii. Highly nonrandom features of synaptic connectivity in local cortical circuits. *PLoS Biol.*, 3(3):e68, 2005.
- [261] O. Sporns. The human connectome: a complex network. *A. NY Acad. Sci.*, 1224(1):109–125, 2011.
- [262] O. Sporns, G. Tononi, and R. Kötter. The human connectome: a structural description of the human brain. *PLoS Comput. Biol.*, 1(4):e42, 2005.
- [263] B. Staude, S. Rotter, and S. Grün. CuBIC: cumulant based inference of higher-order correlations in massively parallel spike trains. *J. Comput. Neurosci.*, 29(1-2):327–350, 2010.
- [264] R. B. Stein. Some models of neuronal variability. *Biophys. J.*, 7(1):37–68, 1967.
- [265] C. F. Stevens and A. M. Zador. Input synchrony and the irregular firing of cortical neurons. *Nat. Neurosci.*, 1(3):210–217, 1998.
- [266] I. H. Stevenson, B. M. London, E. R. Oby, N. A. Sachs, J. Reimer, B. Englitz, S. V. David, S. A. Shamma, T. J. Blanche, K. Mizuseki, A. Zandvakili, N. G. Hatsopoulos, L. E. Miller, and K. P. Kording. Functional connectivity and tuning curves in populations of simultaneously recorded neurons. *PLoS Comput. Biol.*, 8(11):e1002775, 2012.
- [267] R. L. Stratonovich and R. A. Silverman. *Topics in the Theory of Random Noise*, volume 2. Gordon and Breach, New York, 1967.
- [268] N. J. Strausfeld and U. K. Bassemir. Lobula plate and ocellar interneurons converge onto a cluster of descending neurons leading to neck and leg motor neuropil in *Calliphora erythrocephala*. *Cell Tissue Res.*, 240(3):617–640, 1985.
- [269] N. J. Strausfeld, H. S. Seyan, and J. J. Milde. The neck motor system of the fly *Calliphora erythrocephala*. *J. Comp. Physiol. A*, 160(2):205–224, 1987.
- [270] A. Tang et al. A maximum entropy model applied to spatial and temporal correlations from cortical networks in vitro. *J. Neurosci.*, 28:505–518, 2008.
- [271] T. Tetzlaff, M. Buschermöhle, T. Geisel, and M. Diesmann. The spread of rate and correlation in stationary cortical networks. *Neurocomputing*, 52:949–954, 2003.

- [272] T. Tetzlaff, S. Rotter, E. Stark, M. Abeles, A. Aertsen, and M. Diesmann. Dependence of neuronal correlations on filter characteristics and marginal spike train statistics. *Neural Comput.*, 20(9):2133–2184, 2008.
- [273] A. M. Thomson and C. Lamy. Functional maps of neocortical local circuitry. *Front. Neurosci.*, 1(1):19, 2007.
- [274] S. Thorpe, A. Delorme, and R. van Rullen. Spike-based strategies for rapid processing. *Neural Netw.*, 14(6-7):715–725, 2001.
- [275] G. Tkačik, J. S. Prentice, V. Balasubramanian, and E. Schneidman. Optimal population coding by noisy spiking neurons. *P. Natl. Acad. Sci. USA*, 107(32):14419–14424, 2010.
- [276] T. Toyoizumi, K. R. Rad, and L. Paninski. Mean-field approximations for coupled populations of generalized linear model spiking neurons with markov refractoriness. *Neural Comput.*, 21(5):1203–1243, 2009.
- [277] R. D. Traub, N. Kopell, A. Bibbig, E. H. Buhl, F. E. N. LeBeau, and M. A. Whittington. Gap junctions between interneuron dendrites can enhance synchrony of gamma oscillations in distributed networks. *J. Neurosci.*, 21(23):9478–9486, 2001.
- [278] J. Trousdale, Y. Hu, E. Shea-Brown, and K. Josić. Impact of network structure and cellular response on spike time correlations. *PLoS Comput. Biol.*, 8(3):e1002408, 2012.
- [279] H. C. Tuckwell. *Introduction to theoretical neurobiology. Vol. 1, Linear cable theory and dendritic structure and stochastic theories*. Cambridge University Press, 1988.
- [280] H. C. Tuckwell. *Introduction to Theoretical Neurobiology: Volume 2, Nonlinear and Stochastic Theories*, volume 8. Cambridge University Press, 2005.
- [281] E. S. Valenstein. *The War of the Soups and the Sparks*. Columbia University Press, 2005.
- [282] J. H. van Hateren and C. Schilstra. Blowfly flight and optic flow. II. Head movements during flight. *J. Exp. Biol.*, 202(11):1491–1500, 1999.
- [283] J. H. van Hateren and A. van der Schaaf. Independent component filters of natural images compared with simple cells in primary visual cortex. *P. Roy. Soc. Lond. B Bio.*, 265(1394):359–366, Mar 1998.
- [284] C. van Vreeswijk and H. Sompolinsky. Chaos in neuronal networks with balanced excitatory and inhibitory activity. *Science*, 274:1724–1726, 1996.
- [285] C. van Vreeswijk and H. Sompolinsky. *Irregular firing in cortical circuits with inhibition/excitation balance*. Plenum Press, New York, 1997.

- [286] I. Vanzetta, T. Deneux, A. Kaszás, G. Katona, and B. Rozsa. Functional imaging using two-photon microscopy in living tissue. In *Visualization Techniques*, pages 129–164. Springer, 2012.
- [287] J. C. Vasquez, O. Marre, A. G. Palacios, M. J. Berry II, and B. Cessac. Gibbs distribution analysis of temporal correlations structure in retina ganglion cells. *J Physiol.-Paris*, 106(3):120–127, 2012.
- [288] C. Vreeswijk, L. F. Abbott, and G. B. Ermentrout. When inhibition not excitation synchronizes neural firing. *J. Comput. Neurosci.*, 1(4):313–321, 1994.
- [289] J. Wang, F. Wagner, D. A. Borton, J. Zhang, I. Ozden, R. D. Burwell, A. V. Nurmikko, R. van Wagenen, I. Diester, and K. Deisseroth. Integrated device for combined optical neuromodulation and electrical recording for chronic in vivo applications. *J. Neural Eng.*, 9(1):016001, 2012.
- [290] X.-J. Wang. Neurophysiological and computational principles of cortical rhythms in cognition. *Physiol. Rev.*, 90(3):1195–1268, 2010.
- [291] X.-J. Wang and G. Buzsáki. Gamma oscillation by synaptic inhibition in a hippocampal interneuronal network model. *J. Neurosci.*, 16(20):6402–6413, 1996.
- [292] F. Weber, H. Eichner, H. Cuntz, and A. Borst. Eigenanalysis of a neural network for optic flow processing. *New J. Phys.*, 10(1):015013, 2008.
- [293] F. Weber, C. K. Machens, and A. Borst. Disentangling the functional consequences of the connectivity between optic-flow processing neurons. *Nat. Neurosci.*, 15(3):441–448, 2012.
- [294] M. Wehr and A. M. Zador. Balanced inhibition underlies tuning and sharpens spike timing in auditory cortex. *Nature*, 426(6965):442–446, 2003.
- [295] N. Weiler, L. Wood, J. Yu, S. A. Solla, and G. M. G. Shepherd. Top-down laminar organization of the excitatory network in motor cortex. *Nat. Neurosci.*, 11(3):360–366, 2008.
- [296] A. Wertz, A. Borst, and J. Haag. Nonlinear integration of binocular optic flow by DNOVS2, a descending neuron of the fly. *J. Neurosci.*, 28(12):3131–3140, 2008.
- [297] A. Wertz, B. Gaub, J. Plett, J. Haag, and A. Borst. Robust coding of ego-motion in descending neurons of the fly. *J. Neurosci.*, 29(47):14993–15000, 2009.
- [298] A. Wertz, J. Haag, and A. Borst. Local and global motion preferences in descending neurons of the fly. *J. Comput. Phys. A*, 195(12):1107–1120, 2009.
- [299] B. White, L. F. Abbott, and J. Fiser. Suppression of cortical neural variability is stimulus- and state-dependent. *J. Neurophysiol.*, 108(9):2383–2392, November 2012.

- [300] J. G. White, E. Southgate, J. N. Thomson, and S. Brenner. The structure of the nervous system of the nematode *Caenorhabditis elegans*. *Philos. T. Roy. Soc. B*, 314(1165):1–340, 1986.
- [301] R. W. Williams and K. Herrup. The control of neuron number. *Ann. Rev. Neurosci.*, 11(1):423–453, 1988.
- [302] G. K. Wu, R. Arbuckle, B. Liu, H. W. Tao, and Li. I. Zhang. Lateral sharpening of cortical frequency tuning by approximately balanced inhibition. *Neuron*, 58(1):132, 2008.
- [303] Lei Xiao, Dan-ke Zhang, Yuan-qing Li, Pei-ji Liang, and Si Wu. Adaptive neural information processing with dynamical electrical synapses. *Front. Comput. Neurosci.*, 7, 2013.
- [304] N. Xu, M. T. Harnett, S. R. Williams, D. Huber, D. H. O’Connor, K. Svoboda, and J. C. Magee. Nonlinear dendritic integration of sensory and motor input during an active sensing task. *Nature*, 492(7428):247–251, December 2012.
- [305] P. Xue-Kun Song. Multivariate dispersion models generated from gaussian copula. *Scand. J. Stat.*, 27(2):305–320, 2000.
- [306] A. M. Yaglom. *An Introduction to the Theory of Stationary Random Functions*. Courier Dover Publications, 2004.
- [307] Jun Yan. Enjoy the joy of copulas: with a package copula. *J. Stat. Softw.*, 21(4):1–21, 2007.
- [308] S. Yu, H. Yang, H. Nakahara, G. S. Santos, D. Nikolić, and D. Plenz. Higher-order interactions characterized in cortical activity. *J. Neurosci.*, 31(48):17514–17526, 2011.
- [309] L. Zhao, B. Beverlin, T. Netoff, and D. Q. Nykamp. Synchronization from second order network connectivity statistics. *Front. Comput. Neurosci.*, 5:1–16, Jan 2011.
- [310] E. Zohary, M. N. Shadlen, and W. T. Newsome. Correlated neuronal discharge rate and its implications for psychophysical performance. *Nature*, 370(6485):140–143, 1994.